Electromagnetic stirring using a travelling magnetic field

A thesis presented to

The University of Waikato

in fulfillment of the thesis requirement

for the degree of

Doctor of Philosophy

by

Mohd. Noor bin Saad

The University of Waikato
Te Whare Wānanga o Waikato

The University of Waikato

July, 2004

Abstract

Electromagnetic stirring of liquid metal is widely used during continuous casting in iron and steel industries to improve the quality of the products. In this thesis we aim to develop a theory for traveling linear stirrers in closed channels.

We consider a channel filled with an incompressible, electrically conducting viscous fluid. A two dimensional multi Fourier-component magnetic field is moved along the channel. Induced currents in the fluid interact with the field to give a Lorentz force which drives fluid motion. When the magnetic Reynolds number is large the imposed magnetic field is changed significantly.

In this study we consider uniformly-moving and accelerating fields.

For the initial fluid motion due to a two Fourier-component source moving at a constant velocity, with R_m small, an analytical solution is derived. The Lax-Wendroff numerical scheme is used to calculate the flow until a steady state is reached. For effective stirring the width of the channel has to be less than the field wavelength.

The problem of a solid conductor in a steadily-moving field at finite R_m is investigated next. It is shown that as the magnetic Reynolds number increases the flux inclines in the direction of the motion. In the study of the fluid flow at finite R_m it is shown that the narrower the channel the better and stronger will be the magnetic field's penetration. Most effective stirring occurs when magnetic Reynolds number is around 100.

When the magnetic field is given a time-dependent velocity at large R_m we show that more eddies are created immediately after a velocity reversal. In the process, the layers of magnetic fieldlines on the boundaries incline in the opposite direction of the applied field. Simple harmonic motion of the field is also effective, and becomes more so as the frequency increases (at fixed wavelength) but at the expense of overall fluid velocity.

Acknowledgements

I would like to thank and express my sincere appreciation to my chief supervisor Associate Professor Alfred Sneyd for his patient help and encouragement over the years that I have been working part-time to complete this thesis. I have never met anyone who always has so much time for his students. Thanks also to my second supervisor Professor Ian Craig for encouraging me along with his cheerful comments on most Friday afternoons and for his help in Chapter 6.

A special thanks goes to Stephen Joe for his earlier help in Linux and computer support so that I could work from home.

I am sure many staff in the Mathematics Department would be pleased and relieved to finally see the completion of this work and I would like to thank those who have been encouraging me especially Judi and Lyn who were at one stage my fellow graduate students. Thanks to Jacob and Farhad for your help.

I would not have been able to complete this work without the help of many of my close friends who have been helping in looking after Nazuri especially during the last two months. A special appreciation and many thanks go to Rahman and Pam, Nakir and Hanim for giving their time for Nazuri and myself. I will not forget your help.

Last of all but the most important my own family: Adibah, Salina, Shariman and the young one Nazuri who have to sacrifice a lot of their time without me being around especially on the weekends and many school holidays. Daddy loves you all very much for your support and love.

Contents

List of Figures

Chapter 1

MHD channel flow

1.1 Introduction

Magnetohydrodynamics (MHD) plays an important role in Electromagnetic Processing of Materials (EPM) worldwide, especially in the last decade. EPM technologies are widely used in continuous casting of steel for example: electromagnetic stirrers and electromagnetic braking (Garnier [7]). In particular, electromagnetic fields are widely used to generate and control the flow of liquid metal and in the process of solidification.

One of the important early applications of magnetohydrodynamics (MHD) in metallurgy is in the stirring of liquid steel during continuous casting. Electromagnetic stirring improves the quality of the products by helping (i) to eliminate pinholes due to escaping gases, (ii) to remove inclusions, and (iii) to make a more homogeneous interior structure. Magnetic fields have many advantages that have no equivalent in other electrothermal techniques. They offer very clean processes that produce clean materials. A more detailed discussion on electromagnetic stirring in continuous casting of steel is given by Marr [11] and an informative review of electromagnetic stirring is given by Davidson [5]. Fujii [6] gives a more recent and wider discussion of state-of-the-art electromagnetic processing in the Japanese iron and steel industry. The common types of stirrer are rotary, linear(Takeuchi [23])

and (less common) helical. An interesting and informative review on the theory of electromagnetic stirring by AC fields is given by Sneyd [21].

An early theoretical investigation of flow in liquid metal induced by a rotating magnetic field was due to Moffatt [12]. He considered the interior of an insulating cylindrical container which is supposed filled with an incompressible, electrically conducting, viscous fluid. An externally applied magnetic field is caused to rotate uniformly about an axis parallel to the cylinder generators so that the magnetic Reynolds number R_m (based on rotation) is large. He showed that the fluid will rotate as a rigid body inside a viscous boundary layer. Sneyd [19] considered a circular cylinder in an alternating field under the assumption of small R_m. He showed that switching magnetic fields on and off, or placing the cylinder in an alternating field, will produce fluid motion in the form of four cylindrical eddies, one in each quadrant of the cross-section of the cylinder. Dalberg [4] derived a general solution for the velocity field in a circular cylinder generated by a magnetic field rotating at an arbitrary rate and showed that the rate of vorticity generation in a circular cylinder was steady. Sneyd [20] showed that the curl of the Lorentz force ($\boldsymbol{J}\times\boldsymbol{B}$) is independent of time only for the case of two dimensional geometry. Witkowski, Marty and Walker [24] considered a liquid metal flow driven by a rotating magnetic field in a finite-length cylinder as a function of the field frequency. They found that in the high-frequency case, the magnetic field is expelled from the liquid-metal except in a skin-depth layer along the side and top walls of the cylinder.

Kamka and Moffatt [9] considered pressure-driven flow along a channel in the presence of an applied periodic magnetic field. They found that flux expulsion due to reconnection of field lines occurred when the pressure gradient was sufficiently large. This lead to a decrease in Lorentz forces, hence to an acceleration of the flow and stronger flux expulsion. When viscous effects were weak (i.e. at high Hartmann number) this created a "dynamic runaway effect".

1.2 Summary of M.Sc. thesis

In his dissertation Saad [18] investigated the generation of fluid motion in a channel by an applied magnetic field moving at a constant velocity. He considered a channel of infinite length and width, with walls $z = \pm a$ containing an incompressible conducting fluid of density ρ, kinematic viscosity ν, and electrical conductivity σ. An applied two dimensional periodic magnetic field $\mathbf{B} = B_x(x-Ut, z)\hat{\boldsymbol{x}} + B_z(x-Ut, z)\hat{\boldsymbol{z}}$ moved with constant velocity $U\hat{\boldsymbol{x}}$ relative to the channel. The magnetic field on the boundaries is limited to at most two Fourier components:

$$B_z \;=\; B_0\,(\cos[k(x-Ut)] \;+\; b\cos[2k(x-Ut)]) \tag{1.1}$$

where b represents the ratio of the 2nd Fourier-component field to the first, the wavenumber $k = 2\pi/L$ and L is the wavelength of the applied magnetic field. Two assumptions were made. First, the magnetic Reynolds number, $R_m(= Ua/\eta)$ was small, which meant the magnetic field was unaffected by the relative motion of the fluid. Second, the resulting fluid velocity $\boldsymbol{v}$ was small compared to the velocity $\mathbf{U}$ of the applied magnetic field. (This is equivalent to the assumption that the Hartmann number $M = B_0\,a\,(\sigma/\rho\nu)^{\frac{1}{2}}$ is small.)

He showed that the curl of the Lorentz force $\mathbf{J} \times \mathbf{B}$ has only a $y-$component:

$$\nabla \times (\mathbf{J} \times \mathbf{B}) \;=\; \frac{1}{2}\sigma\frac{\partial}{\partial z}\left(B^2\right)\,\hat{\boldsymbol{y}}, \tag{1.2}$$

where $B^2 = B_x^2 + B_z^2$.

In the case of one Fourier component it was shown that the expression for the curl of the Lorentz force is independent of time (Moffatt [12] and Sneyd [20]). For the case of open channel where the mean pressure gradient is zero it was found that as $K(= ka)$ increases, the parabolic shape of the velocity profile flattens towards a plug flow uniform across the channel, apart from two highly sheared layers at $z = \pm a$ of thickness of order of $a\,K^{-1}$. For small values of K the velocity profile takes the form of a parabola as in plane Poiseuille flow. In the closed channel case, i.e. walls at $x = \pm\infty$, it was shown that the adverse pressure gradient required to ensure zero

total flux across the channel, results in reverse flow in the channel. In both cases the flow was purely in the $x-$direction and steady, but the closed channel case has two points of inflection, which indicates that the flow may be unstable according to Fjørtoft's Theorem (Yih [25, page 471]). The ensuring turbulence may be effective in stirring the flow.

In the case of two Fourier components it was shown that the curl of the Lorentz force is time dependent. Only the case of open channel was investigated. It was assumed that the fluid would reach the quasi-steady state which is periodic in time and x (stationary relative to the observer moving with the field.) It was found that the two Fourier-component fields generate only weak cross-flow, and may not be very effective in electromagnetic stirring.

1.3 Thesis plan

When a magnetic field $\boldsymbol{B}$ is moved across an electrically conducting fluid it has the effect of causing fluid motion. The motion of conducting fluid across the magnetic lines of force creates potential differences which, in general, cause electric currents $\boldsymbol{J}$ to flow. The magnetic fields associated with these currents modify the applied magnetic fields to $\boldsymbol{B} + \boldsymbol{b}$, say, where $\boldsymbol{b}$ is called the induced electric field. At the same time, the flow of electric current across a magnetic field results in a body force, called Lorentz force, $\boldsymbol{J} \times \boldsymbol{B}$, which in turns modifies the fluid flow.

The aim of this work is to develop a theory for traveling linear stirrers in closed channels. One simple way of stirring liquid metal is by moving a periodic magnetic field with several Fourier-components, at a uniform speed along the channel. Alternatively the applied magnetic field may be accelerated and decelerated. A further variation is to move the applied field to and fro along the channel.

In the chapters 2–4 we study the flow of the liquid metal subjected to a uniformly moving magnetic field but with the condition that the magnetic Reynolds number R_m and magnetic interaction parameter $\mathcal{N}$ are small. In other words the flow due

the Lorentz Force is not strong enough to affect the applied magnetic field. In chapter 3 the initial motion due to a two Fourier-component field which moves at a constant speed, U, along the channel is considered. If we neglect viscous diffusion and convection this problem has an analytical solution which can be used for comparison with numerical results for initial motion in chapter 4. We examine the effect of channel width and it is shown that the eddies are more pronounced when the aspect ratio $\frac{a}{L} < 0.5$.

In chapter 4 we extend our investigation to the time-dependent fluid flow for small R_m using numerical methods to complete the flow evolution picture. We investigate two cases: (i) flow due to a two Fourier-component field, and (ii) flow due to multi Fourier-component field which moves at a constant velocity $U\hat{\boldsymbol{x}}$. The Lax-Wendroff method is used in these calculations.

In the remaining chapters we turn our attention to finite R_m since in practice the conducting fluid flow is likely to have some significant effect on the applied magnetic field $\boldsymbol{B}$. In chapter 5 we investigate the effect on the applied single Fourier-component magnetic field of a moving solid metal. We test our numerical scheme with this simple problem since it has an analytical solution. In chapter 6 we study the same fluid flow problem as in chapter 4 but with arbitrary R_m. We perform calculations with $R_m \gg 1$ to study the variation of steady state velocity as a function of R_m, and the initial acceleration of the fluid at large R_m.

It is interesting to consider the fluid flow when the velocity of the applied magnetic field is time-dependent. In chapter 7 we investigate two examples of time-dependent velocity: in the first the applied field is accelerated, then moves for a period at constant velocity, then decelerates to a negative velocity; in the second the field is given a simple harmonic motion.

In chapter 8 we summarize the conclusions and outline suggestions for further work.

Chapter 2

Outline of the problem and MHD equations

2.1 Introduction

In this thesis we investigate the flow of an electrically conducting fluid in a closed channel due to travelling periodic applied magnetic field. Since almost the same set of governing magnetohydrodynamic equations are used throughout this thesis and are in dimensionless form it seems logical to cover the non-dimensionalisation process in this chapter. The reason for non-dimensionalisation is that it highlights the relative importance of terms through various dimensionless numbers.

2.2 Outline of the problem

In all chapters in this thesis, with the exception of chapter 5, we consider a channel of infinite length and width, side walls $y = \pm b$, with upper and lower walls $z = \pm a$ containing an incompressible conducting fluid of density ρ, kinematic viscosity ν and electrical conductivity σ. In chapters 3 and 4 at time $t = 0$ an applied two dimensional periodic magnetic field of wavelength L,

$$\boldsymbol{B} = B_x(x - Ut, z)\,\hat{\boldsymbol{x}} + B_z(x - Ut, z)\,\hat{\boldsymbol{z}},$$

is moved with a uniform velocity $U\hat{\boldsymbol{x}}$ relative to the channel, but in chapters 6 and 7 the magnetic field is moved with a time-dependent velocity. It is assumed that: (i) $b \gg a$ and (ii) the walls $z = \pm a$ and $y = \pm b$ are highly conducting so that any current in the $y-$direction has a return path and there is no applied electric field in the y-direction. This is a theoretical idealization of two-dimensional flow where $\boldsymbol{v} = (u(x,z), 0, v(x,z))$ in a wide rectangular duct in which edge effects of the side walls $y = \pm b$ may be neglected (Roberts [17, page 173]). We also assume that the channel is very long in x-direction but closed, so the mean flow has to be zero i.e.

$$\int_{-a}^{a} u(x,z)\, dz \;=\; 0.$$

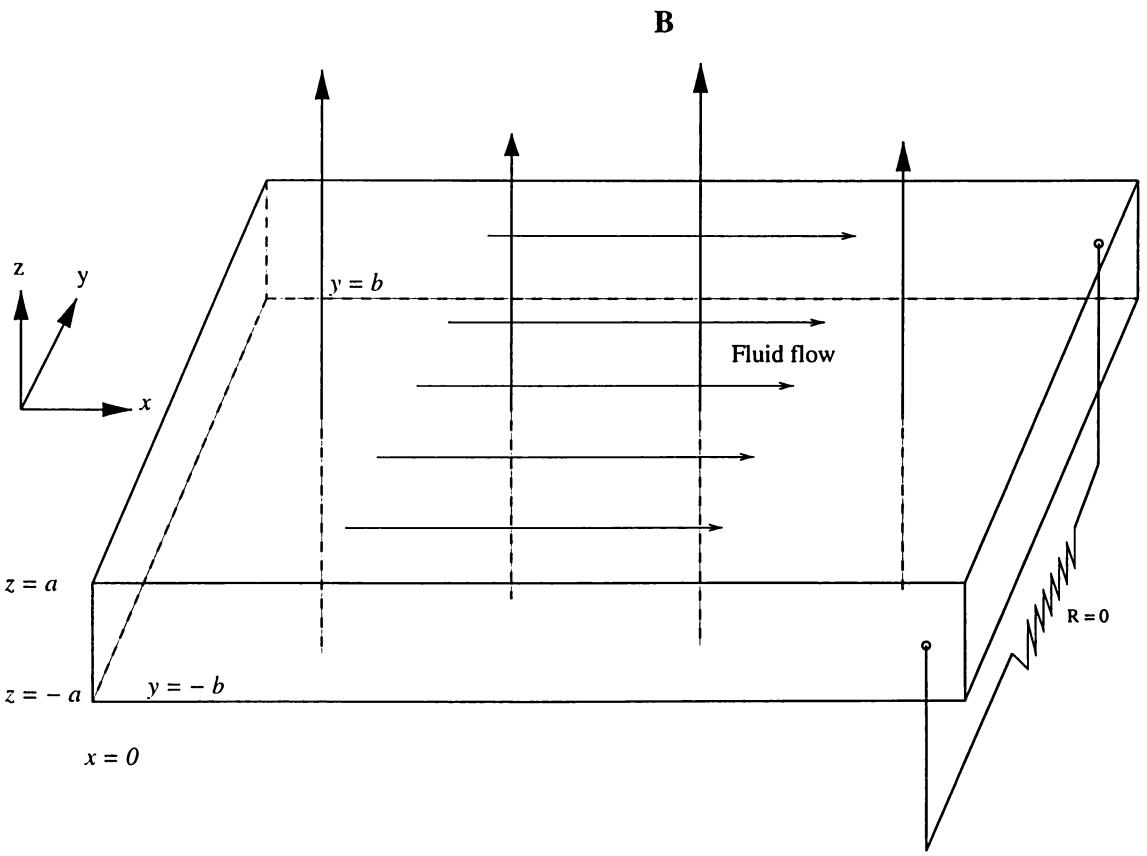

Figure 2.1: Channel flow

We are assuming that the applied magnetic field $\boldsymbol{B}$ is generated by coils (or

permanent magnets) outside the channel. The following irrotational and divergence conditions hold:

$$\nabla \times \boldsymbol{B} = 0, \tag{2.1a}$$

$$\nabla \cdot \boldsymbol{B} = 0. \tag{2.1b}$$

Thus we can write

$$\boldsymbol{B} = \nabla \phi, \tag{2.2}$$

satisfying

$$\nabla^2 \phi = 0, \tag{2.3}$$

which is the Laplace's equation, where ϕ is magnetic potential function.

The applied two dimensional magnetic field is the multi Fourier-component field

$$\left(\frac{\partial \phi}{\partial z}\right)_{z=\pm a} = B_0 \sum_{n=1}^{N} b_n \cos[nk(x - Ut)], \tag{2.4}$$

where b_n are constants and the wavenumber, k is $k = 2\pi/L$, where L is the wavelength of the applied magnetic field. By varying N and b_n we can investigate different problems with a variety of multi Fourier-component fields.

In chapters 2–4 we make two important assumption:

- The magnetic Reynolds number R_m (where $R_m = Ua/\eta$, η the magnetic diffusitivity), is small, which means the magnetic field is unaffected by the relative motion of the fluid;

- The resulting fluid velocity $\boldsymbol{u}$ is small compared to the velocity U of the applied magnetic field. This is equivalent to the magnetic interaction parameter $\mathcal{N} \ll 1$.

In chapter 5 we consider the effect of the motion of the solid conductor in a magnetic field on the applied magnetic field and in chapters 6 and 7, the fluid flow affects the applied field which means the magnetic Reynolds number, R_m, and Hartmann number, M, can be finite.

It can be seen in chapters 6 and 7 that the applied magnetic field plays a very important role in affecting the motion of the fluid.

2.2.1 The applied magnetic field

Let the initial potential field $\boldsymbol{B} = \nabla\phi(x, z, t)$, where $\phi(x, z, t)$ is a magnetic potential satisfying Laplace's equation. To determine ϕ we must therefore solve

$$\nabla^2\phi = 0 \tag{2.5}$$

with boundary conditions (2.4) . It can easily be shown that the solution is

$$\phi(x, z, t) = B_0 \sum_{n=1}^{N} \frac{b_n}{nkc_n} \sinh(nkz)\cos[nk(x - Ut)], \tag{2.6}$$

where $c_n = \cosh(nka)$. Hence

$$B_x = -B_0 \sum_{n=1}^{N} \frac{b_n}{c_n} \sinh(nkz)\,\sin[nk(x - Ut)] \tag{2.7a}$$

$$B_z = B_0 \sum_{n=1}^{N} \frac{b_n}{c_n} \cosh(nkz)\,\cos[nk(x - Ut)]. \tag{2.7b}$$

We choose our frame of reference to be stationary with respect to the applied magnetic field, which is moving at a constant velocity $U\hat{\boldsymbol{x}}$. By writing $X = x - Ut$, equations (2.7) become

$$B_x = -B_0 \sum_{n=1}^{N} \frac{b_n}{c_n} \sinh(nkz)\,\sin(nkX) \tag{2.8a}$$

$$B_z = B_0 \sum_{n=1}^{N} \frac{b_n}{c_n} \cosh(nkz)\,\cos(nkX). \tag{2.8b}$$

Since the magnetic field $\boldsymbol{B}$ has zero divergence it can be expressed in terms of a magnetic stream function ψ such that

$$\begin{aligned} \boldsymbol{B} &= -\nabla\psi\times\hat{\mathbf{y}} \\ &= \left(\frac{\partial\psi}{\partial z}, 0, -\frac{\partial\psi}{\partial X}\right). \end{aligned}$$

Using $\boldsymbol{B} = \nabla\phi$, we have components of $\boldsymbol{B}$ as

$$\frac{\partial\psi}{\partial z} = -B_0 \sum_{n=1}^{N} \frac{b_n}{c_n} \sinh(nkz)\,\sin(nkX) \tag{2.9a}$$

$$-\frac{\partial\psi}{\partial X} = B_0 \sum_{n=1}^{N} \frac{b_n}{c_n} \cosh(nkz)\,\cos(nkX). \tag{2.9b}$$

It can easily be shown that the solution to the above set of equations is

$$\psi(X,z) = -B_0 \sum_{n=1}^{N} \frac{b_n}{nkc_n} \cosh(nkz) \sin(nkX). \tag{2.10}$$

Vector plots and fieldlines of the applied magnetic field $\boldsymbol{B}$ and magnetic stream function for the case of one and two-Fourier component fields are given in figures 2.2 and 2.3.

2.2.2 Derivation of the curl of the Lorentz force

In this section we derive a general expression for the rate of vorticity generation due to the travelling applied field.

Let $\boldsymbol{O}'$ be the frame of reference moving with the magnetic field $\boldsymbol{B}$ at a constant velocity $U\hat{\boldsymbol{x}}$. Let $\boldsymbol{O}$ be the frame of reference at rest. For an observer moving with the magnetic field $\boldsymbol{B}'$, the field appears steady so

$$\boldsymbol{\nabla}\times\boldsymbol{E}' = -\frac{\partial \boldsymbol{B}'}{\partial t} = 0. \tag{2.11}$$

Hence, $\boldsymbol{E}' = 0$, assuming there is no applied electric field at infinity.

If we make use of the transformation law connecting the frame $\boldsymbol{O}$ and $\boldsymbol{O}'$, in the non-relativistic case $|U| \ll c$ (i.e. speed of light), namely

$$\boldsymbol{E}' = \boldsymbol{E} + \boldsymbol{U}\times\boldsymbol{B}, \tag{2.12}$$

we find

$$\boldsymbol{E} = -\boldsymbol{U}\times\boldsymbol{B}. \tag{2.13}$$

Now to an observer stationary with the fluid, the electric field would appear as

$$\boldsymbol{E}_{\text{fluid}} = \boldsymbol{E} + \boldsymbol{v}\times\boldsymbol{B}.$$

Using equation (2.13) we obtain

$$\boldsymbol{E}_{\text{fluid}} = (\boldsymbol{v}-\boldsymbol{U})\times\boldsymbol{B} \approx -\boldsymbol{U}\times\boldsymbol{B}, \tag{2.14}$$

where $|\boldsymbol{v}| \ll U$, due to the second assumption in §2.2.

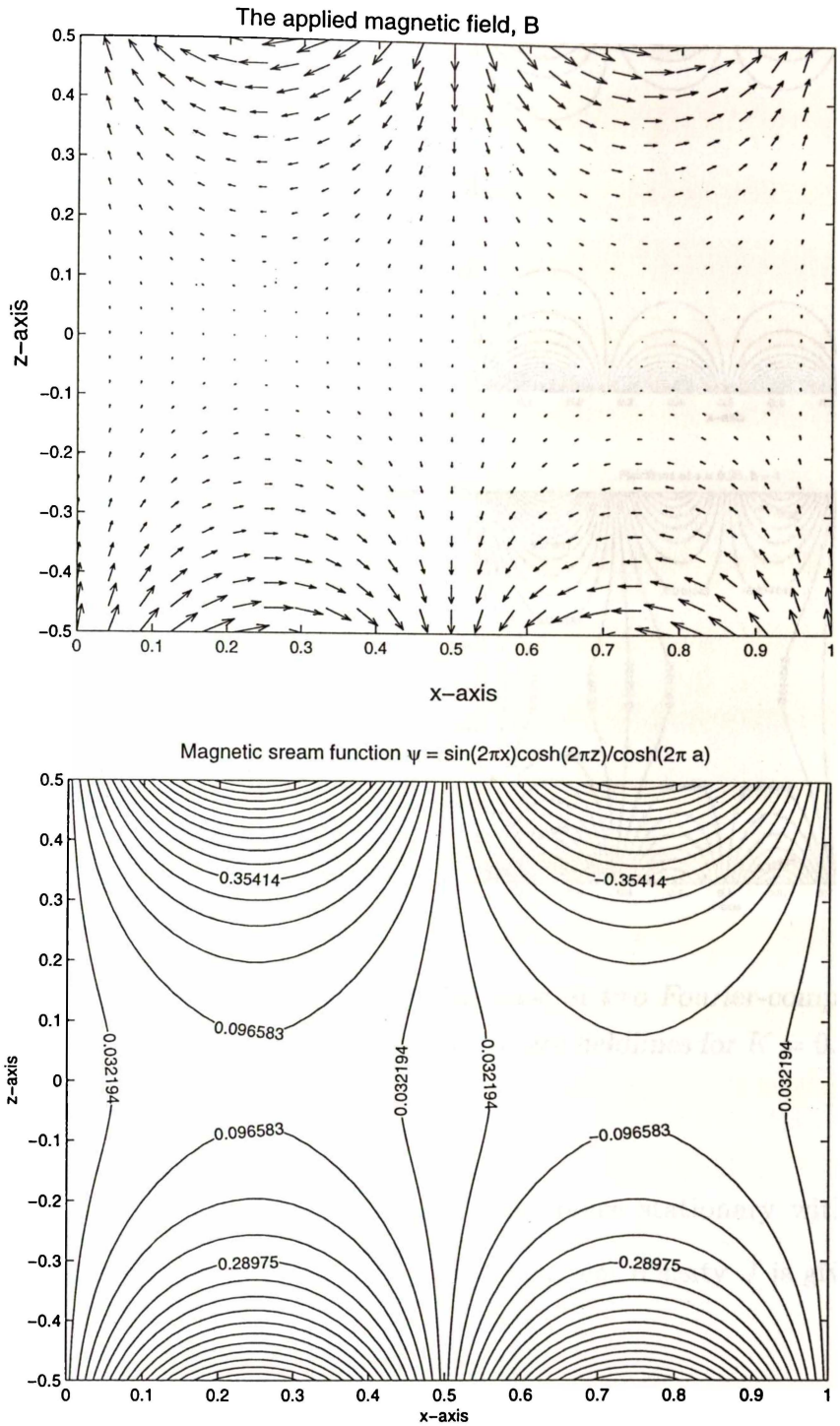

Figure 2.2: The top picture is a vector plot of the applied magnetic field of one Fourier component whose B_x and B_z are given by (2.7a) and (2.7b) respectively. The bottom one shows the contours i.e. fieldlines under the same boundary conditions. The region is $[0,1]\times[-0.5,0.5]$.

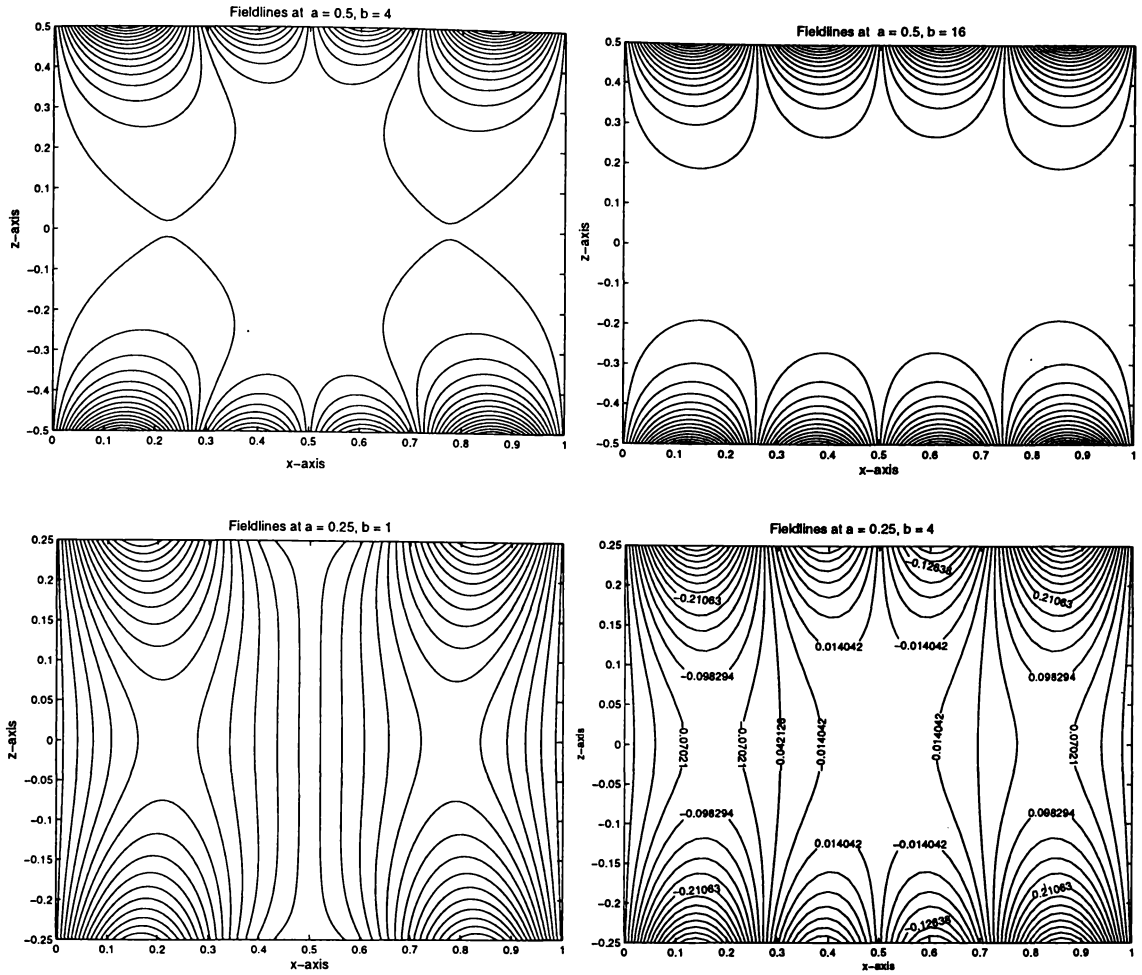

Figure 2.3: The top two are fieldlines for the case of two Fourier-component field where $a = 0.5$, *and* $b = 4, 16$ *and the bottom two are fieldlines for* $K = 0.25$ *and* $b = 1, 4$, *where* $K = 2\pi a/L$.

Ohm's law must be applied in a frame of reference stationary with the fluid (Alonso [1]). Using equation (2.14) the electric current density $\boldsymbol{J}$ is given by

$$\boldsymbol{J} = -\sigma \boldsymbol{U} \times \boldsymbol{B}. \tag{2.15}$$

The components of the Lorentz force $\boldsymbol{J} \times \boldsymbol{B}$ are given by

$$(\boldsymbol{J} \times \boldsymbol{B})_x = \quad \sigma U B_z^2 \tag{2.16a}$$

$$(\boldsymbol{J} \times \boldsymbol{B})_z = -\sigma U B_x B_z, \tag{2.16b}$$

the subscripts indicating the corresponding Cartesian components.

The curl of the Lorentz force $\boldsymbol{J}\times\boldsymbol{B}$ has only a y-component, given by

$$[\boldsymbol{\nabla}\times(\boldsymbol{J}\times\boldsymbol{B})]_y = \sigma U\left[\frac{\partial}{\partial z}(B_z^2)+\frac{\partial}{\partial x}(B_xB_z)\right] \tag{2.17}$$

But

$$\begin{aligned}\frac{\partial}{\partial x}(B_xB_z) &= \frac{\partial B_x}{\partial x}B_z + B_x\frac{\partial B_z}{\partial x},\\ &= -\frac{\partial B_z}{\partial z}B_z + B_x\frac{\partial B_x}{\partial z},\end{aligned} \tag{2.18}$$

making use of the two equations in (2.1) . Using expression (2.18) in equation (2.17) the curl of the Lorentz force becomes

$$\boldsymbol{\nabla}\times(\boldsymbol{J}\times\boldsymbol{B}) = \frac{1}{2}\sigma U\frac{\partial}{\partial z}(B^2)\,\hat{\boldsymbol{y}}, \tag{2.19}$$

where $B^2 = B_x^2 + B_z^2$.

The simple expression (2.19) is the basis of velocity field calculations in chapters 3 and 4.

2.3 MHD equations

2.3.1 The governing equations

Throughout this thesis we assume that the electrically conducting fluid is governed by the magnetohydrodynamics (MHD) equations, which are the combination of Maxwell's equations and the equations of fluid mechanics.

Maxwell's equations are

$$\boldsymbol{\nabla}\times\boldsymbol{B} = \mu_0\,\boldsymbol{J} + \frac{\partial \boldsymbol{D}}{\partial t}, \tag{2.20}$$

$$\frac{\partial \boldsymbol{B}}{\partial t} = -\,\boldsymbol{\nabla}\times\boldsymbol{E}, \tag{2.21}$$

$$\boldsymbol{\nabla}\cdot\boldsymbol{B} = 0, \tag{2.22}$$

and Ohm's law,

$$\boldsymbol{J} = \sigma(\boldsymbol{E} + \boldsymbol{v}\times\boldsymbol{B}), \tag{2.23}$$

where μ_0 denotes magnetic permeability, σ is the electrical conductivity and $\boldsymbol{D}$ is the electric displacement. In this thesis we neglect the displacement current, $\partial \boldsymbol{D}/\partial t$, from the right of (2.20) because the time scale, $\bar{t}$, of the variation in the field is long compared with L/c, where L is the length scale considered and c is the speed of light (Roberts [17]). The induction equation which determines the evolution of the magnetic field $\boldsymbol{B}$ results from eliminating $\boldsymbol{J}$ from (2.20) and (2.21) , then using (2.21) in the resulting equation to eliminate $\boldsymbol{E}$,

$$\frac{\partial \boldsymbol{B}}{\partial t} = \boldsymbol{\nabla} \times (\boldsymbol{v} \times \boldsymbol{B}) + \eta \boldsymbol{\nabla}^2 \boldsymbol{B}, \tag{2.24}$$

where

$$\eta = \frac{1}{\sigma \mu_0},$$

is the magnetic diffusitivity.

The fluid is also governed by the hydrodynamic momentum equation or Navier-Stokes equation and the continuity equation

$$\frac{\partial \boldsymbol{v}}{\partial t} + (\boldsymbol{v} \cdot \boldsymbol{\nabla})\boldsymbol{v} = -\frac{1}{\rho}\boldsymbol{\nabla} p + \frac{1}{\rho}(\boldsymbol{J} \times \boldsymbol{B}) + \nu \boldsymbol{\nabla}^2 \boldsymbol{v}, \tag{2.25}$$

$$\boldsymbol{\nabla} \cdot \boldsymbol{v} = 0,$$

where p is pressure, ν the kinematic viscosity and ρ the density of the fluid.

The velocity of the fluid is in the plane of x and z. Hence the curl of $\boldsymbol{v}$ is in the y direction. The curl of the Navier-Stokes equation (2.25) gives the equation for ω, the $y-$component of vorticity,

$$\rho \frac{\partial \omega}{\partial t} + \rho(\boldsymbol{v} \cdot \boldsymbol{\nabla})\,\omega = [\boldsymbol{\nabla} \times (\boldsymbol{J} \times \boldsymbol{B})]_y + \nu \rho \boldsymbol{\nabla}^2 \omega \tag{2.26}$$

where $\omega\, \hat{\boldsymbol{y}} = \boldsymbol{\nabla} \times \boldsymbol{v}$.

By writing

$$\boldsymbol{v} = -\boldsymbol{\nabla} \times (\chi\, \hat{\boldsymbol{y}}) = \left(\frac{\partial \chi}{\partial z},\, 0,\, -\frac{\partial \chi}{\partial x} \right) \tag{2.27}$$

where χ is the stream function it can be shown that the vorticity, ω, can be written as

$$\nabla^2 \chi = \omega. \tag{2.28}$$

Since the applied magnetic field moves at velocity $\boldsymbol{U}$, its velocity relative to the fluid is $\boldsymbol{U} - \boldsymbol{v}$ and Ohm's law for a moving conductor gives

$$\boldsymbol{J} = \sigma \boldsymbol{E} = \sigma(\boldsymbol{U} - \boldsymbol{v}) \times \boldsymbol{B}. \tag{2.29}$$

2.3.2 Non-dimensionalisation

For chapters 2 to 5 in this thesis we non-dimensionalise velocities with respect to U, the speed of the applied magnetic field. In chapter 6 and 7 we will use the Alfvén speed,

$$V_a = \frac{B_0}{\sqrt{\mu_0 \rho}}.$$

We take the wavelength L of the applied magnetic field as a length scale, B_0, the typical strength of the magnetic field, B_0^2/μ_0 for pressure p, and define dimensionless variables (denoted by bars), setting

$$\begin{aligned} x &= L\bar{x} & \nabla &= \frac{\bar{\nabla}}{L} & \chi &= LU\bar{\chi} \\ z &= L\bar{z} & t &= \frac{L}{U}\bar{t} & \omega &= \frac{U}{L}\bar{\omega} \\ u &= U\bar{u} & p &= \frac{B_0^2}{\mu_0}\bar{p} & J &= (\sigma U B_0)\bar{J} \end{aligned} \tag{2.30}$$

$$v = U\,\bar{v}, \tag{2.31}$$

where $\boldsymbol{v} = (u, 0, v)$. The Navier-Stokes equation then becomes

$$\frac{\partial \bar{\boldsymbol{v}}}{\partial \bar{t}} + (\bar{\boldsymbol{v}} \cdot \bar{\nabla})\bar{\boldsymbol{v}} = -\frac{V_a^2}{U^2}\bar{\nabla}\bar{p} + \frac{M^2}{R}(\bar{\boldsymbol{J}} \times \bar{\boldsymbol{B}}) + \frac{1}{R}\bar{\nabla}^2\bar{\boldsymbol{v}}, \tag{2.32}$$

where the Hartmann number, M is

$$M = LB_0\left(\frac{\sigma}{\nu\rho}\right)^{\frac{1}{2}}, \tag{2.33}$$

and the Reynolds number, R is

$$R = \frac{U\,L}{\nu}. \tag{2.34}$$

The vorticity equation and Poisson's equation become

$$\frac{\partial \bar{\omega}}{\partial \bar{t}} + (\bar{\boldsymbol{v}} \cdot \bar{\nabla})\bar{\omega} = \mathcal{N}\left[\bar{\nabla} \times (\bar{\boldsymbol{J}} \times \bar{\boldsymbol{B}})\right]_y + \frac{1}{R}\bar{\nabla}^2\bar{\omega}, \tag{2.35}$$

$$\bar{\nabla}^2 \bar{\chi} = \bar{\omega}, \tag{2.36}$$

respectively and where the magnetic interaction parameter

$$\mathcal{N} = \frac{M^2}{R}. \tag{2.37}$$

The induction equation becomes

$$\frac{\partial \bar{\boldsymbol{B}}}{\partial \bar{t}} = \bar{\nabla} \times (\bar{v} \times \bar{\boldsymbol{B}}) + \frac{1}{R_m} \bar{\nabla}^2 \bar{\boldsymbol{B}}, \tag{2.38}$$

where the magnetic Reynolds number, R_m is defined as

$$R_m = \frac{U L}{\eta}.$$

From now onwards, just for convenience we use the convention that the governing dimensionless equations will be written with "bars" omitted. So now the governing equations (2.32) – (2.38) become

$$\frac{\partial \boldsymbol{v}}{\partial t} + (\boldsymbol{v} \cdot \nabla)\boldsymbol{v} = -\frac{V_a^2}{U^2} \nabla p + N (\boldsymbol{J} \times \boldsymbol{B}) + \frac{1}{R} \nabla^2 \boldsymbol{v}, \tag{2.39}$$

$$\frac{\partial \omega}{\partial t} + (\boldsymbol{v} \cdot \nabla)\omega = \mathcal{N} \left[\nabla \times (\boldsymbol{J} \times \boldsymbol{B})\right]_y + \frac{1}{R} \nabla^2 \omega, \tag{2.40}$$

$$\nabla^2 \chi = \omega, \tag{2.41}$$

and

$$\frac{\partial \boldsymbol{B}}{\partial t} = \nabla \times (\boldsymbol{v} \times \boldsymbol{B}) + \frac{1}{R_m} \nabla^2 \boldsymbol{B}. \tag{2.42}$$

The rectangular region of interest that will always be refered to in this thesis is $[0, L]$ by $[-a, a]$, (figure 2.4). On the boundary $z = a$, we have $a = L\,\bar{z}$ which gives $\bar{z} = a/L$. So, in dimensionless quantities the domain now becomes $[0, 1]$ by $[-\bar{a}, \bar{a}]$, where $\bar{a} = a/L$. The aspect ratio a/L can be changed by varying the value $\bar{a}$. Unless mentioned otherwise from now onwards we will omit the "bar" for convenience.

2.4 Summary

In this chapter we outlined the main problem being investigated in chapters 3–7. We derived the magnetic stream function for the applied magnetic field for

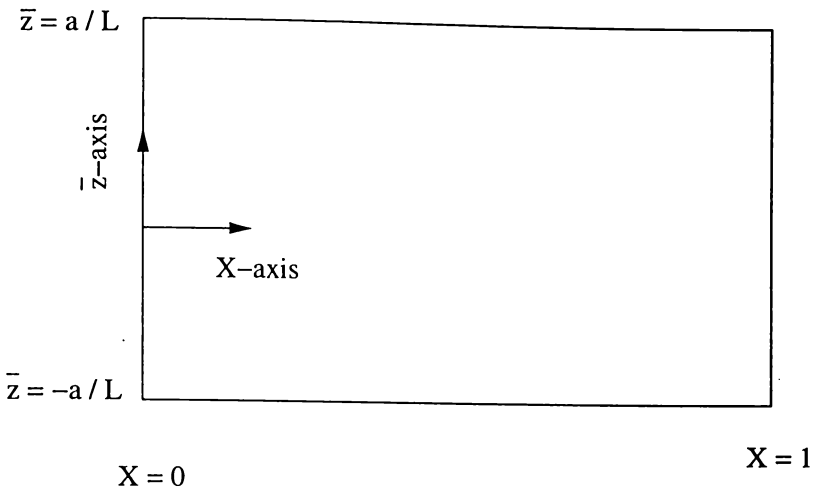

Figure 2.4: The rectangular region $[0,1] \times [-\bar{a}, \bar{a}]$

the general case of multi Fourier-component source. We also derived the curl of the Lorentz force which is the basis of velocity field calculations for the next two chapters. Lastly we covered the governing MHD equations and went through their non-dimensionalisation. In the next chapter we investigate the initial fluid motion due to a two Fourier-component source, R_m and $\mathcal{N}$ being small, for this particular problem has an analytical solution.

Chapter 3

Initial fluid motion due to a two Fourier-component source, R_m small.

3.1 Introduction

In this chapter we investigate situations where the resulting flow hardly changes the applied magnetic field. We are interested in the early velocity field, which means that we can ignore diffusion and convection of vorticity since there is no time for them to take place. We look at the early time development of flow in a channel containing a liquid metal, generated by a two-dimensional magnetostatic field $\mathbf{B}$ which is applied across the channel and moves along the channel at a constant velocity. We study the special case of a two-Fourier component because the vorticity equation has an analytical solution which is to be used for comparison with the numerical results in chapter 4.

In §3.2 we outline the problem. Next we derive the expression for the curl of Lorentz force for the case of two-Fourier component field. Then in §3.3 we write in full the vorticity equation with viscosity and convective terms neglected. The initial flow for four cases is investigated before a consideration of time of validity of the solution in §3.4 followed by conclusions in §3.5.

3.2 Outline of the problem

Consider a channel of infinite length and width containing a conducting fluid as in §2.2. Here the applied magnetic field of multi Fourier-component source is limited to 2 Fourier-component source. So we have on the boundaries:

$$\left(\frac{\partial \phi}{\partial z}\right)_{z=\pm a} = B_0 \sum_{n=1}^{2} b_n \cos[nk(x - Ut)], \tag{3.1}$$

where $b_1 = 1$, and $b_2 = b$. We assume R_m and $\mathcal{N}$ are small so the resulting velocity $\boldsymbol{u}$ is small compared to $\boldsymbol{U}$, the velocity of the applied magnetic field.

The curl of the Navier-Stokes equation (2.25) in the $y-$direction is

$$\frac{\partial \omega}{\partial t} + (\boldsymbol{v} \cdot \nabla)\omega = \frac{1}{\rho}(\nabla \times \mathbf{F})_y + \nu \nabla^2 \omega. \tag{3.2}$$

Now

$$\frac{|(\boldsymbol{v} \cdot \nabla)\omega|}{|\frac{\partial \omega}{\partial t}|} \approx \frac{u\omega_0/L}{U\omega_0/L} = \frac{u}{U},$$

where typical length, vorticity and time scales are L, ω_0 and L/U respectively. By assuming that $(u/U) \ll 1$ we can neglect the convective term, $(\boldsymbol{v} \cdot \nabla)\omega$.

Also

$$\frac{|\nu \nabla^2 \omega|}{|\frac{\partial \omega}{\partial t}|} \approx \frac{\nu\omega_0/L^2}{\omega_0 U/L} = \frac{1}{R}, \tag{3.3}$$

where the Reynolds number, $R = LU/\nu$. Here we can neglect the effect of viscosity, hence the term $\nu \nabla^2 \omega$. The physical meaning of this approximation is that we will be able to look at the early velocity field before diffusion or convection of ω sets in and reduces it to a steady state. At $t = 0$, $\omega = 0$, the applied magnetic field starts moving; vorticity is generated at a rate $(\nabla \times \mathbf{F})_y$. As vorticity is generated it diffuses away over time. Using dimensional analysis the viscous diffusion time is $t_D = a^2/\nu$. The viscous time is quite large compared with a/U, which is the time for the applied magnetic field to move the distance equal to half of the width of the channel, because ν is assumed small. It is worth noting that a delay is needed by the magnetic field to increase from zero to B_0. Therefore, the calculation is relevant only if that time delay is much shorter than a/U.

3.2.1 Curl of Lorentz force for a two Fourier-component source

As in §2.2 we assume a magnetic potential function $\phi(x, z, t)$ that satisfies Laplace's equation and $\boldsymbol{B} = \nabla\phi(x, z, t)$. As was shown in equation (2.6) we get the solution $\phi(x, z, t)$. The x and z-components are

$$B_x = -B_0 \sum_{n=1}^{2} \frac{b_n}{c_n} \sinh(nkz) \sin(nkX) \tag{3.4a}$$

$$B_z = B_0 \sum_{n=1}^{2} \frac{b_n}{c_n} \cosh(nkz) \cos(nkX). \tag{3.4b}$$

where $b_1 = 1$, $b_2 = b$, and $X = x - Ut$, i.e. we are stationary relative to the moving applied magnetic field.

Substituting the above components in

$$B^2 = B_x^2 + B_z^2,$$

and with some manipulation it can be shown that

$$\begin{aligned} B^2 &= \frac{B_0^2}{c_1^2}(\sinh^2 kz + \cos^2 kX) + \frac{b^2 B_0^2}{c_2^2}(\sinh^2(2kz) + \cos^2(2kX)) \\ &+ \frac{bB_0^2}{c_1 c_2}(\cosh(3kz) \cos kX + \cosh kz \cos(3kX).) \end{aligned} \tag{3.5}$$

Substituting equation (3.5) into equation (2.19) for the curl of the Lorentz force we get

$$\begin{aligned} (\nabla \times (\boldsymbol{J} \times \boldsymbol{B}))_y = \frac{1}{2}\sigma k U B_0^2 \Bigg(& \frac{1}{c_1^2} \sinh(2kz) + \frac{2b^2}{c_2^2} \sinh(4kz) \\ & + \frac{b}{c_1 c_2}(3 \sinh(3kz) \cos(k(x - Ut)) + \sinh kz \cos(3k(x - Ut)) \Bigg) \end{aligned} \tag{3.6}$$

where $c_n = \cosh nK$, $n \in \mathbb{N}$ and $K = ak$, (Saad [18]).

3.3 The vorticity equation with viscosity and convective terms neglected

By neglecting the convective term as well as the viscosity term we end up with the simplified vorticity equation

$$\frac{\partial \omega}{\partial t} = \frac{1}{\rho}(\nabla \times (\boldsymbol{J} \times \boldsymbol{B}))_y. \tag{3.7}$$

We non-dimensionalise equation (3.7) based on the time scale L/U as in section 2.3.2. Using (3.6) , (3.7) can be written in dimensionless form (here we purposely omit the bar notation for convenience) as

$$\begin{aligned}\frac{\partial \omega}{\partial t} &= \frac{M^2\pi}{R}\left[\frac{1}{c_1^2}\sinh(4\pi z) + \frac{2b^2}{c_2^2}\sinh(8\pi z)\right. \\ &\left. + \frac{b}{c_1 c_2}\left[3\sinh(6\pi z)\cos(2\pi(x-t)) + \sinh(2\pi z)\cos(6\pi(x-t))\right]\right], \end{aligned} \tag{3.8}$$

where, k, the wavenumber is given by $k = 2\pi/L$, M is the Hartmann number and R the Reynolds number. On integrating (3.8) and applying the initial condition $\omega = 0$ at $t = 0$, we obtain

$$\begin{aligned}\omega &= \frac{M^2\pi}{R}\left[\left(\frac{1}{c_1^2}\sinh 4\pi z + \frac{2b^2}{c_2^2}\sinh 8\pi z\right)t\right. \\ &- \frac{b}{6c_1c_2\pi}\Big(9\sinh 6\pi z\,(\sin 2\pi(x-t) - \sin 2\pi x) \\ &\left. + \sinh 2\pi z\,(\sin 6\pi(x-t) - \sin 6\pi x)\Big)\right]. \end{aligned} \tag{3.9}$$

A graph of $\omega R/M^2$ versus z for $b = 1$, and various values of x and t is given in Figure 3.1. Vorticity starts to increase/decrease steeply as we get to within ~ 0.2 of a, half of the width of the channel for the case where $a = \pm 0.5$.

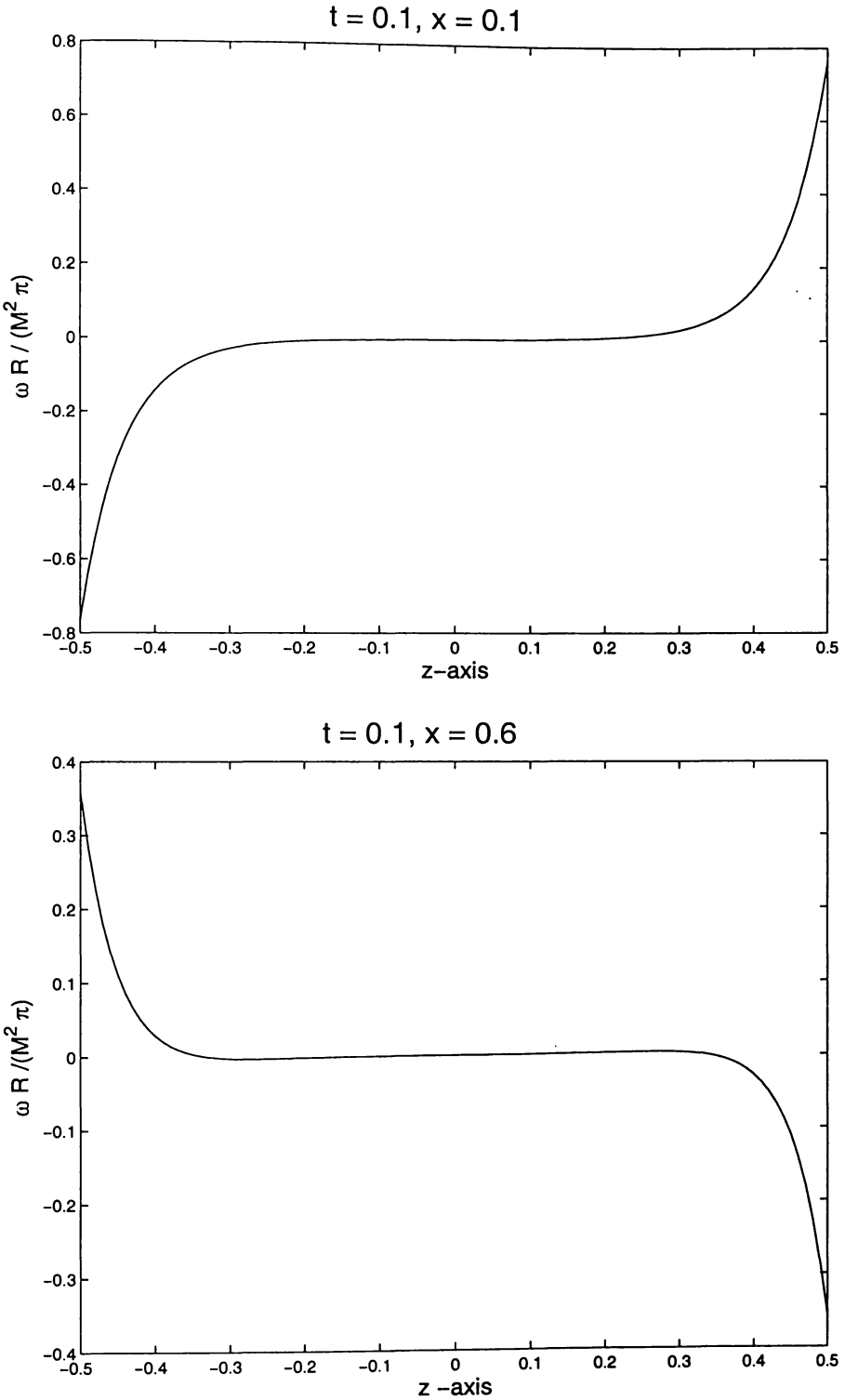

Figure 3.1: Plots of $\omega R/(\pi M^2)$ *versus* z *at* $t = 0.1$, *where* $b = 1$. *The top one is at* $x = 0.1$ *where vorticity value is stronger close to the boundaries than the bottom one at* $x = 0.6$.

3.4 Determining velocity field

By assumption the fluid is incompressible, so there exists a stream function χ such that

$$\boldsymbol{v} = -\nabla\chi \times \hat{\boldsymbol{y}}. = \left(\frac{\partial\chi}{\partial z}, 0, -\frac{\partial\chi}{\partial x}\right). \tag{3.10}$$

On the boundaries $z = \pm a$, the no slip condition means

$$\frac{\partial\chi}{\partial z} = 0,$$

which implies the boundary conditions

$$\chi(\pm a) = 0, \tag{3.11}$$

where the constant is chosen to be zero.

Substituting $\boldsymbol{v}$ from (3.10) in the expression $\boldsymbol{\omega} = \nabla \times \boldsymbol{v}$ we get

$$\nabla^2\chi = \omega, \tag{3.12}$$

which remains unchanged under dimensionalisation (see equation (2.41)).

So using (3.9) in (3.12) and after some manipulation we obtain

$$\begin{aligned}\nabla^2\chi \;=\; & \frac{M^2\pi}{R}\left[\left(\frac{1}{c_1^2}\sinh(4\pi z) + \frac{2b^2}{c_2^2}\sinh(8\pi z)\right)t\right. \\ & + \frac{b}{3\pi c_1 c_2}\Big(\,9\sinh(6\pi z)\,\cos[\pi(2x-t)]\,\sin\pi t \\ & \left.\left. + \sinh(2\pi z)\,\cos[3\pi(2x-t)]\,\sin 3\pi t.\right)\right].\end{aligned} \tag{3.13}$$

To solve equation (3.13) we divide up the right hand side of (3.13) into three separate equations. First consider equation

$$\nabla^2\chi = \left(\frac{M^2\pi}{Rc_1^2}\right) t\,\sinh 4\pi z + \left(\frac{2b^2M^2\pi}{Rc_2^2}\right) t\,\sinh 8\pi z. \tag{3.14}$$

Since the RHS of (3.14) is a function z only we can write $\chi = \chi_0(z)$ to obtain

$$\frac{d^2\chi_0}{dz^2} = \left(\frac{M^2\pi}{Rc_1^2}\right) t\,\sinh 4\pi z + \left(\frac{2b^2M^2\pi}{Rc_2^2}\right) t\,\sinh 8\pi z, \tag{3.15}$$

which on integration gives the solution

$$\chi_0(z) = \left(\frac{M^2}{16\pi c_1^2 R}\right) t\sinh 4\pi z + \left(\frac{b^2M^2}{32\pi Rc^2}\right)\sinh 8\pi z \;+\; Az + B, \tag{3.16}$$

where A and B are arbitrary constants. Since RHS of (3.16) is an odd function of z we get $\chi_0(-z) = -\chi_0(z)$ which implies that $B = 0$.

Second we consider the part of (3.13) that generates the streamlines which fluctuate viz.

$$\nabla^2\chi = \frac{3bM^2}{c_1c_2R}\sinh(6\pi z)\sin\pi t\,\cos[\pi(2x-t)]. \tag{3.17}$$

Note that equation (3.17) is of the form

$$\nabla^2\chi = A\sinh\alpha z\,\cos\beta x, \tag{3.18}$$

which can be shown to have the solution of the form

$$\chi = \frac{A}{\alpha^2-\beta^2}\sinh\alpha z\,\cos\beta x.$$

It can easily be shown that the solution to (3.17) , say χ_1, that satisfies the boundary conditions (3.11) is

$$\chi_1 = \frac{3bM^2}{32\pi^2c_1c_2s_1R}\sin\pi t\cdot(s_1\sinh 6\pi z - s_3\sinh 2\pi z)\cos[\pi(2x-t)], \tag{3.19}$$

where $s_n = \sinh nK, \quad n\in\mathbb{N}$ and $K = ak$.

Third, the remaining equation of (3.13) is

$$\nabla^2\chi = \frac{bM^2}{3c_1c_2R}\sin(3\pi t)\sinh(2\pi z)\cos[3\pi(2x-t)], \tag{3.20}$$

and whose solution is

$$\chi_2 = \frac{bM^2}{96\pi c_1c_2s_3R}\sin 3\pi t\cdot(s_1\sinh 6\pi z - s_3\sinh 2\pi z\,)\cos[3\pi(2x-t)]. \tag{3.21}$$

Making use of equations (3.16), (3.19) & (3.21) we obtain the general solution to (3.13) as

$$\begin{aligned}\chi &= \chi_0 + \chi_1 + \chi_2\\ &= \left(\frac{M^2}{16\pi c_1^2R}\right)t\,\sinh 4\pi z + \left(\frac{b^2M^2}{32\pi Rc^2}\right)t\,\sinh 8\pi z + Az\\ &\quad +\eta(z)\left(9s_3\sin\pi t\cos\pi(2x-t) + s_1\sin 3\pi t\cos 3\pi(2x-t)\right),\end{aligned} \tag{3.22}$$

where

$$\eta(z) = \frac{bM^2}{96\pi^2c_1c_2s_1s_3R}(s_1\sinh 6\pi z - s_3\sinh 2\pi z).$$

Since the channel is closed at both ends the flux across the channel has to be zero viz.

$$\int_{-a}^{a} u_x(x,z)\,dz \;=\; \int_{-a}^{a} \frac{\partial \chi}{\partial z}\,dz \;=\; 0. \tag{3.23}$$

Hence

$$\chi(x,-a) = \chi(x,a)$$

Applying this boundary condition to (3.22) shows that

$$A = -\frac{M^2 s_2 t}{16a\pi c_1^2 R} - \frac{b^2 M^2 s_4 t}{32a\pi c_2^2 R}. \tag{3.24}$$

Making use of the expression for A in (3.22) we get

$$\begin{aligned}\chi \;=\; & \frac{M^2}{16\pi a c_1^2 R}(a\sinh 4\pi z - s_2 z)\,t + \frac{b^2 M^2}{32\pi a c_2^2 R}(a\sinh 8\pi z - s_4 z)\,t \\ & +\eta(z)\big(9s_3 \sin \pi t \cos 2\pi X + s_1 \sin 3\pi t \cos 6\pi X\big),\end{aligned} \tag{3.25}$$

where

$$X = x - \frac{t}{2},$$

and $\eta(z)$ given by (3.22) .

Writing $K = ak = 2\pi a/L = 2\pi\bar{a}$ we finally obtain (in dimensionless form) the solution to equation (3.13) , which is

$$\begin{aligned}\frac{\chi}{(M^2/R)} \;=\; & \frac{1}{8Kc_1^2}(a\sinh 4\pi z - s_2 z)\,t + \frac{b^2}{16Kc_2^2}(a\sinh 8\pi z - s_4 z)\,t \\ & +\Theta(z)\big(9s_3 \sin \pi t \cos 2\pi X + s_1 \sin 3\pi t \cos 6\pi X\big),\end{aligned} \tag{3.26}$$

where

$$\Theta(z) = \frac{b}{96\pi^2 s_1 s_3 c_1 c_2}(s_1 \sinh 6\pi z - s_3 \sinh 2\pi z).$$

For the early time stage of fluid motion we choose a value of $t = 0.1$. Four main cases have been investigated. The case where $b = 0$ is of not much interest since the streamlines are just straight lines, (Saad [18]). $K = 2\pi a$, where a is the aspect ratio which is half of the channel width.

Case I: $K = \pi,\ b \leq 1,$

In cases I and II we examine the the effects of the contribution of the second Fourier-component field b on the streamlines. In both cases the value of $a = 0.5$. In case I it can be seen from figure (3.2) that the streamlines of the fluid tend towards straight line flow due to a single Fourier component field as b decreases. This is due to the fact that as b decreases so does the contribution from the second Fourier component field.

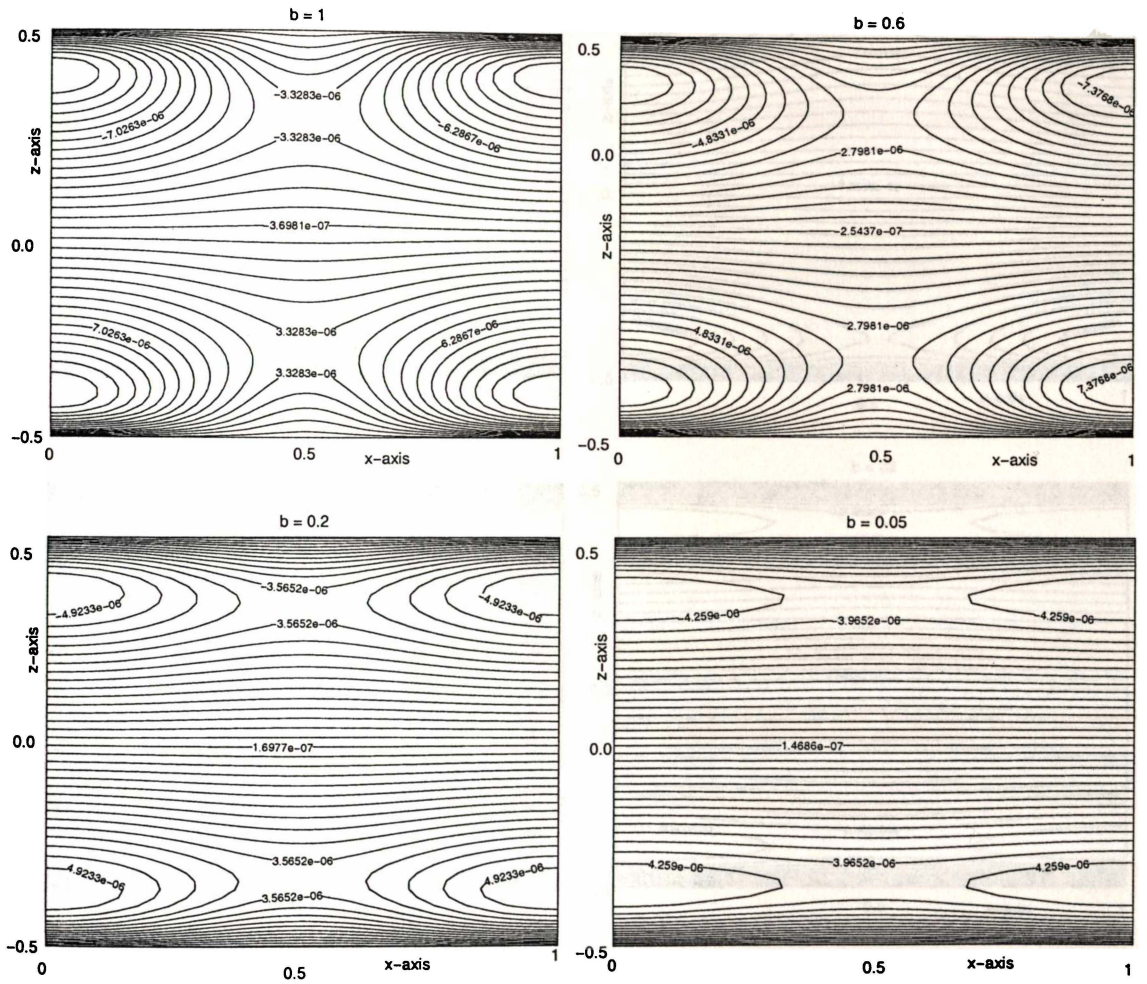

Figure 3.2: Streamlines at early time stage for case I: $K = \pi,\ b = 1, 0.6, 0.2, 0.05,$ and $N = 0.01,$ at $t = 0.02$.

Case II: $K = \pi,\ b > 1,$

Having $b > 1$ means the flow due to the contribution of the second Fourier component is greater than that of the first Fourier component. From figure 3.3 we can see that the streamlines approach the straight line flow like in case I. It can be seen that there are deeper eddies when the contribution from the second Fourier component is about equal to that of the first Fourier component.

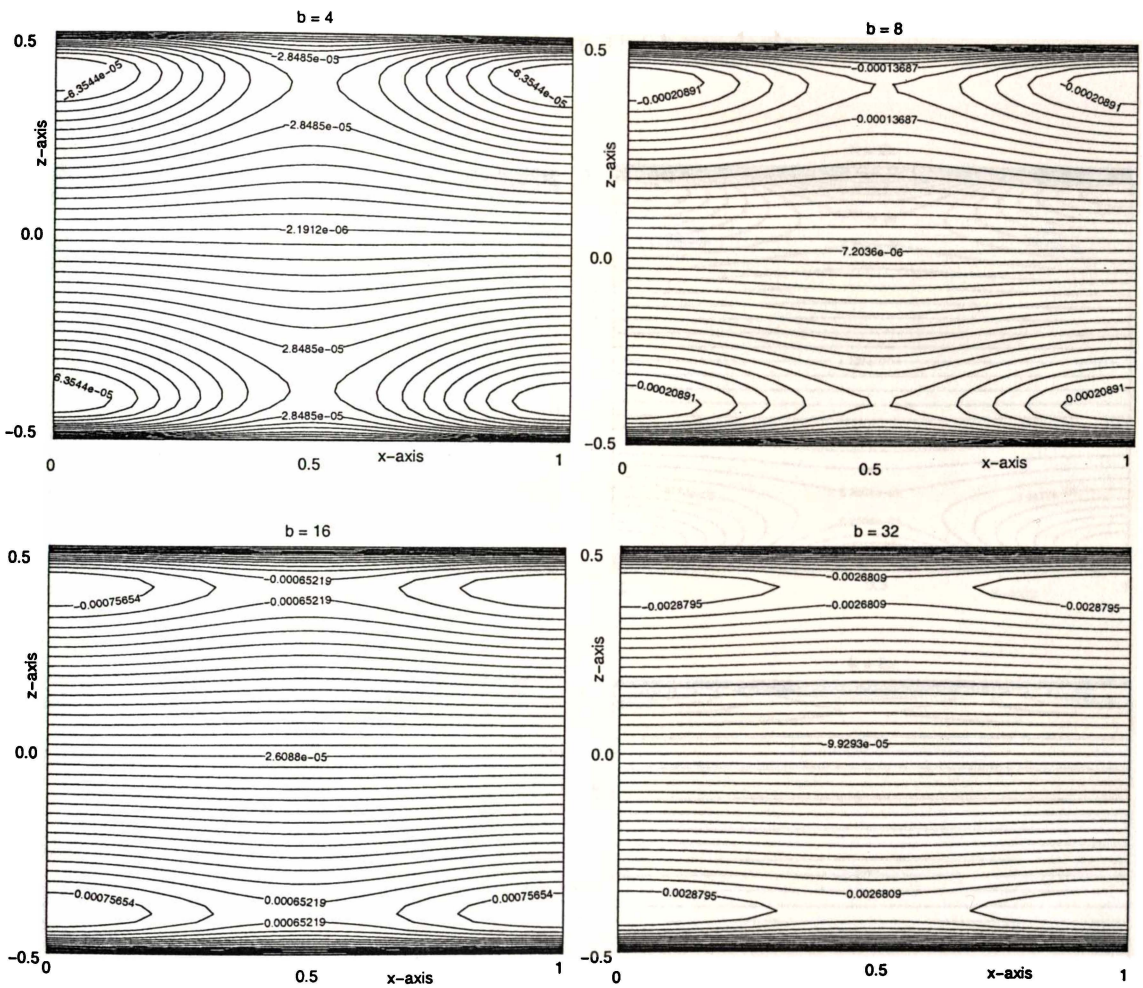

Figure 3.3: Streamlines at early time stage for case II: $K = \pi,\ b > 1$; $b = 4, 8, 16, 32$, and $N = 0.01$, at $t = 0.02$.

Case III: $K > 1,\ b = 1,$

Here we investigate the effects of widening the aspect ratios which are given by the values of K, where $K = ak = 2\pi a$, while keeping the contributions from both first and second Fourier component fields the same viz. $b = 1$. It can be seen from figure 3.4 that the eddies of the flow approach the boundaries $z = \pm a$ as the channel width gets wider, while the remaining streamlines in between the eddies tend to straight lines. This is to be expected since the strength of the magnetic field becomes weaker the further away it is from the boundaries.

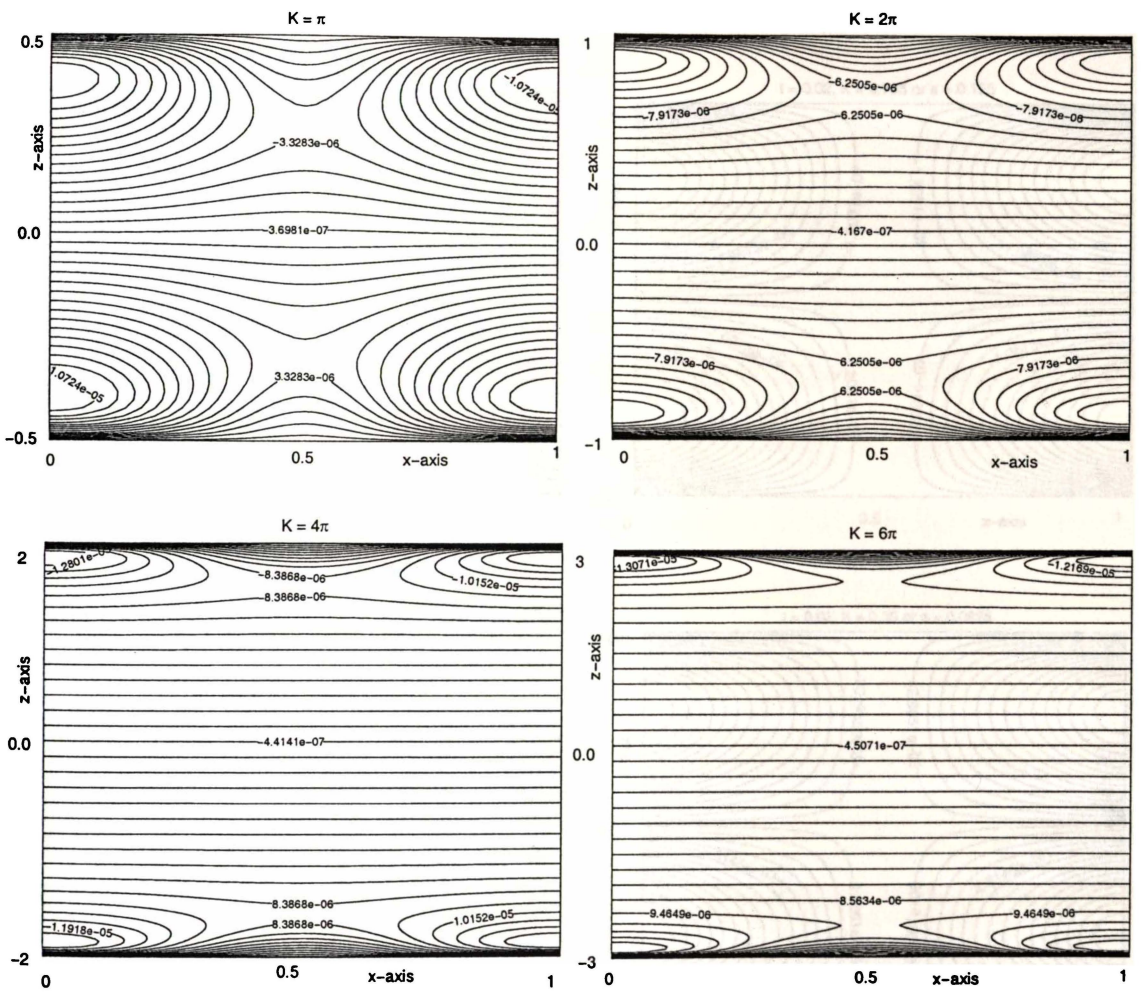

Figure 3.4: Streamlines at early time stage for case III: $b = 1, N = 0.01, t = 0.02$ for $K = \pi,\ 2\pi,\ 3\pi$ and 4π.

Case IV: $K < 1,\ b = 1,$

In this case we keep $b = 1$, but we decrease the aspect ratio a to be < 1. It can be seen from figure 3.5 that the streamlines describe a flow of two eddies, which looks good for the purpose of stirring. This can be explained by the fact that the closer the boundaries are the stronger the magnetic field intensity in creating the eddies. We can see in figure 3.6 that vortex strength spreads out more and more gradually towards the middle of the channel as the width of the channel a decreases from 0.5 to 0.05. In fact when $a = 0.05$ the vortex value increases from -0.5 to 0.5 at an almost uniform rate.

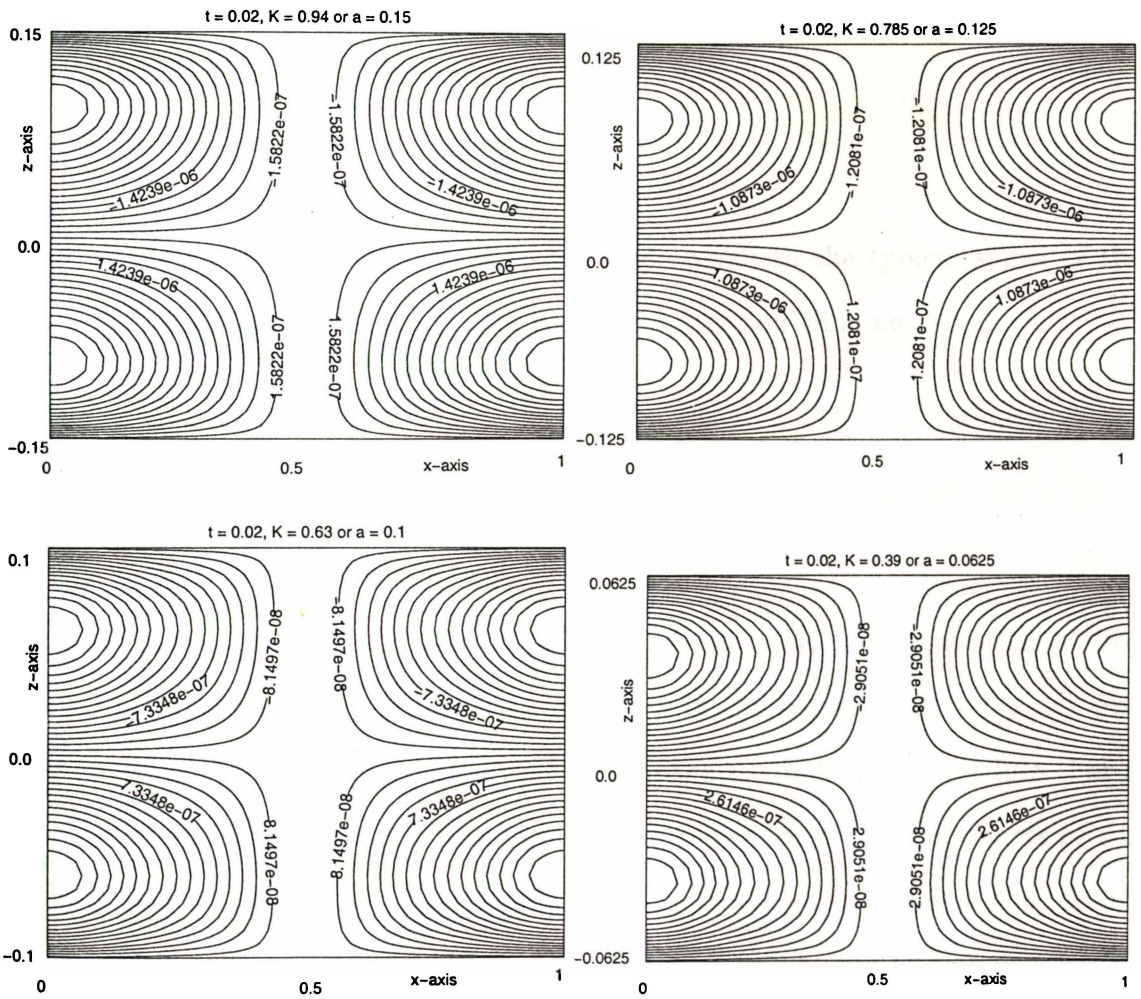

Figure 3.5: Streamlines at early time stage for case IV: $b = 1, N = 0.01, t = 0.02$, for various values of $K < 1$: $K = 0.94$, 0.785, 0.628, and 0.39.

3.5 Upper limits for t_0

We want to look for the upper limit of time, t_0, such that the solution (3.22) holds true for the time that satisfies $0 \leq t \leq t_0$. After this time limit t_0 *diffusion* and *convection* would set in and reduce the flow to a steady state. Using dimensional analysis and making use of the Navier Stoke-Stokes equation (2.25) we obtain the diffusion time as

$$t_d = \frac{L^2}{\nu},$$

where L is the typical wavelength. The time for convection to take place is

$$t_c = \frac{L}{u},$$

where u is the typical speed of the fluid.

Now, surely t_0 must satisfy

$$t_0 \ll min\{t_c, t_d\}.$$

Since the viscosity of the fluid is very small compared to the typical speed of the fluid, the upper limit must be smaller than the advection time i.e.

$$t_0 \ll \frac{L}{u}.$$

3.6 Conclusions

We have shown that for the case of the applied magnetic field consisting of two Fourier components a pair of eddies is generated in the region $[0, 1] \times [-a, a]$. For very small or very large b, the fluid flow tends towards that of straight line. For a fixed value of $b = 1$, (i.e. equal contributions from both Fourier components of the applied field) the bigger the aspect ratio a the more the streamlines in the middle tend to straight lines while the eddies get closer relatively to the boundary. Overall we conclude that for good stirring we need to have the contributions from both first and second Fourier component fields to be roughly equal and the aspect ratio $a < 0.5$. In the next chapter we extend this fluid flow, R_m small, to complete the flow evolution picture.

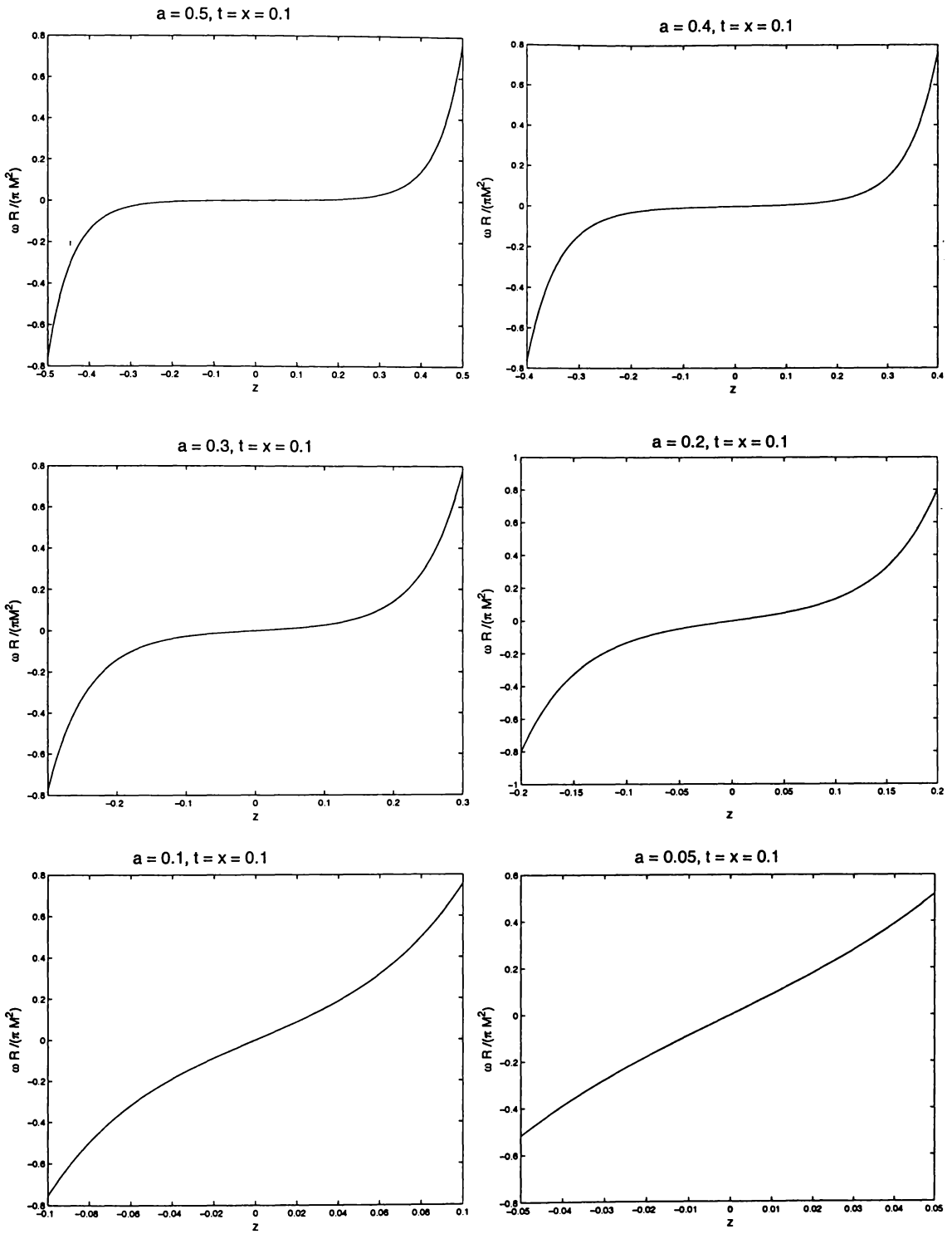

Figure 3.6: The vortex strength spreads out gradually to the middle of the channel as the width a gets narrower i.e. from 0.5 to 0.05. The value of $x = 0.1$ is chosen to get intense vortices because it is close to the centre of the vortex.

Chapter 4

Numerical methods, R_m and $\mathcal{N} \ll 1$

4.1 Introduction

In the previous chapter we looked at the initial fluid motion. Here we extend our investigation by examining the time-dependent problem under the assumption of both R_m and magnetic interaction parameter $\mathcal{N}$ being small. The final steady state for an open channel was investigated in (Saad [18]) but we need numerical methods to complete the flow evolution picture for a closed channel.

In §4.2 we give an overview of the numerical method for small R_m. We describe the Lax-Wendroff method in §4.3, followed by §4.4 where we solve Poisson's equation numerically and test the validity of the solution. In §4.5 we investigate fluid motion due to a two Fourier-component source and §4.6 covers fluid flow due to a multi Fourier-component source. Our conclusions are summarised in the last section. The reason for considering the multi Fourier-component source separately from the two Fourier-component source is that, in the former case we we can derive an analytical expression for the source term $[\nabla \times (\boldsymbol{J} \times \boldsymbol{B})]_y$. In the latter case we use numerical methods to calculate the right-hand side of the expression for the source term (2.19) since this becomes complicated as the number m, of Fourier components increases.

4.2 Overall view

The dimensionless governing equations (2.40) and (2.41) can be rewritten as

$$\frac{\partial \omega}{\partial t} + (\boldsymbol{v} \cdot \boldsymbol{\nabla})\omega = \frac{M^2}{R} S(x,z,t) + \frac{1}{R}\nabla^2 \omega, \tag{4.1}$$

$$\nabla^2 \chi = \omega. \tag{4.2}$$

Like many physical equations in nature neither equation has an analytical solution and can be solved only by numerical methods. After some investigation we chose the two-step Lax-Wendroff method due to its stability and fairly simple implementation. It is assumed throughout this chapter that the magnetic Reynolds number $R_m \ll 1$, which means that the applied magnetic field is unaffected by the resulting fluid flow. In short, Lax-Wendroff updates the vorticity ω which is then used to solve Poisson's equation for the stream function χ, and hence $\boldsymbol{v}$. To solve Poisson's equation we use a spectral method and the NAG Fast Fourier transform algorithm.

4.3 Lax-Wendroff method

The two-step Lax-Wendroff method (Lax and Wendroff [10] , Richtmyer [14] , Richtmyer and Morton [15]), time-centres the integration by defining temporary or intermediate values of the dependent variables at the half time step $n + \frac{1}{2}$.

The set of equations, (4.1) and (4.2) , may now be differenced on an Eulerian mesh in the conventional way. The first (or auxiliary) step of the Lax-Wendroff method is the Lax step implemented by the following difference scheme:

$$\begin{aligned} u^n_{i,j} &= \frac{1}{2\Delta}(\chi^n_{i,j+1} - \chi^n_{i,j-1}) \\ v^n_{ij} &= -\frac{1}{2\Delta}(\chi^n_{i+1,j} - \chi^n_{i-1,j}) \end{aligned} \tag{4.3}$$

$$\begin{aligned} \omega^{n+\frac{1}{2}}_{ij} &= \frac{1}{4}(\omega^n_{i,j-1} + \omega^n_{i+1,j} + \omega^n_{i-1,j} + \omega^n_{i,j+1}) \\ &\quad -\frac{\Delta t}{4\Delta} u^n_{i,j}(\omega^n_{i+1,j} - \omega^n_{i-1,j}) \\ &\quad -\frac{\Delta t}{4\Delta} v^n_{i,j}(\omega^n_{i,j+1} - \omega^n_{i,j-1}) + \frac{\Delta t M^2}{2R} S(i,j), \end{aligned} \tag{4.4}$$

where Δ = the grid spacing, Δt is the increment in time, and $u_{i,j}^n$ and $v_{i,j}^n$ are velocity components in the x and $z-$directions respectively at position (x_i, z_j). Here for convenience we take the grid spacing to be the same in both x and $z-$ directions. Due to our assumption of R_m small this means that the source term $S(i,j)$ is independent of time i.e. it is considered as being constant.

Having updated the vorticity, we solve Poisson's equation,

$$\nabla^2 \chi = \omega^{n+\frac{1}{2}},$$

to determine numerically the auxiliary stream function. These auxiliary variable values are now used to determine the velocity at the next time step $n+1$, via the following difference scheme:

$$\begin{aligned} u_{i,j}^{n+\frac{1}{2}} &= \frac{1}{2\Delta}(\chi_{i,j+1}^{n+\frac{1}{2}} - \chi_{i,j-1}^{n+\frac{1}{2}}) \\ v_{ij}^{n+\frac{1}{2}} &= -\frac{1}{2\Delta}(\chi_{i+1,j}^{n+\frac{1}{2}} - \chi_{i-1,j}^{n+\frac{1}{2}}), \end{aligned} \tag{4.5}$$

$$\begin{aligned} \omega_{ij}^{n+1} &= \omega_{i,j}^n - \frac{\Delta t}{2\Delta} u_{i,j}^{n+\frac{1}{2}}(\omega_{i+1,j}^{n+\frac{1}{2}} - \omega_{i-1,j}^{n+\frac{1}{2}}) - \frac{\Delta t}{2\Delta} v_{i,j}^{n+\frac{1}{2}}(\omega_{i,j+1}^{n+\frac{1}{2}} - \omega_{i,j-1}^{n+\frac{1}{2}}) \\ &+ \frac{\Delta t}{2\Delta^2 R}(\omega_{i+1,j+1}^n + \omega_{i-1,j+1}^n + \omega_{i+1,j-1}^n + \omega_{i-1,j-1}^n - 4\omega_{i,j}^n) \\ &+ \frac{\Delta t M^2}{R} S(i,j). \end{aligned} \tag{4.6}$$

The term containing the viscous diffusion of vorticity has been included by a first-order explicit method. Finally, to complete the time step, Poisson's equation is solved to determine the stream function at time step $n+1$. For convenience we make sure that the space mesh spacing Δ is the same on both x and z-axes.

To ensure stability the time step Δt must satisfy the Courant-Friedrichs-Lewy condition (Potter [13, pages 72, 75]) for two dimensions,

$$\Delta t \leq \frac{\Delta}{\sqrt{2}\,|v|_{max}}, \tag{4.7}$$

where the characteristic velocity here is the advective fluid velocity. To satisfy the von Neumann criterion for stability the time step must satisfy (Potter [13, page

54])

$$\begin{aligned} \Delta t &\leq 0.5\frac{\Delta^2}{\nu} \\ \text{or } \Delta t &\leq 0.5R\Delta^2. \end{aligned} \tag{4.8}$$

Since the viscosity is small (Reynolds number is large) it can be concluded that the time step will be limited by the advection time not the diffusion time (Potter [13, page 211]). Hence, the viscous diffusion term is included only in the main stage where it is calculated to first-order accuracy.

4.3.1 Numerical scheme

All calculations are carried out based on the rectangular region $[0, L]$ by $[-a, a]$, (figure 2.4). The $x-$axis and $z-$axis are divided into m equal partitions and $n-1$ equal partitions respectively. Throughout we set the partition widths to be the same in both axes we get $a = \frac{(n-1)}{2m}$. So, we can vary the value of a by varying m and n. The initial conditions at $t = 0$ in dimensionless form are

$$u = -1, \quad v = 0 \quad \omega = 0, \quad \chi = -(z + a).$$

It is important to note that since we use a frame of reference stationary with respect to the applied magnetic field which moves with velocity $U\hat{\boldsymbol{x}}$, the source term S is independent of time.

The Lax-Wendroff scheme updates ω at interior grid points only. To calculate the vorticity values on the boundaries we use a technique described by Roache [16, page 141]. The Taylor series expansion in z of $\chi(x, z)$ about $(x, -a)$ is:

$$\begin{aligned} \chi(x, -a + h) &= \chi(x, -a) + h\left(\frac{\partial \chi}{\partial z}\right)(x, -a) + \frac{h^2}{2!}\chi_{zz}(x, -a) + [h^3] \\ &\approx -Uh + \frac{1}{2}h^2\omega(x, -a) \end{aligned}$$

since $\chi(x, -a) = 0, \quad \chi_z(x, -a) = -U$, and where $h = \Delta x$. Hence the vorticity on the boundary $z = -a$ is given by

$$\omega(x, -a) \approx \frac{2}{h^2}\left[\chi(x, -a + h) + Uh\right]. \tag{4.9}$$

Similarly, on the boundary $z = a$, the Taylor series expansion in z for $\chi(x, z)$ about (x, a) is

$$\begin{aligned}\chi(x, a-h) &= \chi(x, a) - h\left(\frac{\partial \chi}{\partial z}\right)(x, a) + \frac{h^2}{2!}\chi_{zz}(x, a) + [h^3] \\ &\approx -2Ua + Uh + \frac{1}{2}h^2\,\omega(x, a),\end{aligned}$$

where $\chi(x, a) = -2Ua$. Therefore, we get

$$\omega(x, a) \approx \frac{2}{h^2}\left(\chi(x, a-h) - Uh + 2Ua\right). \tag{4.10}$$

4.4 Solving Poisson's equation

To recover the stream function χ we need to solve the Poisson's equation $\nabla^2\chi = \omega$, using the updated vorticity ω given by the Lax-Wendroff method. The boundary conditions are

$$\begin{aligned}\chi(x, -a) &= 0, \\ \chi(x,\ a) &= -2Ua.\end{aligned}$$

We set $\chi(-a) = 0$. To find the boundary condition at $z = a$,

$$(\boldsymbol{v})_{z=\pm a} = -U\,\hat{\boldsymbol{x}},$$

We note that in the frame of reference moving with the magnetic field the mean flow rate is $-U$, since the channel is closed, and

$$-\int_{-a}^{a} U\,dz = -2Ua = \chi(x,\ a).$$

The next task is to solve the differential equation

$$\nabla^2\chi = \omega(x, z), \quad \text{where} \quad \chi(-a) = 0,\ \chi(a) = -2U\,a. \tag{4.11}$$

Now let us break the problem into two parts.

Problem 1:

$$\nabla^2\chi = \omega(x, z), \quad \chi(-a) = 0,\ \chi(a) = 0, \tag{4.12}$$

Problem 2:

$$\nabla^2\chi = 0, \quad \chi(-a) = 0, \ \chi(a) = -2Ua. \tag{4.13}$$

Let $\chi = \chi_1$ be the solution to problem 1 and $\chi = \chi_2$ be the solution to problem 2. It then follows that $\chi = \chi_1 + \chi_2$. It can easily be seen that the solution to problem 2 is

$$\chi_2(x, z) = -U(z + a),$$

and hence that

$$\chi = \chi_1 - U(z + a). \tag{4.14}$$

A spectral method involving a Fast Fourier Transform (FFT) is used to solve Poisson's equation. The applied magnetic field is periodic, hence it is logical to expect that the vorticity and stream function will also be periodic. Let the Fourier Series for ω be

$$\omega(x, z) = \sum_{n=-\infty}^{\infty} \alpha_n(z) e^{2n\pi \mathrm{i} x/L} \tag{4.15}$$

where L is the period (or wavelength) and the Fourier coefficients α_n are given by

$$\alpha_n(z) = \frac{1}{L}\int_0^L \omega(z, x)\, e^{-2n\pi \mathrm{i} x/L}\, dx. \tag{4.16}$$

Similarly for the stream function we have

$$\chi(x, z) = \sum_{-\infty}^{\infty} \beta_n(z)\, e^{2\pi \mathrm{i} nx/L}, \tag{4.17}$$

with boundary conditions $\chi(x, -a) = 0, \quad \chi(x, a) = -2Ua.$

By substituting the Fourier series for ω and χ in the Poisson equation (4.2) we obtain a sequence of ordinary differential equations

$$\beta_n'' - \left(\frac{2n\pi}{L}\right)^2 \beta_n = \alpha_n(z). \tag{4.18}$$

Problem 1 can be reduced to

$$\begin{aligned} \beta_n'' - \left(\frac{2n\pi}{L}\right)^2 \beta_n &= \alpha_n(z), \\ \beta_n(\pm a) &= 0, \quad n \in \mathbb{I}. \end{aligned}$$

By discretising the above differential equation we get a tridiagonal system. To solve for β we use a procedure tri which will be discussed in the following sub-section. Now the values of β are known we use the inverse Fourier transform to determine χ, and hence the solution to Poisson's equation.

4.4.1 Discretisation of differential equation

The differential equation to be solved is of the form

$$f'' - \gamma^2 f = g(z), \quad f(\pm a) = 0. \tag{4.19}$$

We divide the line segment between $[-a, a]$ into $n-1$ equal segments of length h where $h = 2a/(n-1)$.

Let

$$f_1 = f(-a) = 0, \qquad f_n = f(a) = 0.$$

Equation (4.19) is approximated by the discrete form

$$\frac{f_{i+1} + f_{i-1} - 2f_i}{h^2} - \gamma^2 f_i = g_i,$$

which can be rearranged to give

$$f_{i-1} - Df_i + f_{i+1} = h^2 g_i,$$

where $D = (2 + h^2\gamma^2)$.

The system of equations, in matrix form, becomes

$$\begin{pmatrix} -D & 1 & & & & \\ 1 & -D & 1 & & & \\ & 1 & -D & 1 & & \\ & & & 1 & -D & 1 \\ & & & & 1 & -D \end{pmatrix} \begin{pmatrix} f_2 \\ f_3 \\ f_4 \\ \vdots \\ f_{n-2} \\ f_{n-1} \end{pmatrix} = h^2 \begin{pmatrix} g_2 \\ g_3 \\ g_4 \\ \vdots \\ g_{n-2} \\ g_{n-1} \end{pmatrix}, \tag{4.20}$$

since $f_1 = 0$ and $f_n = 0$.

Tridiagonal method

The tridiagonal routine, which is called procedure Tri here, is discussed in Cheyney& Kincaid [2, pages 274-276]. It is designed to solve a tridiagonal system of n linear equations of n unknowns. In this method one step of a Gaussian elimination is carried out first followed by the back substitution. In our system of equations (4.20) back substitution gives $f_{n-1}, f_{n-2}, \ldots, f_2$.

4.4.2 Testing the Poisson solver

The code to solve Poisson's equation

$$\nabla^2 \chi = \omega,$$

was tested using two problems that have analytical solutions. The first test has the analytical solution χ which depends on z only whereas the second test problem involves both x and z and is periodic along the $x-$axis. For each test we calculate Δ_{diff}, which is the square root of "the differences" between the numerical values, $f_n(i, j)$, and analytical values, $f_a(i, j)$, over the total number of points in the domain. The Δ_{diff} is defined as

$$\Delta_{\text{diff}} = \left[\sum_{i=1}^{m+1} \sum_{j=1}^{n} \left(f_n(i,j) - f_a(i,j) \right)^2 / \left(n(m+1) \right) \right]^{\frac{1}{2}} \tag{4.21}$$

Test 1

The problem

$$\nabla^2 \chi = -U(z+a), \quad \chi(-a) = 0, \ \chi(a) = -2Ua,$$

has the analytical solution

$$\chi(x,z) = -U \left[\frac{1}{6} z^3 + \frac{1}{2} a z^2 + \left(1 - \frac{1}{6} a^2 \right) z + a - \frac{1}{2} a^3 \right]$$

Test 2

The problem

m	n	Δ_{diff}
60	61	3.6522993E-16
90	91	2.2603284E-16
100	101	2.4262470E-16
100	51	4.2878925E-17
150	76	4.1219499E-17
200	101	3.7402253E-17

Table 4.1: The Δ_{diff} values in double precision for various values of m and n, for Test 1.

$k = 2$			$k = 6$		
m	n	Δ_{diff}	m	n	Δ_{diff}
30	31	2.1128288E-16	30	31	5.2689480E-15
40	41	1.6983080E-16	60	61	1.5963220E-15
80	41	1.6612021E-16	100	51	2.6283681E-16
100	51	1.4401860E-16	120	61	9.2224720E-17

Table 4.2: The Δ_{diff} values in double precision for cases $k = 2$ & $k = 6$, Test 2 for various values of m and n.

has the analytical solution

$$\chi(x, z) = \sin(2\pi kx)\,(a^2 - z^2) - U(z + a).$$

Table 4.1 gives the Δ_{diff} for various increasing number of partitions for Test 1. For Test 2 table 4.2 gives the Δ_{diff} for cases of $k = 2$, and $k = 6$. Both numerical test results show that the Poisson solver codes are excellent. The bigger the number of partitions the better the convergent is, as indicated by the square root of "the differences," Δ_{diff}, getting smaller.

4.5 Fluid motion due to a two Fourier-component source

As in §2.2 we consider the flow of incompressible conducting fluid contained in a channel of infinite length and width driven by a two Fourier-component source field:

$$\left(\frac{\partial \phi}{\partial z}\right)_{z=\pm a} = B_0 \left[\cos k(x - Ut) + b \cos 2k(x - Ut)\right], \tag{4.22}$$

where b is a constant, which travels down the channel with velocity $U\hat{\boldsymbol{x}}$. At time $t = 0$ the applied magnetic field $\boldsymbol{B}$ is suddenly moved at a uniform velocity $U\hat{\boldsymbol{x}}$.

As derived in §2.3.2 the dimensionless governing equations are

$$\frac{\partial \omega}{\partial t} + (\boldsymbol{v} \cdot \boldsymbol{\nabla})\,\omega = \frac{M^2}{R} S(x, z, t) + \frac{1}{R} \nabla^2 \omega \tag{4.23}$$

$$\nabla^2 \chi = \omega, \tag{4.24}$$

where $R = UL/\nu$ is the Reynolds number, M is the Hartmann number,

$$M = LB_0 \left(\frac{\sigma}{\nu \rho}\right)^{\frac{1}{2}}, \tag{4.25}$$

and

$$\boldsymbol{\omega} = \nabla \times \boldsymbol{v}.$$

The velocity $\boldsymbol{v}$ of the fluid is expressed in terms of a stream function:

$$\boldsymbol{v} \;=\; -\nabla \times (\chi\, \hat{\boldsymbol{y}}) = \left(\frac{\partial \chi}{\partial z},\, 0,\, -\frac{\partial \chi}{\partial x}\right). \tag{4.26}$$

The curl of the Lorentz force, (3.6) , can be written as $\frac{M^2}{R} S(x, z, t)$ where

$$\begin{aligned} S(x, z, t) \;&=\; \pi U \left[\frac{1}{c_1^2} \sinh 2kz + \frac{2b^2}{c_2^2} \sinh 4kz \right. \\ &\left. + \frac{b}{c_1 c_2} \left(3 \sinh 3kz \cos k(x - Ut) + \sinh kz \cos 3k(x - Ut)\right)\right], \end{aligned} \tag{4.27}$$

$c_n = \cosh(nK)$, n is a natural number and $K = ak$. The initial condition (in dimensional form) is

$$(\boldsymbol{v})_{t=0} \;=\; -U\,\hat{\boldsymbol{x}}$$

and the boundary conditions are

$$(\boldsymbol{v})_{z=\pm a} \;=\; -U\,\hat{\boldsymbol{x}}.$$

The analytical expression for the source term is given by (4.27) . The vorticity equation (4.23) is nonlinear in the advection term.

4.5.1 Main program

In the main program we use the following input quantities:

m	-	number of partitions along the x-axis
n	-	number of points along the z-axis
b	-	the second Fourier component
t	-	final time
R	-	Reynolds number
M	-	Hartmann number.

The strength of the source term $S(x, z, t)$ depends on the value of the magnetic interaction parameter $\mathcal{N}(= M^2/R)$. The program outputs the stream function χ relative to the applied magnetic field which moves at the velocity of $U\hat{\boldsymbol{x}}$, to which $U(z+a)$ must be added to give the stream function in a stationary frame. In other words, all the graphs of the streamlines are with respect to the stationary frame.

4.5.2 Numerical results

It is important to see how the results of this main program compare with the analytical results for $b = 0$, and the initial fluid motion due to a two Fourier-component source, R_m small as investigated in Chapter 3.

Comparison with the analytical result for $b = 0$

The main program is run for $b = 0$, (i.e. one Fourier component) over time $t = 0.5, \text{and } 8.0$ to produce the velocity which, in this case, is in the $x-$direction only. The stationary case for $b = 0$ has an analytical solution (Saad [18]),

$$u(z) = \frac{M^2 U}{64K^3{c_1}^2}\left[4K(c_2 - \cosh(2Kz)) + 3(s_2 - 2Kc_2)(1 - z^2)\right],$$

where $c_n = \cosh nK$, $s_n = \sinh nK$, $n \in \mathbb{N}$ and $K = ak$.

The graphs of the velocity versus z for both analytical and numerical cases are in figure 4.1. It can be seen that the numerical velocity values approach the analytical values as time t increases as expected.

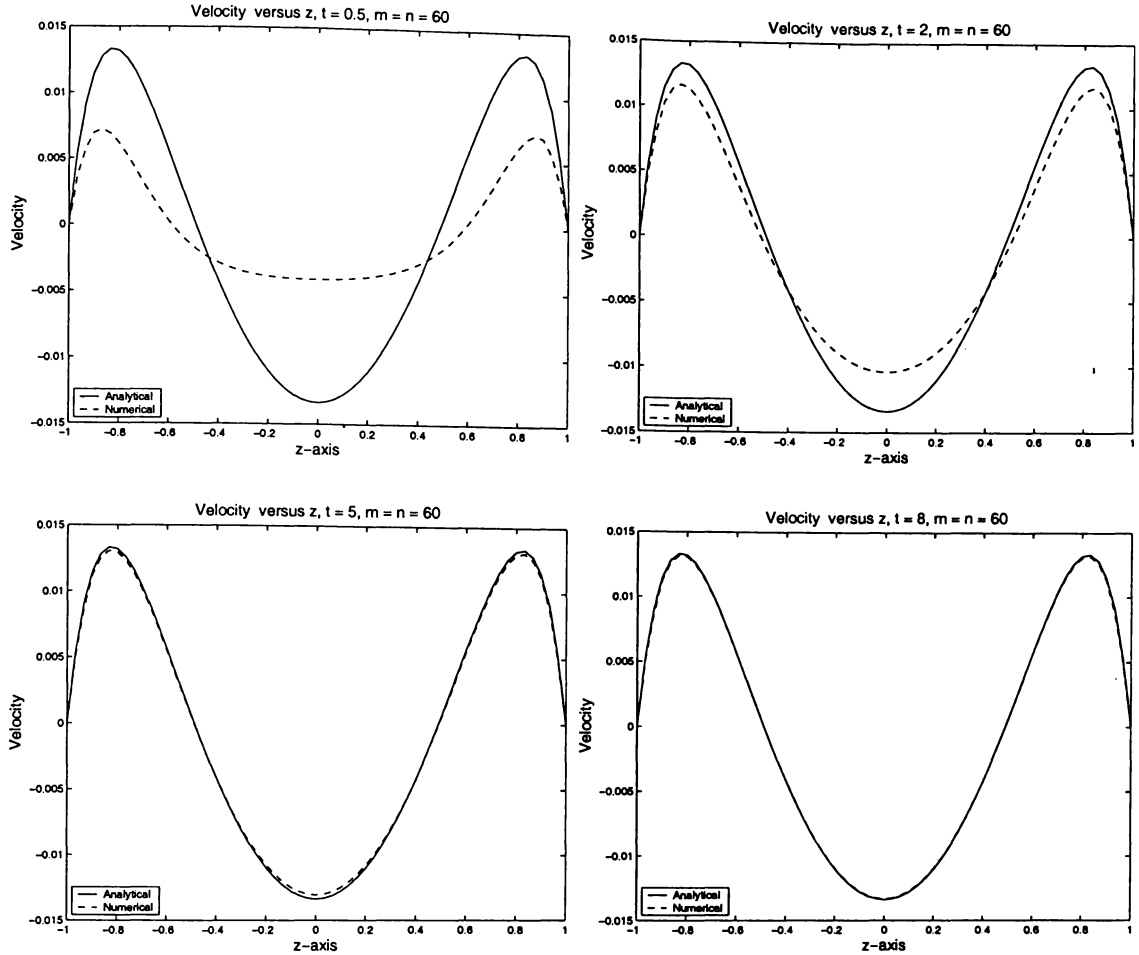

Figure 4.1: Graphs of velocity versus z , $b = 0$ for both analytical and numerical results at various times, $t = 0.5$, 2, 5, 8 where $\mathcal{N} = 0.16$ and $a = 0.5$. The broken line corresponds to the numerical solution and the continuous line is for the analytical solution. The number of partitions is 60×60.

Comparison with the initial fluid flow

Here we compare the early time streamlines due to the initial flow for a two Fourier-component source (3.26) with the streamlines from the numerical results of this section at Hartmann number $M = 2$ and Reynolds number $R = 400$, so that the magnetic interaction parameter $\mathcal{N} = 0.01$. We take the time to be $t = 0.02$, so that it is early enough to agree with the initial fluid flow where the viscosity term is neglected in chapter 3. Four cases are investigated in this chapter: figures 4.2–4.5. The corresponding cases in chapter 3 are figures 3.2–3.5. It can be seen that the

initial corresponding streamlines agree well in all cases. Some effect close to the boundaries are due to the viscosity even though it is small.

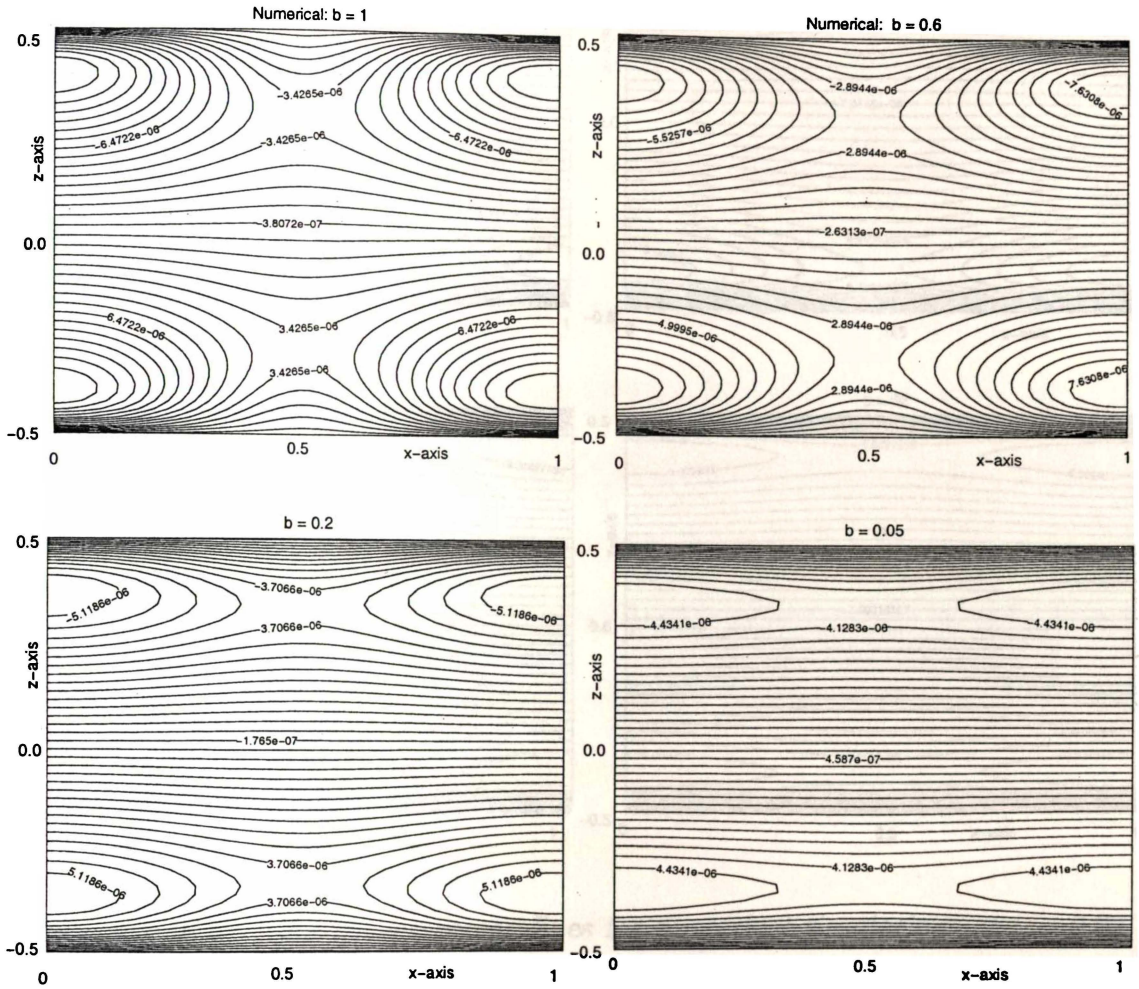

Figure 4.2: Early time stage: Streamlines for numerical simulations at $t = 0.02$, $\mathcal{N} = 0.01$. *The corresponding case in chapter 3 is Case I (figure 3.2). Streamlines tend towards straight line flow as b gets smaller.*

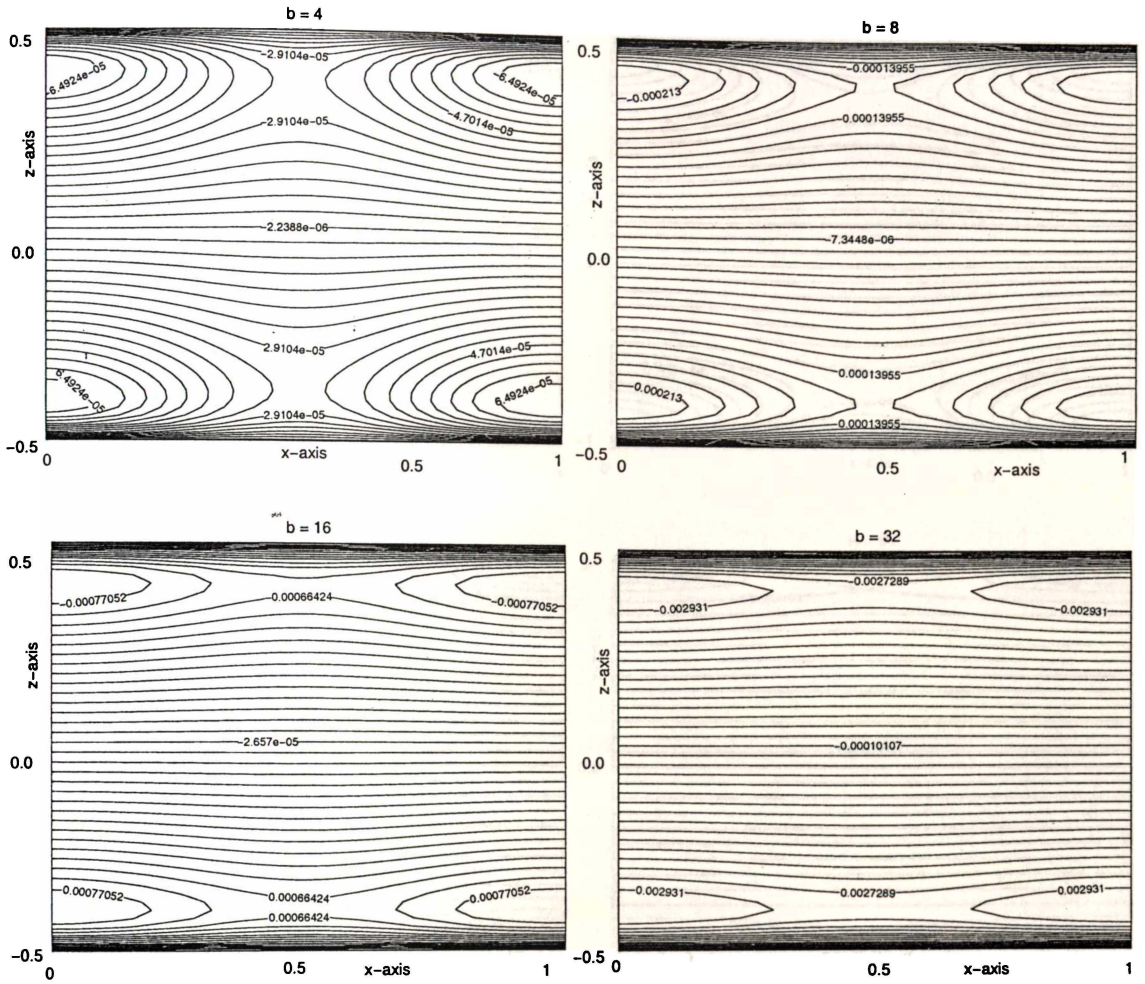

Figure 4.3: Early time stage: Streamlines for numerical simulations at $t = 0.02$ *,* $\mathcal{N} = 0.01$*. The corresponding case in chapter 3 is Case II (figure3.3). As b increases the streamlines tend towards straight line with vanishing vortices.*

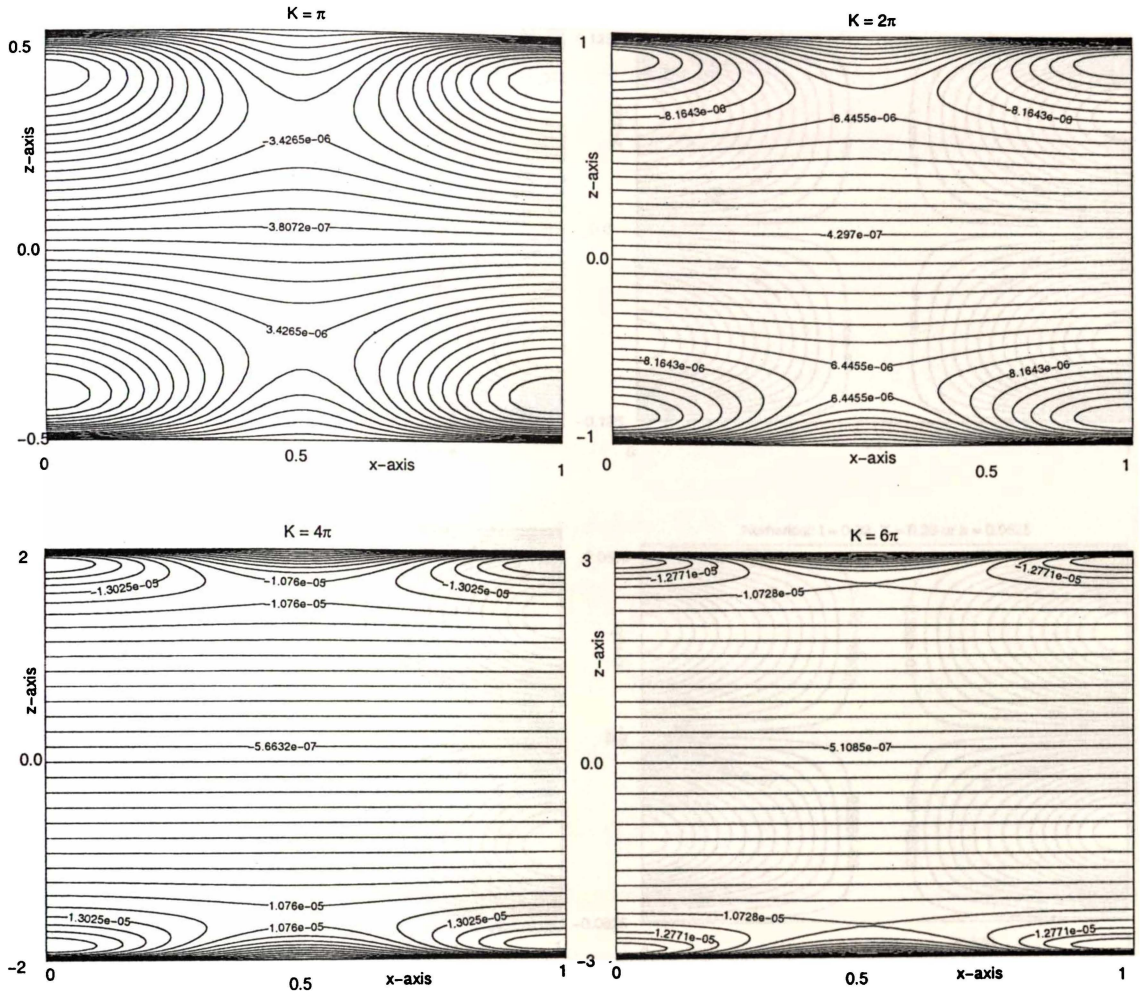

Figure 4.4: Early time stage: Streamlines for numerical simulations at $t = 0.02$, $\mathcal{N} = 0.01$, $b = 1.$ *and* $K = \pi, 2\pi, 3\pi, 4\pi$. *The corresponding case in chapter 3 is Case III (figure 3.4). As* K *(or equivalently,* a*) increases the streamlines become more straight line with a thin layer of vortices on the boundaries.*

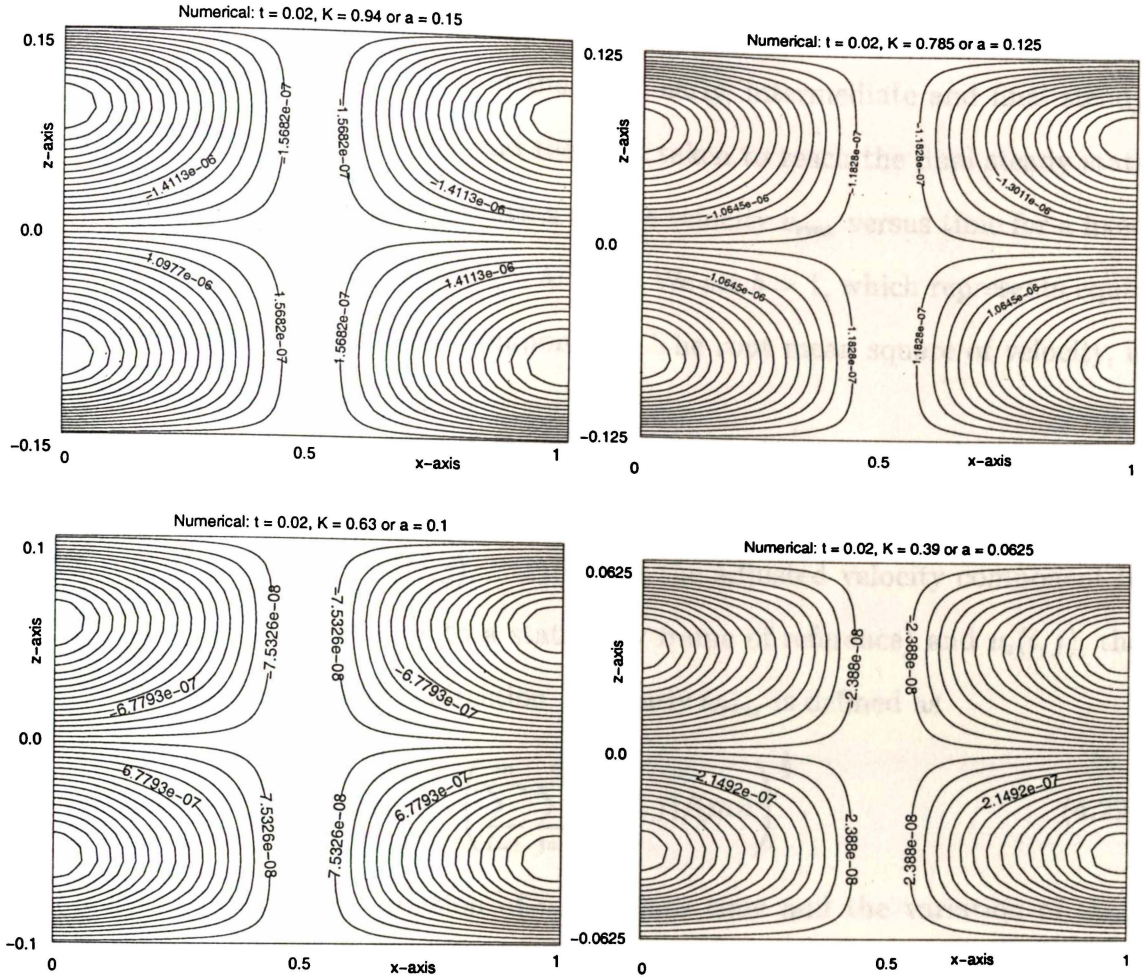

Figure 4.5: Early time stage: Streamlines for numerical simulations at $t = 0.02$, $\mathcal{N} = 0.01$, $b = 1.$ *and* $a = 0.15, ..., 0.0625$. *The corresponding case in chapter 3 is Case IV (figure 3.5). The shorter the aspect ratio* a *the more well-formed the vortices in the streamlines become.*

4.5.3 Flow development with time

We are interested in three stages of the flow: early, intermediate and final steady state. To see changes in the flow and the time taken to reach the final steady state we investigate the variation of the mean square velocity v_{rms} versus time for a fixed magnetic interaction parameter $\mathcal{N}$ $(= M^2/R)$. We set $b = 1$, which represents equal contributions from both Fourier components. The root mean square of velocity, is given by

$$v_{rms} = \left(\sum_{i=1}^{m} \sum_{j=1}^{n} v^2(i,j)/(mn) \right)^{\frac{1}{2}} \tag{4.28}$$

where $v^2(i,j) = v_x^2(i,j) + v_z^2(i,j)$, $v_x(i,j)$ is the adjusted velocity component in the $x-$ direction (i.e. relative to a stationary frame of reference) and $v_z(i,j)$, the velocity component in the $z-$ direction. Similarly ω_{rms} is defined as

$$\omega_{rms} = \left(\sum_{i=1}^{m} \sum_{j=1}^{n} \omega^2(i,j)/(mn \right)^{\frac{1}{2}}. \tag{4.29}$$

Figure 4.6 shows the variation of v_{rms} versus time and the variation of ω_{rms} vs. time respectively for $\mathcal{N} = 0.05$ and $R = 1000$. Both reach a steady state simultaneously. The steady state is reached when vorticity generation is balanced by diffusion.

We investigate the growth of v_{rms} versus time for increasing values of the magnetic interaction parameter $\mathcal{N} \ll 1$. From figure 4.7 we can see that the steady state v_{rms} increases with $\mathcal{N}$. This is supported by figure 4.8 that shows a linear relationship between steady state v_{rms} and the magnetic interaction parameter $\mathcal{N}$. Also from the dimensionless equation (4.23) it can be seen that in the steady state

$$v, \omega \propto \mathcal{N},$$

which explains the linear relationship as shown by figure 4.8. It is interesting to note that the times, t_{max}, for the flow to reach a steady state say are about equal i.e. ≈ 80 time units, for different values of $\mathcal{N}$ as can be seen in figure 4.7.

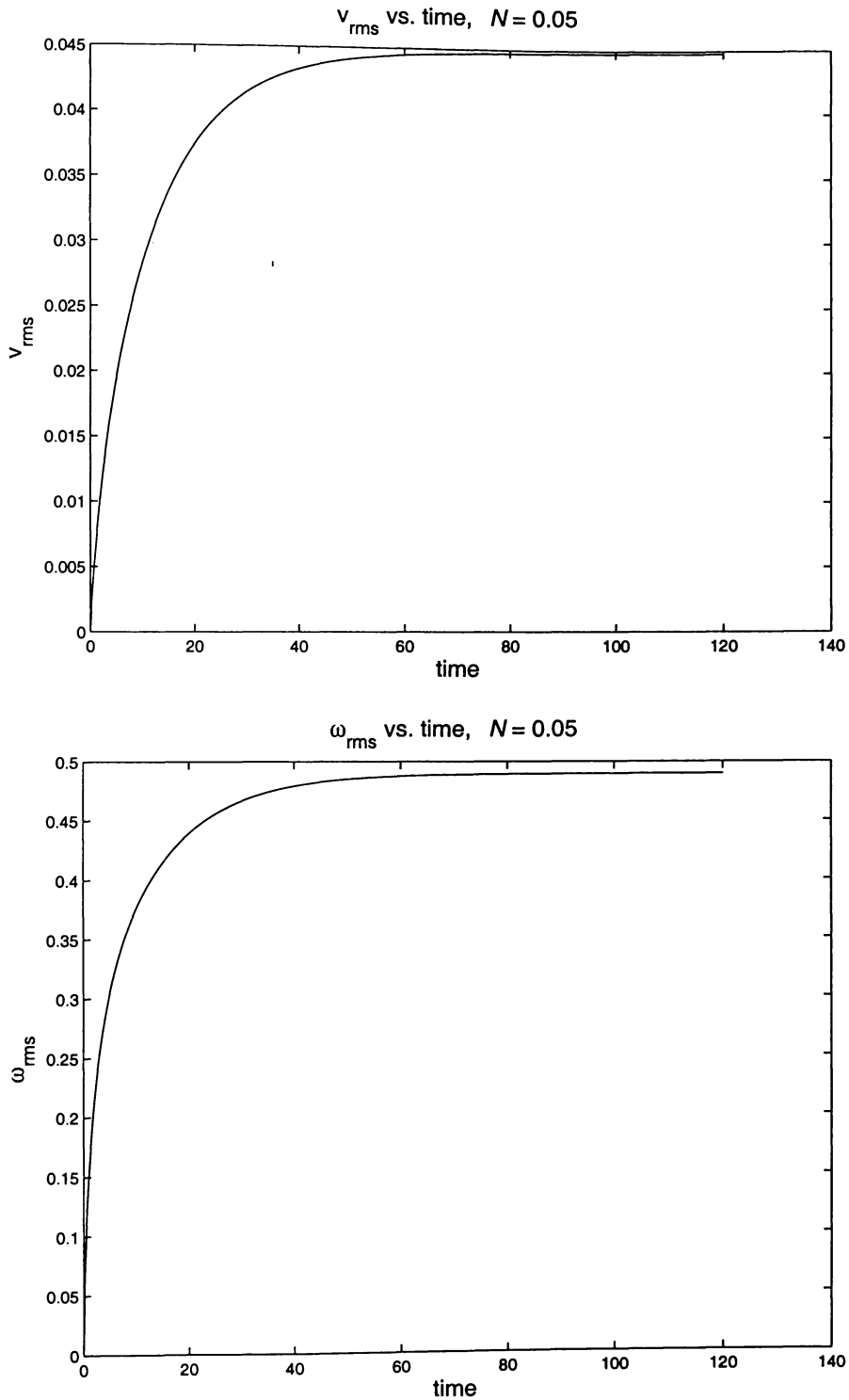

Figure 4.6: Variation of v_{rms} and ω_{rms} vs. time respectively for $\mathcal{N} = 0.05$, and $R = 1000$.

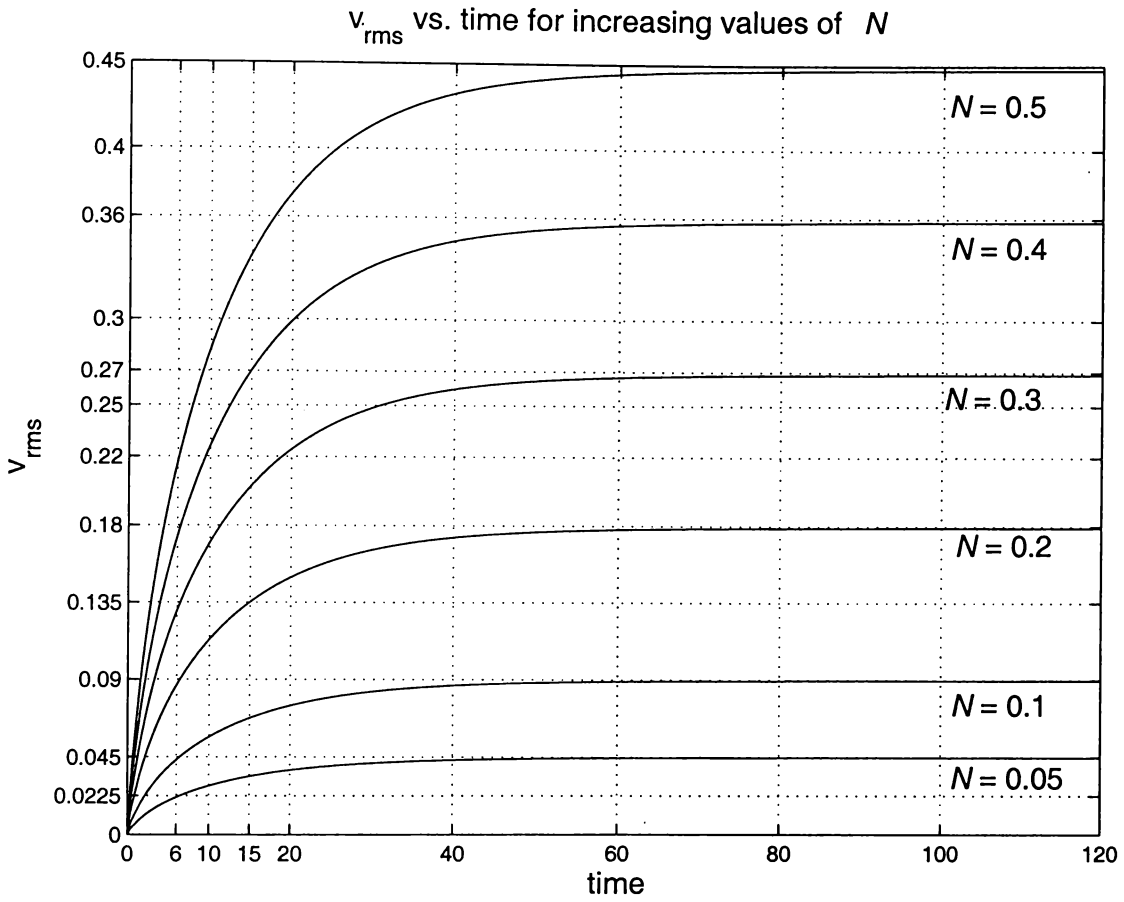

Figure 4.7: Steady state v_{rms} vs. time at increasing values of $\mathcal{N} \ll 1$, *and* $R = 1000$.

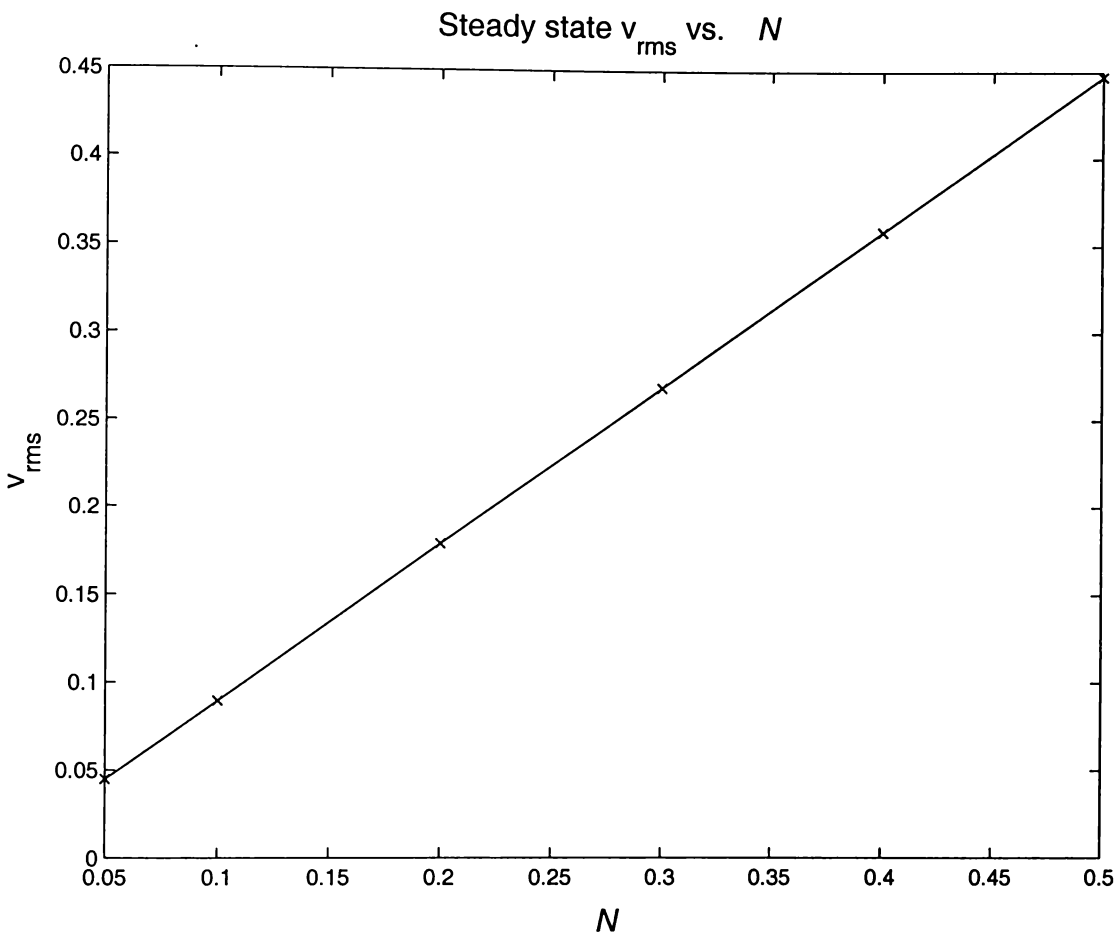

Figure 4.8: A linear relation between steady state v_{rms} and $\mathcal{N}$ while $R = 1000$.

Early stage

In the early stage the velocity field is not affected by diffusion or convection which do not have enough time to take effect. In figure 4.7 v_{rms} increases rapidly to half its steady state value within 6 time units or 8% of t_{max}. This rapid acceleration is due to the applied magnetic field being impulsively accelerated to velocity $U\hat{x}$. Similarly ω_{rms} accelerates simultaneously with v_{rms} as can be seen in figure 4.9. As with v_{rms}, there is a linear relation between ω_{rms} and $\mathcal{N}$, figure 4.10.

In the case of initial motion due to a two Fourier-component source, where R_m is small (§3.2) the convective and viscosity terms are ignored. To compare the analytical solution with a best precision numerical calculation we set the value of $R = 400$ and $M = 2$ so that $\mathcal{N} = 0.01$. The results agree well in all cases investigated as covered in §4.5.2 under "Comparison with the initial fluid flow." A large Reynolds number e.g. 400 makes the effect of the viscosity term $\frac{1}{R}\nabla^2$ negligible, especially in the early time stage.

Intermediate stage

During the intermediate stage vorticity is increasing but at a rate that is slow and levelling off as in figure 4.7. This is because the rate of vorticity generation due to the source term $\mathcal{N}S$, is still greater than the rate at which the vorticity is being annihilated (which is increasing). As time increases the influence of the diffusion and convective terms becomes more and more important. In most cases except for Case IV the streamlines begin to straighten. Streamlines during the intermediate stage for Cases I and IV are given in figures 4.11 and 4.12.

Steady state

When the flow reaches a steady state stage $\partial\omega/\partial t = 0$. The rate at which vorticity is being created is balanced by the term $\frac{1}{R}\nabla^2\omega$, which corresponds to the rate which vorticity is being annihilated by viscous diffusion. The streamlines for this stage are

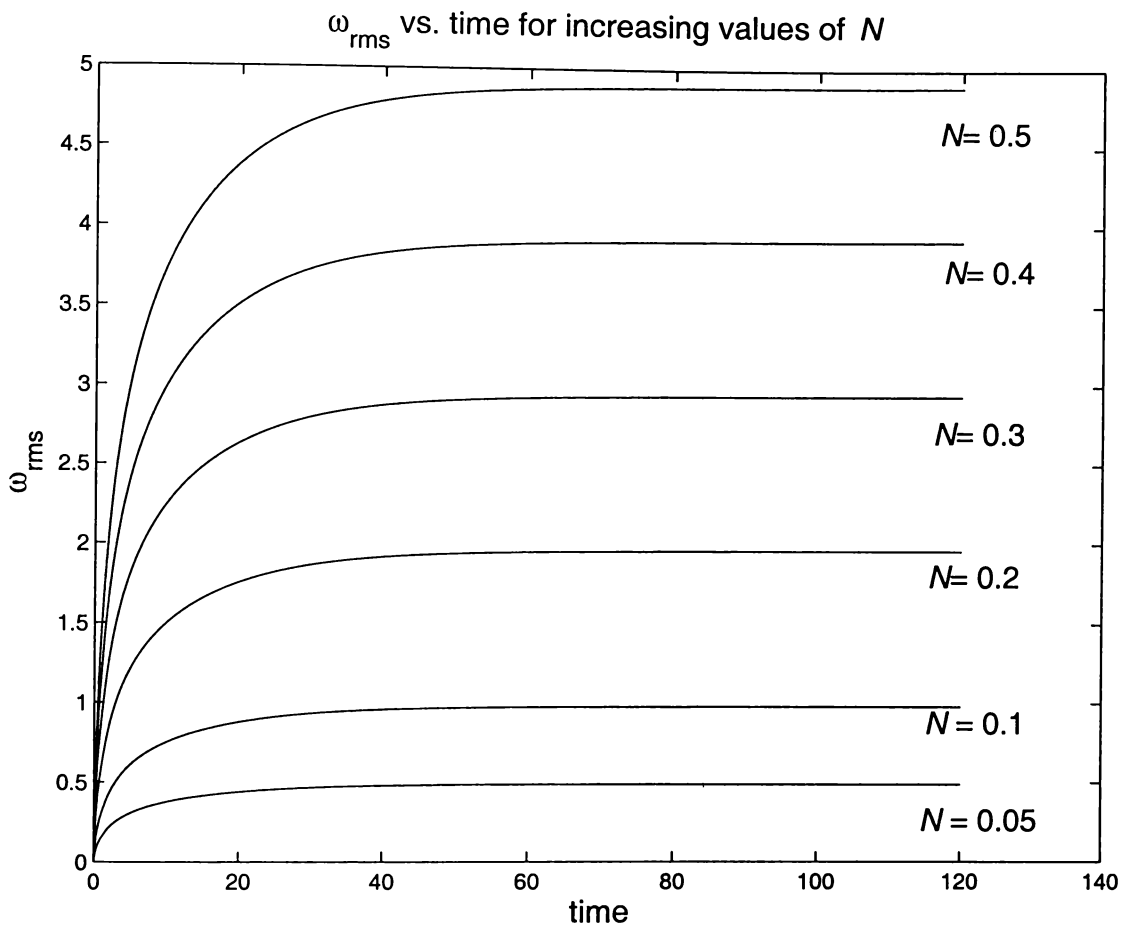

Figure 4.9: ω_{rms} vs. time for increasing values of $\mathcal{N} \ll 1$.

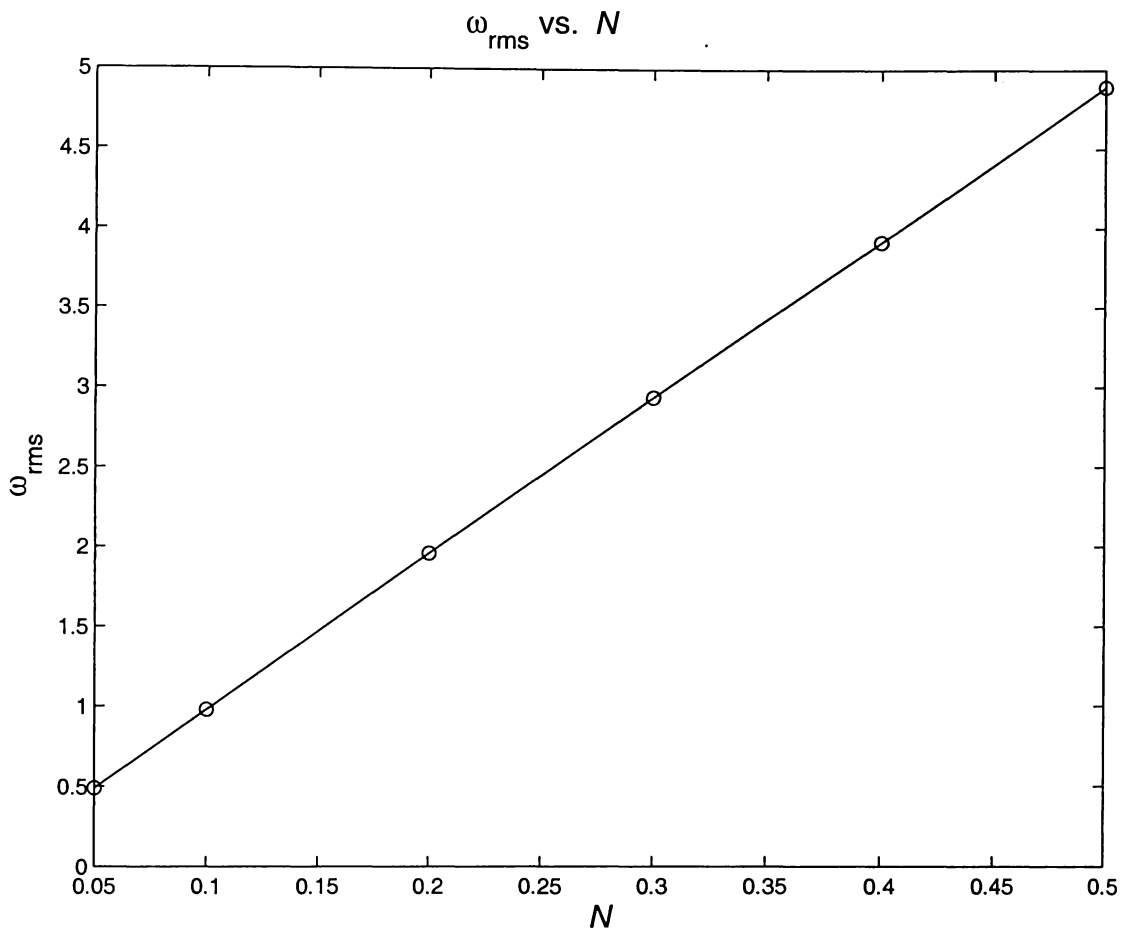

Figure 4.10: A graph of ω_{rms} vs. $\mathcal{N}$ which is linear.

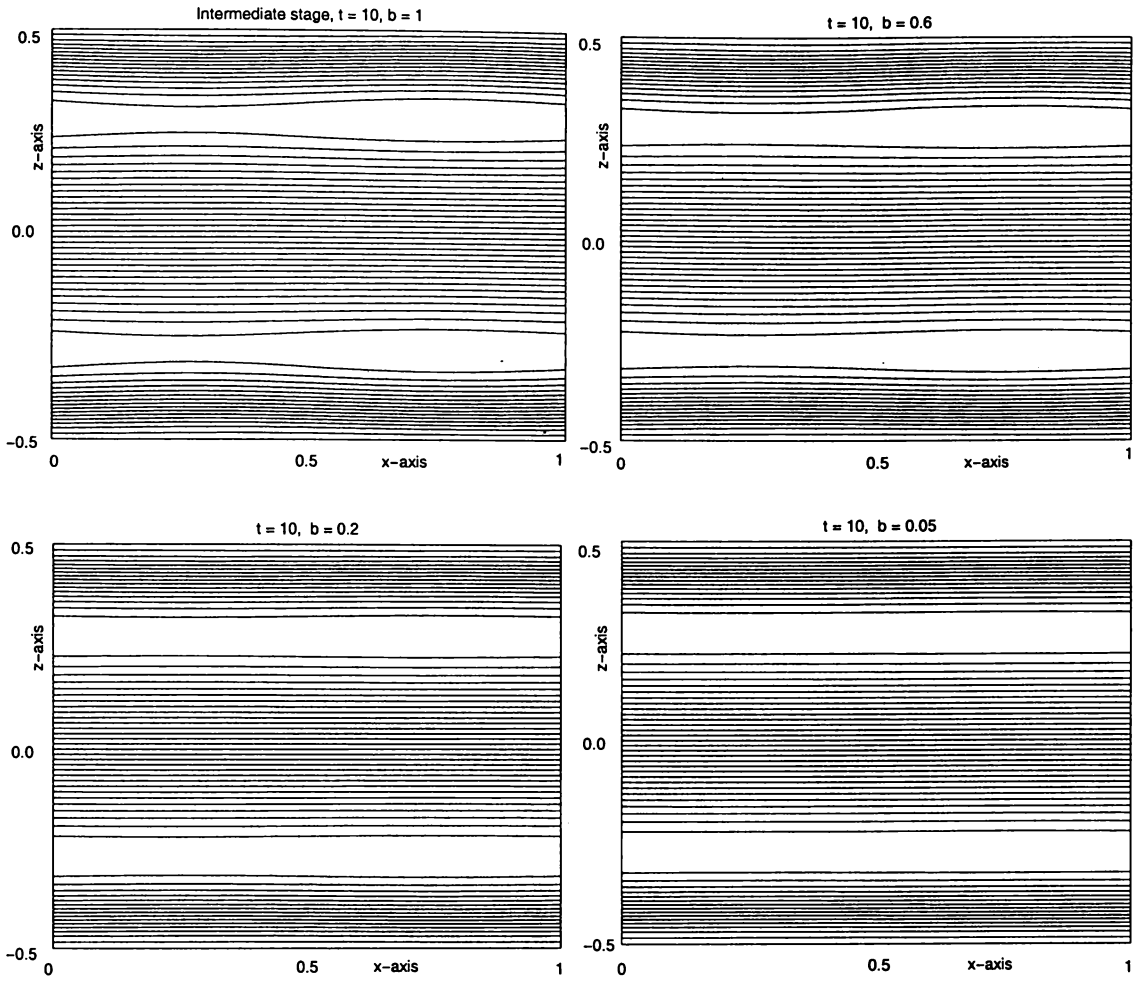

Figure 4.11: Streamlines at intermediate stage (Case I for the early state), $t = 10$ for various values of b. Here $\mathcal{N} = 0.2$.

given by figures 4.13 and 4.14.

In conclusion, for effective stirring of the fluid to take place the width of the channel has to be smaller than or equal to the length L, the wavelength along the x-axis. In a narrow channel the field penetrates the fluid more deeply, hence stirring is more effective, (figure 4.14). We can see that the upper vortex rotates clockwise (figure 4.15) whereas the lower one rotates in the opposite sense. The fluid close to the boundaries flows in the direction of the applied field since it is being swept along by the fieldlines, but the central fluid flows in the opposite direction because the channel is closed. This flow description is true for flows in figures 4.2 to 4.5.

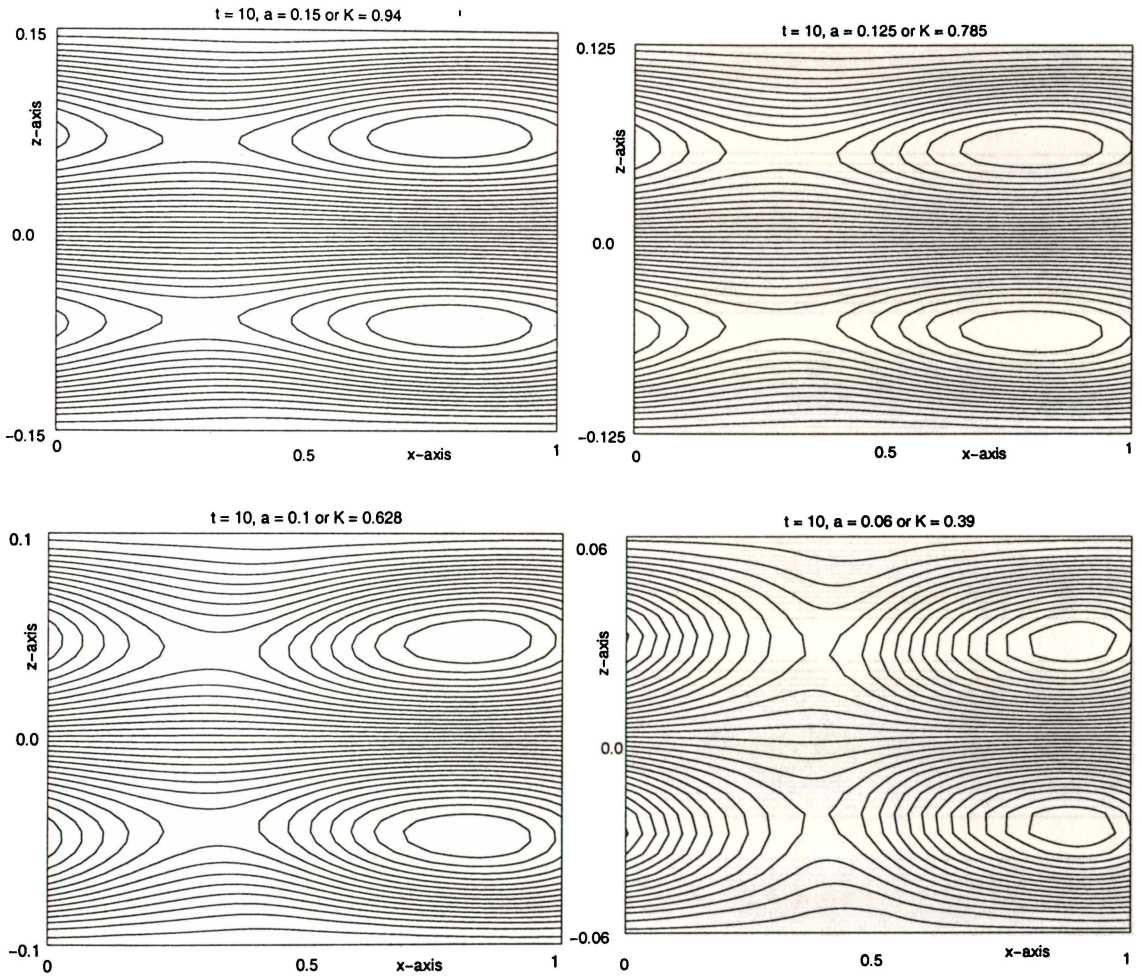

Figure 4.12: Streamlines at the intermediate stage, (Case IV for the early state), $t = 10$ for various values of K. Here $\mathcal{N} = 0.2$.

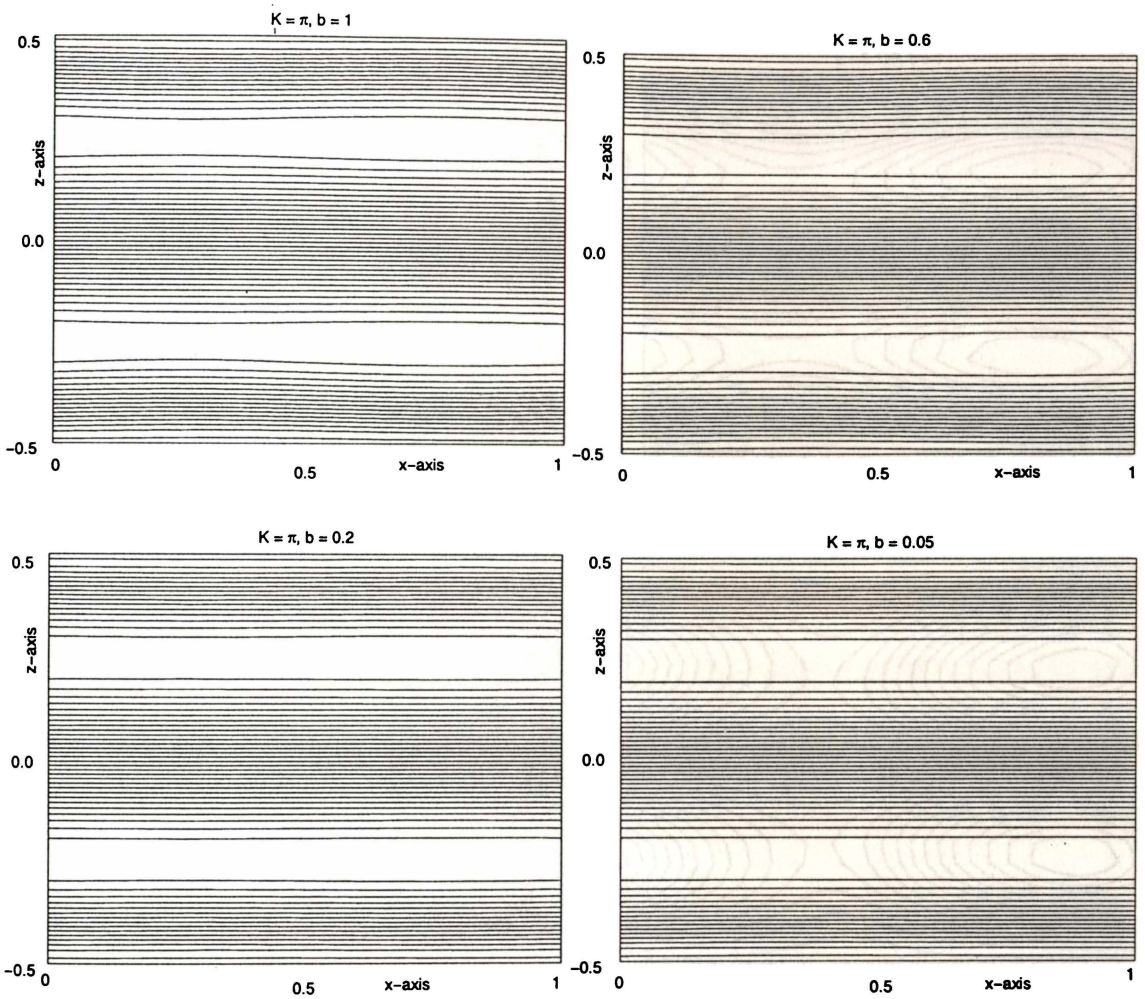

Figure 4.13: Streamlines at steady state, $t = 80$ for various values of a, with $\mathcal{N} \ll 1$. (Case I for the early state.)

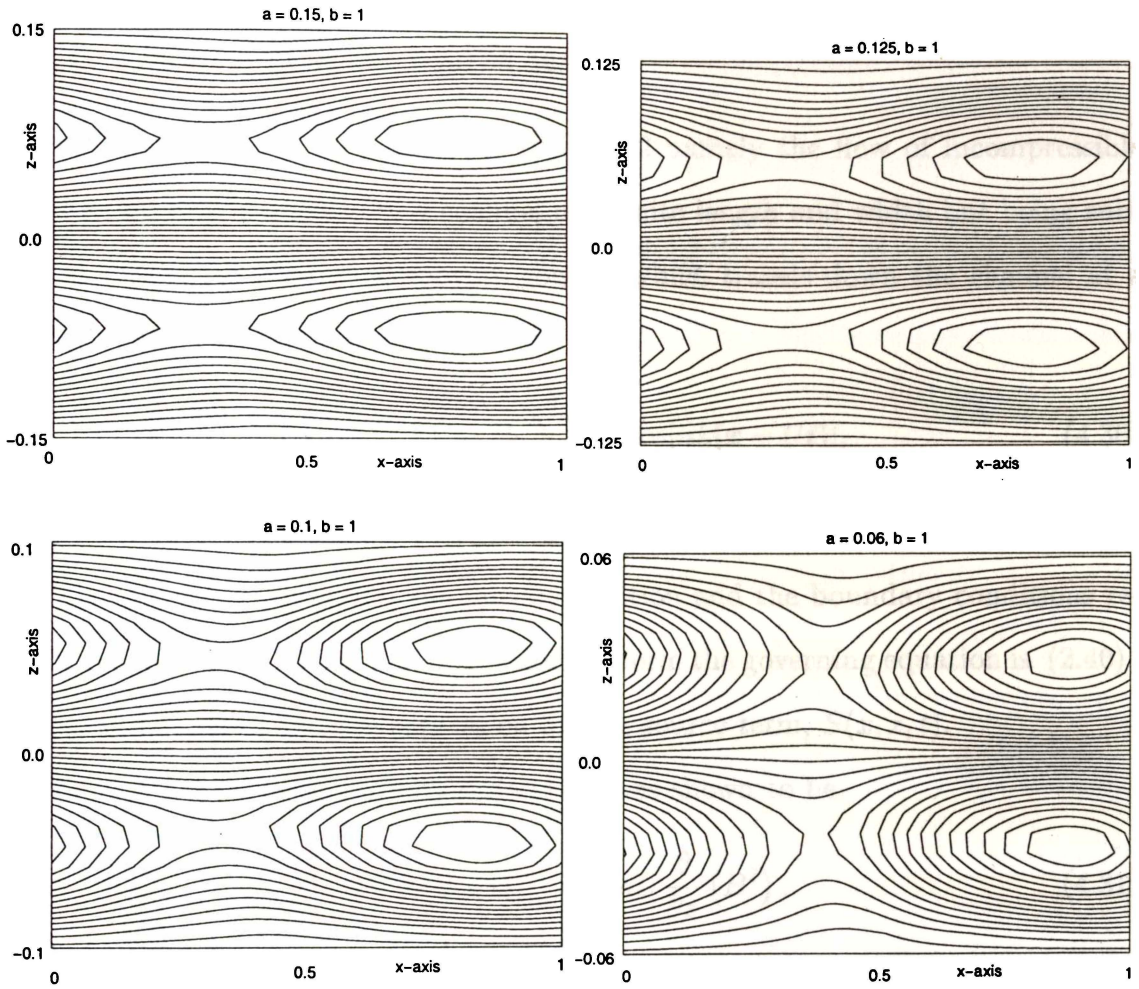

Figure 4.14: Streamlines at steady state, $t = 80$ for various values of a, with $\mathcal{N} \ll 1$. (Case IV for the early stage.)

4.6 Fluid motion due to a multi Fourier-component source

In the previous section the fluid motion was due to a two Fourier- component source. In this section we consider several Fourier components with R_m small as before. The same numerical scheme is used to complete the flow evolution picture for the early time stage, the intermediate and the final steady-state flow.

4.6.1 Derivation of the source term

Here we consider the same problem as in §2.2 namely the flow of incompressible conducting fluid contained in a channel of infinite length and width but being subjected to a multi Fourier-component source, which travels down the channel at a velocity $U\hat{\boldsymbol{x}}$. The field is defined by

$$\left(\frac{\partial \phi}{\partial z}\right)_{z=\pm a} = B_0 \sum_{n=1}^{N} b_n \cos[nk(x-Ut)], \tag{4.30}$$

where the b_n are constants. As in §2.2 we assume R_m is small.

The governing equations, the initial condition and the boundary conditions remain the same as in §3.2 and in dimensionless form the governing equation is (2.40) . Our task here is to find the expression for the source term, $S(x,z,t)$.

In §2.2.2 the rate of vorticity generation was shown to be

$$[\nabla \times (\boldsymbol{J} \times \boldsymbol{B})]_y = \frac{1}{2}\sigma U \frac{\partial}{\partial z}\left(B^2\right). \tag{4.31}$$

Now

$$\begin{aligned} \frac{\partial B^2}{\partial z} &= \frac{\partial}{\partial z}\left({B_x}^2 + {B_z}^2\right), \\ &= 2B_x \frac{\partial B_x}{\partial z} + 2B_z \frac{\partial B_z}{\partial z} \\ &= 2(\phi_x \phi_{xz} + \phi_z \phi_{zz}), \end{aligned} \tag{4.32}$$

where $\boldsymbol{B} = B_x\hat{\boldsymbol{x}} + B_z\hat{\boldsymbol{z}}$.

From equation (2.6) we get the following derivatives

$$\begin{aligned}
\phi_x &= -\sum_{n=1}^{N} \frac{B_0 b_n}{c_n} \sinh(nkz) \sin[nk(x-Ut)] \\
\phi_{xz} &= -\sum_{n=1}^{N} \frac{nkB_0 b_n}{c_n} \cosh(nkz) \sin[nk(x-Ut)] \\
\phi_z &= \sum_{n=1}^{N} \frac{B_0 b_n}{c_n} \cosh(nkz) \cos[nk(x-Ut)] \\
\phi_{zz} &= \sum_{n=1}^{N} \frac{nkB_0 b_n}{c_n} \sinh(nkz) \cos[nk(x-Ut)].
\end{aligned} \tag{4.33}$$

From (2.26) , (4.31) and (4.32) the vorticity equation becomes

$$\frac{\partial \omega}{\partial t} + (\boldsymbol{u} \cdot \boldsymbol{\nabla})\omega = \frac{\sigma U}{\rho} (\phi_x \phi_{xz} + \phi_z \phi_{zz}) + \nu \nabla^2 \omega. \tag{4.34}$$

Using the same equations of dimensionless quantities as in §2.3.2 we non-dimensionalise (4.34) to give

$$\frac{\partial \bar{\omega}}{\partial \bar{t}} + (\bar{\boldsymbol{u}} \cdot \bar{\boldsymbol{\nabla}})\bar{\omega} = 2\pi \frac{M^2}{R} . \frac{1}{{B_0}^2 k} (\phi_x \phi_{xz} + \phi_z \phi_{zz}) + \frac{1}{R} \bar{\nabla}^2 \bar{\omega}, \tag{4.35}$$

where R is the Reynolds number and M is the Hartmann number. We know that $k = \frac{2\pi}{L}$ and by writing the dimensionless quantities $z = L\bar{z}$, and $t = \frac{L}{U}\bar{t}$, (4.35) becomes (in dimensionless form)

$$\frac{\partial \bar{\omega}}{\partial \bar{t}} + (\bar{\boldsymbol{u}} \cdot \bar{\nabla})\bar{\omega} = \frac{M^2}{R} S(\bar{x}, \bar{z}, \bar{t}) + \frac{1}{R} \bar{\nabla}^2 \bar{\omega}, \tag{4.36}$$

where

$$\begin{aligned}
&S(\bar{x}, \bar{z}, \bar{t}) = \\
&\quad 2\pi \left(\sum_{n=1}^{N} \frac{b_n}{c_n} \sinh(2\pi n \bar{z}) \sin[2\pi n(\bar{x} - \bar{t})] \right) \left(\sum_{n=1}^{N} \frac{n b_n}{c_n} \cosh(2\pi n \bar{z}) \sin[2\pi n(\bar{x} - \bar{t})] \right) \\
&+ \quad 2\pi \left(\sum_{n=1}^{N} \frac{b_n}{c_n} \cosh(2\pi n \bar{z}) \cos[2\pi n(\bar{x} - \bar{t}] \right) \left(\sum_{n=1}^{N} \frac{n b_n}{c_n} \sinh(2\pi n \bar{z}) \cos[2\pi n(\bar{x} - \bar{t}] \right).
\end{aligned} \tag{4.37}$$

4.6.2 Numerical coding of equations

The numerical coding for this section is the same as in §4.2 except for the source term, (4.37) , and some corresponding changes for some of the input data and

output results. In this section we can have any number of Fourier Components by specifying the vector b of b_n values in equation (4.30) . The algebra becomes enormously complicated due to the fact that so many combinations are possible: we can vary the number of Fourier Components as well as the values b_n.

4.6.3 Numerical results

The general problem of multi-Fourier component source covers the previous section on the two Fourier-component case (§4.5) by just setting $b_1 = 1$, and $b_2 = b$. In this section we will just produce some results which are of interest based on a set of b_n values and the number of Fourier components used.

As found in §4.5 stronger vorticity occurs in regions where the moving magnetic field lines are stronger. This is evidenced by the streamlines for cases III and IV (figures 4.4, 4.5) and the multi-Fourier source (figure 4.16). Figure 4.4 shows clearly that in wider channels the streamlines straighten and the layer of eddies on the boundaries gets thinner. By making the aspect ratio $a \leq 0.5$ vorticity is spread out over the width of the channel. This is due to the fact that in narrower channels the magnetic field has better penetration as can be seen in figure 4.16. In the same figure we can see the another pair of vortices which should make stirring during metal casting more effective. In our multi Fourier-component experiments we focus on the interesting case of narrow channels where stirring is more intense.

If we assume that the applied field is moved from left to right then the upper eddies are always clockwise and the lower ones counter clockwise. The central flow will always be in the opposite direction of the applied magnetic field. Briefly we conclude that this description of the flow is also true for the flow where there are more than one pair of eddies.

We can make sure that the resolution is sufficient to capture multi-Fourier mode structure by limiting the number of Fourier components to no more than 10. This ensures that the smallest wavelength of the applied magnetic field is 0.1, which is much longer than the largest resolution i.e. 0.03, if we take the number of partitions

to be at least 30.

4.7 Conclusions

Under the section of fluid motion due to a two Fourier-component source we found that both v_{rms} and ω_{rms} are proportional to $\mathcal{N}$. The flow evolution picture is divided into early stage, intermediate stage and steady state. In the steady state vorticity is being produced at a steady rate and there are only two vortices per field wavelength. Overall, for effective stirring the width of the channel has to be at most equal to the wavelength L.

In the case of multi-Fourier component source we could get four vortices, instead of two, in a channel of length L when $\boldsymbol{b}$ takes the values as given in figure 4.16. The combination values of b_n is reached through a "calculated" trial and error.

We find that the central flow is always opposite to the direction of the applied field. For every pair of eddies one has to be clockwise and the other anti-clockwise.

The next chapter is on a solid conductor in a moving field where R_m is finite.

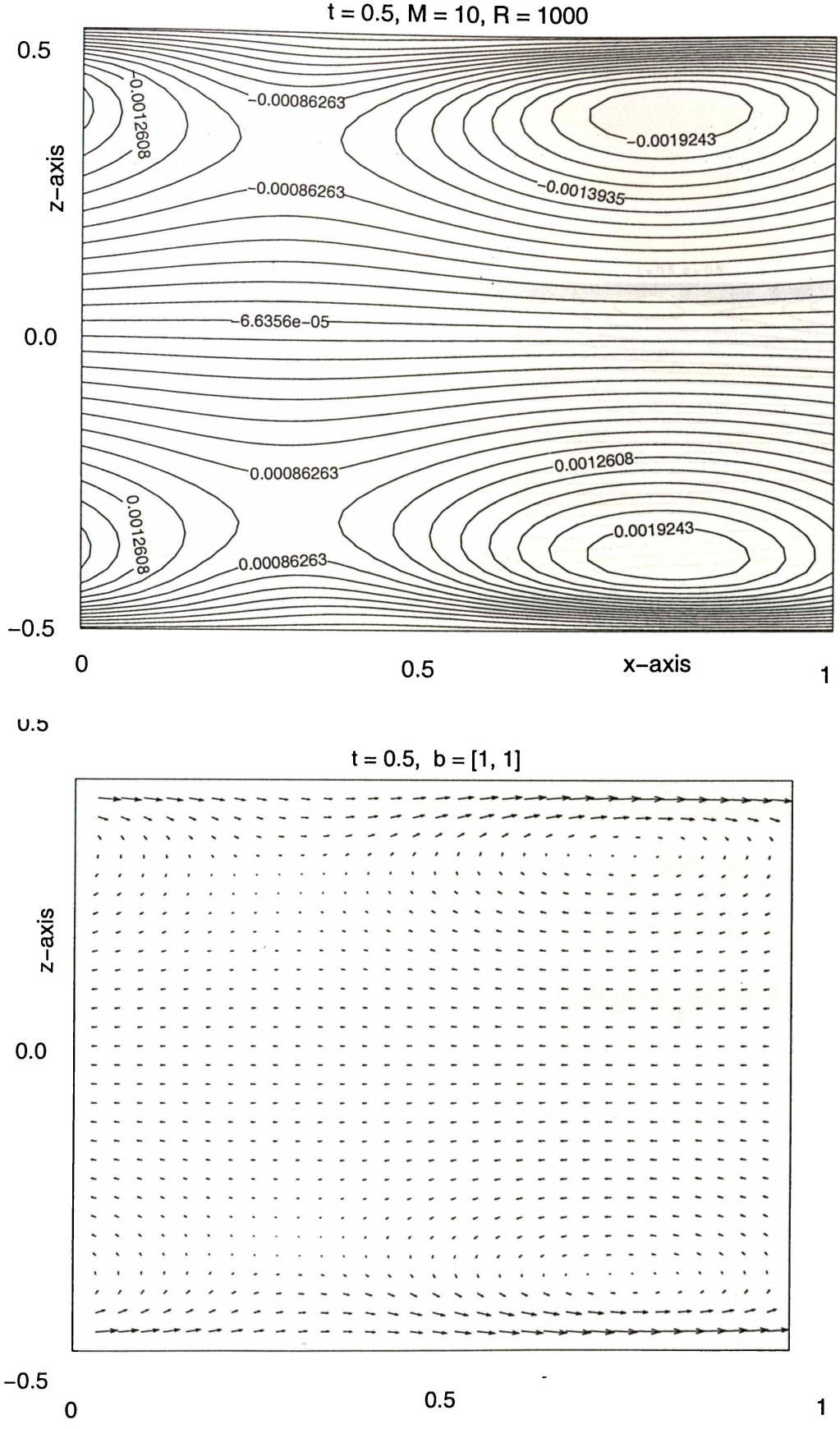

Figure 4.15: The top diagram shows streamlines and the bottom contains the velocity vectors at $t = 0.5$, with $b_n = [1, 1]$, $\mathcal{N} = 0.1$ and $R = 1000$. The "average velocity" is $v_{rms} = 0.0075U$.

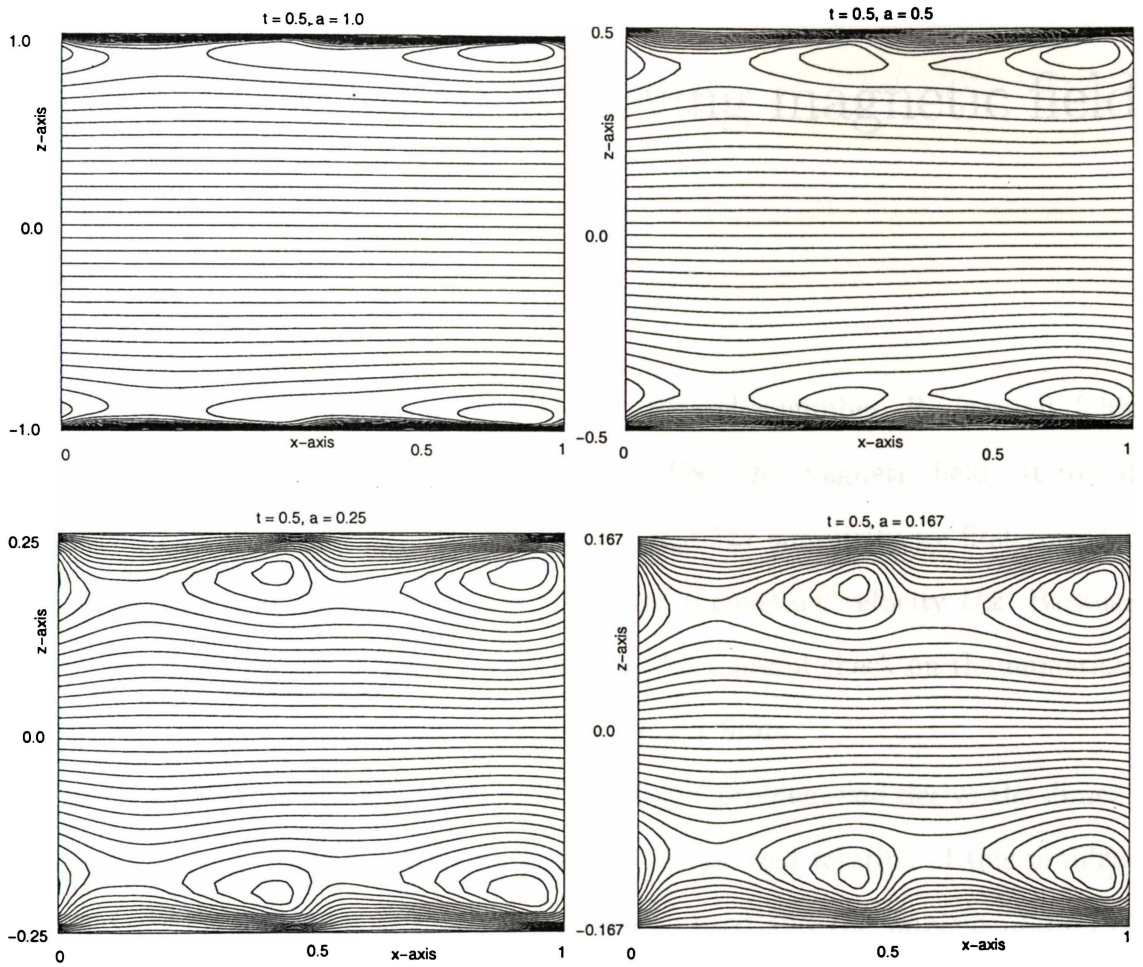

Figure 4.16: Streamlines at $t = 0.5$, *for various aspect ratios* $a = 0.1, 0.5, 0.25,$ *and* 0.167 *where* $b_n = 0.1, 0.8, 0.0, 0.8, 0.1, 0.6, 0.1, 2.5, 0.1, 2.5,$ $N = 0.1$.

Chapter 5

Solid conductor in a moving magnetic field

5.1 Introduction

Up to now we have assumed that the magnetic Reynolds number, R_m is small. This assumption means that the flow, $\boldsymbol{u}$, does not affect the magnetic field. It would be interesting to consider the effects of finite, R_m. For simplicity we first consider a solid metal which at time $t = 0$ is moved at a constant velocity $U\hat{\boldsymbol{x}}$. Because this problem can be solved analytically it provides a useful check on the numerical scheme we use later to investigate flow where R_m is finite.

In section §5.2 we formulate the solid conductor problem and derive the dimensionless governing equation. We investigate the analytical solution of this problem in §5.3. In §5.4 we derive the numerical scheme used and the implementation of the boundary conditions. The following §5.5 gives numerical results and lastly the conclusions are summarised in §5.6.

5.2 Solid conductor problem

Consider a channel $-a \leq z \leq a$ of infinite length and width containing a solid metal of magnetic permeability μ, electrical conductivity σ, and magnetic diffusivity η,

where

$$\eta = \frac{1}{\sigma\mu},$$

being subjected to an applied two-dimensional periodic magnetostatic field $\boldsymbol{B}$ which travels parallel to the channel with a uniform velocity $-U\hat{\boldsymbol{x}}$. The magnetic boundary conditions are

$$\left(\frac{\partial\phi}{\partial z}\right)_{z=\pm a} = B_0 \sum_{n=1}^{N} b_n \cos[nk(x+Ut)], \tag{5.1}$$

as in chapter 2. We make the assumption that the edge effects of the side walls $y = \pm b$, where $b \gg a$, may be neglected.

Now this problem is equivalent to the situation where the applied magnetic field is stationary but at $t = 0$, the solid metal in the channel is suddenly moved at the velocity $U\,\hat{\boldsymbol{x}}$.

The governing induction equation is

$$\frac{\partial \boldsymbol{B}}{\partial t} = \nabla \times (\boldsymbol{v} \times \boldsymbol{B}) + \eta \nabla^2 \boldsymbol{B}.$$

By putting

$$\boldsymbol{B} = -\nabla\psi \times \hat{\boldsymbol{y}} = -\nabla \times (\psi\hat{\boldsymbol{y}})$$

in the induction equation we obtain

$$\nabla \times \left[\frac{\partial\psi}{\partial t}\,\hat{\boldsymbol{y}} + \boldsymbol{v} \times \boldsymbol{B} - \eta \nabla \times \boldsymbol{B}\right] = 0,$$

which implies that

$$\frac{\partial\psi}{\partial t}\,\hat{\boldsymbol{y}} + \boldsymbol{v} \times \boldsymbol{B} - \eta \nabla \times \boldsymbol{B} = \nabla\varphi, \tag{5.2}$$

where φ is some scalar field and η is constant in space and time (which is likely for liquid metal).

Taking the $y-$component of (5.2) we get a simpler governing equation

$$\frac{\partial\psi}{\partial t} + \boldsymbol{v} \cdot \nabla\psi = \eta \nabla^2 \psi, \tag{5.3}$$

where $\partial\varphi/\partial y = 0$, because the $y-$boundaries are assumed to be perfectly conducting or short circuited, so that the $y-$component of $\boldsymbol{E} = 0$.

5.2.1 Non-dimensionalisation

To non-dimensionalise (5.3) we write

$$x = L\bar{x}, \quad z = L\bar{z}$$

$$\psi = LB_0\ \bar{\psi}$$

where B_0 is the typical strength of the magnetic field, which leads to

$$\frac{\partial\bar{\psi}}{\partial\bar{t}} + \bar{\boldsymbol{v}}\cdot\bar{\nabla}\bar{\psi} = \frac{1}{R_m}\bar{\nabla}^2\bar{\psi}.$$

As in earlier chapters we will abandon the "bars" for convenience, so the governing equation in terms of the magnetic stream function,ψ, becomes

$$\frac{\partial\psi}{\partial t} + \boldsymbol{v}\cdot\boldsymbol{\nabla}\psi = \frac{1}{R_m}\nabla^2\psi. \tag{5.4}$$

Since $\boldsymbol{v} = U\,\hat{\boldsymbol{x}}$ or in dimensionless form $\bar{v} = 1\hat{\boldsymbol{x}}$, (5.4) becomes

$$\frac{\partial\psi}{\partial t} + \frac{\partial\psi}{\partial x} = \frac{1}{R_m}\nabla^2\psi. \tag{5.5}$$

Next we will derive an alternative formulation in terms of Poisson brackets. Using the expression for $\boldsymbol{v}$ from (2.27) the term $\boldsymbol{v}\cdot\boldsymbol{\nabla}\psi$ becomes

$$\begin{aligned}\boldsymbol{v}\cdot\boldsymbol{\nabla}\psi &= \frac{\partial\chi}{\partial z}\cdot\frac{\partial\psi}{\partial x} - \frac{\partial\chi}{\partial x}\cdot\frac{\partial\psi}{\partial z}\\ &= [\psi,\,\chi],\end{aligned} \tag{5.6}$$

where the Poisson bracket notation is defined as

$$[\psi,\chi] = \psi_x\chi_z - \psi_z\chi_x.$$

Hence equation (5.4) can also be written as

$$\frac{\partial\psi}{\partial t} + [\psi,\chi] = \frac{1}{R_m}\nabla^2\psi. \tag{5.7}$$

This is the form of equation used in the later numerical calculations.

5.3 Analytical solution

We consider the simple case of one Fourier component, where a solid conductor is subjected to an applied magnetic field

$$\left(\frac{\partial \phi}{\partial z}\right)_{z=\pm a} = B_0 \cos k(x+Ut), \tag{5.8}$$

because it has an analytical solution. In a frame of reference stationary relative to the applied magnetic field, (5.8) can be written as

$$\left(\frac{\partial \phi}{\partial z}\right)_{z=\pm a} = B_0 \cos kX,$$

where $X = x + Ut$. From now onwards we use x instead of X just for convenience.

At steady state $\partial \boldsymbol{B}/\partial t = 0$, i.e. $\partial \psi/\partial t = 0$. So from (5.5) and (2.10) we obtain

$$\nabla^2 \psi = R_m \frac{\partial \psi}{\partial x}, \qquad \psi(\pm a) = -\frac{B_0}{k} \sin kx, \tag{5.9}$$

respectively.

In order to solve (5.9) we try a solution of the form

$$\psi = \mathrm{Im}[\, f(z)\, e^{\mathrm{i}kx}].$$

Substituting this trial form into (5.9) we find

$$f''(z) - \omega^2 f(z) = 0,$$

where $\omega = \pm\sqrt{k^2 + kR_m\,\mathrm{i}}$. We write

$$\sqrt{k^2 + kR_m\,\mathrm{i}} = \alpha + \beta\,\mathrm{i}, \quad \text{where} \quad \alpha, \beta \text{ are real.}$$

This leads to

$$\alpha^2 - \beta^2 = k^2$$

$$2\alpha\beta = kR_m.$$

The two solutions to these simultaneous equations can be shown to be

$$\alpha = \sqrt{\frac{k}{2\Omega}}\, R_m \qquad \text{and} \qquad \beta = \sqrt{\frac{k}{2}\,\Omega}$$

$$\alpha = -\sqrt{\frac{k}{2\Omega}}\, R_m \qquad \text{and} \qquad \beta = -\sqrt{\frac{k}{2}\,\Omega},$$

where $\Omega = \sqrt{R_m^2 + k^2} - k.$

Now we can write

$$f(z) = A\,e^{\omega z} + B\,e^{-\omega z} \quad \text{where} \quad \omega = \alpha + \beta\,\mathrm{i}\,. \tag{5.10}$$

From the boundary conditions

$$\psi(\pm a) = -\frac{B_0}{k}\sin kx$$

we get

$$f(\pm a) = -\frac{B_0}{k}.$$

By applying these boundary conditions to (5.10) we get

$$A = B = -\frac{B_0}{2k\cosh\omega a}.$$

So the solution of equation (5.9) is

$$\psi = \mathrm{Im}\left\{-\frac{B_0}{k}\frac{\cosh\omega z}{\cosh\omega a}\,e^{\mathrm{i}\,kx}\right\}. \tag{5.11}$$

Using $\omega = \alpha + \beta\,\mathrm{i}$ equation (5.11) becomes

$$\psi = Im\left\{-\frac{B_0}{k}\frac{\cosh(\alpha z + \beta z\,\mathrm{i})(\cos kx + \mathrm{i}\,\sin kx)}{\cosh(\alpha a + \beta a\,\mathrm{i})}\right\}$$

so

$$\psi = -\frac{B_0}{k}.\frac{R(z)\sin kx + S(z)\cos kx}{P} \tag{5.12}$$

where

$$\begin{aligned} R(z) &= \cosh(\alpha z)\cosh(\alpha a)\cos(\beta z)\cos(\beta a) + \sinh(\alpha z)\sinh(\alpha a)\sin(\beta z)\sin(\beta a), \\ S(z) &= \sinh(\alpha z)\cosh(\alpha a)\sin(\beta z)\cos(\beta a) - \cosh(\alpha z)\sinh(\alpha a)\cos(\beta z)\sin(\beta a), \\ \text{and} \quad & P = \cosh^2(\alpha a)\cos^2(\beta a) + \sinh^2(\alpha a)\sin^2(\beta a). \end{aligned}$$

Fieldlines are shown in figures 5.1 and 5.2. It can be seen that as the magnetic Reynolds number increases from 1 to 120, the more the lines of force are swept in the direction of motion of the solid conductor. This is to be expected since as R_m increases, the field lines tend to become more "frozen-in" to the conductor.

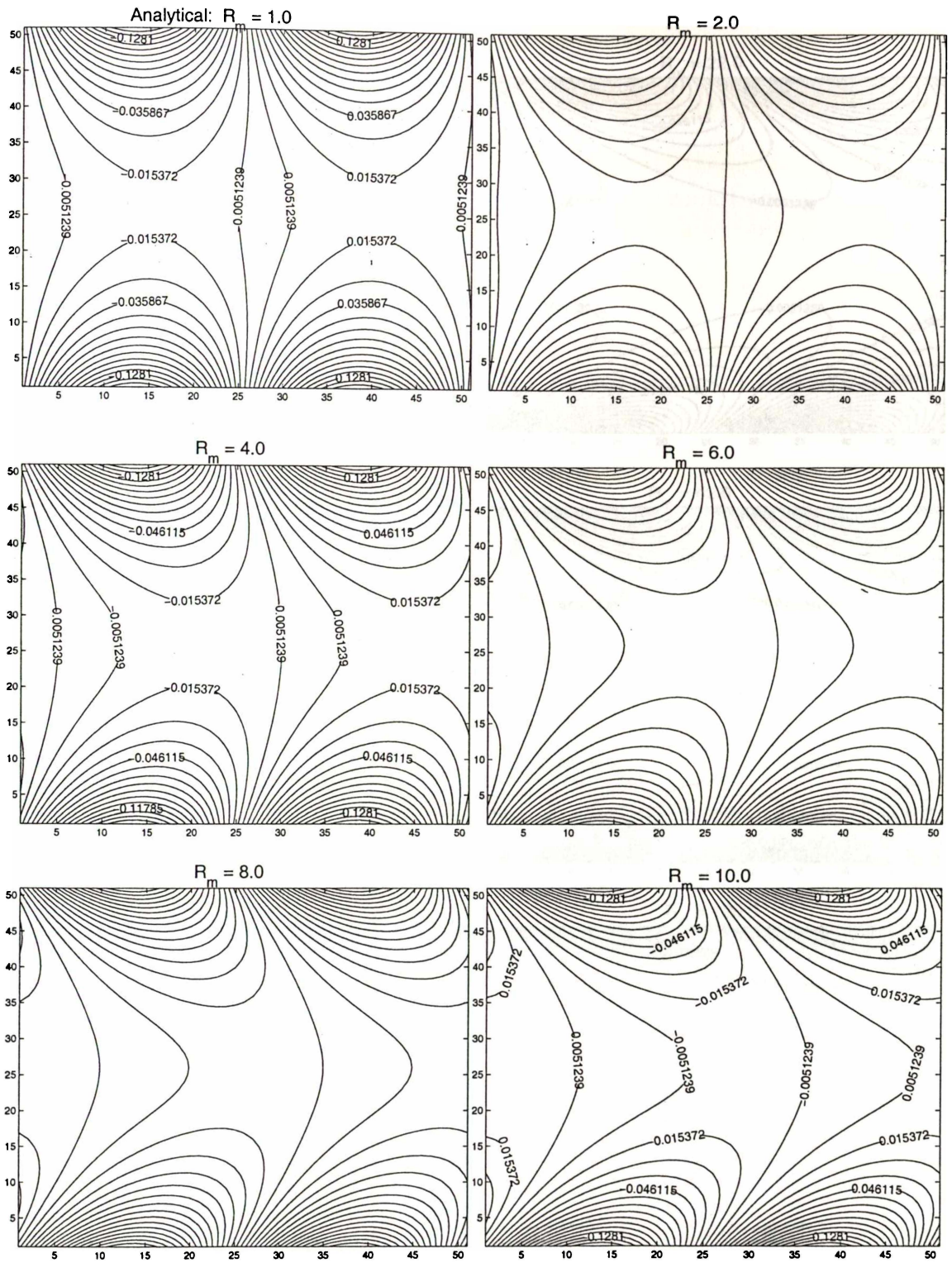

Figure 5.1: Contours of the analytical streamfunction for magnetic Reynolds number, R_m, which takes the values from 1 to 10. The number of contour lines is 30. The resolution is 50 by 50. The region is [0,1] by [-0.5,0.5].

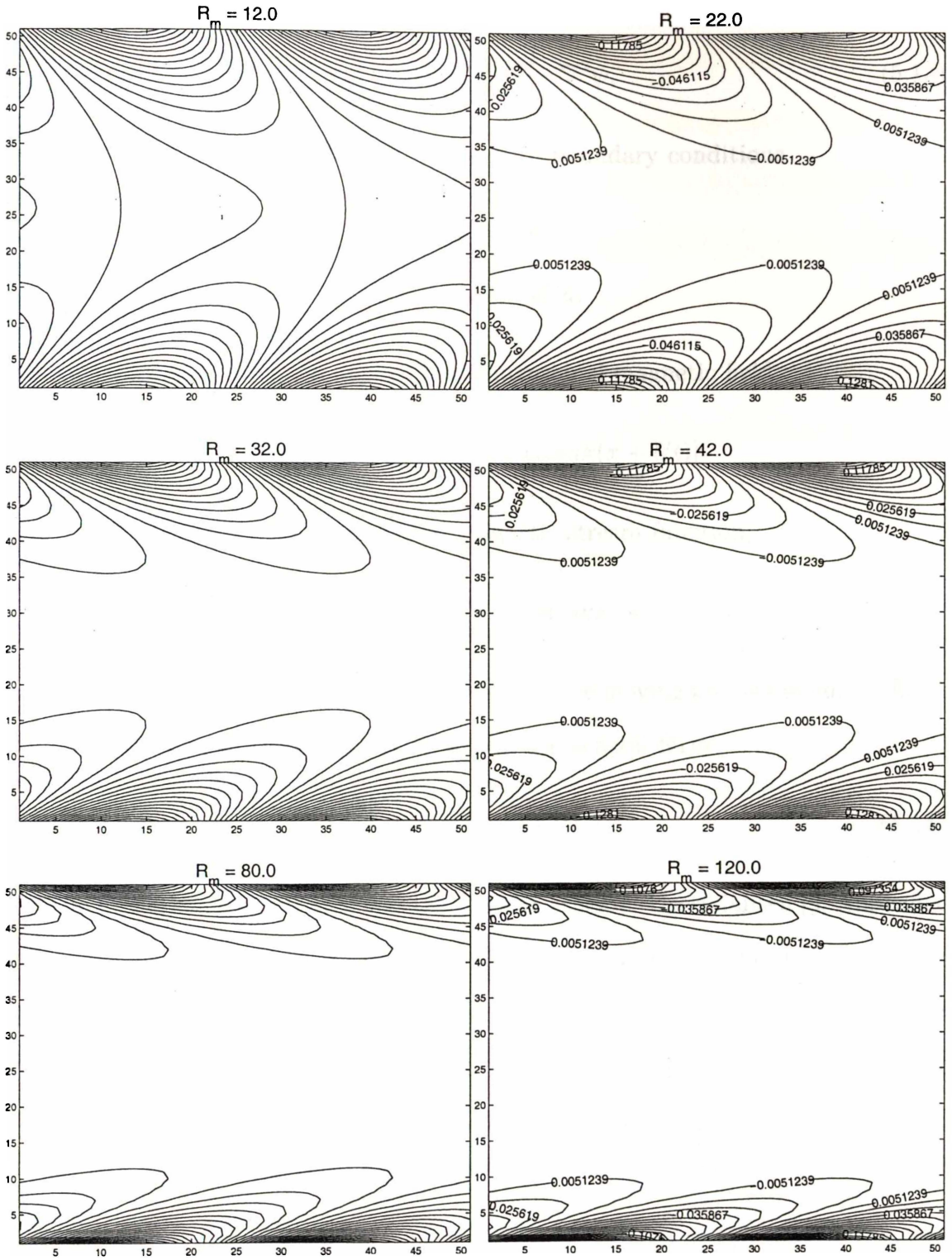

Figure 5.2: The analytical streamfunction for $R_m = 12$ to 120.

5.4 Numerical scheme

The problem is to solve the governing equation

$$\frac{\partial \psi}{\partial t} + [\psi, \chi] = \frac{1}{R_m} \nabla^2 \psi, \tag{5.13}$$

numerically on the domain $[0,1] \times [-a,a]$, with boundary conditions

$$\begin{aligned} \chi(x,-a) &= 0, \\ \chi(x,\ a) &= 2Ua. \end{aligned}$$

As can be seen in §2.2.1 the applied two dimensional magnetic field,

$$\left(\frac{\partial \phi}{\partial z}\right)_{z=\pm a} = B_0 \sum_{n=1}^{N} b_n \cos[nk(x+Ut)]$$

can be expressed in terms of the initial magnetic stream function,

$$\psi(X,z) = -B_0 \sum_{n=1}^{N} \frac{b_n}{nkc_n} \cosh(nkz) \sin(nkX),$$

in a frame of reference stationary with respect to the moving applied magnetic field.

The governing equation can be written in the general form

$$\frac{\partial \psi}{\partial t} + [\psi, \chi] = \frac{1}{R_m} \nabla^2 \psi. \tag{5.14}$$

The numerical method used was the Russian scheme (Heerikhuisen [8, Appendix A]). Briefly the scheme works like this. Based on the induction equation (5.13) we calculate the predictor step, ψ^{n+1*} (5.15) at time step $n+1*$. Then we use the predicted values of ψ^{n+1*} to calculate the corrector value ψ^{n+1} (5.16) at time step $n+1$, while using the same values of χ^n_{ij}, and $\nabla^2 \psi^n_{ij}$ as in (5.15) .

We first calculate the predictor step, ψ^{n+1*},

$$\psi^{n+1*}_{ij} = \psi^n_{ij} - (\psi^n_x \chi^n_z - \psi^n_z \chi^n_x)\Delta t + \frac{1}{R_m} \nabla^2 \psi^n_{ij} \Delta t, \tag{5.15}$$

where

$$\psi_x^n = \frac{\psi_{i+1,j}^n - \psi_{i-1,j}^n}{2\Delta},$$
$$\psi_z^n = \frac{\psi_{i,j+1}^n - \psi_{i,j-1}^n}{2\Delta},$$
$$\chi_x^n = \frac{\chi_{i+1,j}^n - \chi_{i-1,j}^n}{2\Delta},$$
$$\chi_z^n = \frac{\chi_{i,j+1}^n - \chi_{i,j-1}^n}{2\Delta},$$
$$\nabla^2\psi_{ij}^n = \frac{\psi_{i+1,j}^n - 2\psi_{ij}^n + \psi_{i-1,j}^n}{2\,h^2} + \frac{\psi_{i,j+1}^n - 2\psi_{ij}^n + \psi_{i,j-1}^n}{2\,h^2}.$$

The predictor values, ψ^{n+1*}, are then used to calculate the corrector step ψ^{n+1}, for the next time step $t + \Delta t$,

$$\psi_{ij}^{n+1} = \psi_{ij}^n - (\psi_x^{n+1*}\chi_z^n - \psi_z^{n+1*}\chi_x^n)\Delta t + \frac{1}{R_m}\nabla^2\psi_{ij}^n\Delta t, \tag{5.16}$$

where

$$\psi_x^{n+1*} = \frac{\psi_{i+1,j}^{n+1*} - \psi_{i-1,j}^{n+1*}}{2\Delta},$$
$$\psi_z^{n+1*} = \frac{\psi_{i,j+1}^{n+1*} - \psi_{i,j-1}^{n+1*}}{2\Delta},$$

and $\nabla^2\psi_{ij}^n$ unchanged.

As in Chapter 3, to ensure stability the time step, Δt, for 2-D must satisfy the Courant-Friedrichs-Lewy condition

$$\Delta t \leq \frac{\Delta}{\sqrt{2}\,|\boldsymbol{v}|_{\max}}, \tag{5.17}$$

where $|\boldsymbol{v}|_{\max}$ is the modulus of the maximum velocity of the fluid taken over all grid points. Since

$$|\boldsymbol{v}|_{\max} \leq U = 1$$

we find

$$\frac{1}{|\boldsymbol{v}|_{\max}} \geq 1.$$

Hence,

$$\Delta t \leq \frac{\Delta}{\sqrt{2}}. \tag{5.18}$$

In addition, the time step must also satisfy the von Neumann criterion for stability [15] arising from the viscous term, which leads to

$$\Delta t \leq \frac{\Delta^2}{\nu} = R_m \Delta^2. \tag{5.19}$$

5.4.1 Boundary values

The domain is $[0,1] \times [-a,a]$. The calculations are carried out over all the points of the mesh including the boundaries. The point (x_i, z_j) corresponds to the point with co-ordinates

$$\begin{aligned} x_i &= (i-1) * \Delta, \qquad i = 0, \ldots, m+1 \\ z_j &= -a + (j-1) * \Delta, \quad j = 1, \ldots, n. \end{aligned}$$

In the finite difference expression for $\nabla^2 \psi$

$$\nabla^2 \psi = \frac{\psi_{i+1,j} - 2\psi_{ij} + \psi_{i-1,j}}{2\,h^2} + \frac{\psi_{i,j+1} - 2\psi_{ij} + \psi_{i,j-1}}{2\,h^2},$$

the calculations of the values of ψ on the boundaries i.e. $\psi(i,0)$ and $\psi(i,n+1)$, require the values of ψ on the ghostpoints. For example, in the calculation for $j = 1$ (boundary $z = -a$) we need to the values of $\psi(i,2)$ and the ghostpoint $\psi(i,0)$. Similarly for $j = n$ we need the values $\psi(i,n-1)$ and the ghostpoint $\psi(i,n+1)$. We solve this by the "mirror image" technique where we set

$$\begin{aligned} \psi(i,0) &= \psi(i,2), \\ \psi(i,n+1) &= \psi(i,n-1), \quad i = 0, \ldots, m+1. \end{aligned}$$

The justification is the $x-$component of the applied magnetic field on the boundaries $z = \pm a$ is zero i.e.

$$\frac{\partial \psi}{\partial z} \sim \frac{\psi_{i,j+1} - \psi_{i,j-1}}{2\,h} = 0$$

which implies that ψ does not change between the points on either side of the boundaries namely $(i,0)$, $(i,2)$ and $(i,n-1)$, $(i,n+1)$.

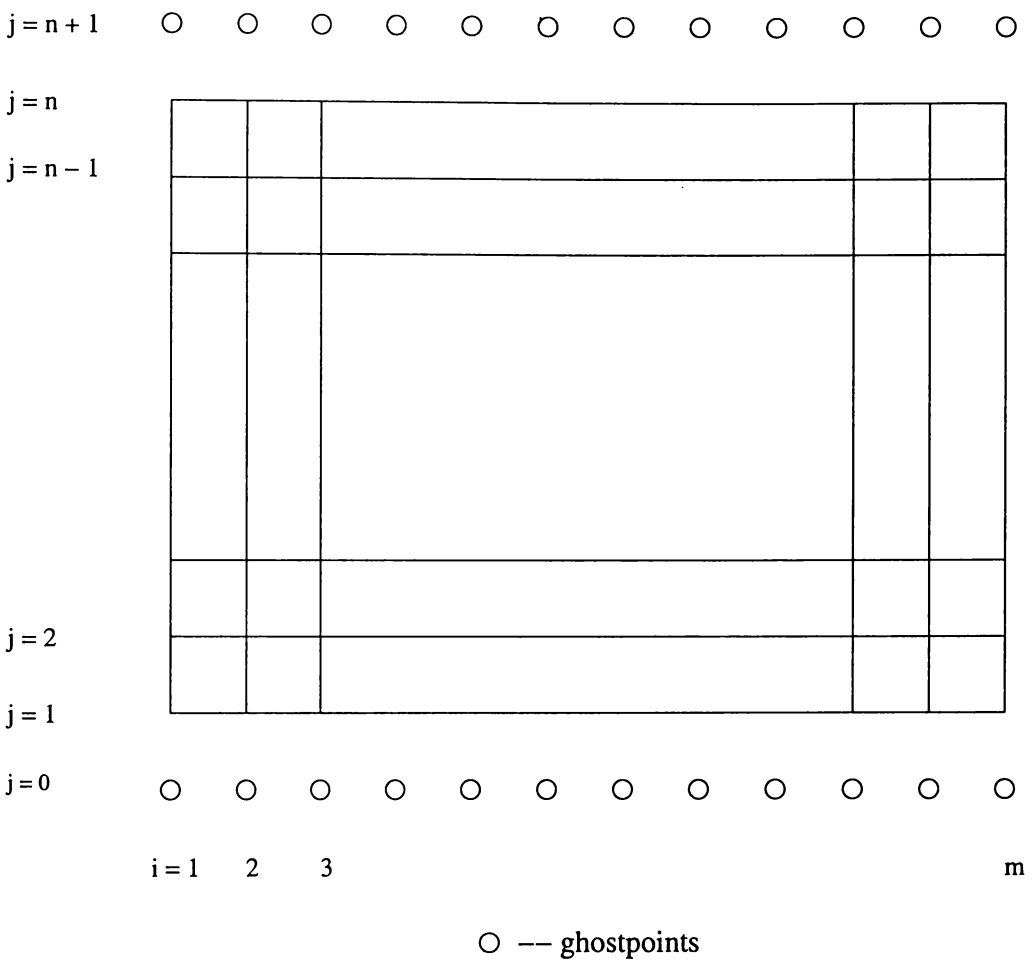

Figure 5.3: The mesh of the domain $[0,1] \times [-a,a]$ *showing the ghostpoints next to the boundaries* $z = \pm a$.

5.5 Numerical results

The simulations were continued until a steady state was reached for a given value of magnetic Reynolds number in the range 1 to 120. The number of partitions is 50 by 50. When we compare the analytical streamlines for the steady state (which appear in the first column of figures 5.4 – 5.6) with the numerically calculated streamlines (in the second column) for the same magnetic Reynolds number they look remarkably similar. As the magnetic Reynolds number increases the solid metal behaves more and more like a perfect conductor. The fieldlines in the shape of half-a-loop on the boundaries are swept in the direction of the motion and become flatter as R_m increases as shown in figures 5.5 and 5.6. For values of R_m of about 800, the fieldlines are swept into a narrow layer on the boundaries. The collapsing boundary layers look stable as R_m increases. To see whether they are accurate for the given grid spacing we increase the resolution of the magnetic fieldlines just for the case of $R_m = 800$ (figure 5.7). It can be seen that the narrow layer of fieldlines on the boundaries has a thickness of approximately within 8% of a, the channel width. When the resolutions are increased from 50 by 50 to 150 by 150, the thin boundary layers of magnetic field remain within 4 grid points for 50 by 50; within 8 grid points for 100 by 100; and within 12 grid points for 150 by 150.

To study the evolution of fieldlines with time, at high R_m, two simulations for $R_m = 42$ and $R_m = 800$ were carried out. For $R_m = 800$ it is clear from figures 5.10 to 5.11 that both pairs of vortices travel the whole wavelength (of 1 unit length) in 1 time unit. During the travel "frozen-in" effect is at work with reconnections of fieldlines taking place on the boundaries. The initial fieldline shape remains unchanged.

Some half loops are severed from the boundaries but connect to form vortices as shown in figure 5.10 where two new pairs of loops are formed. After $t = 0.7$ twelve new pairs of loops are formed but as time goes on loops of vortices gradually disappear through reconnection with the flux on the boundaries and through ohmic losses. By $t = 3$, only one pair of loops is left. In the end what remains is a

thin layer of flux on the boundaries as shown in figure 5.6. In figures 5.8 to 5.9 where $R_m = 42$, the severing of fieldlines mostly involves those that join the two boundaries. Within just a period of $t = 2.0$, only closed loop fieldlines originating from the boundaries remain and they are inclined in the direction of motion of the solid metal. A similar flux expulsion effect was found by Kamkar and Moffatt [9]. They studied a pressure-driven flow along a channel in the presence of an applied periodic magnetic field.

We define r.m.s. of $\boldsymbol{B}$ as

$$\boldsymbol{B}_{rms} = \left(\sum_{i=1}^{m} \sum_{j=1}^{n} B^2(i,j) \,/\, (m \times n) \right)^{\frac{1}{2}},$$

where $B^2(i,j) = B_x^2(i,j) + B_z^2(i,j)$. In the plots of $\boldsymbol{B}_{rms}$ versus time from figures 5.13 and 5.14 it can be seen that the time for magnetic flux to reach a steady state increases as R_m increases. The better the conductor the longer it takes for the flux loops to gradually disappear through ohmic losses. For example in the case of $R_m = 800, t = 18$ in figure 5.12 only a thin layer of flux on the boundaries remains. This corresponds to the shape of B_{rms} which varies very little at $t = 18$ in figure 5.14.

5.6 Conclusions

The numerical and analytical results agree well for the case of one Fourier-component source, for R_m in the range of 1 to 1200. We found that as R_m increases the solid metal behaves more and more like a perfect conductor where the fieldlines are frozen in the moving solid metal. The fieldlines are swept in the direction of the motion. It would be interesting to extend the present problem to the case where we have a conducting fluid instead a solid metal. This is to be the topic of the next chapter.

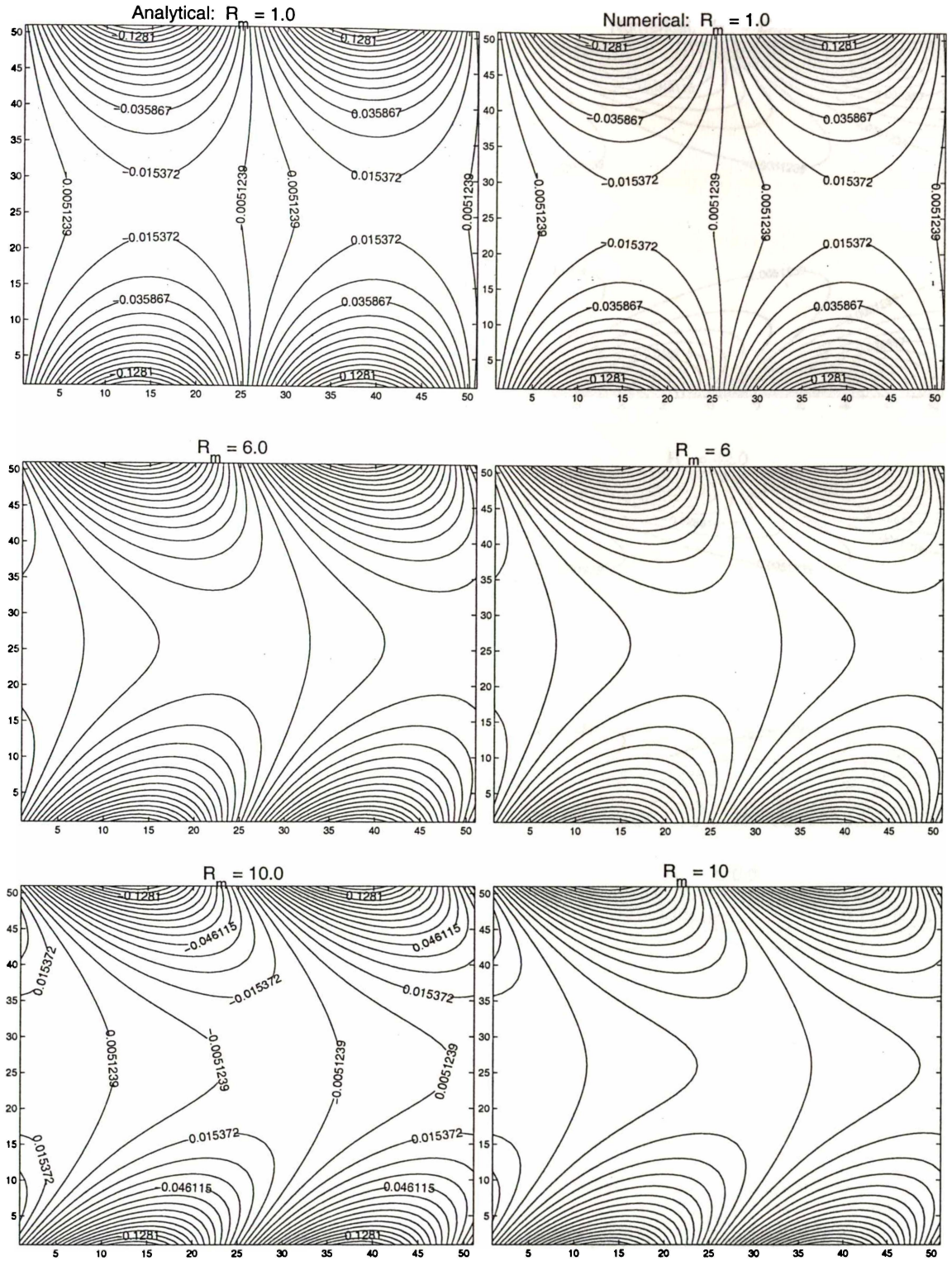

Figure 5.4: The left column shows the analytical fieldlines and the second column shows steady state numerical fieldlines for increasing values of magnetic Reynolds number. The number of streamfunction contour lines is 30. *The region is* $[0, 1] \times [-0.5, 0.5]$. *The number of partitions is* 50 *by* 50.

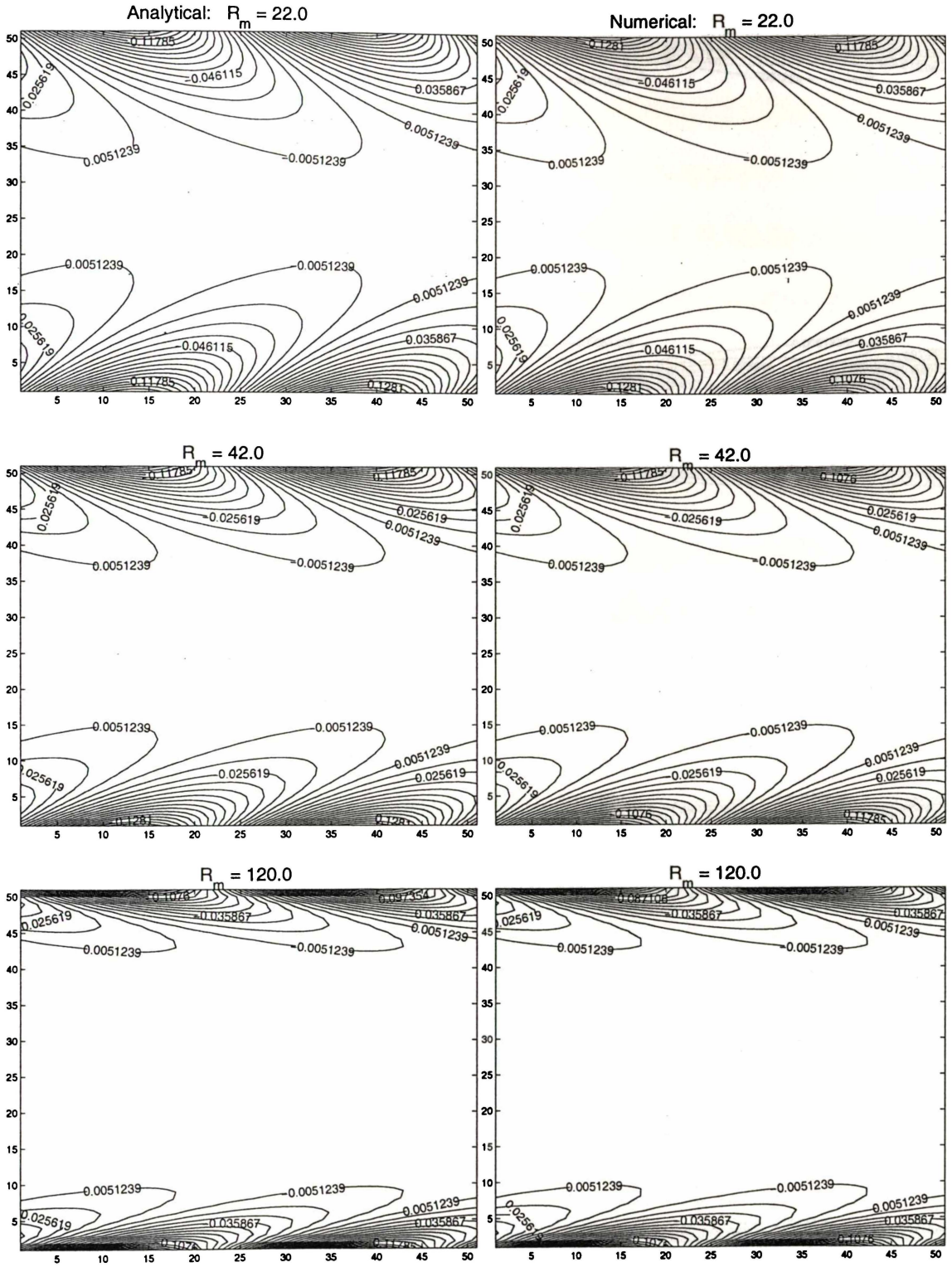

Figure 5.5: The left column shows the analytical fieldlines and the second column shows steady state numerical fieldlines for increasing values of magnetic Reynolds number. The number of streamfunction contour lines is 30. *The number of partitions is* 50 *by* 50.

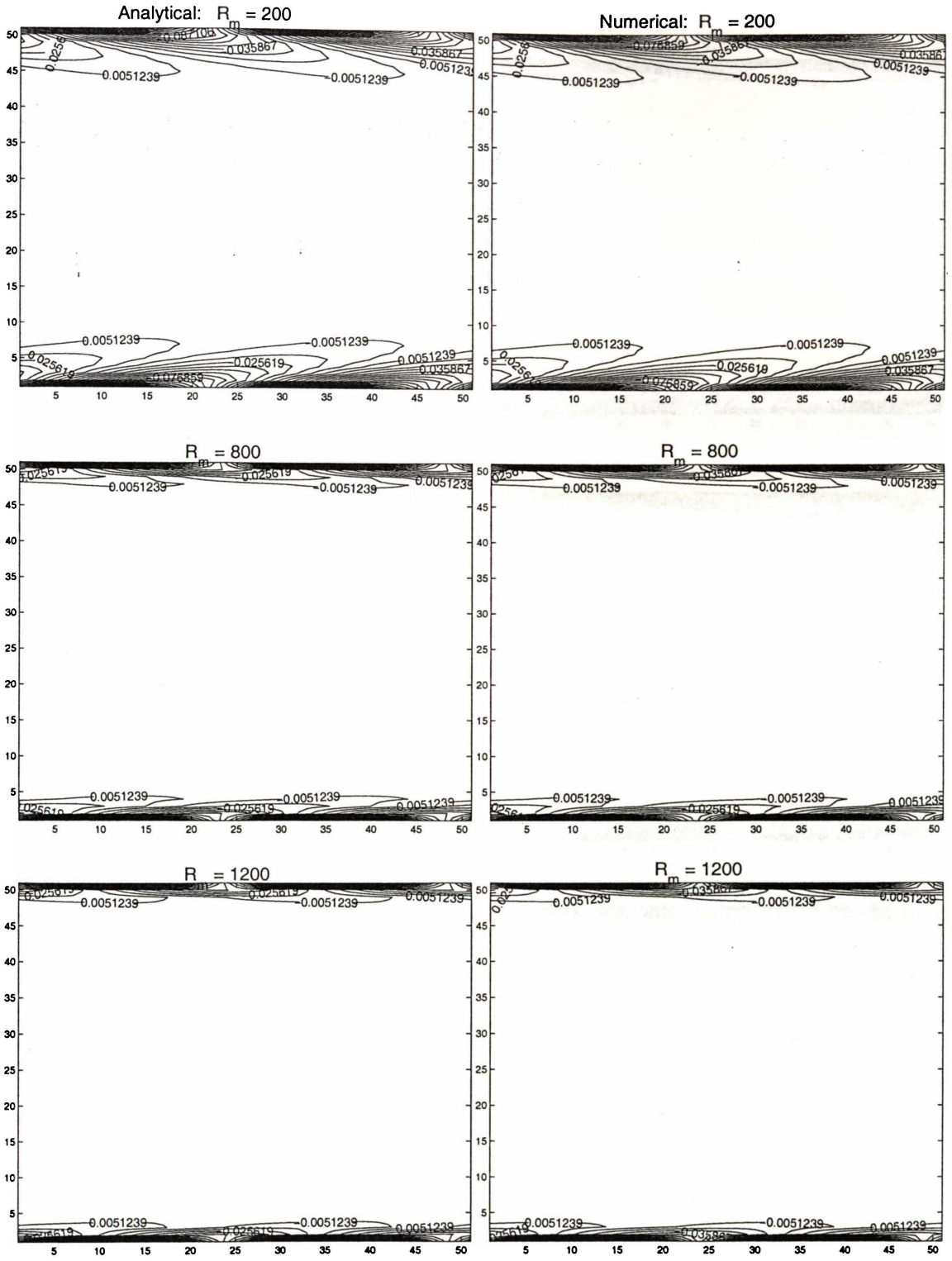

Figure 5.6: The left column shows the analytical fieldlines and the second column shows steady state numerical fieldlines for increasing values of magnetic Reynolds number. The number of streamfunction contour lines is 30. *The number of partitions is* 50 *by* 50.

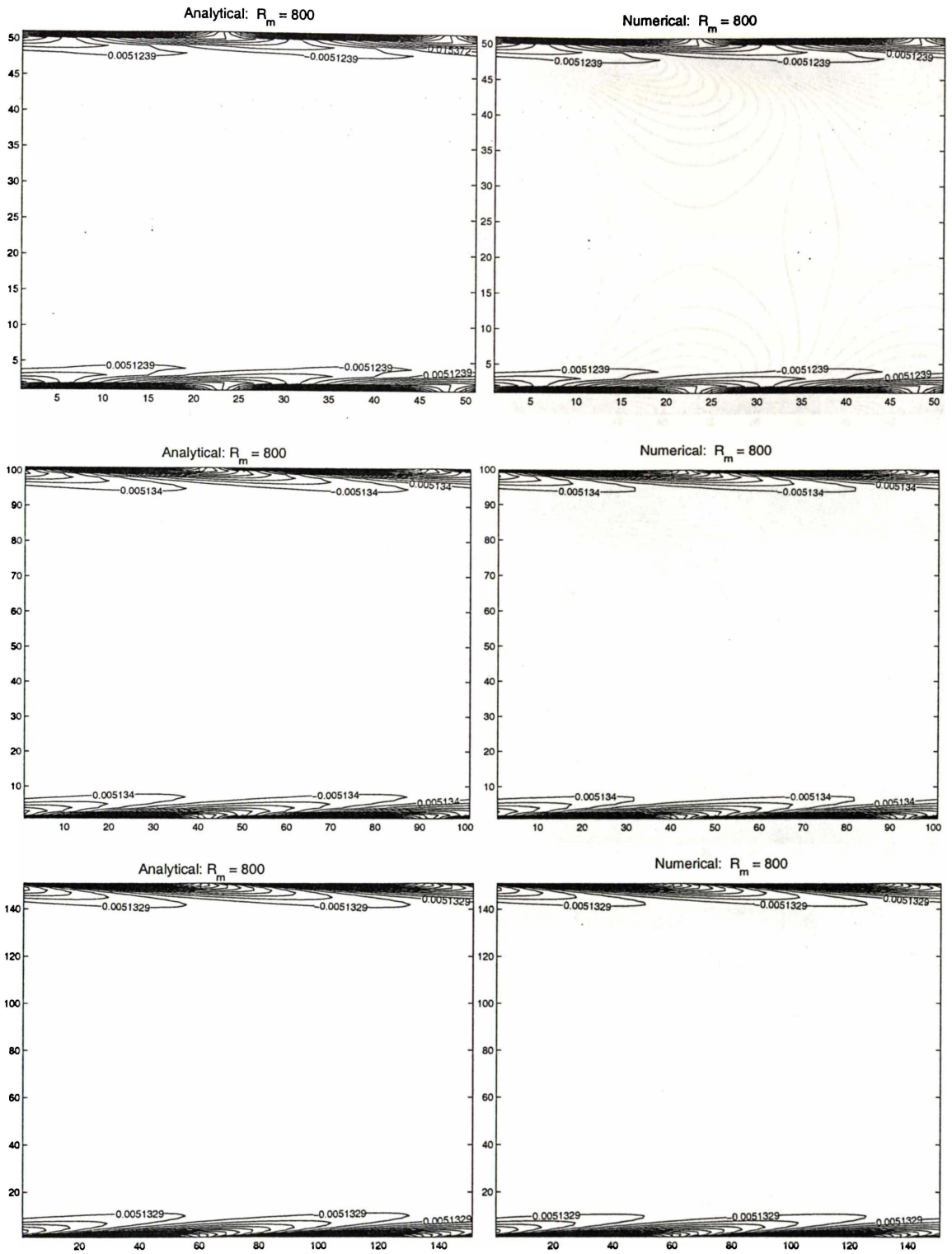

Figure 5.7: The left column shows the analytical fieldlines and the second column shows steady state numerical fieldlines for increasing resolutions from 50 *by* 50 *to* 150 *by* 150, *for* $R_m = 800$.

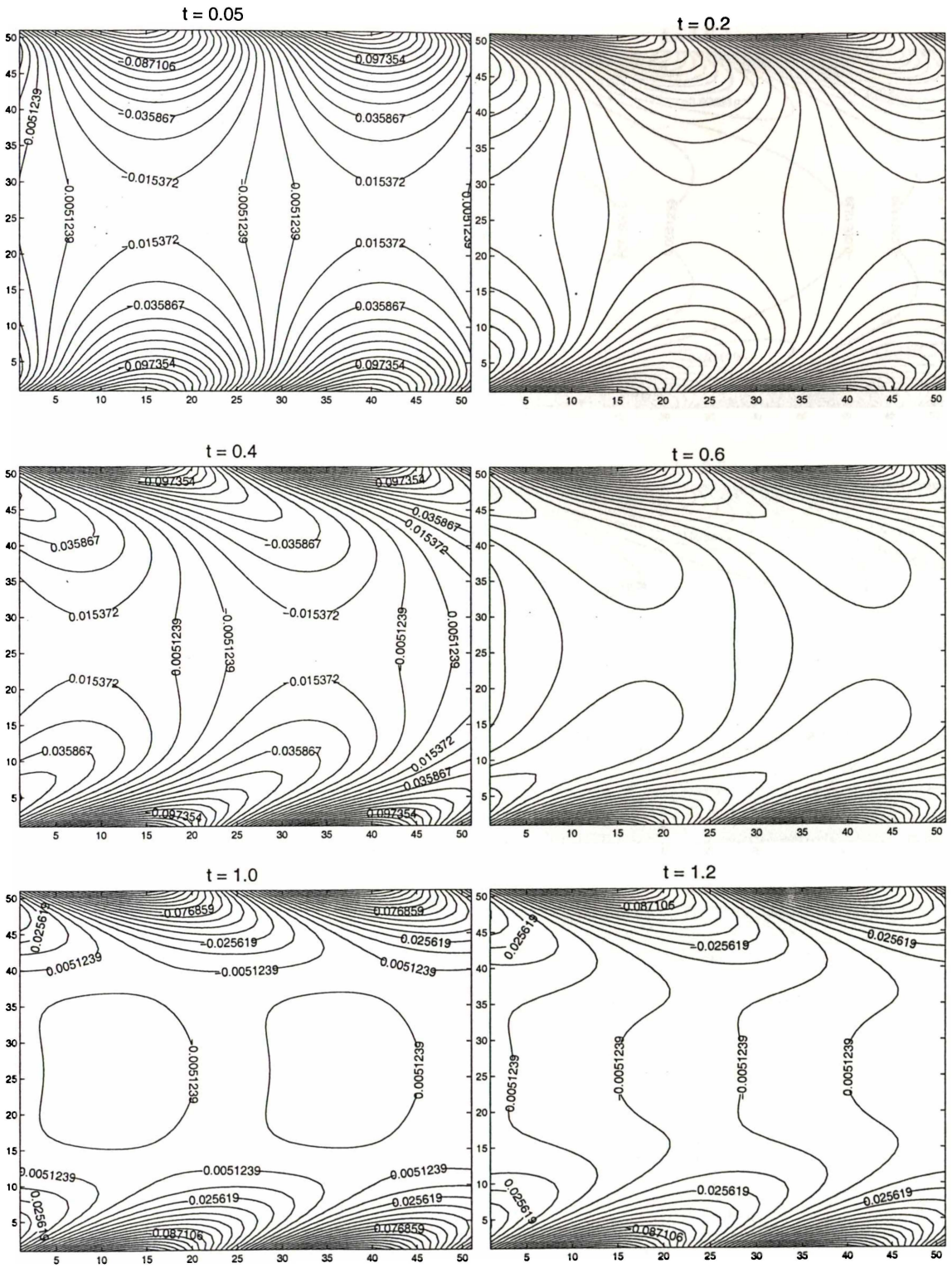

Figure 5.8: Evolution of fieldlines for time varying from 0.05 *to* 1.2, *where* $R_m = 42.0$ *The number of contour lines is* 30.

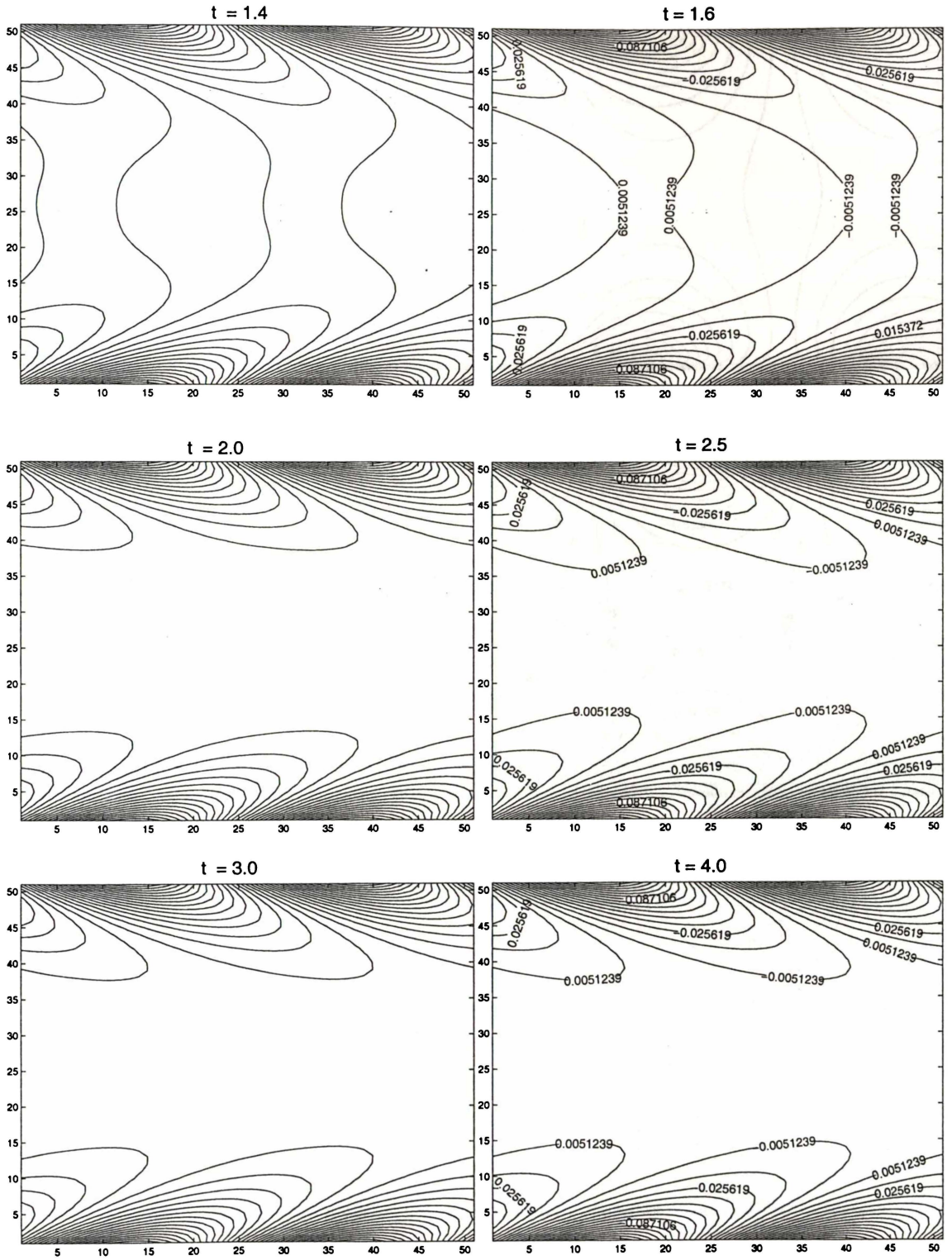

Figure 5.9: Fieldlines for $t = 1.4$ to 4.0, where $R_m = 42$.

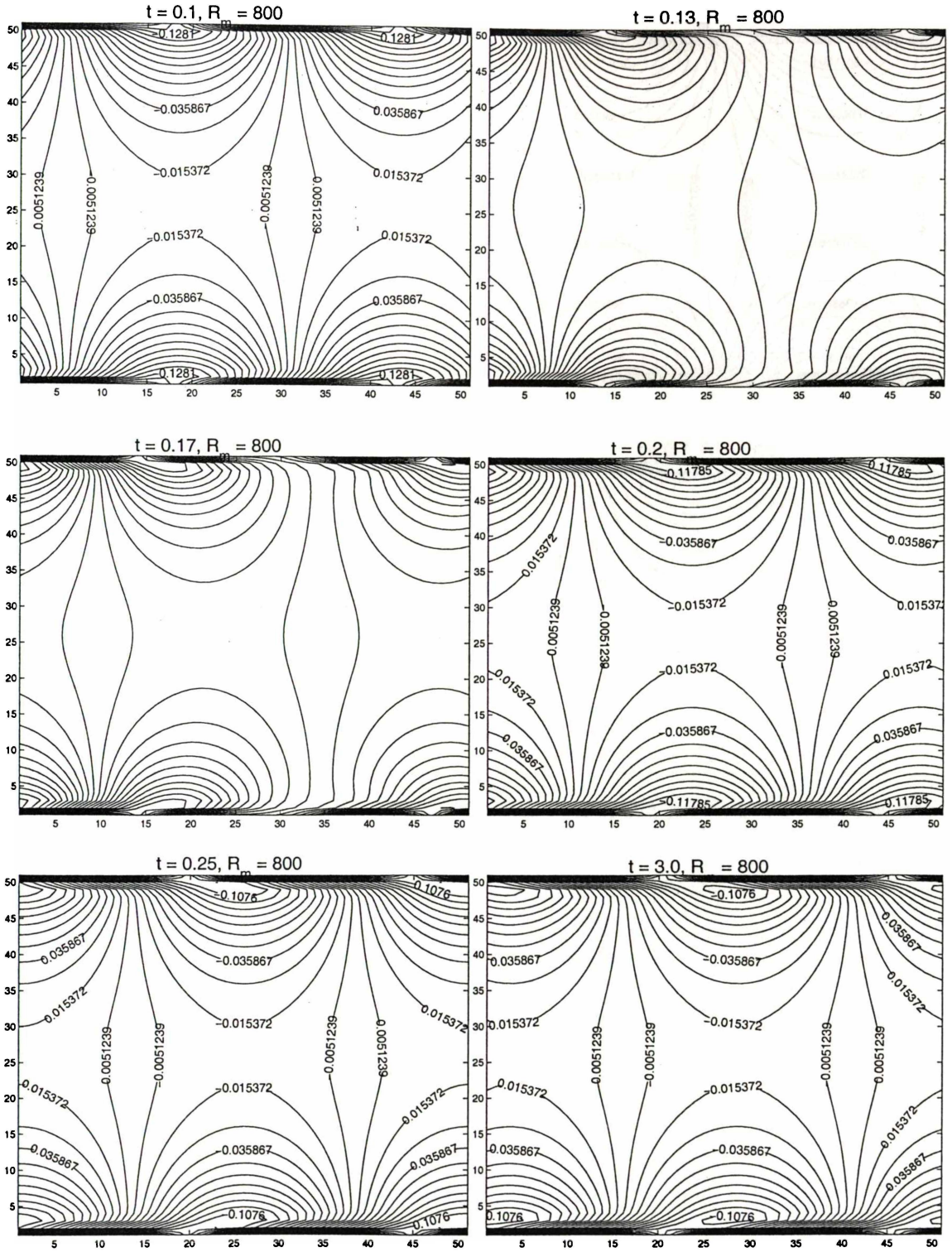

Figure 5.10: Evolution of fieldlines for $t = 0.1$ to 0.3 showing "frozen-in" effect of magnetic field at high $R_m = 800$.

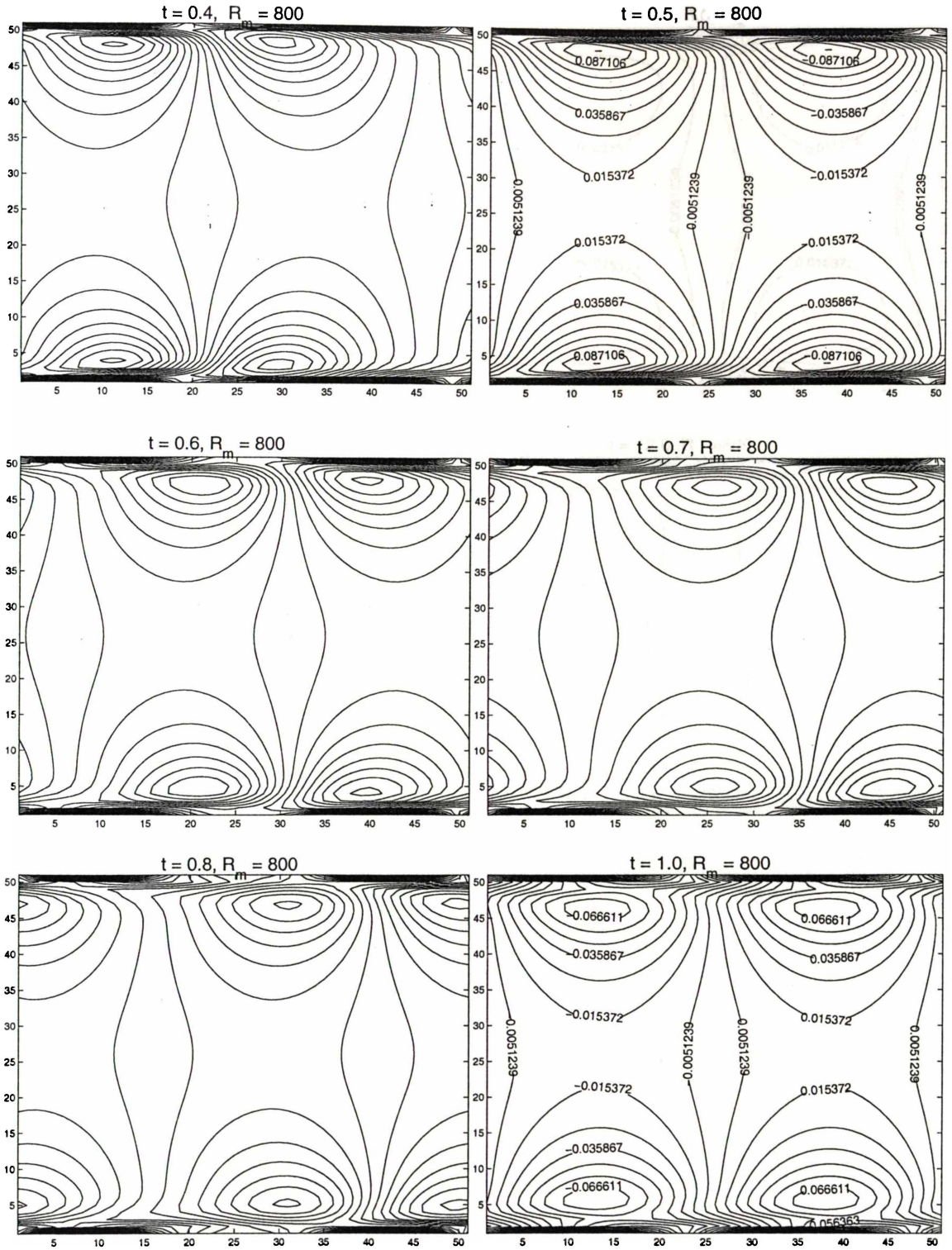

Figure 5.11: Evolution of fieldlines for $t = 0.4$ to 1.0 showing "frozen-in" effect of magnetic field at high $R_m = 800$.

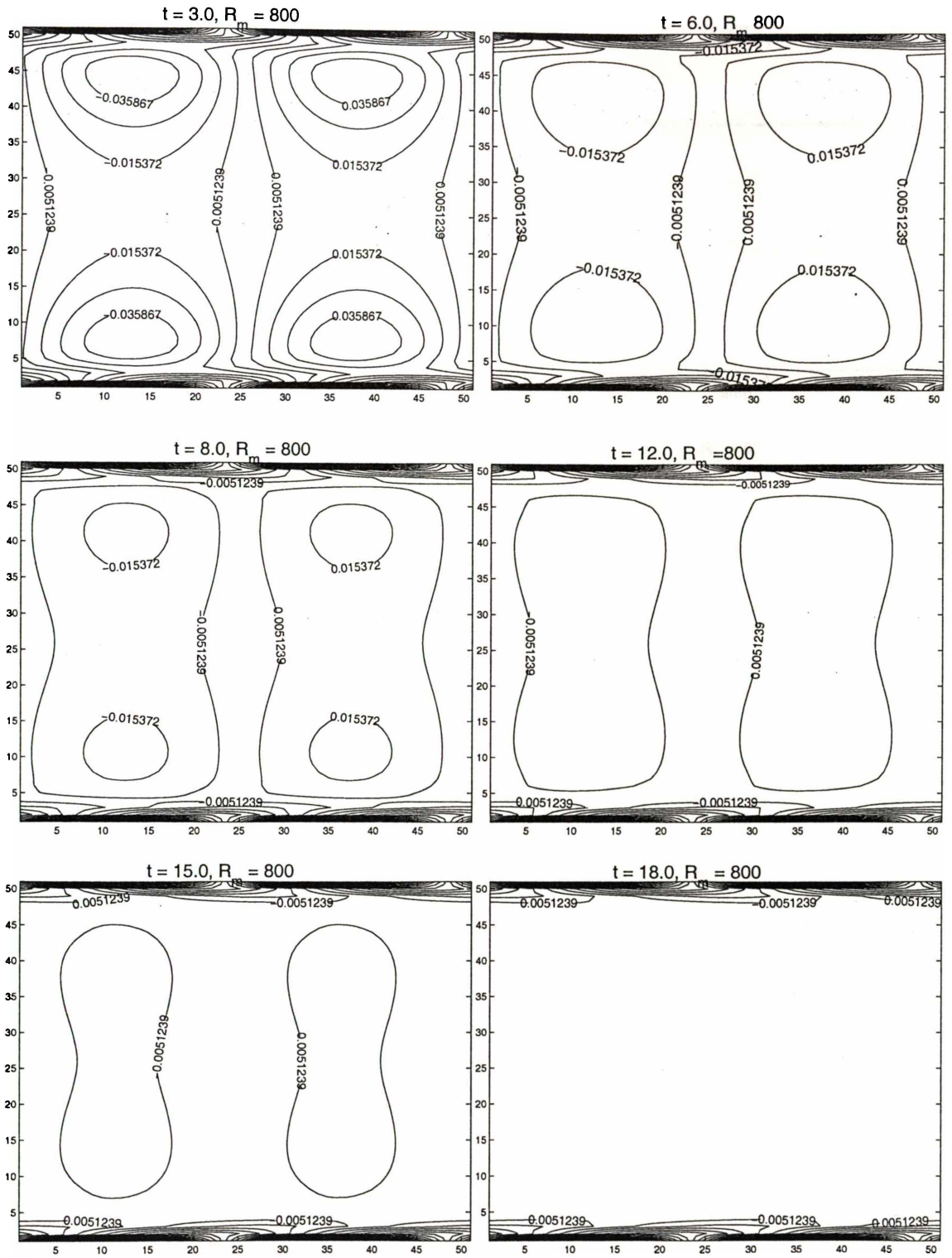

Figure 5.12: Evolution of fieldlines for $t = 3.0$ to 18 showing "frozen-in" effect of magnetic field at high $R_m = 800$.

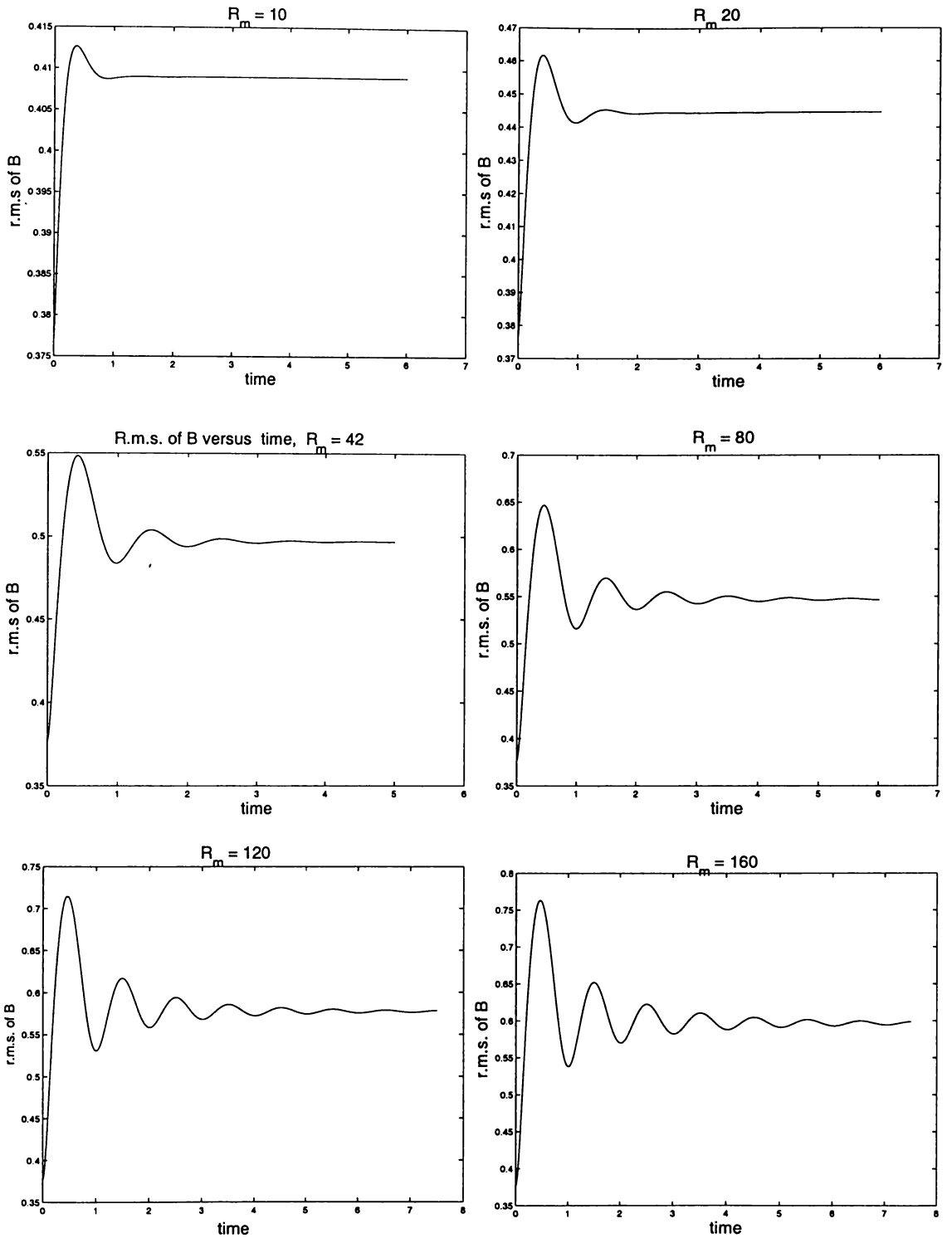

Figure 5.13: B_{rms} versus time for values of R_m from 10 to 160, to show the regularity of peaks, every $t = 1$.

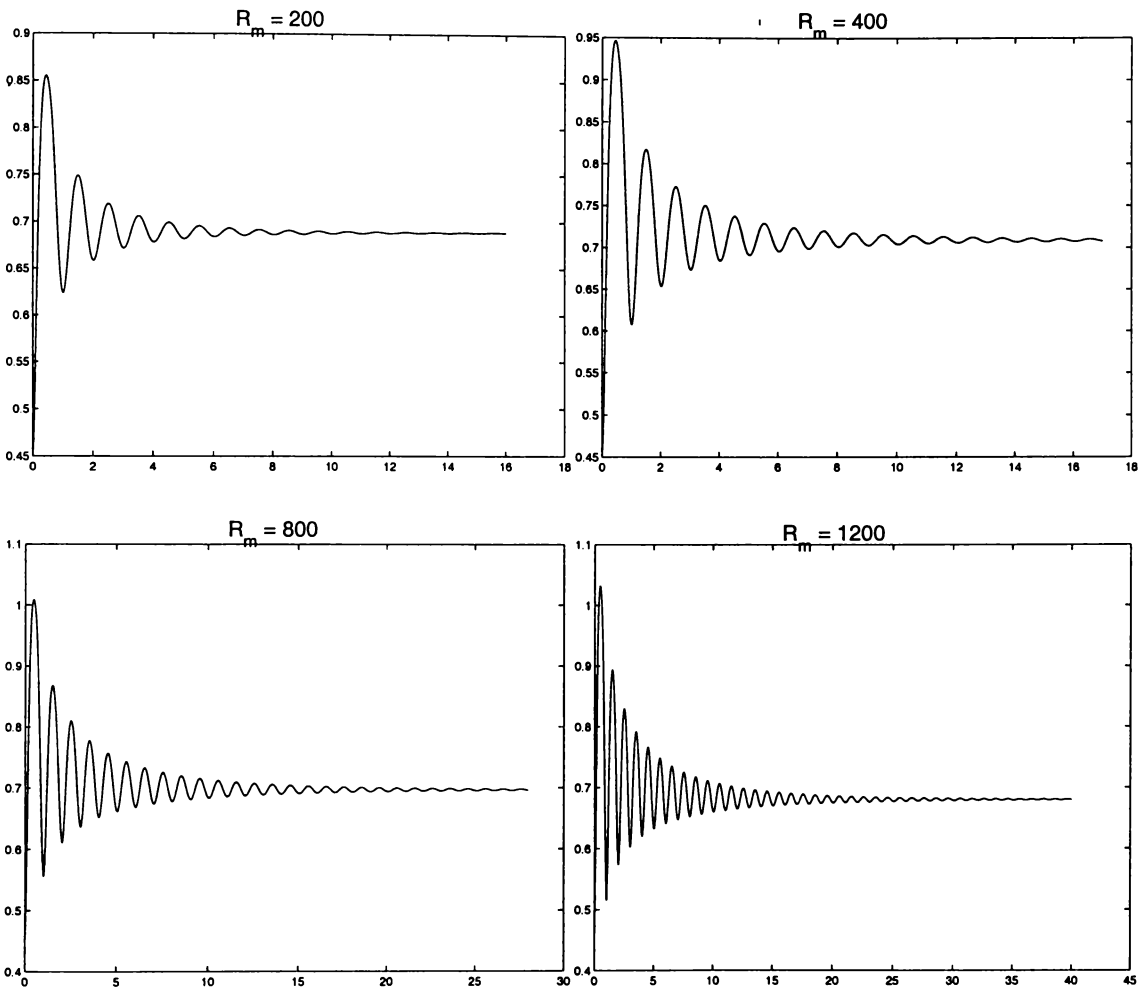

Figure 5.14: B_{rms} versus time for values of R_m from 200 to 1200, to show that B_{rms} takes longer time to settle to a fixed value as R_m increases.

Chapter 6

Fluid motion due to a multi Fourier-component source, finite R_{mA}

6.1 Introduction

In the previous chapters we considered flow at small magnetic Reynolds numbers in which the magnetic field is unaffected by the relative motion of the fluid. But in practice the opposite may be true, and changes in $\boldsymbol{B}$ due to induced currents are likely to be important.

We consider the same problem as in chapter 3 — the flow of incompressible conducting fluid contained in a channel of infinite length and width, with walls $z = \pm a$, being subjected to an applied two dimensional periodic field $\boldsymbol{B}$ which travels parallel to the channel with a uniform velocity $U\hat{\boldsymbol{x}}$. The multi Fourier-component field is determined by the boundary conditions

$$\left(\frac{\partial \phi}{\partial z}\right)_{z=\pm a} = B_0 \sum_{n=1}^{N} b_n \cos[nk(x - Ut)], \tag{6.1}$$

where b_n are constants and the wavenumber, $k = 2\pi/L$, where L is the wavelength of the applied magnetic field.

In this chapter there is no restriction on the value of the magnetic Reynolds number R_m which means that the initial applied magnetic field is affected by the

relative motion of the fluid. The motion of the conducting fluid across magnetic lines of force results in currents $\boldsymbol{J}$ which modify $\boldsymbol{B}$. The resulting Lorentz force, $\boldsymbol{J}\times\boldsymbol{B}$, in turn modifies the fluid flow.

In section §6.2 we outline the governing MHD equations, derive the dimensionless equations. The Russian numerical scheme is covered in §6.3. In this section also we discuss the calculation of vorticity and current density on the boundaries. In §6.4 comparison is made between this chapter's numerical results and those where $R_m \ll 1$. We investigate the variation in steady state velocity with magnetic Reynolds number and the initial acceleration of fluid. Lastly the conclusions are summarised in §6.5.

6.2 MHD equations

6.2.1 Governing equations

As well as Maxwell's equations (2.20) to (2.22) and Ohm's law (2.23) the evolutions of $\boldsymbol{\omega}$ and $\boldsymbol{B}$ are governed by both vorticity and induction equations:

$$\frac{\partial\omega}{\partial t} + (\boldsymbol{v}\cdot\boldsymbol{\nabla})\omega = \frac{1}{\rho}\left[\boldsymbol{\nabla}\times(\boldsymbol{J}\times\boldsymbol{B})\right]_y + \nu\nabla^2\omega, \tag{6.2}$$

and

$$\frac{\partial\boldsymbol{B}}{\partial t} = \boldsymbol{\nabla}\times(\boldsymbol{v}\times\boldsymbol{B}) + \eta\nabla^2\boldsymbol{B}. \tag{6.3}$$

Both $\boldsymbol{v}$ and $\boldsymbol{B}$ satisfy the constraints

$$\boldsymbol{\nabla}\cdot\boldsymbol{B} = 0, \tag{6.4}$$

$$\boldsymbol{\nabla}\cdot\boldsymbol{v} = 0. \tag{6.5}$$

By writing the magnetic field $\boldsymbol{B}$ in the form

$$\boldsymbol{B} = -\boldsymbol{\nabla}\psi\times\hat{\boldsymbol{y}} = \left(\frac{\partial\psi}{\partial z}, 0, -\frac{\partial\psi}{\partial x}\right) \tag{6.6}$$

where the Reynolds number is

$$R_A = \frac{V_A L}{\nu}.$$

We purposely omit "bars" for convenience from now onwards.

In dimensionless form the induction equation (6.3) and (6.7) become

$$\frac{\partial \boldsymbol{B}}{\partial t} = \boldsymbol{\nabla}\times(\boldsymbol{v}\times\boldsymbol{B}) + \frac{1}{R_{mA}}\nabla^2\boldsymbol{B}, \tag{6.14}$$

$$\nabla^2\psi = J, \tag{6.15}$$

where the Alfvén velocity-based magnetic Reynolds number

$$R_{mA} = \frac{V_A L}{\eta}.$$

Both vorticity and induction equations will be written using the Poisson bracket notation:

$$[\psi, \chi] = \psi_x \chi_z - \psi_z \chi_x.$$

Using equation (6.8) we get

$$\begin{aligned} \boldsymbol{v}\cdot\boldsymbol{\nabla}\omega &= \frac{\partial\chi}{\partial z}\frac{\partial\omega}{\partial x} - \frac{\partial\chi}{\partial x}\frac{\partial\omega}{\partial z} \\ &= [\omega, \chi]. \end{aligned} \tag{6.16}$$

Also

$$\boldsymbol{J}\times\boldsymbol{B} = \left(-J\frac{\partial\psi}{\partial x}, 0, -J\frac{\partial\psi}{\partial z}\right),$$

where $\boldsymbol{J} = (0, J, 0)$. So we can obtain the $y-$component of curl of the Lorentz force (which is the only non-zero component)

$$\begin{aligned} [\boldsymbol{\nabla}\times(\boldsymbol{J}\times\boldsymbol{B})]_y &= \frac{\partial J}{\partial x}\frac{\partial\psi}{\partial z} - \frac{\partial J}{\partial z}\frac{\partial\psi}{\partial x} \\ &= [J, \psi]. \end{aligned} \tag{6.17}$$

Hence using (6.16) and (6.17) the vorticity equation (6.12) can be written as

$$\frac{\partial\omega}{\partial t} + [\omega, \chi] = [J, \psi] + \frac{1}{R_A}\nabla^2\omega. \tag{6.18}$$

Similarly the induction equation (6.14) can be transformed into

$$\frac{\partial\psi}{\partial t} + [\psi, \chi] = \frac{1}{R_{mA}}\nabla^2\psi. \tag{6.19}$$

In order to do some comparisons at $R_m \ll 1$ between the results of the codes that use Lax-Wendroff method (Chapter 4) and the scheme in this chapter we need to find relations between dimensionless constants being referred in both schemes. From the two types of definition of Reynolds number

$$R = \frac{U\,L}{\nu}, \qquad R_A = \frac{V_A L}{\nu} \tag{6.20}$$

we obtain

$$\frac{R}{R_A} = \frac{U}{V_A} = r, \quad \text{say}$$

or

$$U = r\,V_A. \tag{6.21}$$

We can simplify the comparison by setting $U = V_A$, i.e. $r = 1$ in the Lax-Wendroff code. Note also that when we take V_A as a velocity scale

$$M^2 = R\,R_m. \tag{6.22}$$

It is interesting to note here that in chapters 2 to 4, $M^2/R = \mathcal{N}$, which is the magnetic interaction parameter. Hence, here by letting $U = V_A$ we have $R_m = \mathcal{N}$. This is consistent with the condition that $\mathcal{N} \ll 1$.

6.3 Numerical methods

The numerical method used in this chapter is very similar to the Russian scheme used by Craig and Watson [3] in their codes to solve the vorticity equation (6.18) and the induction equation (6.19) . The Poisson solver described in Chapter 4 is used in this code for it is written for a rectangular domain of $[0,1] \times [-a,a]$, where a is the aspect ratio. My code is basically different from the one written by Craig and Watson [3] because of the different boundary conditions, the rectangular domain and different initial conditions. However I follow their style of coding due to its conciseness and simplicity.

6.3.1 Outline of scheme

In general the following four dimensionless governing equations are used in the code:

$$\nabla^2 \chi = \omega, \tag{6.23}$$

$$\nabla^2 \psi = J, \tag{6.24}$$

$$\frac{\partial \omega}{\partial t} + [\omega, \chi] = [J, \psi] + \frac{1}{R_A} \nabla^2 \omega, \tag{6.25}$$

$$\frac{\partial \psi}{\partial t} + [\psi, \chi] = \frac{1}{R_m} \nabla^2 \psi. \tag{6.26}$$

A flow chart of the code is briefly given in figure 6.1. We calculate the initial values of stream function χ_b and magnetic stream function (flux) ψ_b, then the initial vorticity ω_b using (6.23) . (We use the subscript $_b$ to denote "before" the main loop.)

The main loop starts with calculation of current density J_b from equation (6.24) . The new vorticity ω_n is calculated from the vorticity equation (6.18) using the Russian scheme to be described in the next subsection. To get the new stream function χ_n we solve the Poisson equation (with boundary conditions $\chi(\pm a) = 0$,) using the Poisson solver of chapter 4 followed by the addition of a particular solution to satisfy the boundary conditions $\chi(-a) = 0$ and $\chi(a) = -2Ua$. The next step uses the Russian scheme to calculate the new flux ψ_n from the induction equation (6.26) . This main loop is repeated until the specified time, while making sure that the stability conditions (to be explained in the following subsection) are met.

The initial stream function is

$$\chi(z) = -U(z + a), \quad -a \leq z \leq a,$$

which represents a uniform flow of straightlines. The initial (magnetic) flux function is

$$\psi(x, z) = -B_0 \sum_{n=1}^{N} b_n \cosh(nkz) \sin(nk(x - Ut)). \tag{6.27}$$

6.3.2 The Russian scheme and coding

The Russian scheme is used to advect equations (6.25) and (6.26) . Briefly this is how it works. For the vorticity equation (6.25) we first calculate the predictor value ω^{n+1*} (6.28) at time step $n+1*$, and then we use the predicted values of ω^{n+1*} to calculate the corrector value ω^{n+1} (6.29) at time step $n+1$, while using the same χ_{ij}^n and keeping the term

$$\left([J_{ij}^n,\, \chi_{ij}^n] + \frac{1}{R_A}\nabla^2 \omega_{ij}^n\right)$$

unchanged as in (6.28) .

The following contains the detailed steps. The predictor method gives

$$\omega_{ij}^{n+1*} = \omega_{ij}^n - (\omega_x^n \chi_z^n - \omega_z^n \chi_x^n)\Delta t + \left([J_{ij}^n,\, \chi_{ij}^n] + \frac{1}{R_A}\nabla^2 \omega_{ij}^n\right)\Delta t, \tag{6.28}$$

where

$$\begin{aligned}
\omega_x^n &= \frac{\omega_{i+1,j}^n - \omega_{i-1,j}^n}{2\Delta}, \\
\omega_z^n &= \frac{\omega_{i,j+1}^n - \omega_{i,j-1}^n}{2\Delta}, \\
\chi_x^n &= \frac{\chi_{i+1,j}^n - \chi_{i-1,j}^n}{2\Delta}, \\
\chi_z^n &= \frac{\chi_{i,j+1}^n - \chi_{i,j-1}^n}{2\Delta}, \\
J_{ij}^n &= \nabla^2 \psi_{ij}^n.
\end{aligned}$$

The predictor values, ω^{n+1*}, are then used to calculate the corrector ω^{n+1}, for the next time step $t+\Delta t$,

$$\omega_{ij}^{n+1} = \omega_{ij}^n - (\omega_x^{n+1*} \chi_z^n - \omega_z^{n+1*} \chi_x^n)\Delta t + \left([J_{ij}^n,\, \chi_{ij}^n] + \frac{1}{R_A}\nabla^2 \omega_{ij}^n\right)\Delta t, \tag{6.29}$$

where

$$\begin{aligned}
\omega_x^{n+1*} &= \frac{\omega_{i+1,j}^{n+1*} - \omega_{i-1,j}^{n+1*}}{2\Delta}, \\
\omega_z^{n+1*} &= \frac{\omega_{i,j+1}^{n+1*} - \omega_{i,j-1}^{n+1*}}{2\Delta},
\end{aligned}$$

χ_x^n, χ_z^n and

$$\left([J_{ij}^n,\, \chi_{ij}^n] + \frac{1}{R_A}\nabla^2 \omega_{ij}^n\right)$$

are unchanged as in the previous predictor.

Similarly, for predictor ψ^{n+1} we get

$$\psi_{ij}^{n+1*} = \psi_{ij}^{n} - (\psi_x^n \chi_z^n - \psi_z^n \chi_x^n)\Delta t + \frac{1}{R_m}\nabla^2 \psi_{ij}^n \Delta t, \tag{6.30}$$

where

$$\begin{aligned}
\psi_x^n &= \frac{\psi_{i+1,j}^n - \psi_{i-1,j}^n}{2\Delta}, \\
\psi_z^n &= \frac{\psi_{i,j+1}^n - \psi_{i,j-1}^n}{2\Delta}, \\
\chi_x^n &= \frac{\chi_{i+1,j}^n - \chi_{i-1,j}^n}{2\Delta}, \\
\chi_z^n &= \frac{\chi_{i,j+1}^n - \chi_{i,j-1}^n}{2\Delta}.
\end{aligned}$$

We calculate the corrector ψ^{n+1} from

$$\psi_{ij}^{n+1} = \psi_{ij}^{n} - (\psi_x^{n+1*} \chi_z^n - \psi_z^{n+1*} \chi_x^n)\Delta t + \frac{1}{R_m}\nabla^2 \psi_{ij}^n \Delta t, \tag{6.31}$$

where

$$\begin{aligned}
\psi_x^{n+1*} &= \frac{\psi_{i+1,j}^{n+1*} - \psi_{i-1,j}^{n+1*}}{2\Delta}, \\
\psi_z^{n+1*} &= \frac{\psi_{i,j+1}^{n+1*} - \psi_{i,j-1}^{n+1*}}{2\Delta},
\end{aligned}$$

χ_x^n, χ_z^n and $\frac{1}{R_m}\nabla^2 \psi_{ij}^n$ are unchanged as in the predictor (6.30) .

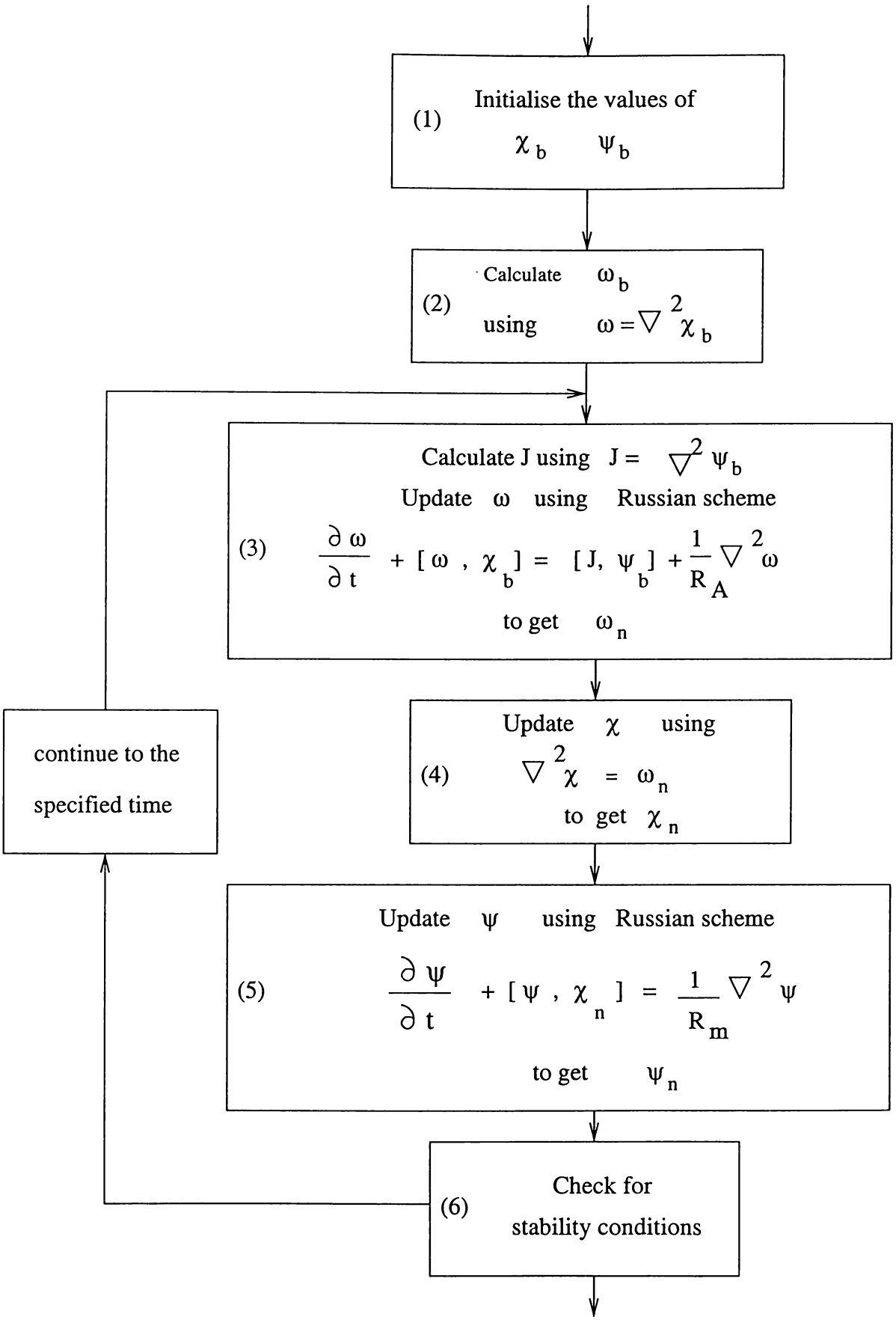

Figure 6.1: Flow chart of the code where the Russian scheme is used.

The value U of the velocity of the applied magnetic field can be varied by varying r where $r = U/V_A$. The value (up to 4 decimal places) of the typical Alfvén velocity,

$$V_A = 0.0892\,\mathrm{m\ s^{-1}} \quad \text{or} \quad 0.3211\,\mathrm{km/h},$$

if we choose typical values

$$B_0 = 0.01\,\text{webers m}^{-2}, \quad \mu = 4.0\pi \times 10^{-7}\,\text{henry m}^{-2}, \quad \rho = 10000\,\text{kg m}^{-3}.$$

Calculations of vorticity, $\omega = \nabla^2\chi$ can be carried out using the finite difference approximations at the point (x_i, z_j):

$$\omega_{ij} = \frac{\chi_{i+1,j} - 2\chi_{ij} + \chi_{i-1,j}}{2\Delta^2} + \frac{\chi_{i,j+1} - 2\chi_{ij} + \chi_{i,j-1}}{2\Delta^2},$$

where Δ = the width of the $x-$partition = the width of $z-$partition. But on the boundaries $z = \pm a$, we use the technique of Roache[6, page 141], as covered in §4.3.1.

The same finite difference approximations is used for current density, $J = \nabla^2\psi$. For the calculation of the current density J on the boundaries $z = \pm a$, we can write

$$\boldsymbol{J} = -\sigma r V_A \hat{\boldsymbol{x}} \times \boldsymbol{B}, \tag{6.32}$$

or in dimensionless form,

$$J = R_m B_z, \qquad \text{where} \quad \boldsymbol{B} = (B_x, 0, B_z).$$

In terms of the magnetic stream function the current density becomes

$$J = -R_m \frac{\partial\psi}{\partial x} = -r R_{mA} \frac{\partial\psi}{\partial x}.$$

To ensure that the calculation remains stable we check the Courant-Friedrich-Lewys condition and the von Neumann criterion involving viscosity and magnetic diffusivity for stability

$$\begin{aligned} \Delta t &\le \frac{\Delta_x}{\sqrt{2}|\boldsymbol{v}|_{\max}}, \\ \Delta t &\le 0.5 R_{mA} \Delta^2, \\ \Delta t &\le 0.5 R_A \Delta^2. \end{aligned} \tag{6.33}$$

Here we take Δt to be the minimum of the three above conditions. The stability analysis for the Russian scheme for both advection equation and diffusion equation can be found in Heerikhuisen [8].

6.4 Numerical results

6.4.1 Comparisons with earlier results for $R_m \ll 1$.

As discussed in §6.2.2 by setting $U = V_A$ we obtain $R = R_A$ and $R_m = R_{mA}$. Due to the different ways of non-dimensionalising under Lax-Wendroff scheme and Russian scheme the source term of both equation differ in value in the order of 10^4. By ensuring that the source terms of the vorticity equation under the two schemes are equal for corresponding Reynolds number, R, and magnetic Reynolds number, R_m, we produce the streamlines at various times $t = 0.1$ to $t = 1.5$, for the code using Lax-Wendroff scheme and the code using Russian, (figures 6.2 and 6.3.) It can be seen that the results agree quite well.

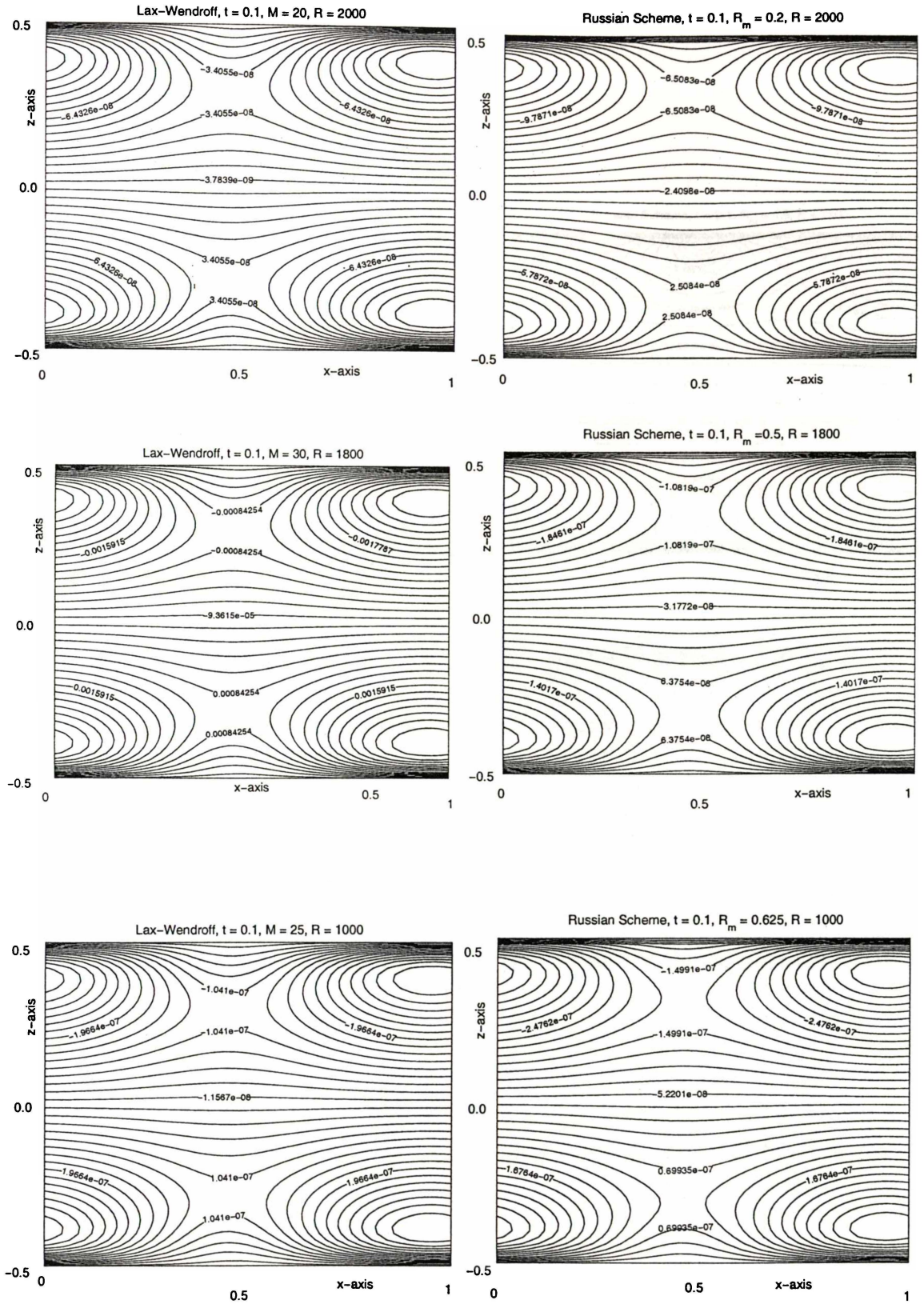

Figure 6.2: Streamlines calculated by the Lax-Wendroff scheme (on the left column) and streamlines calculated by the Russian scheme (on the second column) for $R_m = 0.2,\ 0.5,\ 0.625$. *The velocity is* $U = V_A$, $b_n = [1.0, 1.0]$ *and* $t = 0.1$.

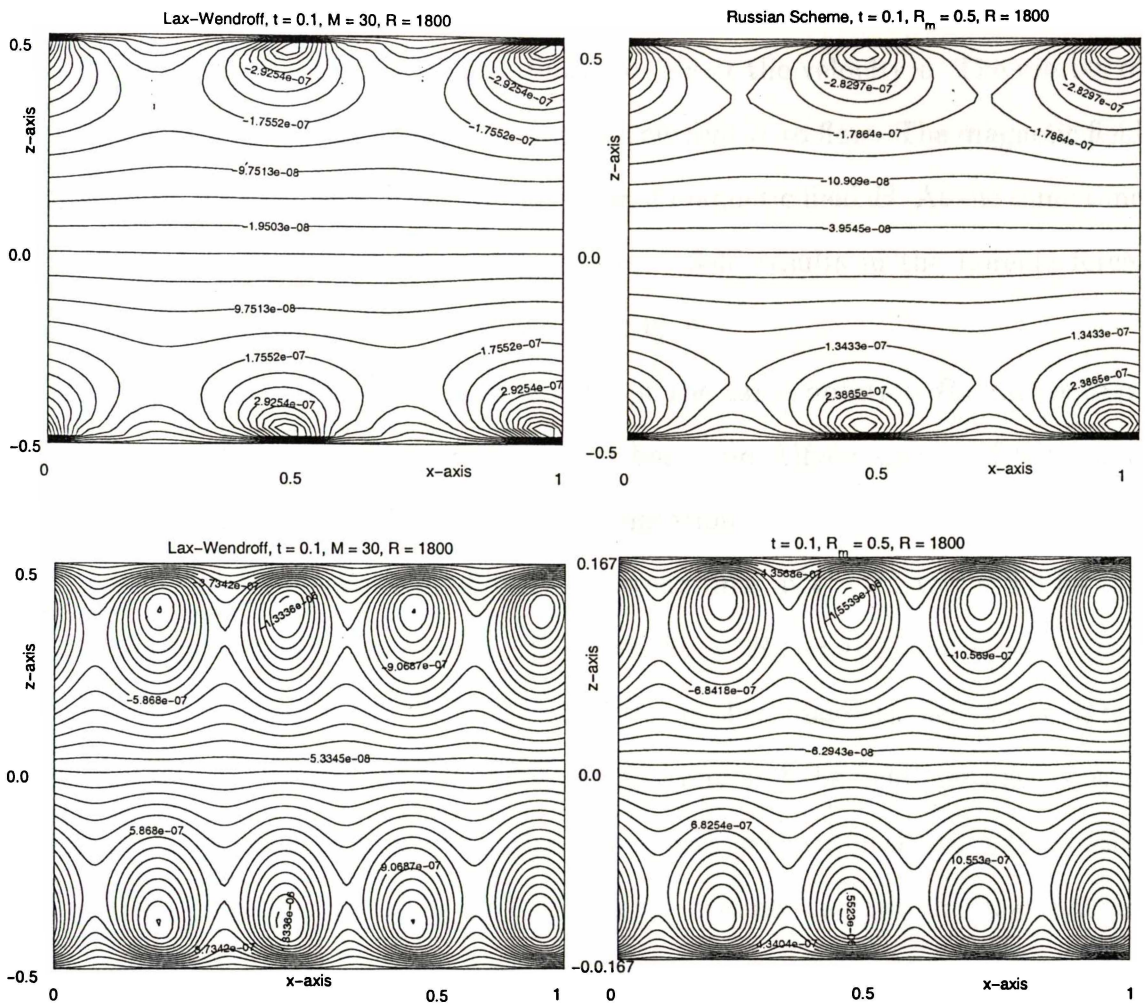

Figure 6.3: Left column: Streamlines calculated by the Lax-Wendroff scheme for $R_m = 0.5$ *at* $t = 0.2, \boldsymbol{b} = [0.1 \quad 0.8 \quad 0.0 \quad 0.8 \quad 0.1 \quad 0.6 \quad 0.1 \quad 2.5 \quad 0.1 \quad 2.5]$ *for the top one; and* $t = 0.1$, $\boldsymbol{b} = [2.1 \quad 0.1 \quad 0.0 \quad 0.1 \quad 6.1 \quad 0.1 \quad 0.1 \quad 0.1 \quad 2.5 \quad 0.1]$ *for the bottom one. Right column: Streamlines calculated using the Russian scheme for* $R_m = 0.5$ *for corresponding values of* $\boldsymbol{b}$ *as on the left column.*

6.4.2 Results $R_m \gg 1$.

In chapters 2 to 4 one of our main assumptions is that the applied magnetic field remains unaffected by the flow i.e. $R_m \ll 1$. But from this chapter onwards it is important to note that the applied magnetic field $\boldsymbol{B}$ is affected by the fluid flow. Hence, R_m can be a lot bigger than 1. The motion of the applied magnetic field at velocity $U\,\hat{\boldsymbol{x}}$ results in the conducting fluid moving at the velocity $\boldsymbol{v}$. The motion of conducting fluid across magnetic field causes a current $\boldsymbol{J}$ to flow. The magnetic field associated with this current modifies the applied magnetic field $\boldsymbol{B}$. At the same time the flow of electric current $\boldsymbol{J}$ across a magnetic field results in the Lorentz force, $\boldsymbol{J}\times\boldsymbol{B}$, which in turns modifies the fluid velocity $\boldsymbol{v}$.

In this chapter and chapter 7 we will adopt the same notation R_m rather than R_{mA} to refer to magnetic Reynolds number based on Alfvén speed. If there is a need for comparison we will use the original notation.

The evolution of magnetic fieldlines and streamlines at $t = 0.1$ to $t = 5.0$ for the two Fourier-component case ($b = [1, 1]$) where $R_A = R_m = 100$, and $U = V_A$, can be seen in the figures 6.4–6.7. The motion of the applied magnetic field through the conducting fluid results in the field being swept away and the fieldlines lines broken except for the those along the boundaries, which lean in the opposite direction of the field motion, (Second column, figure 6.8.) As the channel narrows the flow changes its topology from nearly straight streamlines to a flow containing eddies. This is due to the fact that the narrower the channel the deeper the penetration of the magnetic field (figure 6.8).

From the streamline diagrams, figure 6.9, it is interesting to note that by reducing the velocity of the applied magnetic field from $U = 0.5V_A$ to $0.1V_A$ vortices are less elongated because less stretched. This can be explained qualitatively as follows. The slower the magnetic field the longer the time available for the field lines to be carried away by the fluid due to "frozen-in" effect at high R_m. This is confirmed by the weaker transport of fieldlines in the direction of the flow as U decreases from $0.5V_A$ to $0.1V_A$, as shown by the fieldlines in column 2, figure 6.9.

So far, for most array combinations of Fourier coefficients b_n, we see only one pair of vortices per field wavelength. But for $\boldsymbol{b}$ = [1.1 0.8 0.0 2.0 0.1 2.6 0.1 2.5 0.1 2.5], we get two pairs of vortices, and for $\boldsymbol{b}$ = [10.1 0.1 0.0 0.1 60.1 0.1 0.1 0.1 25.1 0.1] four intense vortices are created (figure 6.11) which obviously means enhanced stirring, since in diagram (I) of figure 6.11 the v_{rms} of the fluid attains 0.6. Figure 6.10 shows the variation in the four vortices at large R_m and R, with $U = V_A$. Figure 6.12 shows the evolution of two pairs of vortices, when the velocity of the applied magnetic field is $U = 0.5V_A$.

Relative size of the boundary layers to the grid spacing

As the flow evolves the system generates boundary layers. To ensure the convergence of the numerical solutions we take the size of the grid spacing, Δ, to be smaller than the thickness of the boundary layer, $\delta = L/\sqrt{R}$. In most of our calculations we set the value of Reynolds number to be at least 100. This gives $\delta = 0.1$, since $L = 1$. We normally take the partition number to be at least 30, which means that the grid spacing is no more than 0.03. This ensures that the boundary layer is at least 3.3 times bigger than the grid spacing for the worst case.

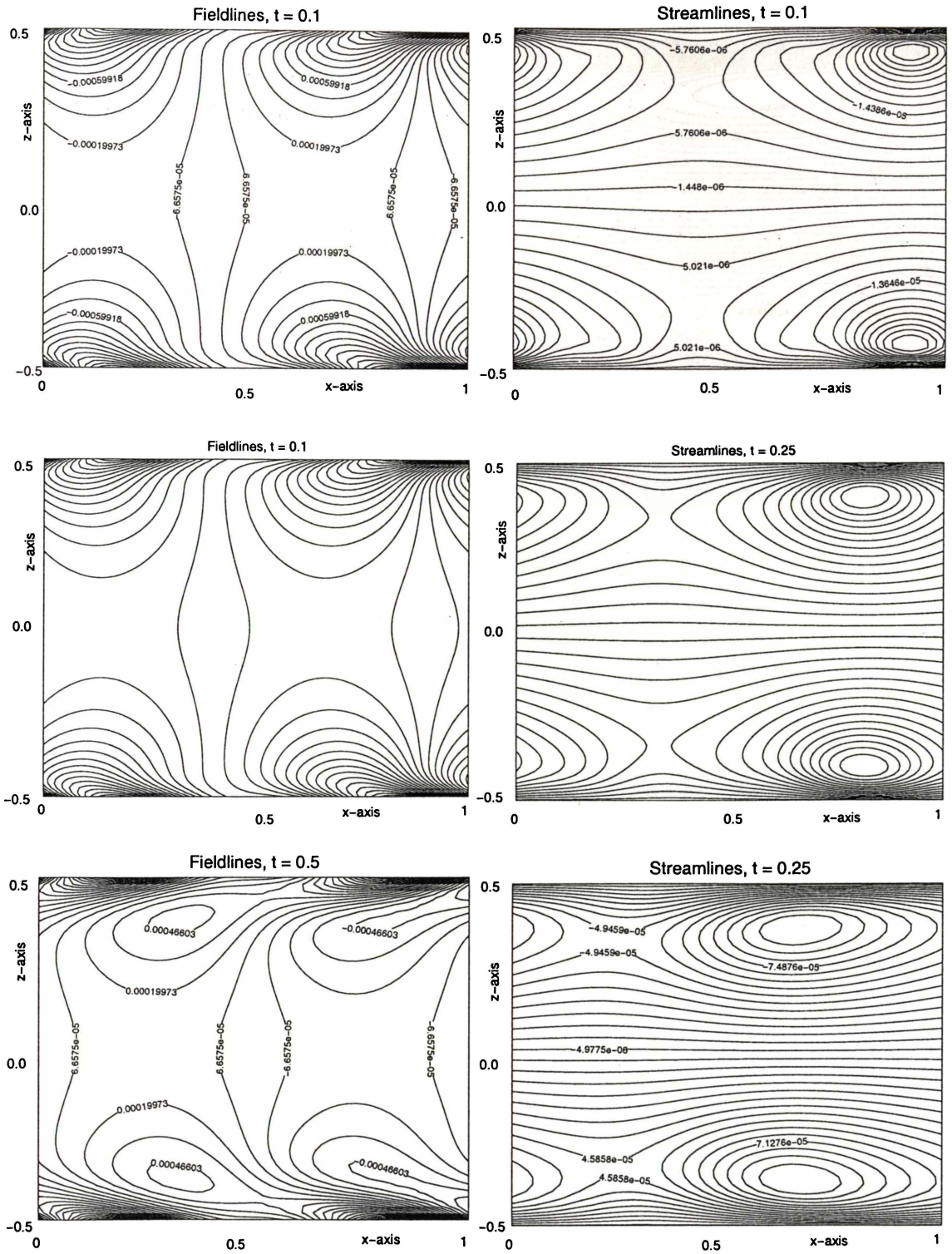

Figure 6.4: Magnetic fieldlines in the first column and streamlines in the second column at $t = 0.1, 0.25, 0.5$, for $R_A = 100$, and $R_m = 100$, $\boldsymbol{b} = [1, 1]$ and $U = V_A$

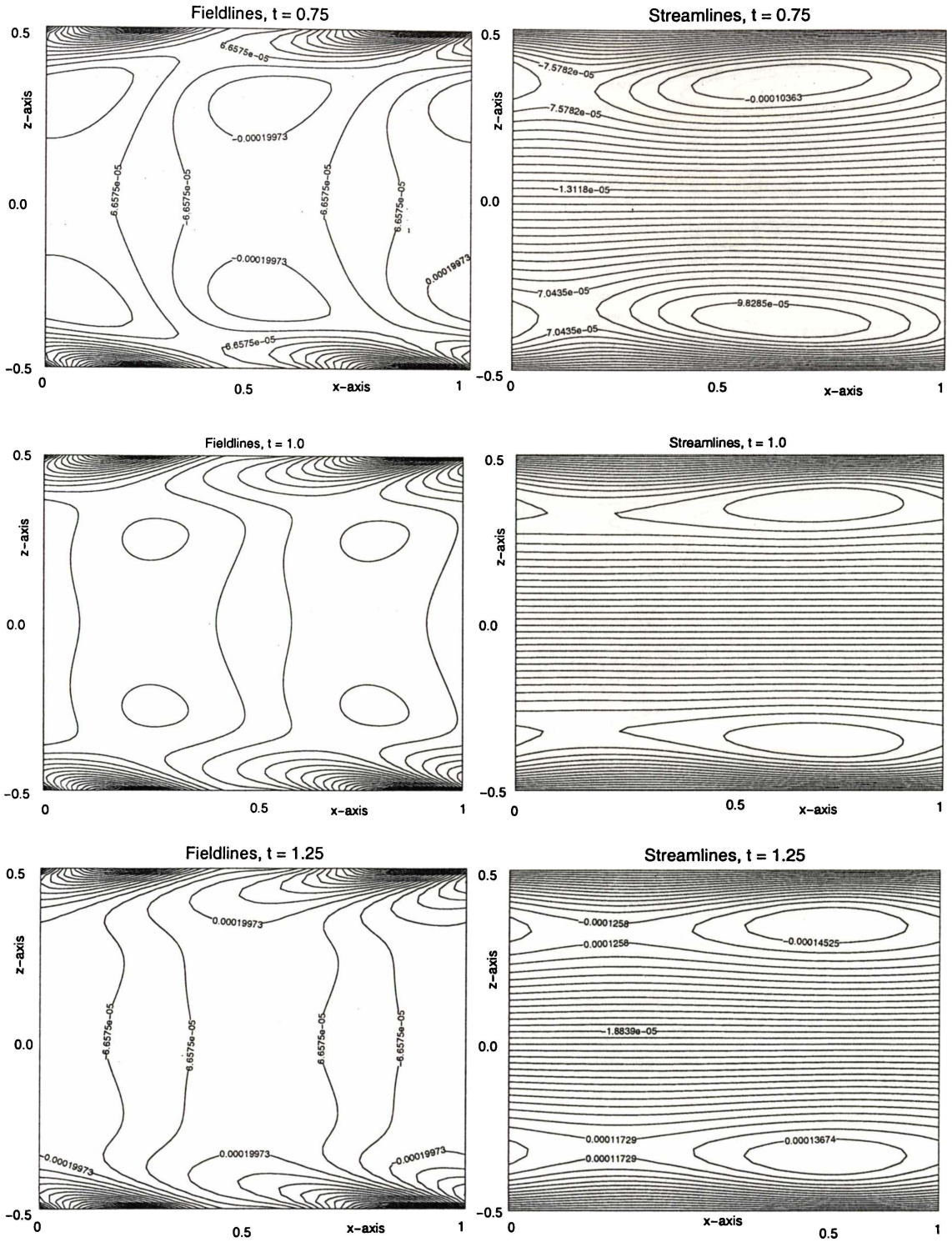

Figure 6.5: Magnetic fieldlines in the first column and streamlines in the second column at $t = 0.75, 1.0, 1.25$, for $R_A = 100$, and $R_m = 100$, $\boldsymbol{b} = [1, 1]$ and $U = V_A$.

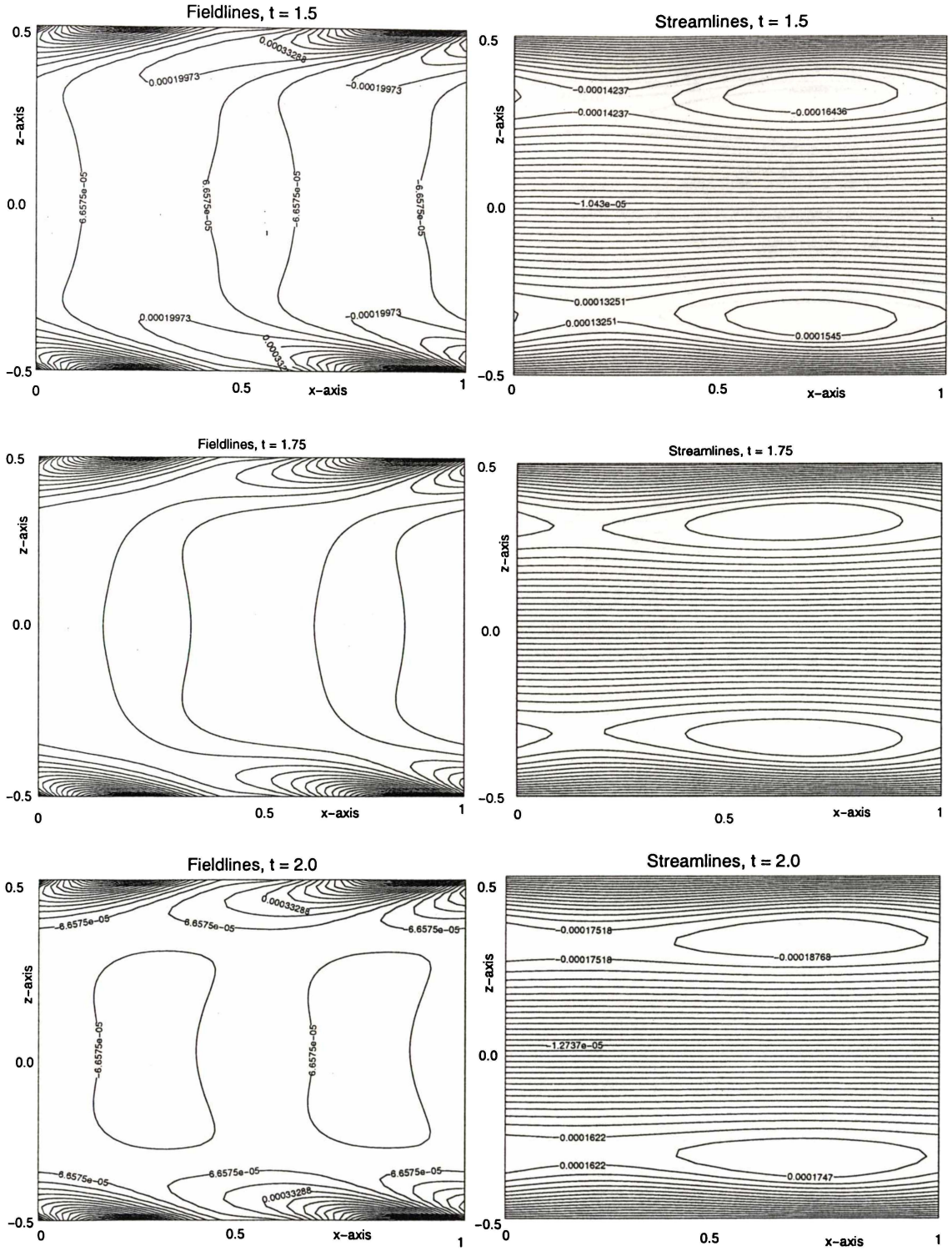

Figure 6.6: Magnetic fieldlines in the first column and streamlines in the second column at $t = 1.5, 1.75, 2.0$, for $R_A = 100$, and $R_m = 100$, $\boldsymbol{b} = [1, 1]$ and $U = V_A$.

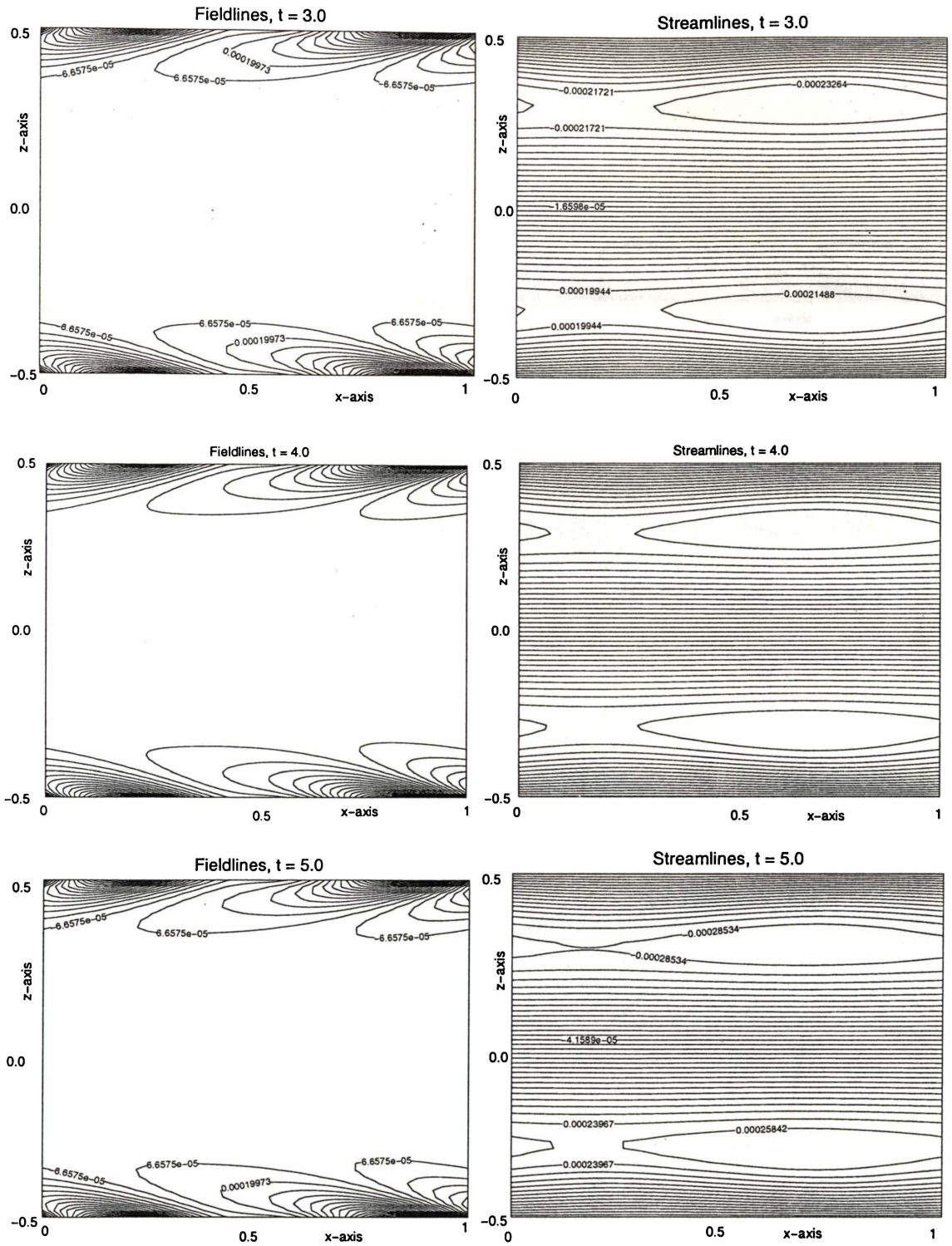

Figure 6.7: Magnetic fieldlines in the first column and streamlines in the second column at $t = 3, 4, 5$, for $R_A = 100$, and $R_m = 100.$, $\boldsymbol{b} = [1, 1]$ and $U = V_A$.

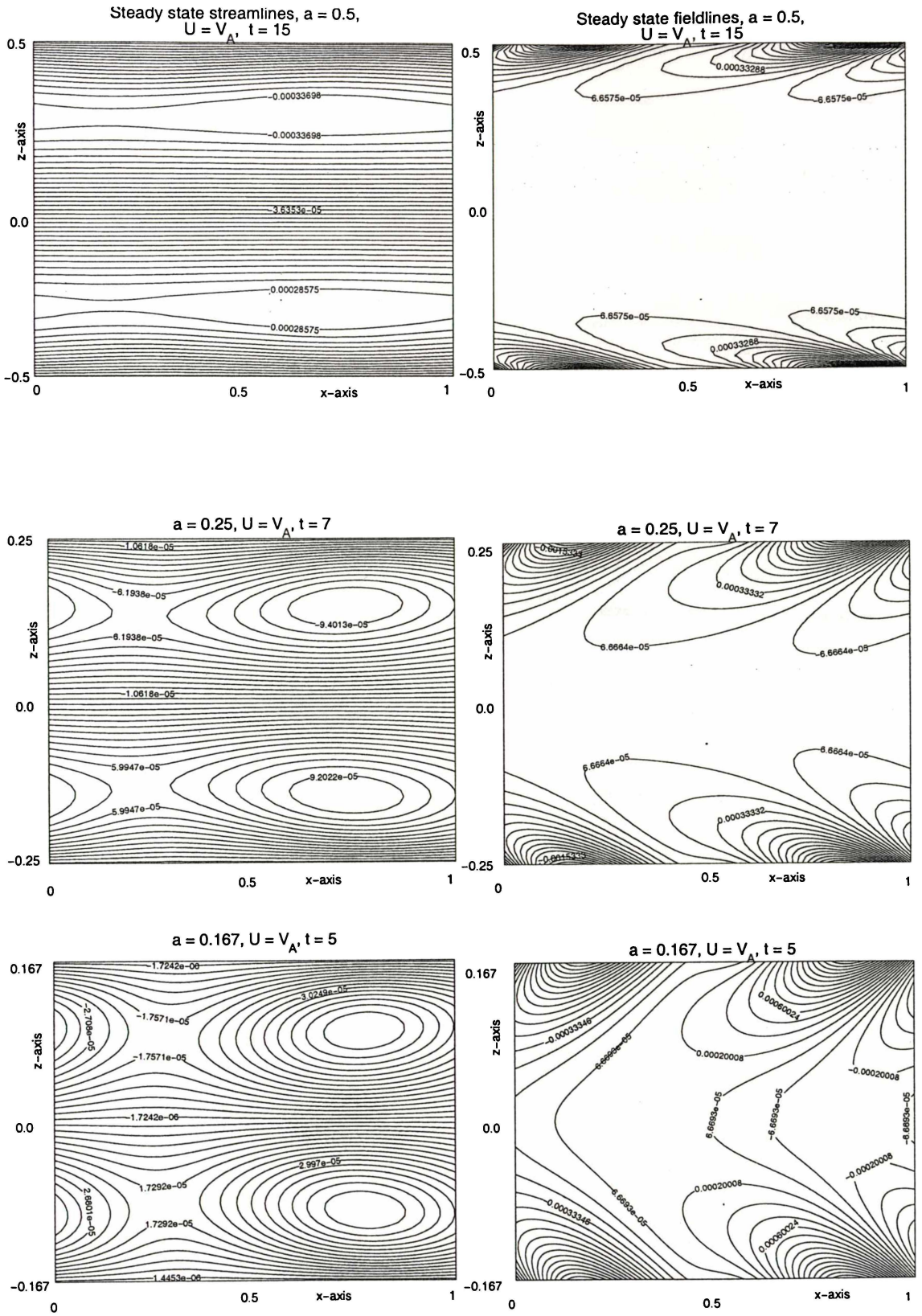

Figure 6.8: Steady state streamlines in the first column and fieldlines in the second column at decreasing channel widths, $a = 0.5,,\ \ 0.25,\ \ 1/6$ where $U = V_A, R_A = R_m = 100$, and $\boldsymbol{b} = [1, 1]$.

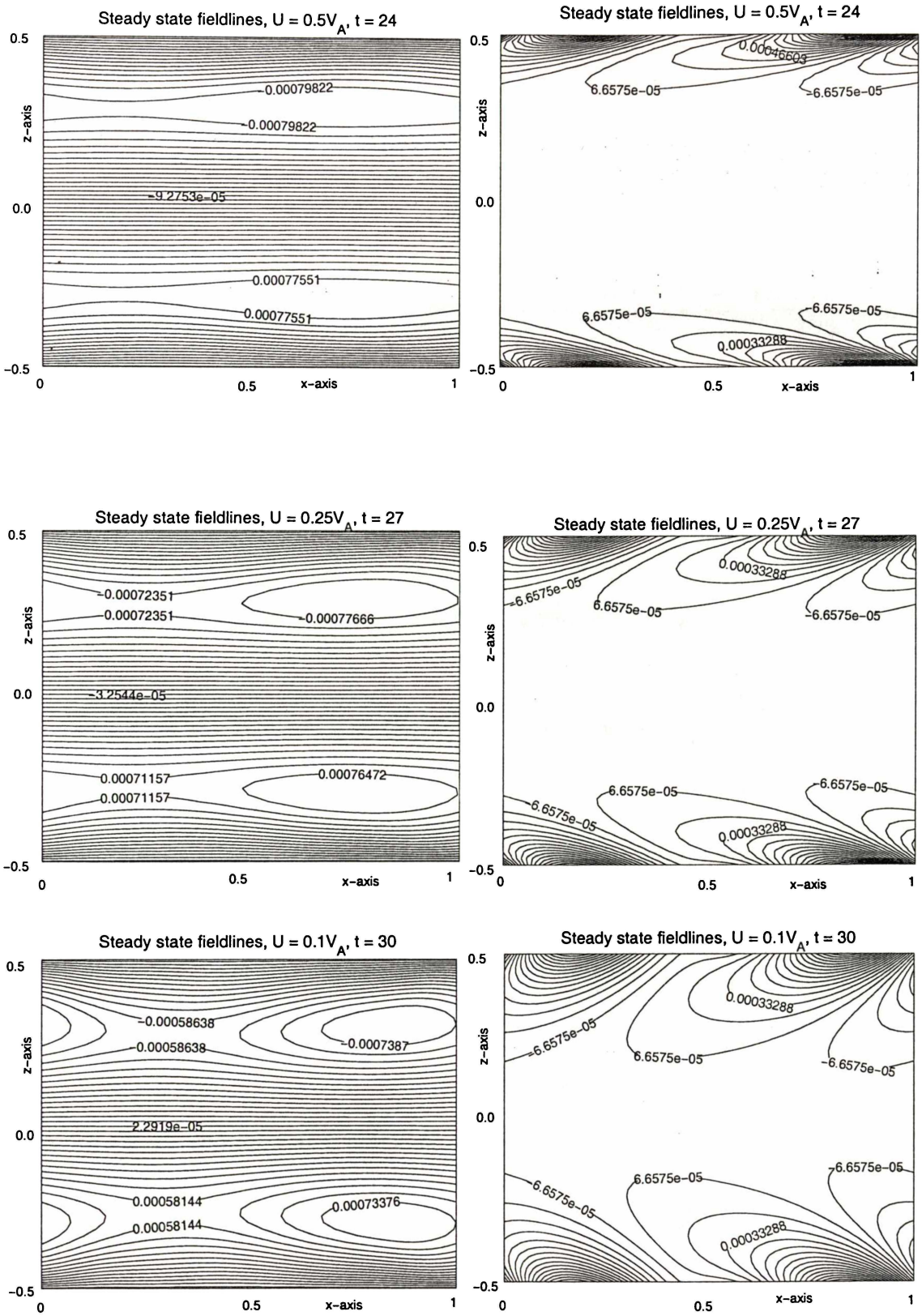

Figure 6.9: Steady state streamlines in the first column and fieldlines in the second column at a fixed channel width, $a = 0.5$, and decreasing applied velocity U, from $0.5V_A$ to $0.1V_A$, where $R_A = R_m = 200$, and $\boldsymbol{b} = [1, 1]$.

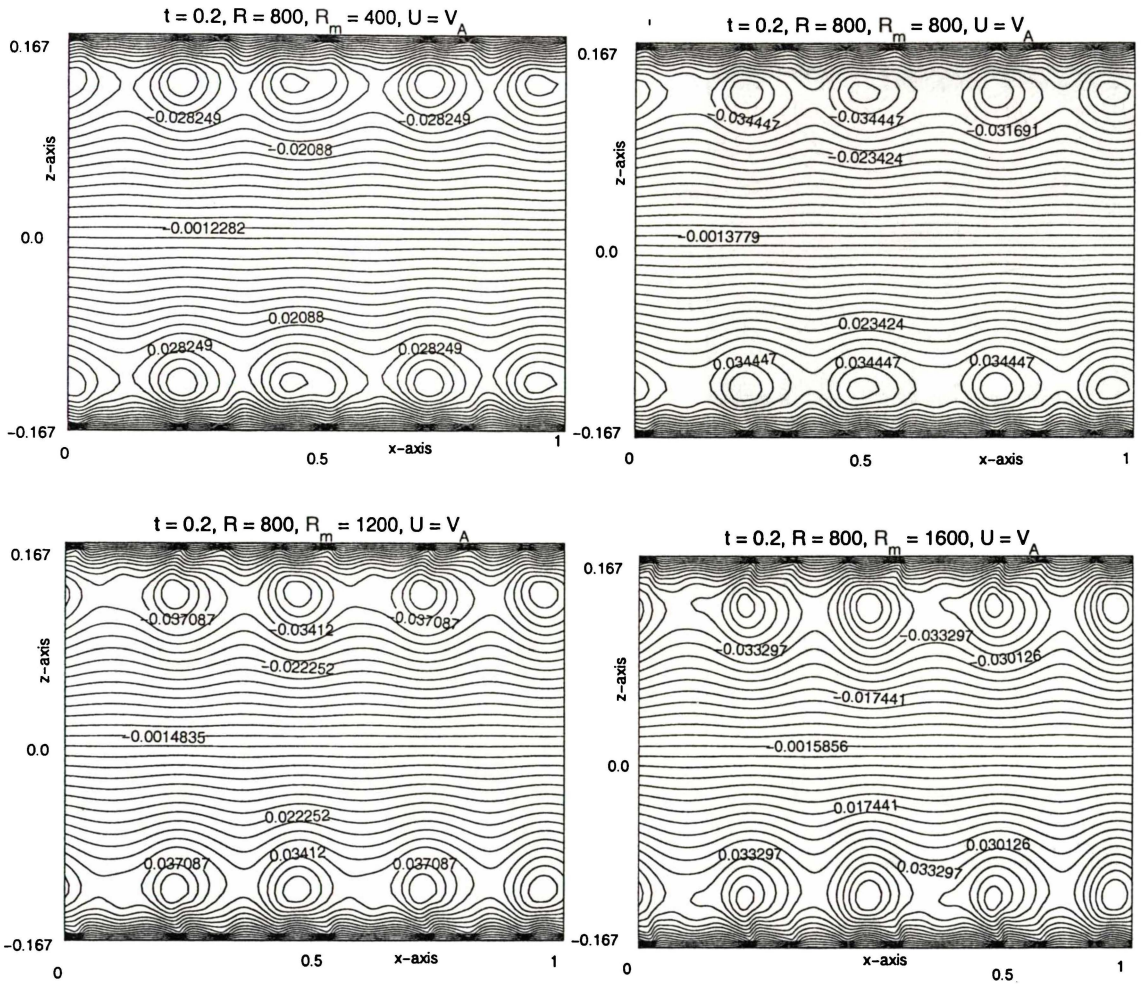

Figure 6.10: Streamlines at $t = 0.2, R = 800, U = V_A$ at increasing values of R_m showing four pairs of vortices at $\boldsymbol{b} = [10.1 \;\; 0.1 \;\; 0.0 \;\; 0.1 \;\; 60.1 \;\; 0.1 \;\; 0.1 \;\; 0.1 \;\; 25.1 \;\; 0.1]$

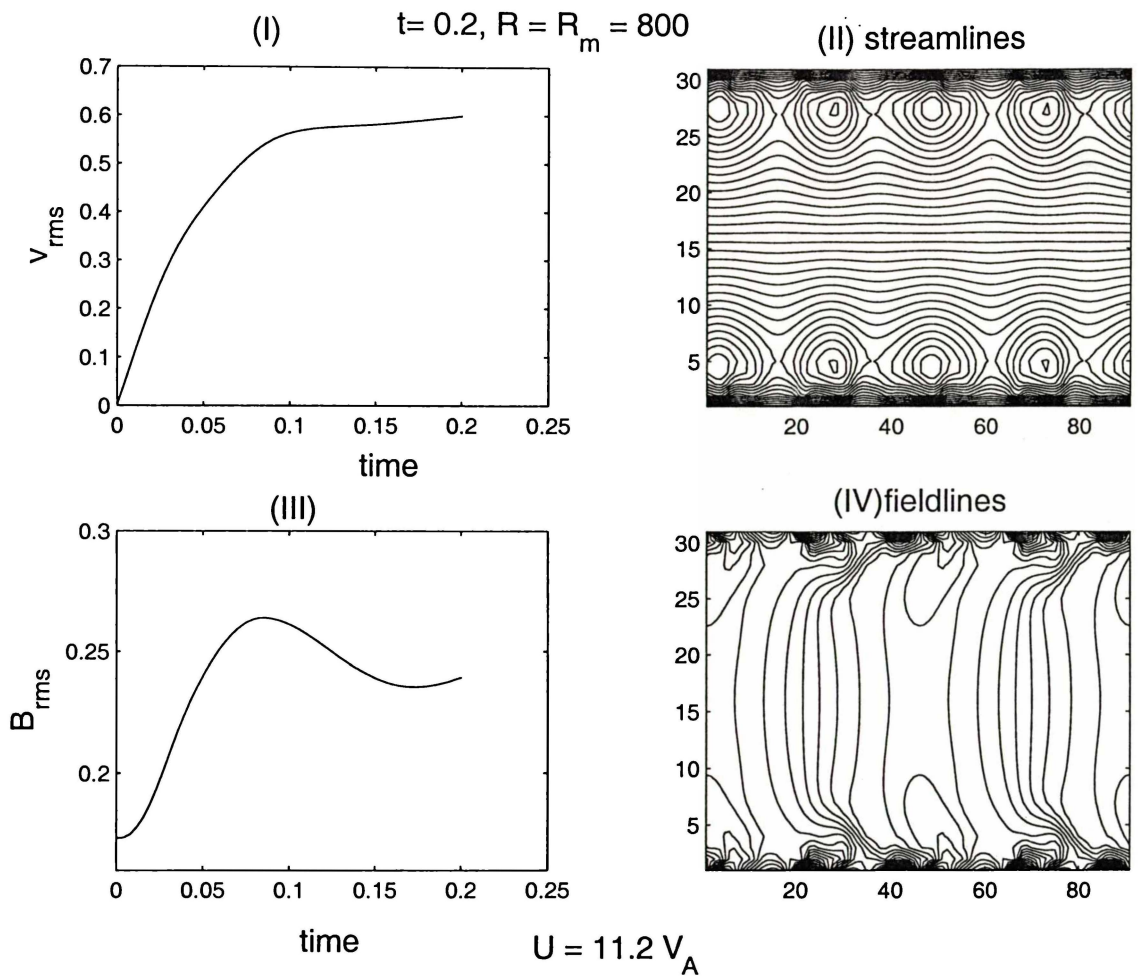

Figure 6.11: (I) Graph of v_{rms} versus time, (II) streamlines at $t = 0.2$, (III) B_{rms} versus time and (IV) fieldlines at $t = 0.2$. $U = V_A$.

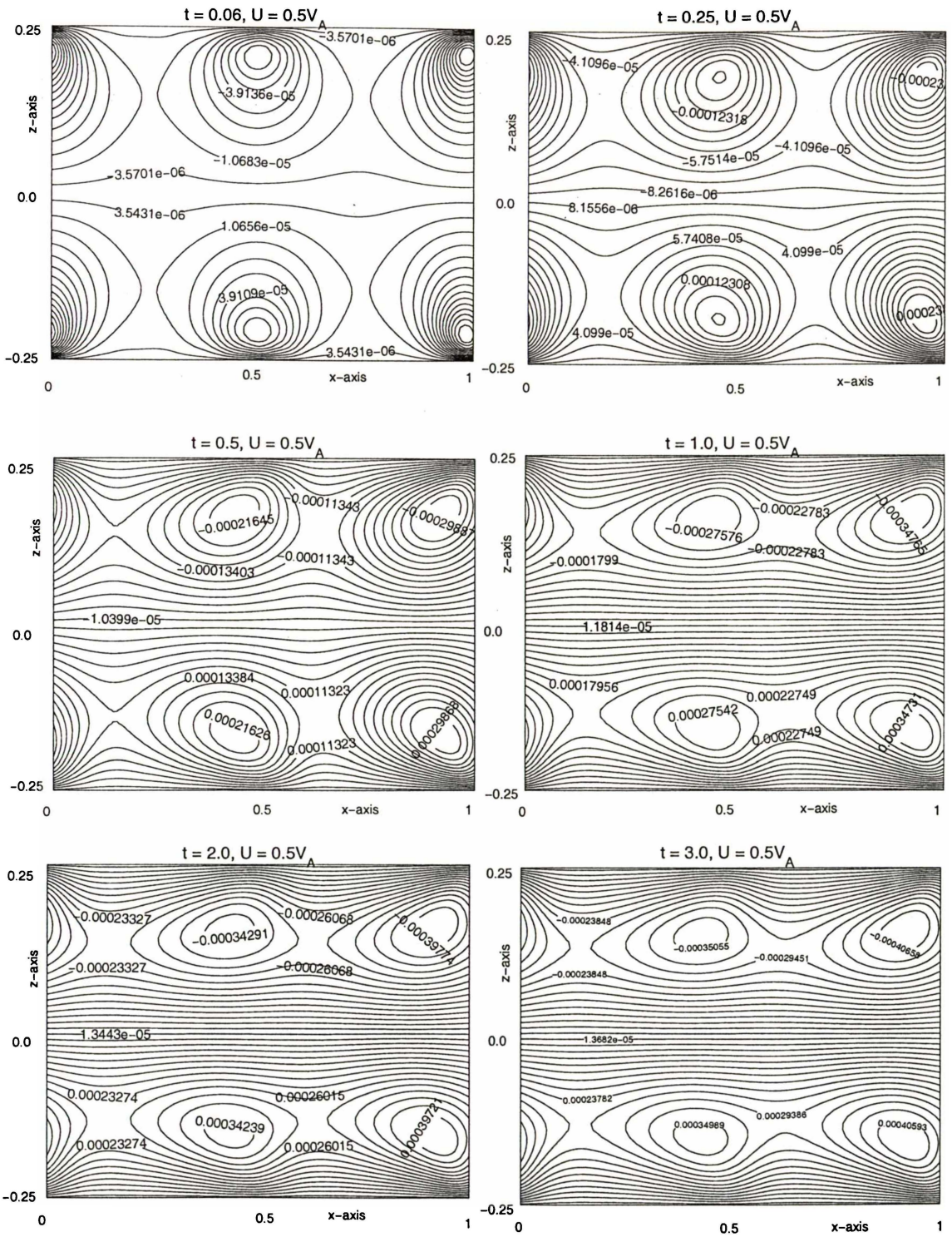

Figure 6.12: The evolution of streamlines from $t = 0.06$ to $t = 3$ for the case where $U = 0.5V_A, R = R_m = 100$ and $\boldsymbol{b} = [1.1 \quad 0.8 \quad 0.0 \quad 2.0 \quad 0.1 \quad 2.6 \quad 0.1 \quad 2.5 \quad 0.1 \quad 2.5]$.

6.5 Conclusions

The smaller the aspect ratio is the better and stronger will be the magnetic field's penetration. Intermediate $R_m \sim 100$ gives most effective stirring for the case $b_n = [1, 1]$. It is possible to generate two to four pairs of vortices for some combinations of $\boldsymbol{b}$, which means better stirring. We also find that lowering the value of U helps in creating more less-elongated vortices in the flow. In order to avoid a sudden increase of velocity of the fluid it maybe more practical to consider the similar problem but with the velocity of the applied magnetic field increasing gradually. This is to be the subject of the next chapter.

Steady state velocity v_{rms} versus R_m

A graph of steady state velocity, v_{rms}, versus R_m, $R = 2000$ and $b_n = [1, 1]$, is given in figure 6.13. A low magnetic Reynolds number, R_m, means low electrical conductivity, which gives a weak induced current and hence a weak Lorentz force driving the fluid motion. When R_m is small we expect a weak induced flow. For example in the extreme case of water there will not be any fluid motion at all when the applied magnetic field is moved.

The graph shows that the steady state, v_{rms}, increases sharply as the magnetic Reynolds number increases and reaches a maximum when R_m is between 100 and 110, and starts to decrease as magnetic Reynolds number continues to increase. As R_m increases the fluid becomes almost a perfect conductor where the field lines are frozen in. As can be seen in figures 6.14 and 6.15 as R_m increases, the thickness of the magnetic field layer on the boundaries decreases as more and more of the central field lines are expelled. This means that as the magnetic field penetration decreases, the current density also decreases. Therefore the resultant Lorentz force that drives the fluid to move also becomes weaker which means a low value of steady state velocity v_{rms}. So the maximum steady state v_{rms} occurs at an intermediate value of R_m.

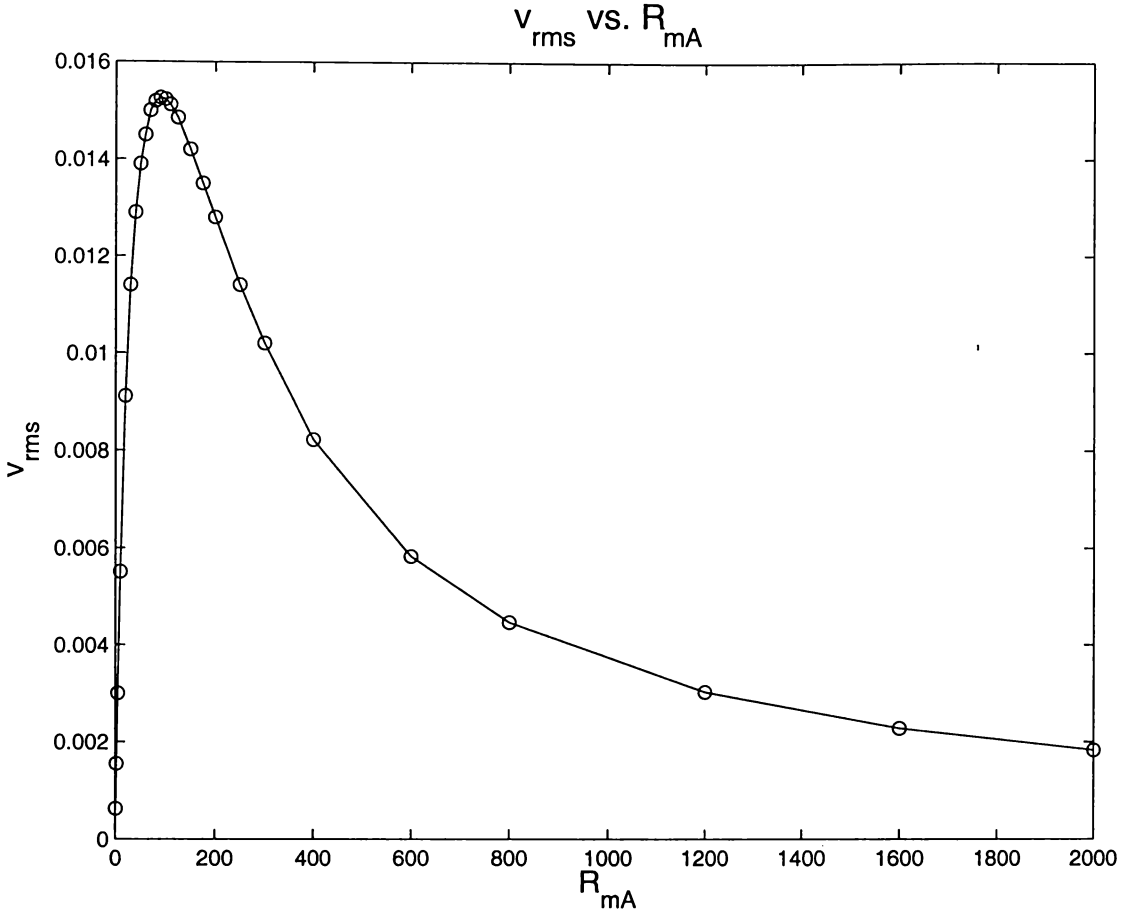

Figure 6.13: Graph of steady state v_{rms} versus R_m where $R = 2000$.

Initial acceleration of fluid at large R_m

When the applied magnetic field is impulsively moved at a velocity of U at time $t = 0$, it is reasonable to expect that the fluid is rapidly accelerated as can be seen in figure 6.16 for $R_m = 100$. As R_m increases so does the initial acceleration. For example for the case of $R_m = 1500, R = 800$, (figure 6.16), the velocity of the fluid increases from 0 to 1.6×10^{-3} in just a short time of 0.25. To avoid the high initial acceleration of the fluid of this nature it would be interesting to consider the effect of gradual acceleration, until it reaches a fixed value of U. This will be studied in the next chapter.

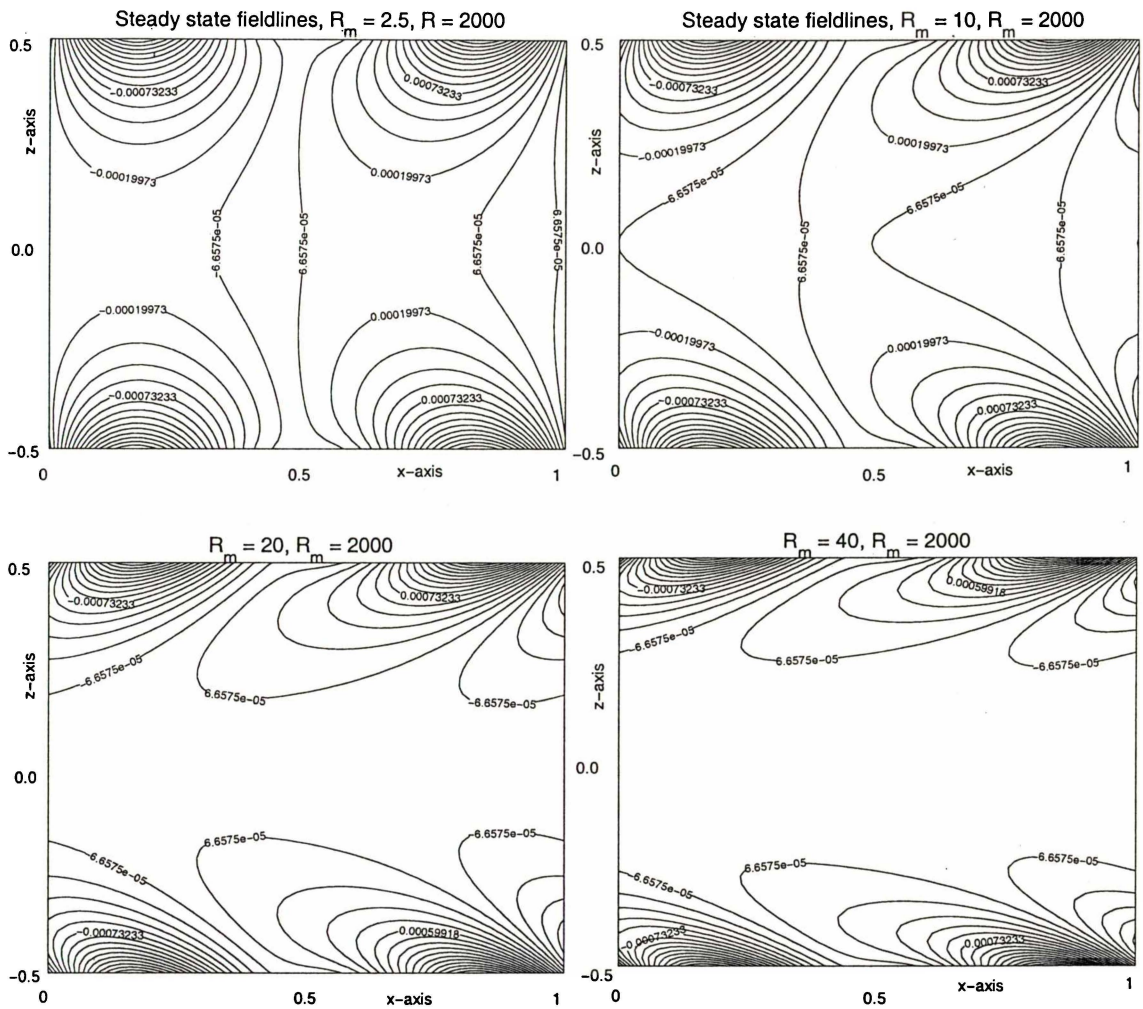

Figure 6.14: Magnetic fieldlines at steady state showing increasing fieldlines expulsion as magnetic Reynolds number increases from 2.5 *to* 40. *Reynolds number is* 2000 *and* $b = [1, 1]$.

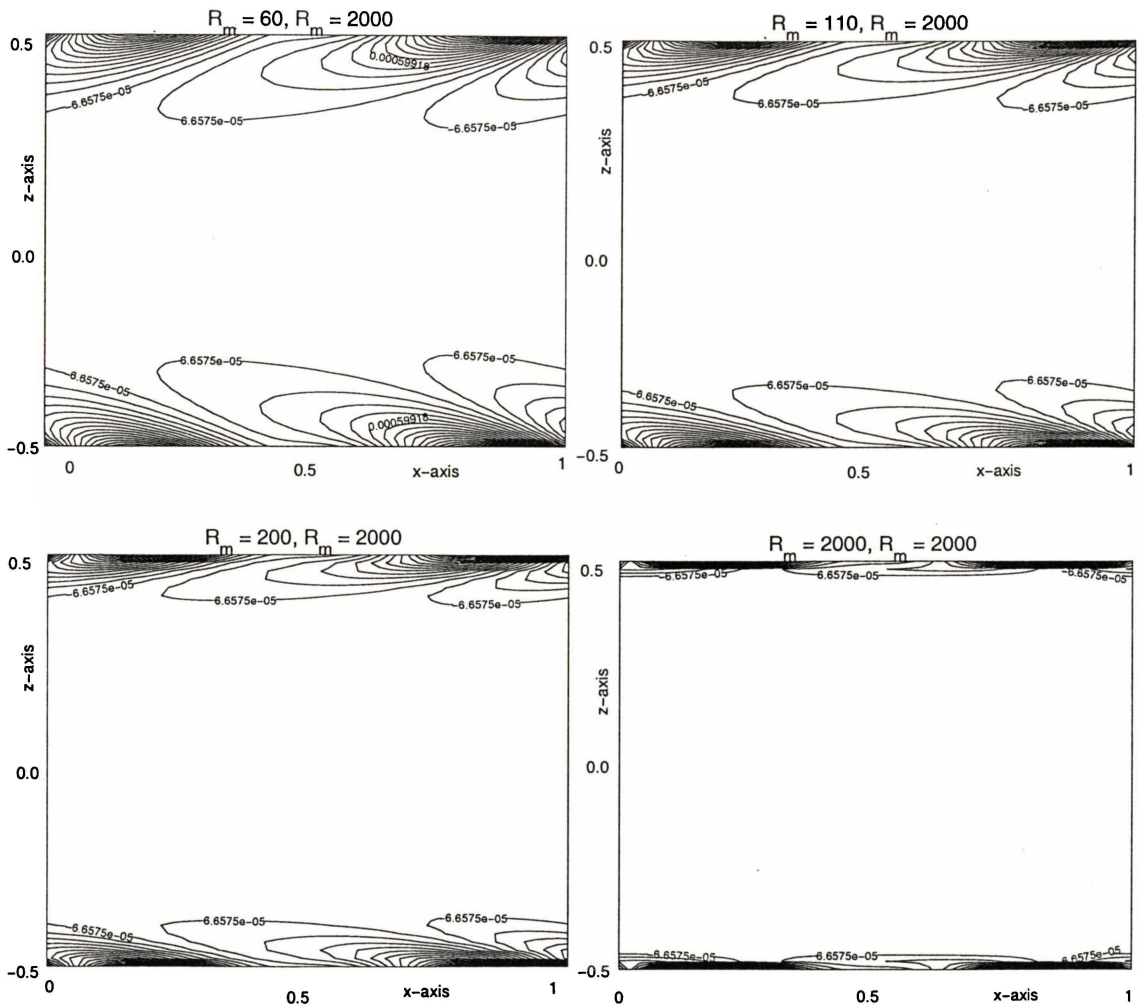

Figure 6.15: Magnetic field lines at steady state showing increasing fieldlines expulsion as magnetic Reynolds number increases from 60 to 2000. Reynolds number is 2000 and $b = [1, 1]$.

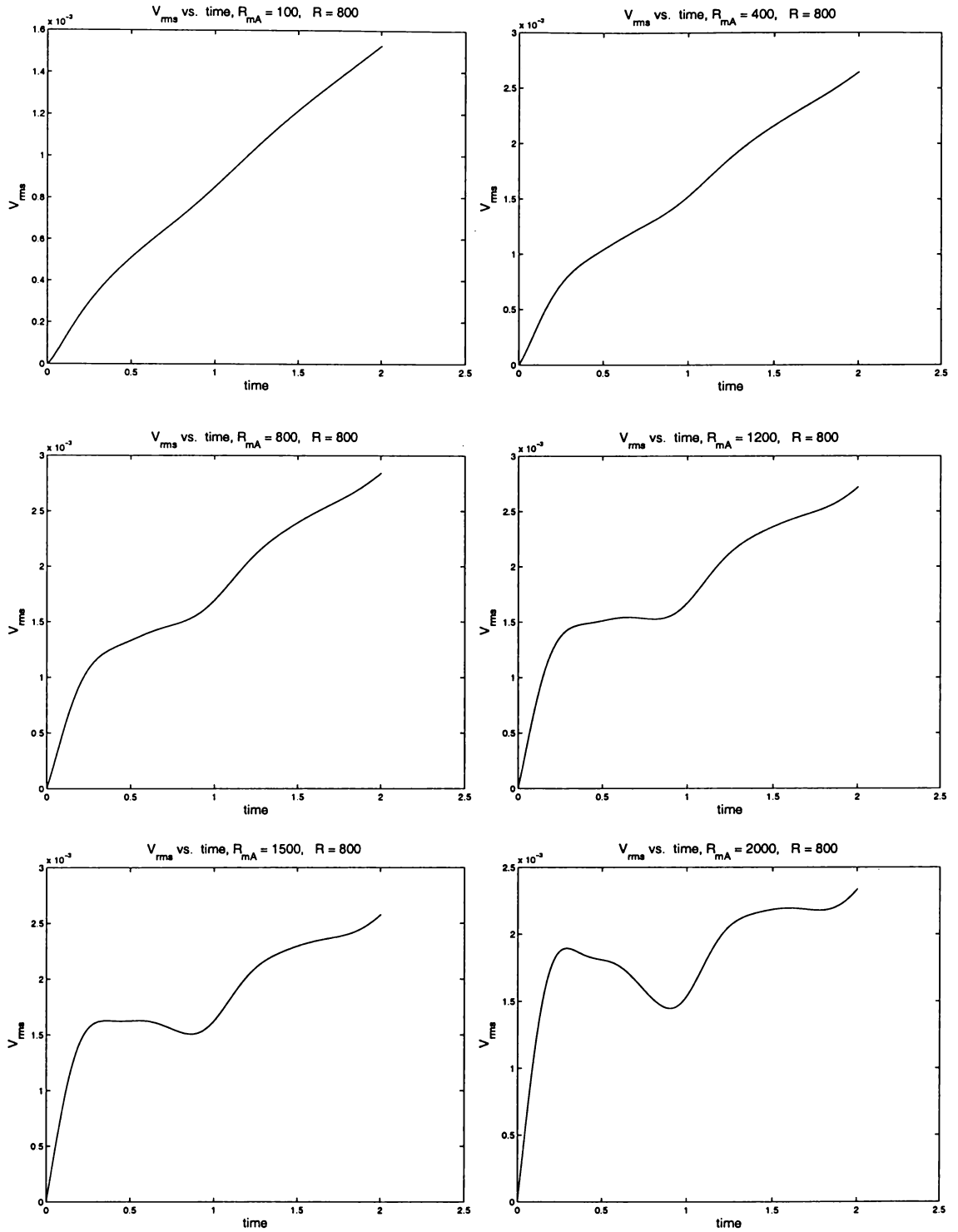

Figure 6.16: Graphs of v_{rms} in the early time at increasing values of R_m and $R = 800$, showing sudden increases in v_{rms} at large R_m.

6.6 Conclusions

The smaller the aspect ratio is the better and stronger will be the magnetic field's penetration. Intermediate $R_m \sim 100$ gives most effective stirring for the case $b_n = [1, 1]$. It is possible to generate two to four pairs of vortices for some combinations of $\boldsymbol{b}$, which means better stirring. We also find that lowering the value of U helps in creating more less-elongated vortices in the flow. In order to avoid a sudden increase of velocity of the fluid it maybe more practical to consider the similar problem but with the velocity of the applied magnetic field increasing gradually. This is to be the subject of the next chapter.

Chapter 7

Effects of time-dependent magnetic field velocity at finite R_m

7.1 Introduction

So far we have assumed that the magnetic field is impulsively started from rest and thereafter moves at a constant speed $U\hat{\boldsymbol{x}}$. In this chapter we consider the effects of a time-dependent magnetic field velocity. For example we could imagine a gradual increase in applied velocity $u_a(t)\hat{\boldsymbol{x}}$, which is then kept constant for a duration, followed by a deceleration until $u_a(t)\hat{\boldsymbol{x}}$ becomes negative. We also investigate the case when the velocity $u_a\hat{\boldsymbol{x}}$ is sinusoidal in time.

As in chapter 6 suppose that the conducting fluid is contained in a channel of infinite length and width, with boundaries $z = \pm a$. The multi Fourier-magnetic field $\boldsymbol{B}$

$$\left(\frac{\partial \phi}{\partial z}\right)_{z=\pm a} = B_0 \sum_{n=1}^{N} b_n \cos[nk(x - u_a(t)\, t)], \tag{7.1}$$

where b_n are constants, is moved at a velocity $u_a(t)\,\hat{\boldsymbol{x}}$ along the channel.

All governing equations in this chapter are the same as in §6.2.1 except for the momentum equation (2.25) which must have a term $-\rho a_c \hat{\boldsymbol{x}}$ to compensate for the force exerted on the fluid particle when the applied magnetic field is given an acceleration. Due to the inertia the fluid tends to stay stationary when the magnetic

field is given the acceleration a_c. (We must remember here that our assumption is we are stationary with respect to the applied magnetic field.)

$$\frac{\partial \boldsymbol{v}}{\partial t} + (\boldsymbol{v} \cdot \boldsymbol{\nabla})\boldsymbol{v} = -\frac{1}{\rho}\boldsymbol{\nabla} p - \rho\, a_c\, \hat{\boldsymbol{x}} + \frac{1}{\rho}(\boldsymbol{J} \times \boldsymbol{B}) + \nu \nabla^2 \boldsymbol{v}, \tag{7.2}$$

But taking the curl of both sides of (7.2) we end up with the same vorticity equation (6.12) since $\boldsymbol{\nabla} \times (a_c \hat{\boldsymbol{x}}) = 0$.

In §7.2 we briefly outline the numerical method used. We consider one example in §7.3 and another in §7.4 to investigate improved methods of stirring.We end with conclusions in §7.5.

7.2 Numerical methods

Here we consider the same problem as in §6.3 but this time the applied magnetic field is initially at rest, so the initial stream function is 0. The initial (magnetic) flux function is

$$\psi(x, z) = -\, B_0 \sum_{n=1}^{N} \frac{b_n}{n k c_n} \cosh(nkz) \sin[nk(x - u_a(t)\, t)], \tag{7.3}$$

where $u_a(0) = 0$.

The main change in the code is that the velocity $u_a(t)$ of the applied magnetic field depends on time.

The current density $J = \nabla^2 \psi$ on the boundaries $z = \pm\, a$ is given by

$$\boldsymbol{J} = -\sigma \boldsymbol{u} \times \boldsymbol{B}, \tag{7.4}$$

or in dimensionless form as

$$J = -R_{mA}\, u\, \frac{\partial \psi}{\partial x}. \tag{7.5}$$

7.3 Example 1

The following terms are used to describe the various stages of the velocity in our first time-dependent field example.

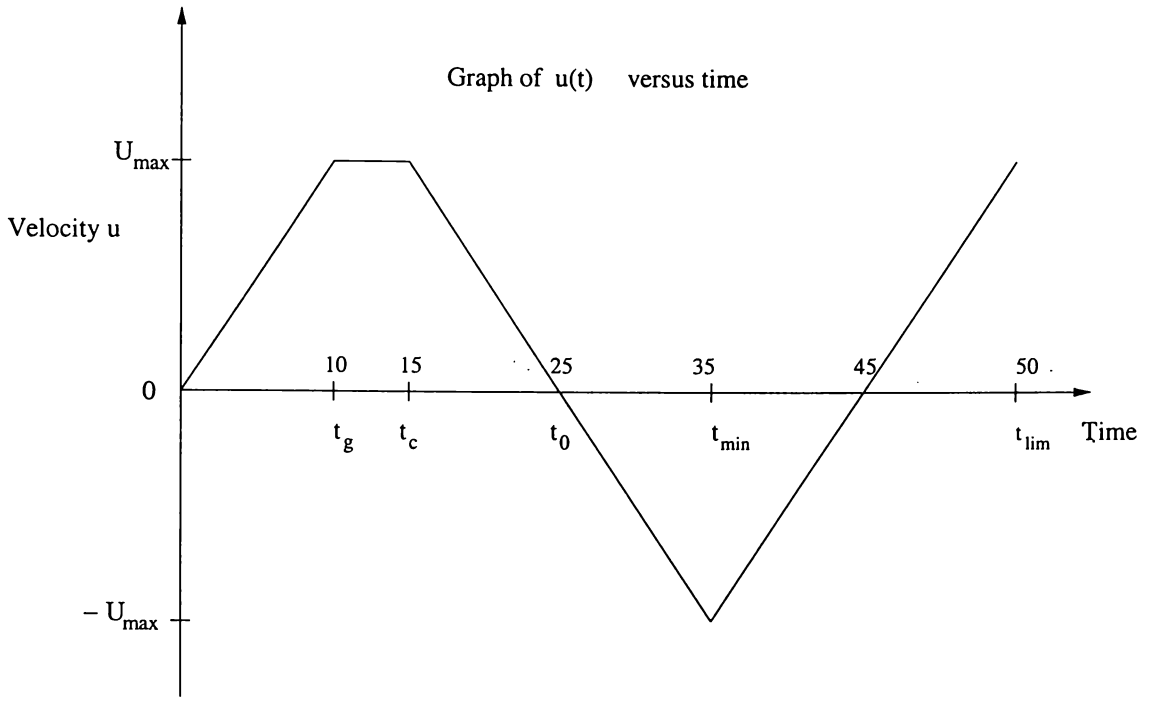

Figure 7.1: Graph of the velocity $u_a(t)\hat{\boldsymbol{x}}$ of the applied magnetic field versus time.

t_g	-	time where the acceleration stops
t_c	-	time where the velocity changes from constant to deceleration
t_0	-	time where the velocity is zero
t_{min}	-	time where the velocity is a minimum
t_{lim}	-	time where the calculation stops.

Since we are interested in instances where there is good and effective stirring we will limit our investigations to only one example that creates two pairs of vortices:

$$\boldsymbol{b} = [1.1 \;\; 0.8 \;\; 0.0 \;\; 2.0 \;\; 0.1 \;\; 2.6 \;\; 0.1 \;\; 2.5 \;\; 0.1 \;\; 2.5].$$

In all investigations of this chapter we will set the following parameters as :

$U_{max} = V_A$, $R_A = R_{mA} = 800$ and the region is $[0, 1] \times [-0.25, 0.25]$, unless mentioned otherwise.

Two main stages will be considered. The applied magnetic field's velocity follows the graph of $u_a(t)$ as a function of time t (figure 7.1) in both stages.

7.3.1 Stage I: $0 \leq t \leq t_c$

For our first calculation we use the $u_a(t)$ shown in figure 7.1. From figure 7.2 we see that v_{rms} increases gradually from 0 and still is increasing slowly even at $t = 15$. Here because of the gradual increase we avoid the impulsive increase in velocity (or high acceleration) as faced in fluid flow in chapter 6. It is interesting to note that eddies are being formed from the moment the magnetic field begins to move, (figure 7.3). The eddies are convected away from the boundaries and diffuse away within a time of 0.6 of t_g (figure 7.4). This may be explained by figure 7.5 at $t = 6$: some magnetic field lines detach from the boundaries to form closed loops in the middle of the channel.

At the end of this stage the magnetic field lines have been broken and swept to the channel walls leaving a thin layer of magnetic field lines on the boundaries; also the vortices have diffused away and streamlines are almost straight.

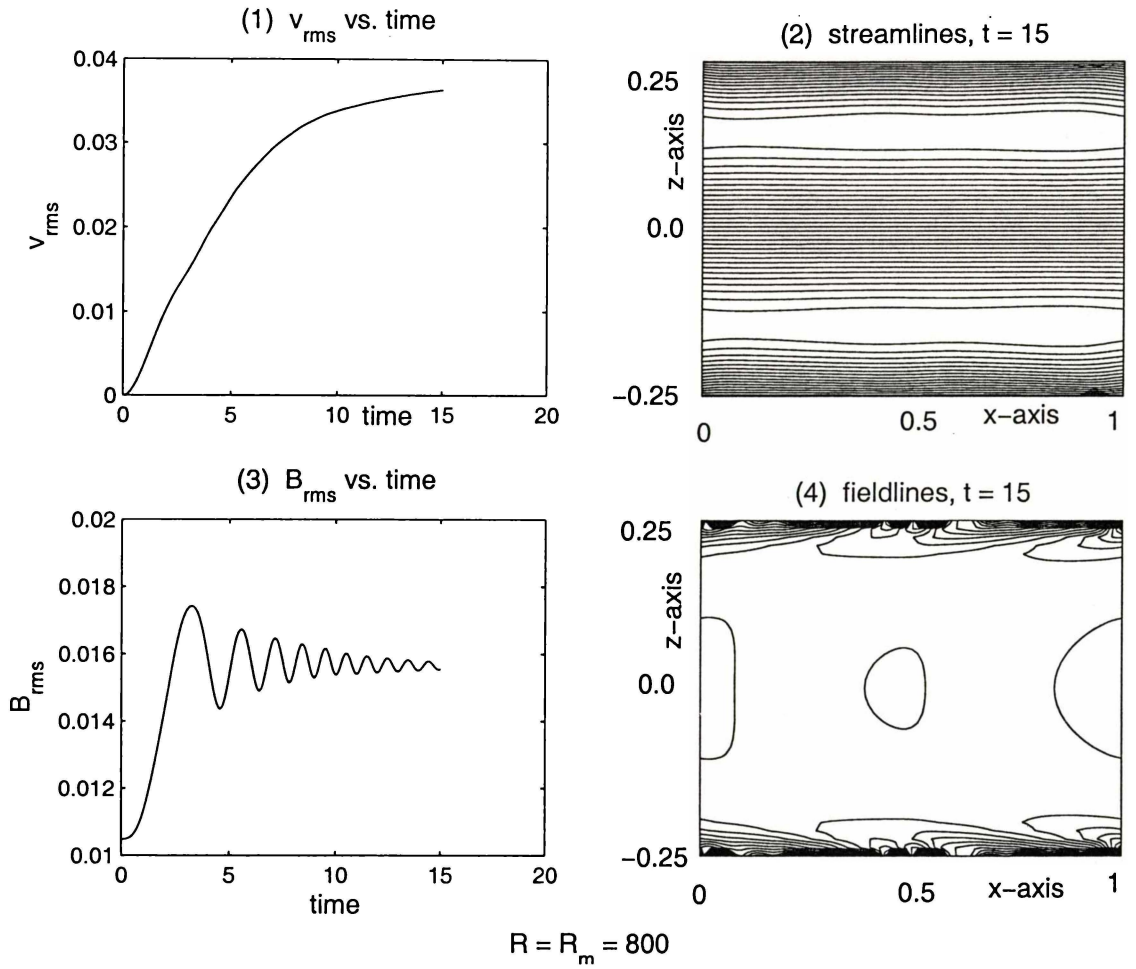

Figure 7.2: (1) v_{rms} as a function of t, (2) streamlines at $t = 15$, (3) B_{rms} versus time, (4) magnetic field lines at $t = 15$. The velocity $u_a(t)$ remains constant starting from $t = 10$.

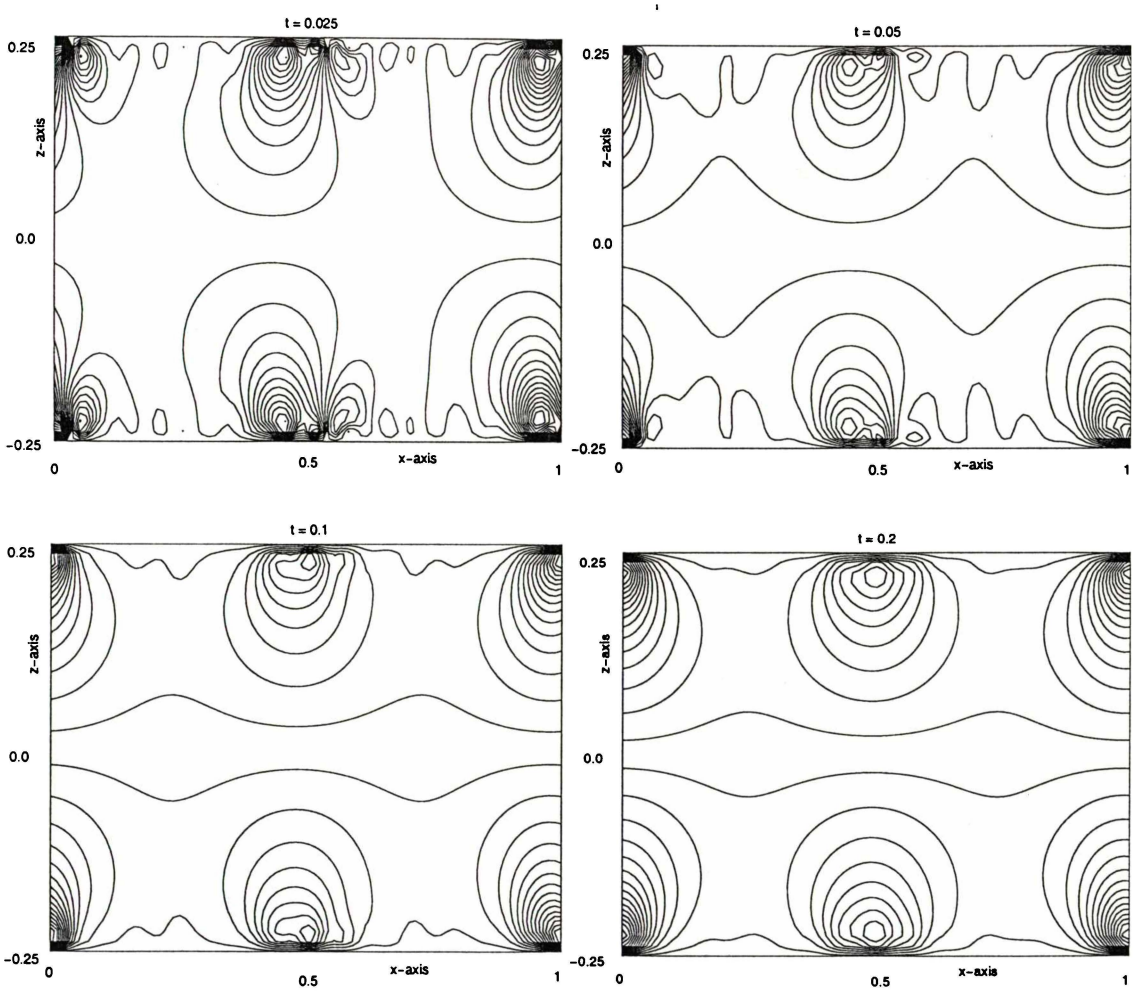

Figure 7.3: Formation of eddies as the magnetic field accelerates, $R = R_m = 800$.

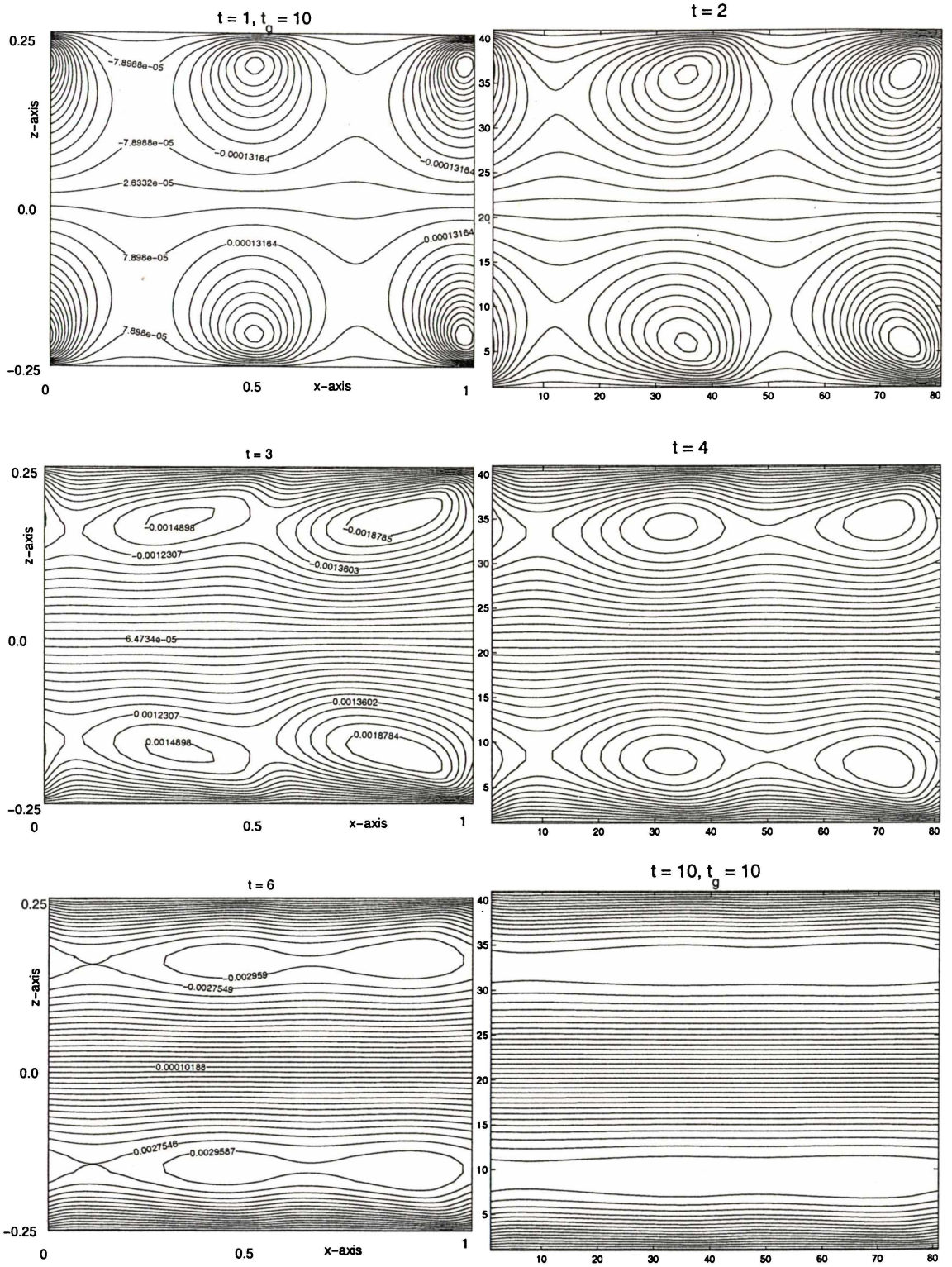

Figure 7.4: Evolution of streamlines from $t = 1$ to $t = 10$, $R = R_m = 800$. The rectangular region is $[0, 1] \times [-0.25, 0.25]$.

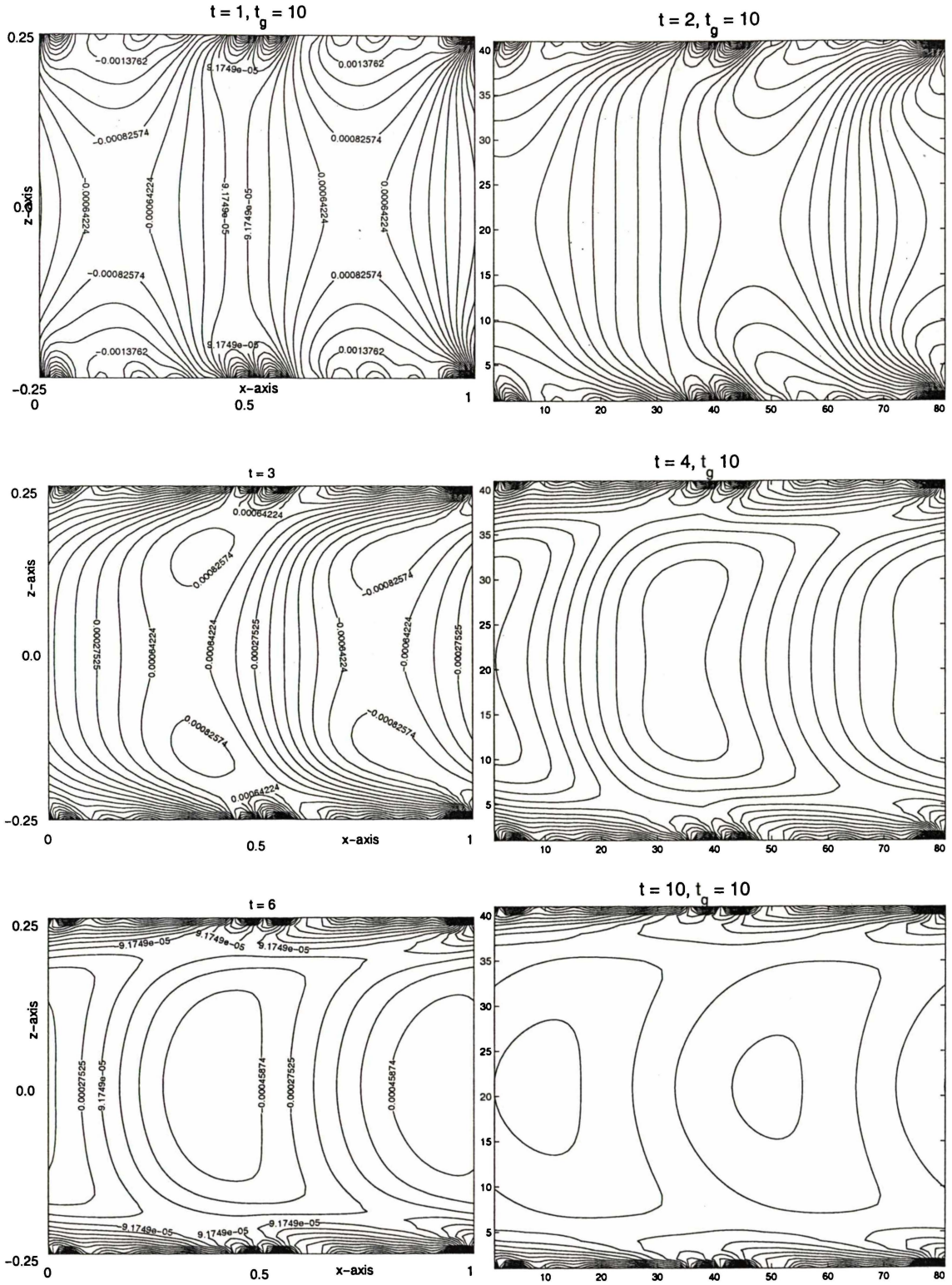

Figure 7.5: Evolution of magnetic field lines for $t = 1$ to $t = 10.$, $R = R_m = 800$. The rectangular region is $[0, 1] \times [-0.25, 0.25]$.

7.3.2 Stage II: $t_c \leq t \leq t_{min}$

During this stage the velocity $u_a(t)$ of the applied magnetic field decreases under a deceleration (whose magnitude equals the acceleration in stage I) until $u_a(t) = -U_{max}$. The evolution of streamlines from $t = t_c$ until $t = t_{min}$ is given in figures 7.10 and 7.11. The change of direction of the applied magnetic field takes place after $t = 25$ in figures 7.6 and 7.14. The applied field is momentarily at rest at $t = 15$. This is also the time when B_{rms} is a minimum but this does not imply a simultaneous drastic change in the flow pattern. There is a delay of about 3.5 time units of time before the flow pattern starts to change significantly. Also, picture (1) of figure 7.6 shows that it takes the fluid $\sim$ 3.5 units of time to decelerate to the minimum value of v_{rms}. This is an example of using magnetic field to "brake" the motion of a fluid. The force generated by the acceleration of the field between $t = 25$ to $t = 28.5$ slows down the fluid motion so that v_{rms} decreases to its minimum value. It is also important to note that it is during this delay that two new pairs of vortices are generated as shown in figures 7.10 and 7.11. The two new pairs of vortices become stronger and are convected away from the boundaries while the two old pairs diffuse away in the central region of the channel as the fluid velocity increases. With time, more of the central field lines are broken and swept away by the flow leaving magnetic field layers which decrease in thickness on the boundaries.

It is also interesting to note that the magnetic field loops on the boundaries are inclined in the direction of the central flow, which is opposite to the direction of the field as can be seen from figure 7.7. During the deceleration stage from $t = 15$ to $t = 25$, (figures 7.12 and 7.13) the magnetic field lines penetrate further into the central region but become less inclined in the flow direction. After the velocity of the applied magnetic field changes sign the field lines penetrate deeper especially between $t = 25$ and $t = 28$ but are swept to right, in the direction of the new flow.

The velocity vector diagrams of the flow from $t = 25$ to 30, as can be seen from figures 7.14 to 7.18, provide a good picture on the direction of the streamlines and the sense of the eddies turning. When the applied field is momentarily stationary at

$t = 25$ the fluid topology continues briefly in its momentum before it commences to change. So far all flow have these three characteristics: 1. The flow which is close to the boundaries (which we call boundary flow) is always in the direction of the field due to the frozen-in effects especially at high R_m. 2. The central flow is opposite to the velocity of the applied field, and 3. The vortices, if there is any, come in pairs and are always opposite—one is clockwise, the other is anti-clockwise. During the delay time of ≈ 3.5 time units we can see that two new vortex pairs are being created and the old two pairs diffuse away. At $t = 28$ of figure 7.16 as the two new eddies pair become more intense two new region of flow are generated which are in the opposite direction of the applied field. The old central region is still flowing in the previous direction which is now the direction of the applied field but is losing momentum due to viscosity. It can be seen that at $t = 29$, there is hardly any flow in the central region of the channel. The diffusion of the two old vortex pairs results in the onset of the central fluid flowing in the opposite direction of the applied field (figure 7.18).

Sensivity of the results to the size of the mesh

The relatively narrow magnetic boundary layers may give rise to problems in resolution. In order to verify the resolution of the calculation we recalculate the bottom diagram of figure 7.7 with grids of increasing refinement. It can be seen from figures 7.8 and 7.9 that the shape of the fieldlines does not change significantly.

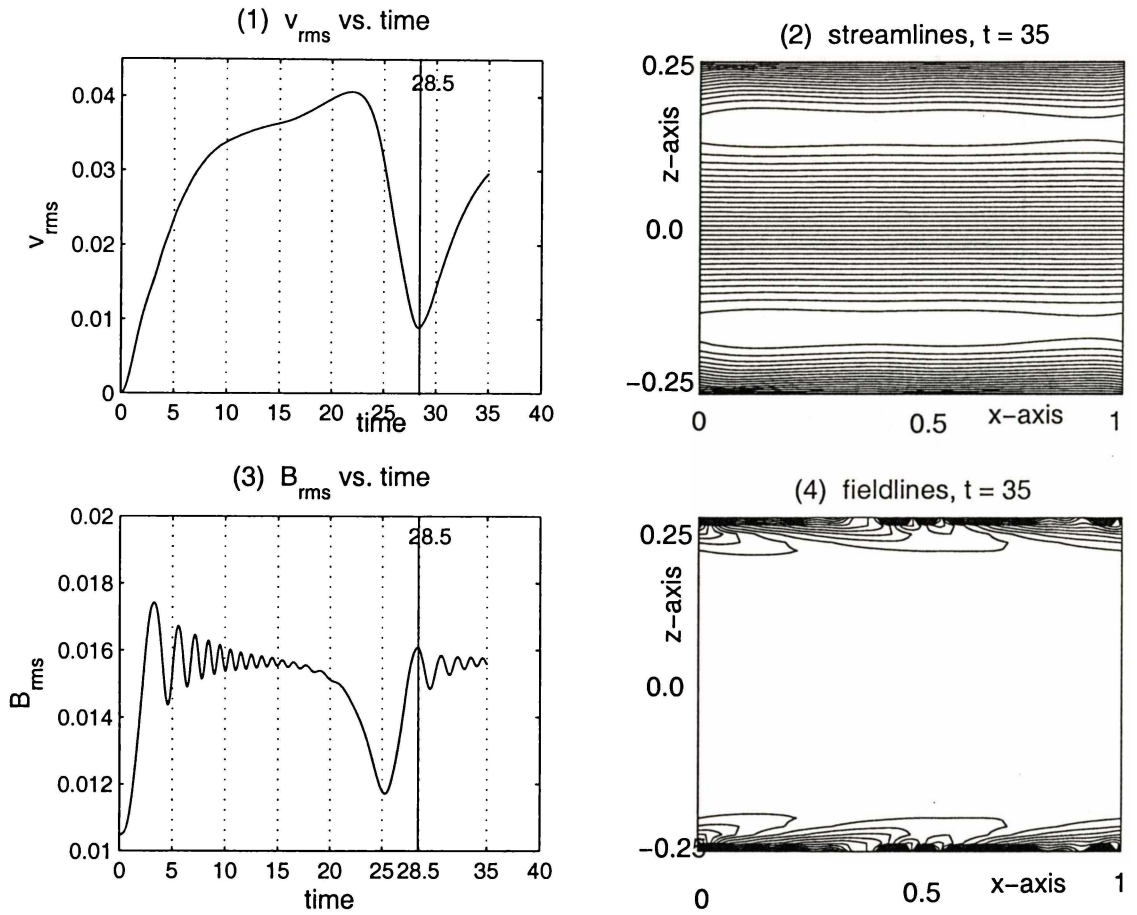

Figure 7.6: (1) v_{rms} vs. time, (2) streamlines, $t = 35$, (3) B_{rms} vs. time, and (4) fieldlines at $t = 35$, where $t_g = 10, t_c = 15$.

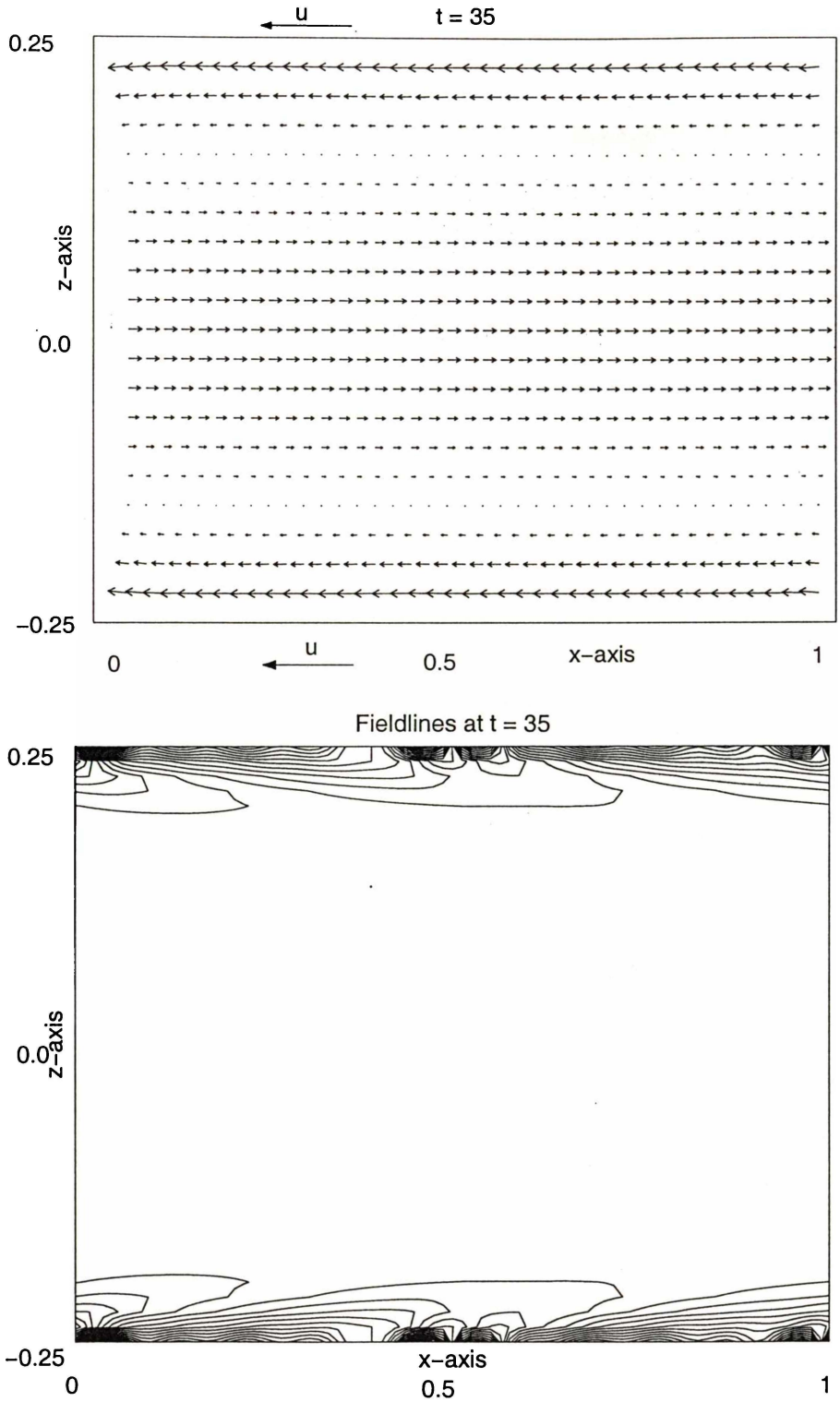

Figure 7.7: Top: Velocity vectors at $t = 35, R = R_m = 800$ for partition 40 by 20 to show the arrows clearly. The corresponding streamlines are given by diagram (2) of figure 7.6. The velocity of the applied magnetic field is $\boldsymbol{u}$ in the direction of the arrow, and $v_{rms} = 0.00918V_A$. Bottom: The field loops on the boundaries are inclined in the direction of the flow of the central section for partition numbers 80 by 40 and at $t = 35$.

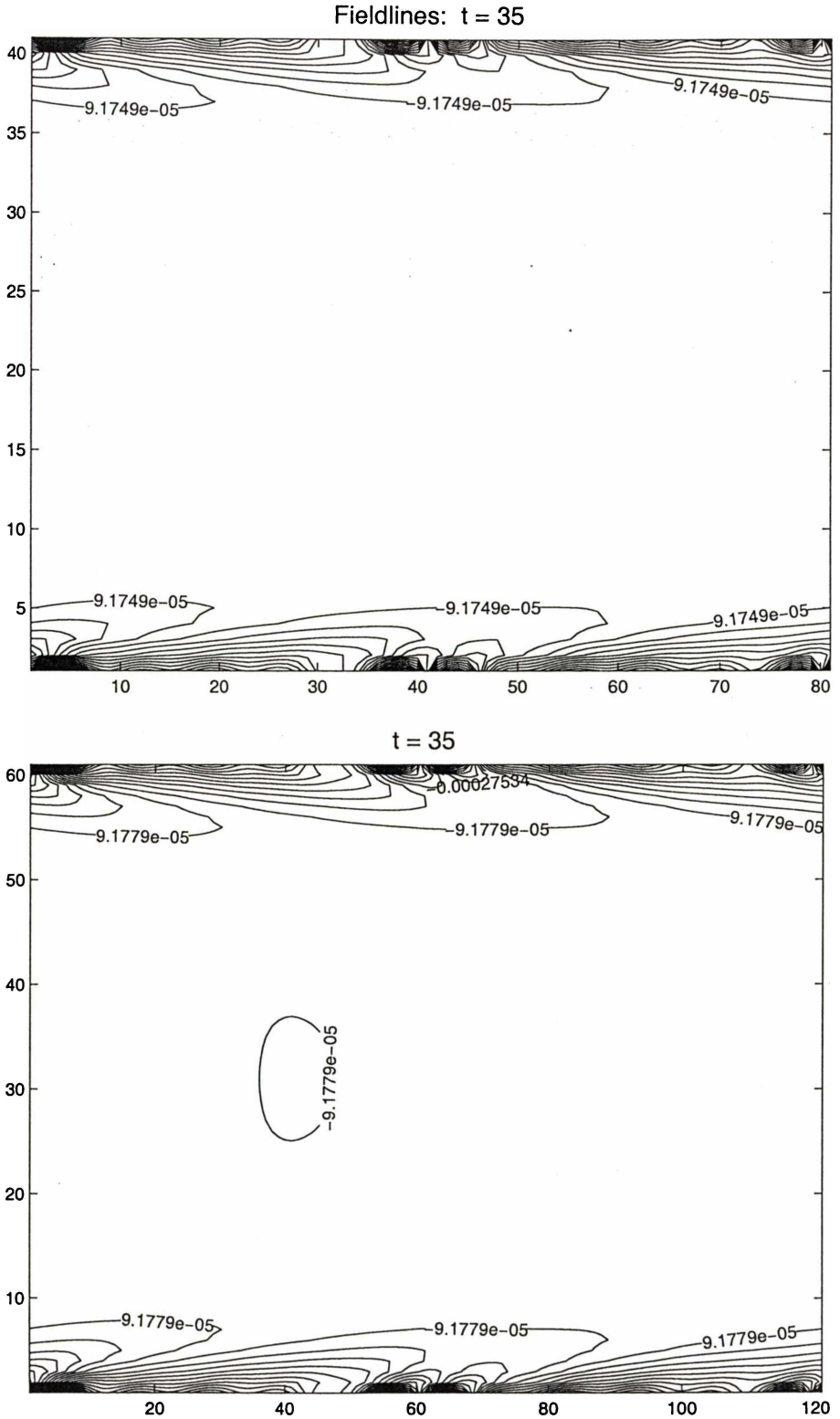

Figure 7.8: Fieldlines for resolutions of 80 *by* 40 *and* 120 *by* 60.

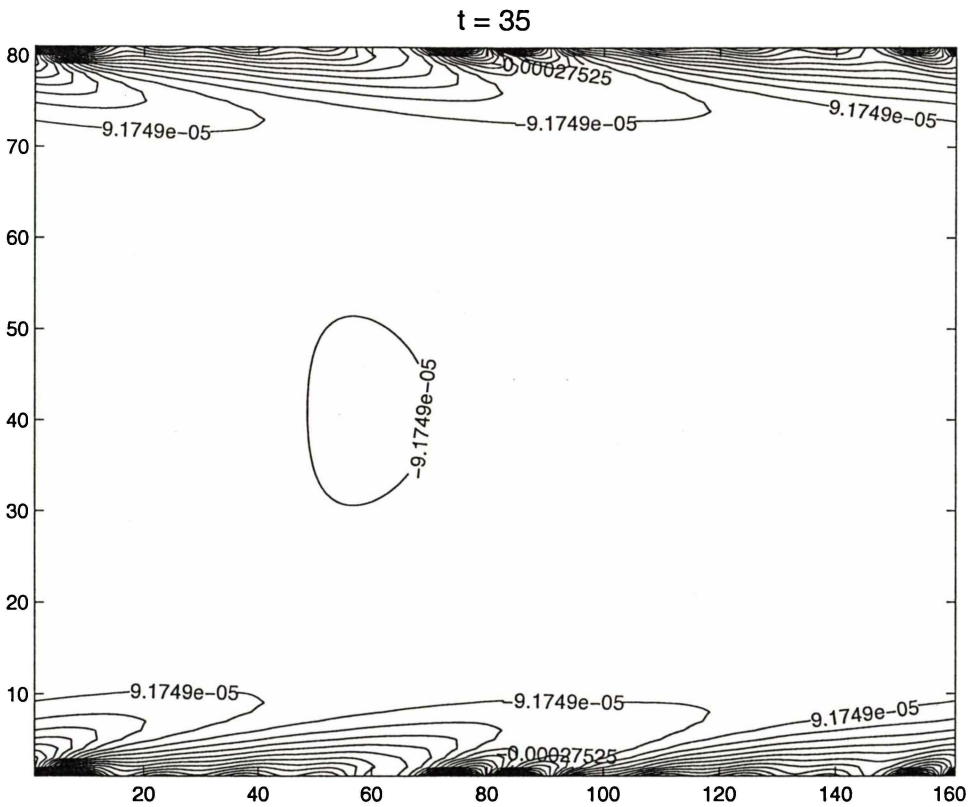

Figure 7.9: Fieldlines for resolution of 160 *by* 80.

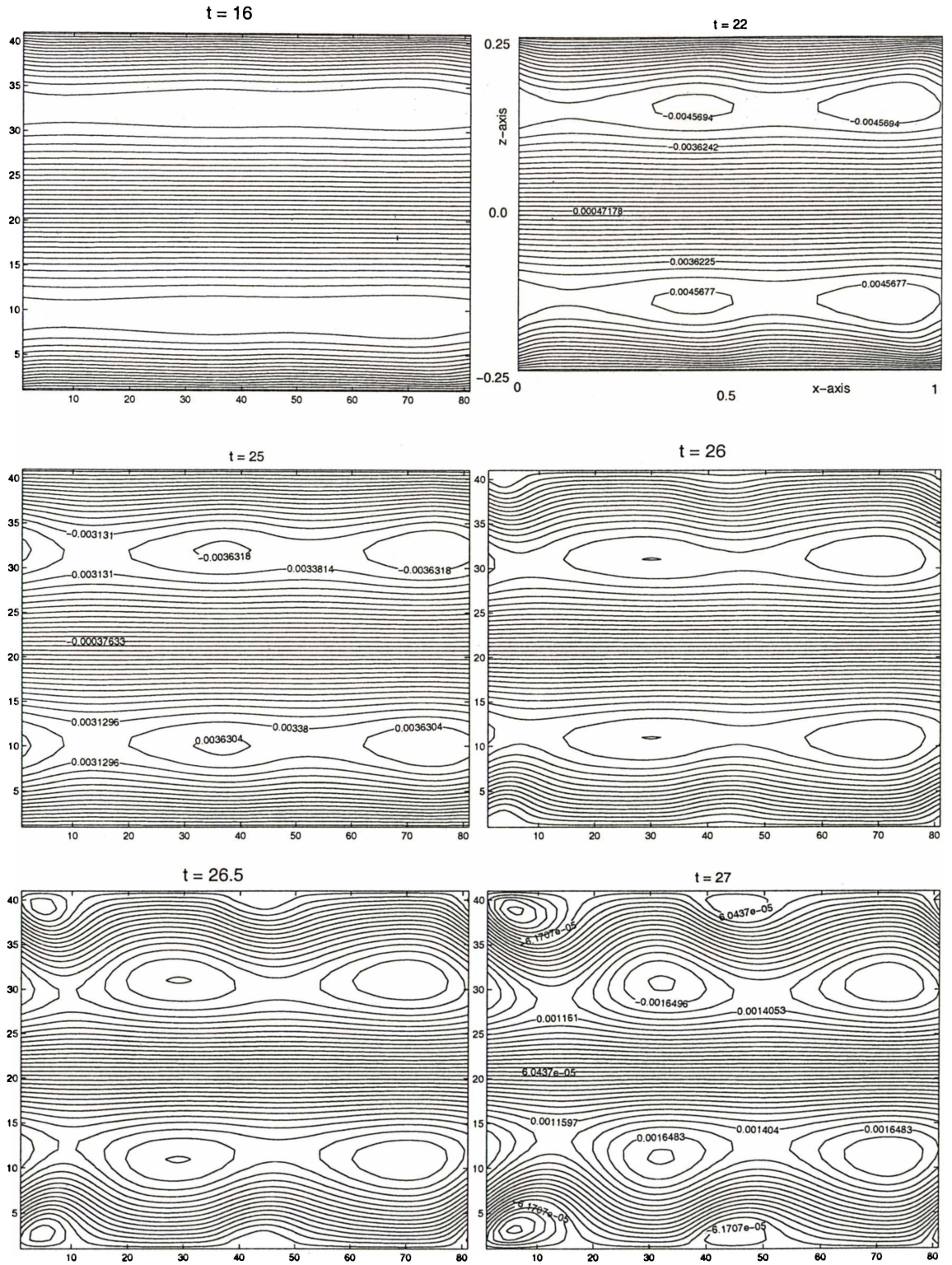

Figure 7.10: Evolution of streamlines from $t = 16$ to $t = 27$, where $t_c = 15, t_0 = 25$, during stage 2.

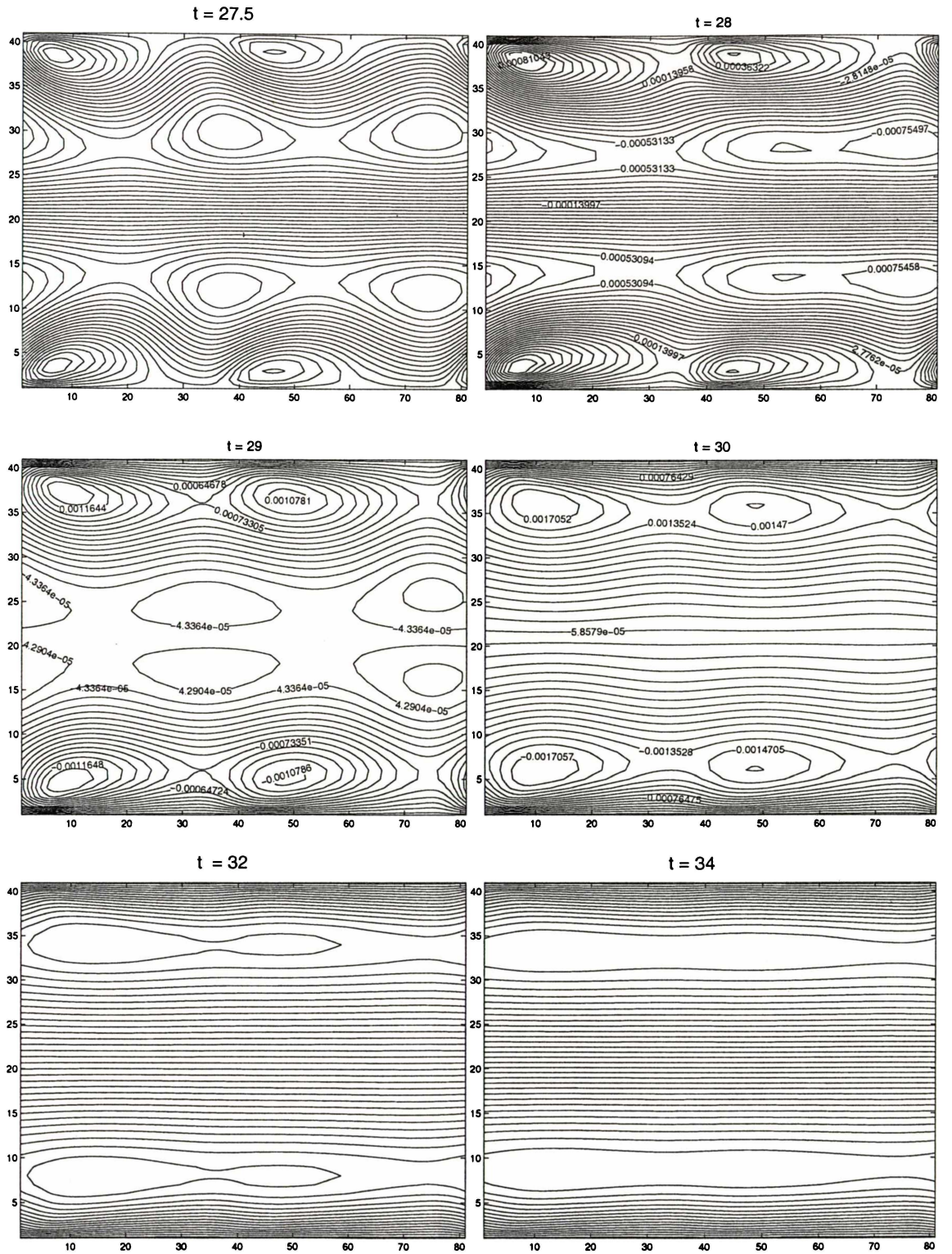

Figure 7.11: Continuation from figure 7.10, of evolution of the streamlines from $t = 27.5$ to $t = 34$ during negative deceleration, where $t_{min} = 35$.

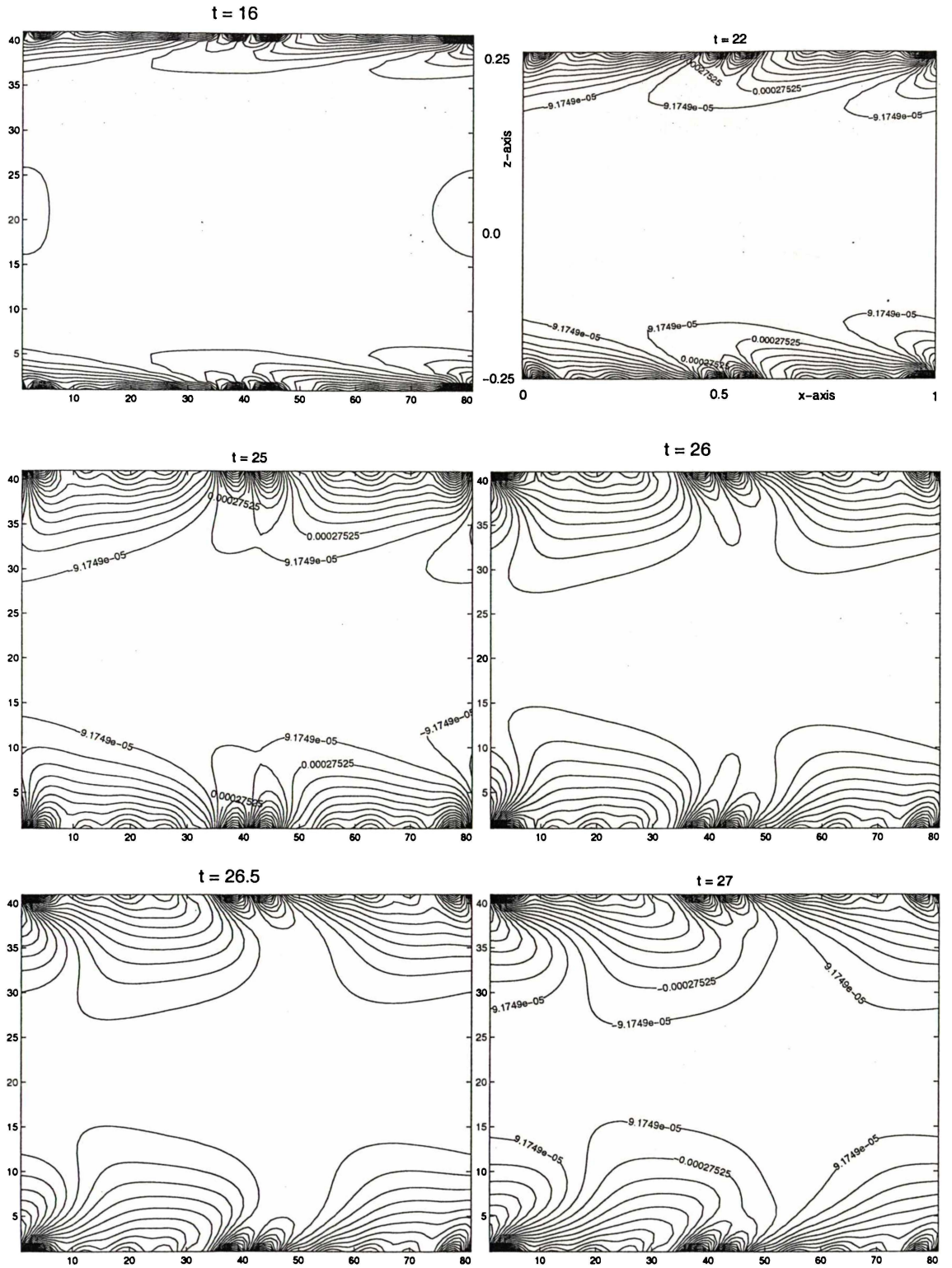

Figure 7.12: Evolution of fieldlines from $t = 16$ to $t = 27$, where $t_c = 15, t_0 = 25$, during stage 2.

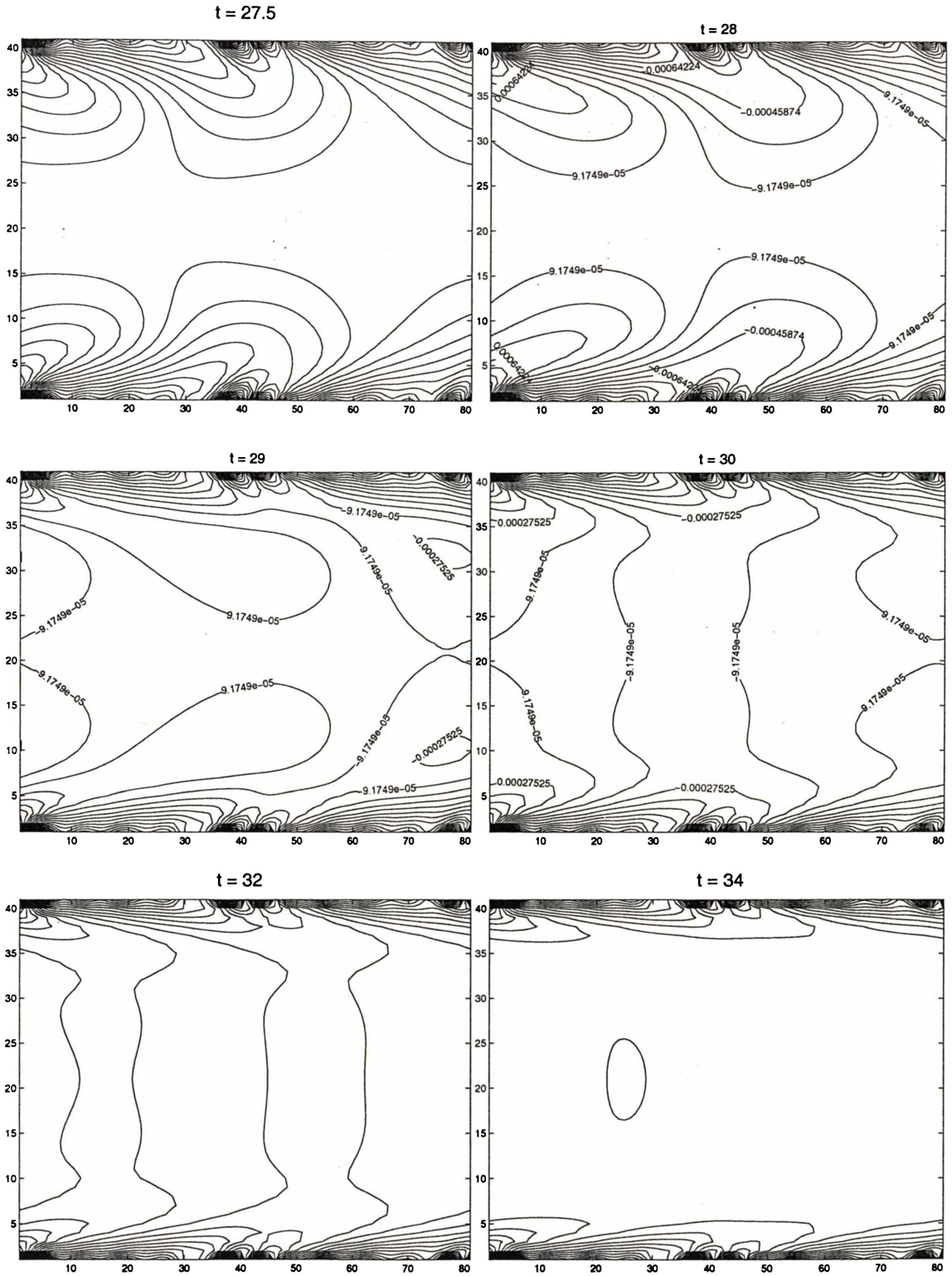

Figure 7.13: Continuation from figure 7.12, of evolution of fieldlines from $t = 27.5$ to $t = 34$ where $t_{min} = 35$, during negative deceleration.

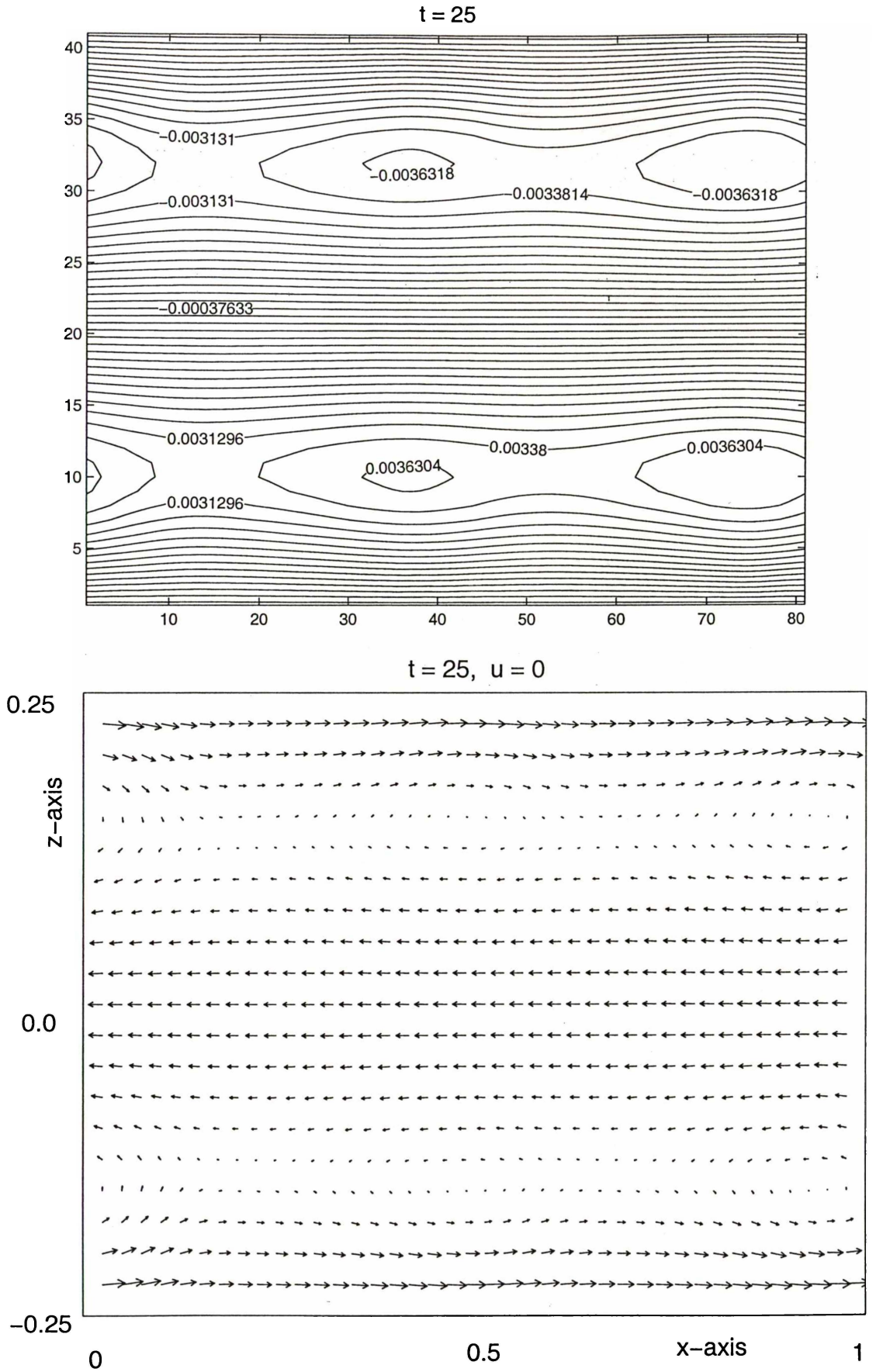

Figure 7.14: Top: Streamlines, and Bottom: Velocity vectors at $t = 25, R = R_m = 800$, *for partition of* 40 *by* 20. *The velocity of the applied field is 0 at this instance. It is about to move in the reverse direction i.e. to the left.* $v_{rms} = 0.0136 V_A$.

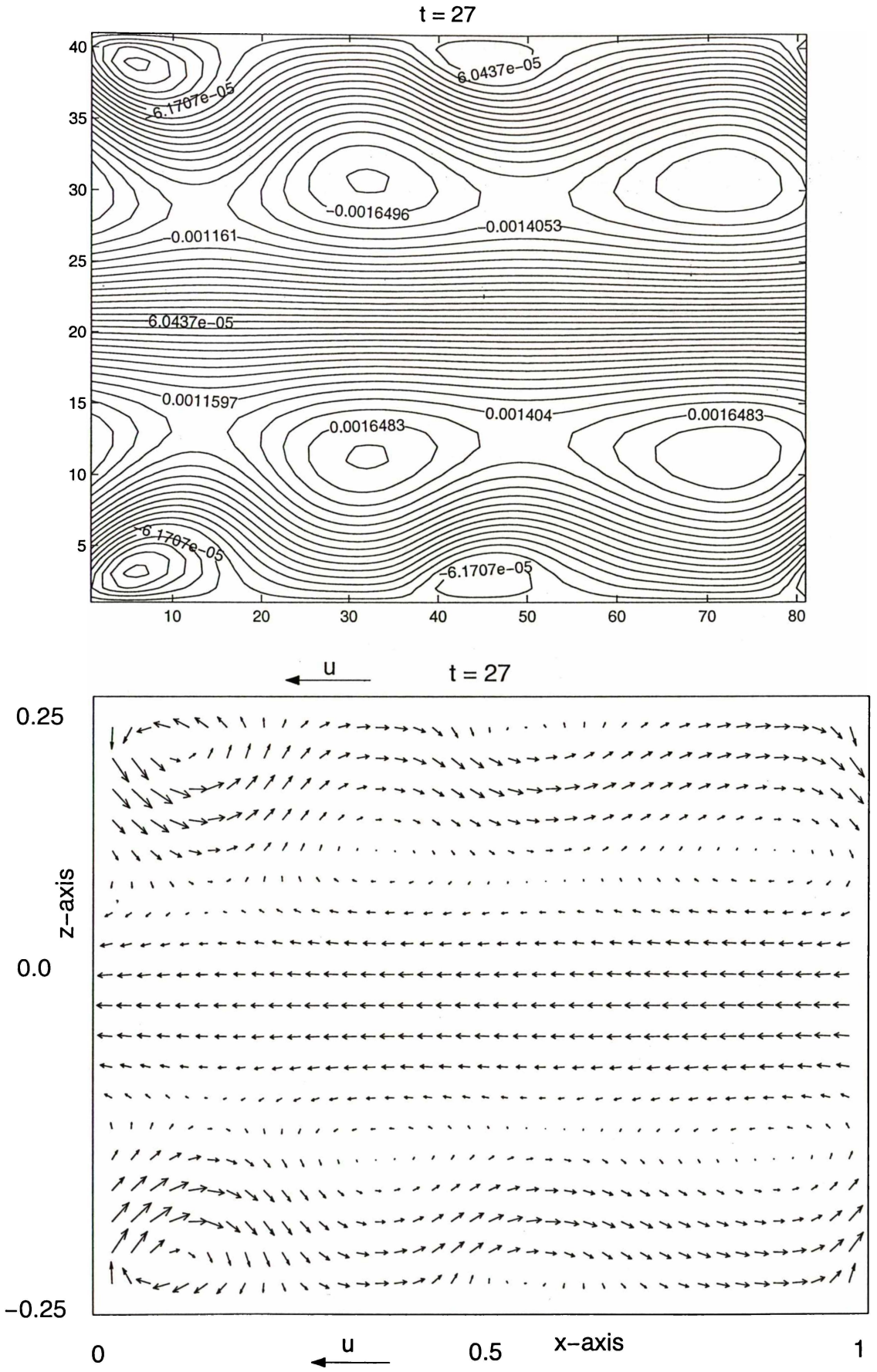

Figure 7.15: Top: Streamlines, and Bottom: Velocity vectors at $t = 27, R = R_m = 800$, *for partition of* 40 *by* 20. *The applied field moves at speed* u *in the direction of the arrow.* $v_{rms} = 0.00631 V_A$.

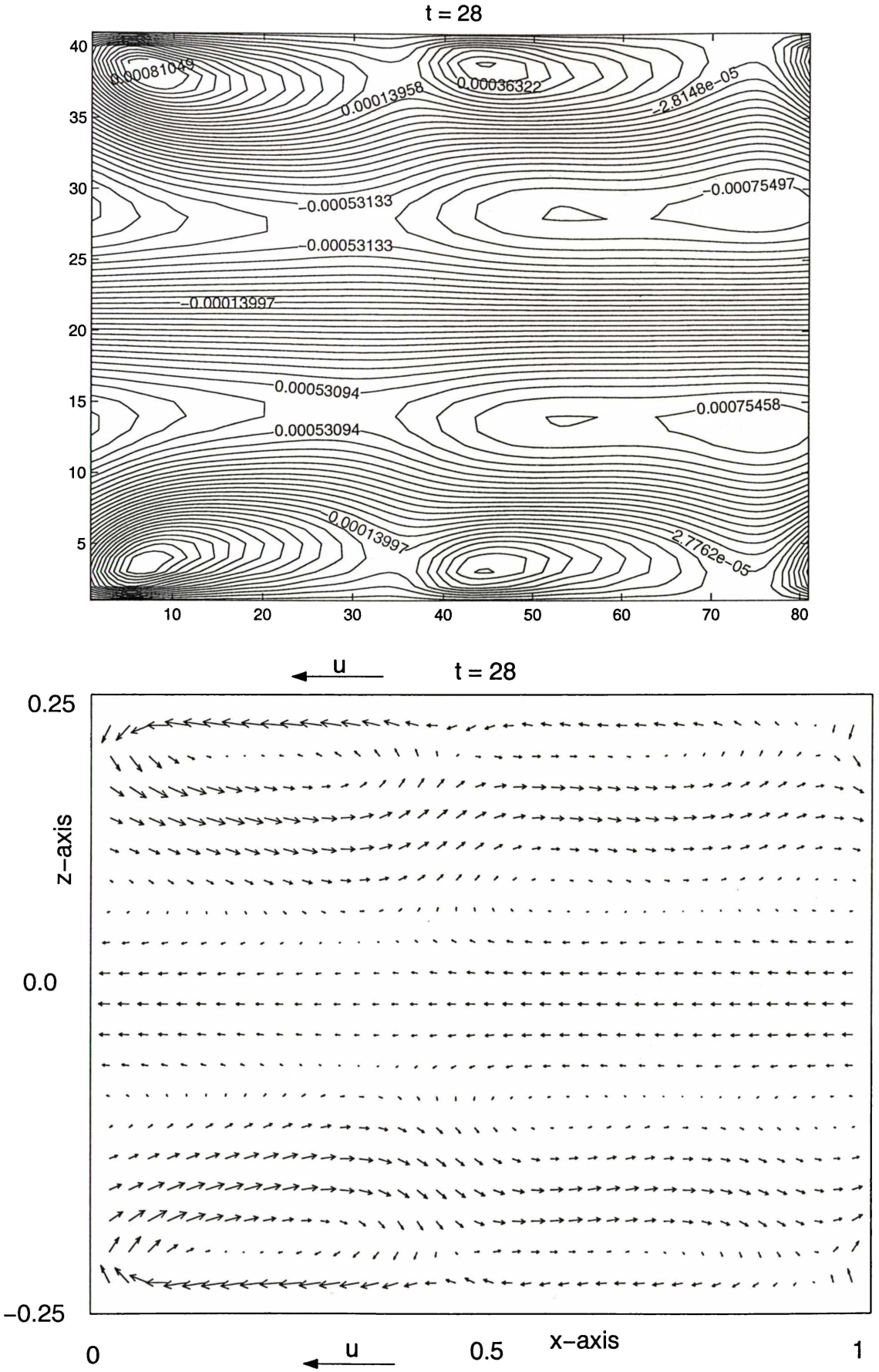

Figure 7.16: Top: Streamlines, Bottom: Velocity vectors at $t = 28, R = R_m = 800$. $v_{rms} = 0.00382 V_A$.

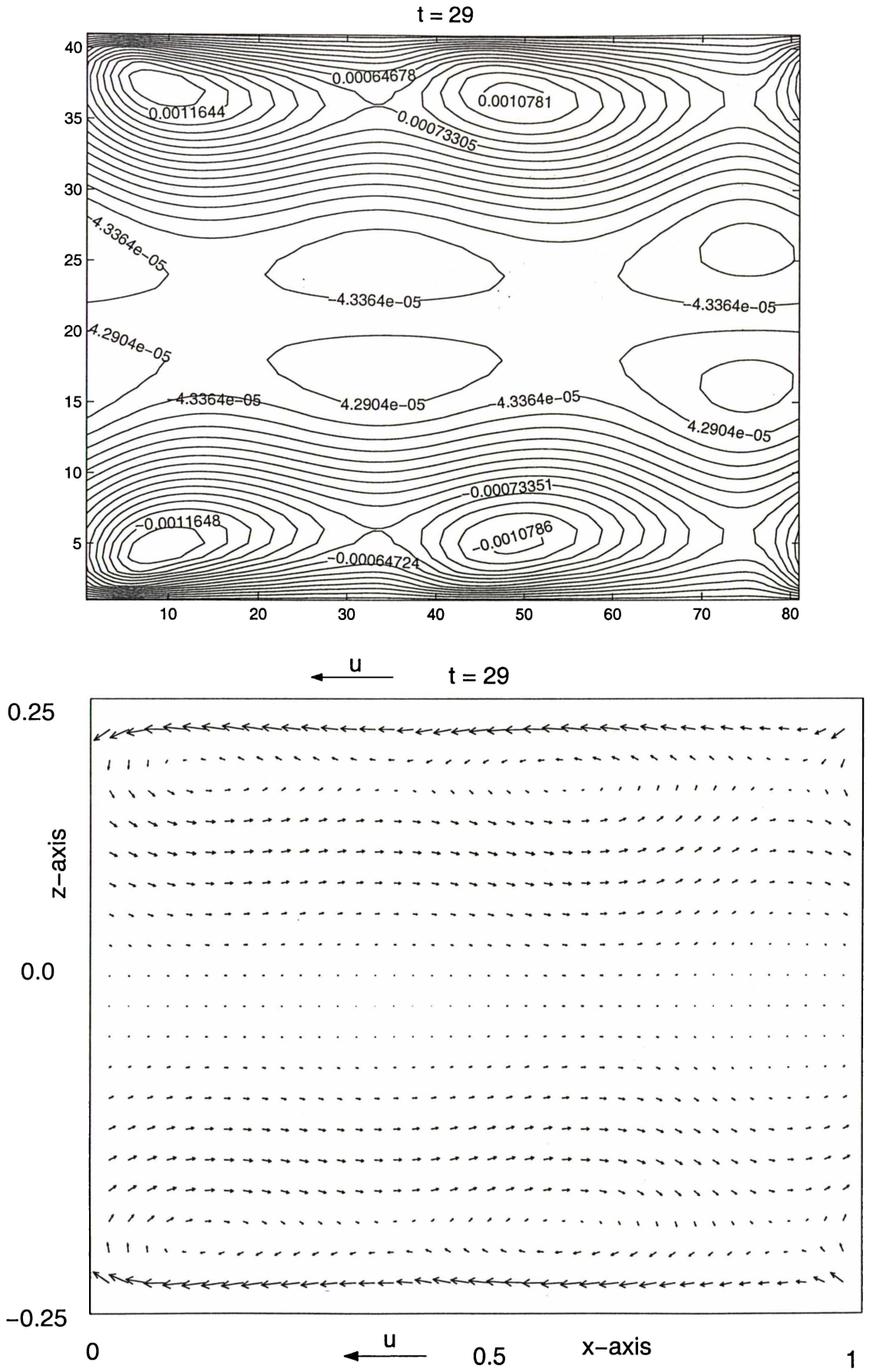

Figure 7.17: Top: Streamlines, Bottom: Velocity vectors at $t = 29, R = R_m = 800$. $v_{rms} = 0.00429 V_A$.

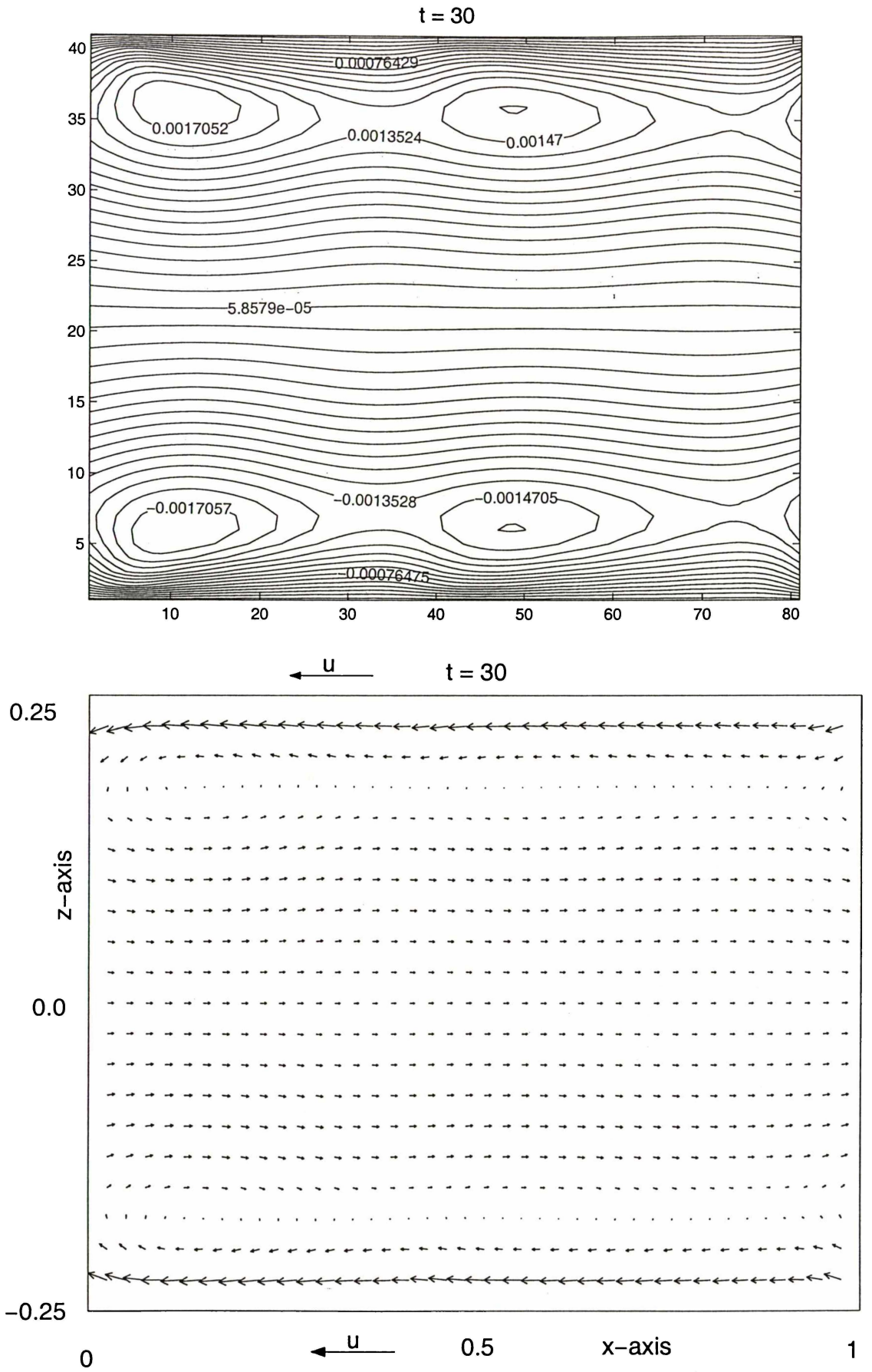

Figure 7.18: Top: Streamlines, Bottom: Velocity vectors at $t = 30, R = R_m = 800$. $v_{rms} = 0.00572 V_A$.

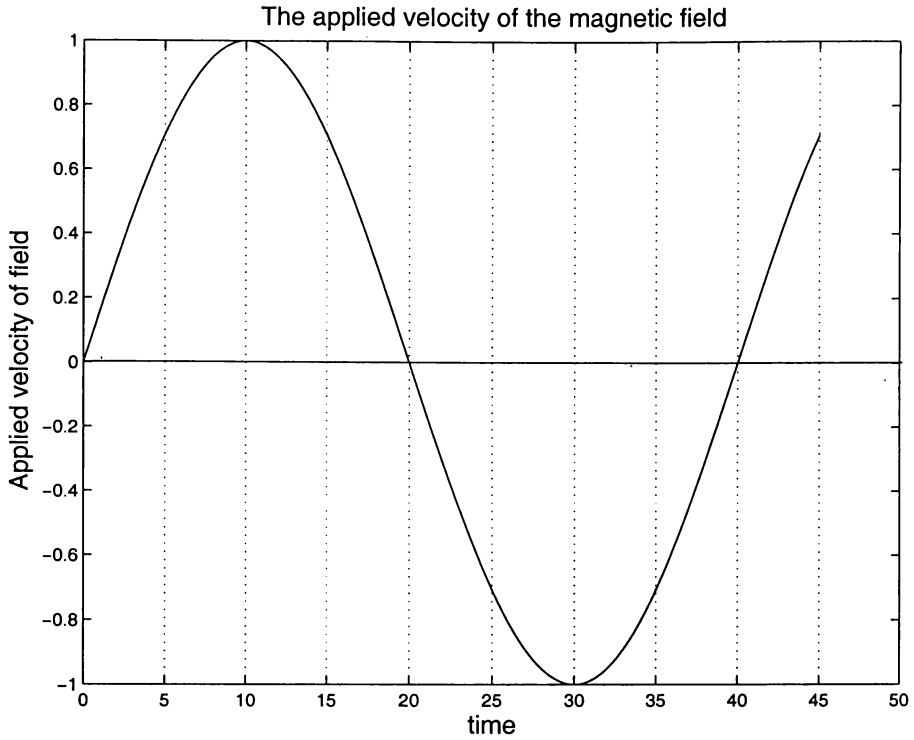

Figure 7.19: Graph of $u = \sin(\pi t/20)$, *wave period,* $\lambda = 40$.

7.4 Example 2

As in Case II of example 1 the most intense stirring occurs when there is a change in direction of the velocity. Here we introduce a field velocity that is sinusoidal in time. Consider

$$u = \sin(2\pi t/\lambda), \tag{7.6}$$

where λ is the wave period. Here we let $\lambda = 40$, to be comparable with the period of example 1. A graph of $u_a(t)$ is shown in figure 7.19. We study the evolution of the flow and magnetic field lines for first 60 units of time.(Figure 7.20).

The evolution of the streamlines during acceleration and deceleration stages for $t = 1$–25 is given by figures 7.21 and 7.23. The corresponding magnetic field lines during the same acceleration and deceleration stages are given by figures 7.22 and 7.24.

Initially vortices are more well-formed and less elongated. They start to diffuse away after $t = 5$, (figure 7.21), at which time the field has travelled only about one

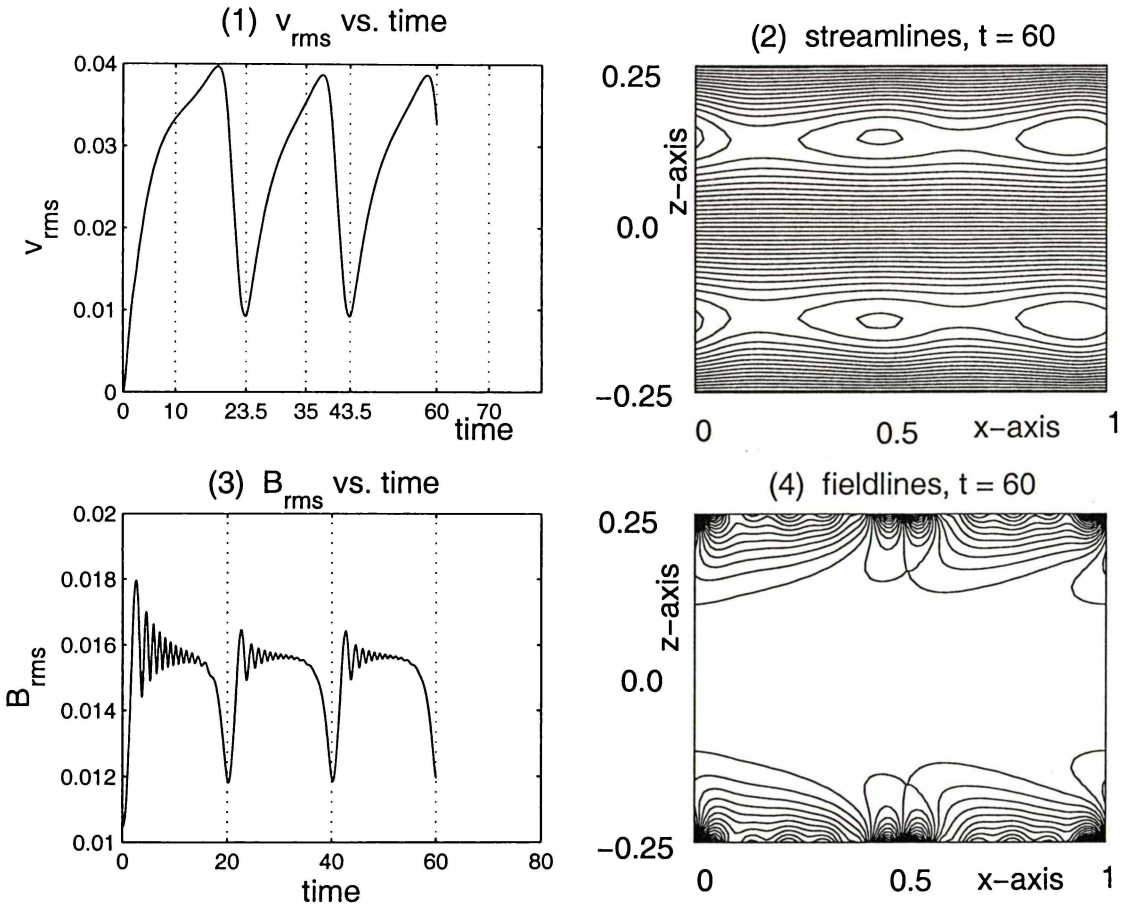

Figure 7.20: (1) v_{rms} as a function of time, (2) streamlines at $t = 60$, (3) fieldlines at $t = 60$, and (4) B_{rms} as a function of time.

eighth of the wavelength.

From the graph of B_{rms} as a function of time (figure 7.25) , we can see that the minimum values of B_{rms} occur at the times $t = 20,\ 40,\ 60$, i.e. when the velocity of the applied magnetic field changes in direction. As in stage II of Example 1, there is a delay of around ≈ 3.5 units of time for the v_{rms} to reach the minimum value. From the streamlines at $t = 21$ to $t = 24$ (≈ 3.5 units of time) of figure 7.23 we can notice that two more pairs of vortices, originating from the boundaries, are being formed and finally "dominate" (i.e. become stronger) while the other two pairs diffuse away. We can also see that the magnetic field lines on the boundaries change direction according to the central flow direction.

Since the most intense stirring takes place around the time when the velocity changes in direction it seems stirring would be enhanced by making the period of the applied field (7.6) shorter. We increase the rate of new vortex pair generation when we increase the frequency of the applied magnetic field. New vortex pairs appear every 20 time units in the case of period = 40. We can safely conclude that new vortex pairs appear every $\frac{1}{2}$ of the period of the applied velocity $u_a(t)$, but this also means decreasing value of the average of the steady state maximum and the minimum of v_{rms}. As shown by the graph of the figure 7.27 the average of the steady state maximum and the minimum v_{rms} decreases as the frequency of the simple harmonic motion increases.

It is possible to produce at least 3 pairs of vortices, as in chapter 6. Four pairs can be produced by $\boldsymbol{b}$ = [20.1 0.1 0.0 0.1 40.1 0.1 0.1 0.1 40.1 0.1], (figure 7.28). The value of v_{rms} is 0.1, which is 10% of U_{max} which should be effective for stirring.

Up to now we have been inferring that more vortices or higher values of v_{rms} lead to better mixing. However we do not see an easy way of measuring the level of mixing or stirring apart from what has been done so far in this investigation.

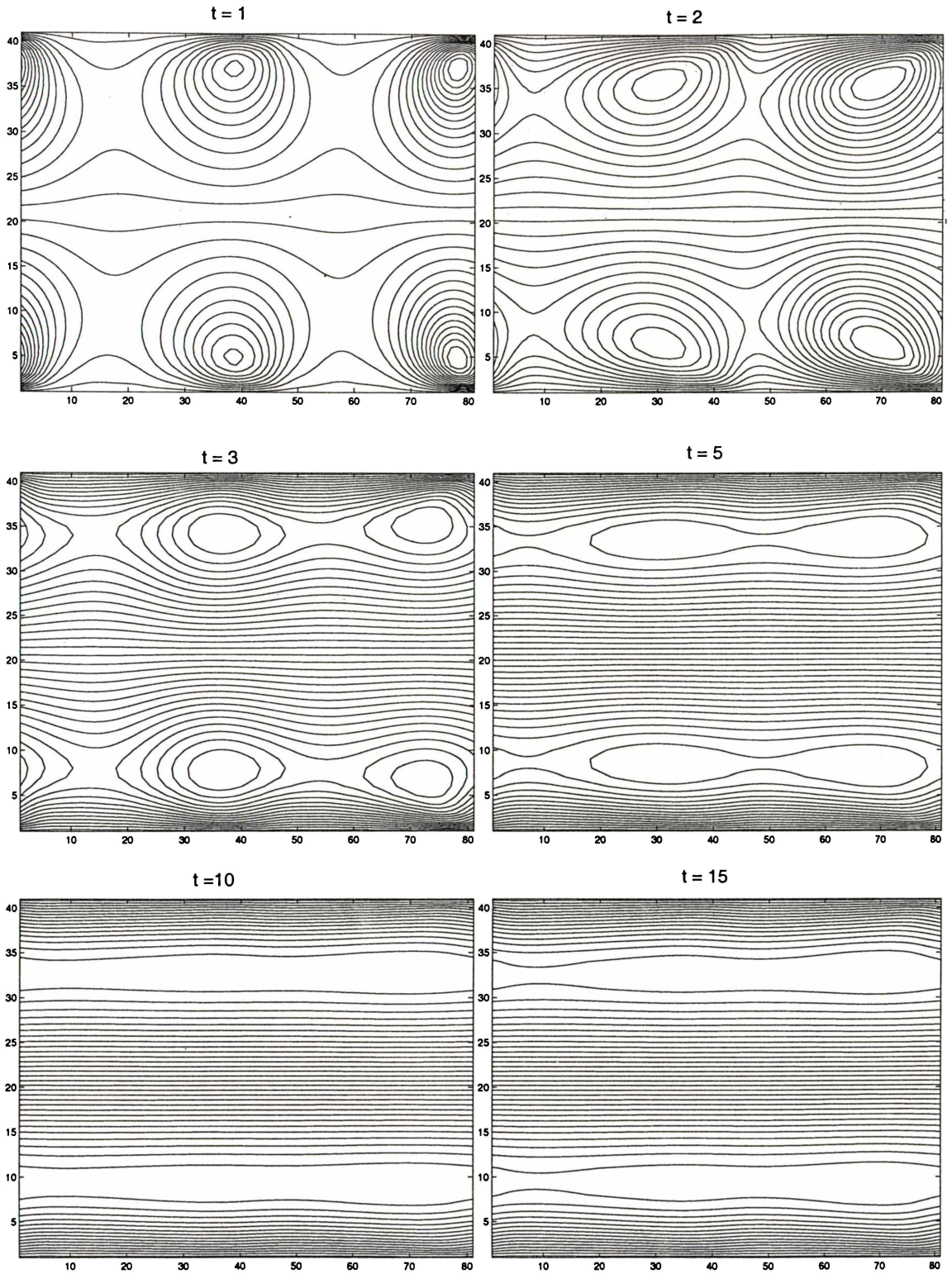

Figure 7.21: Evolution of streamlines for a duration of about a half period.

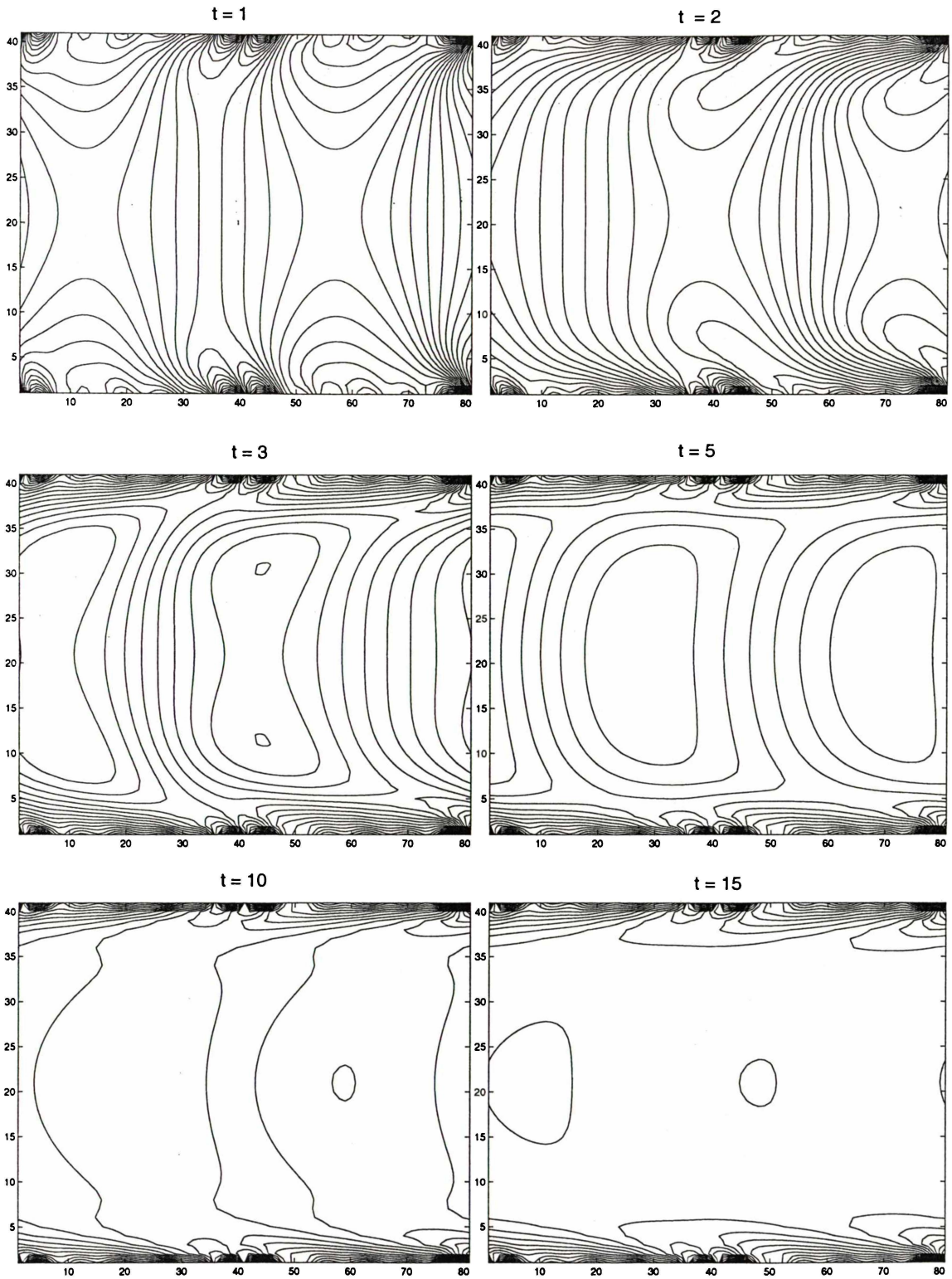

Figure 7.22: Evolution of field lines for about half a period duration.

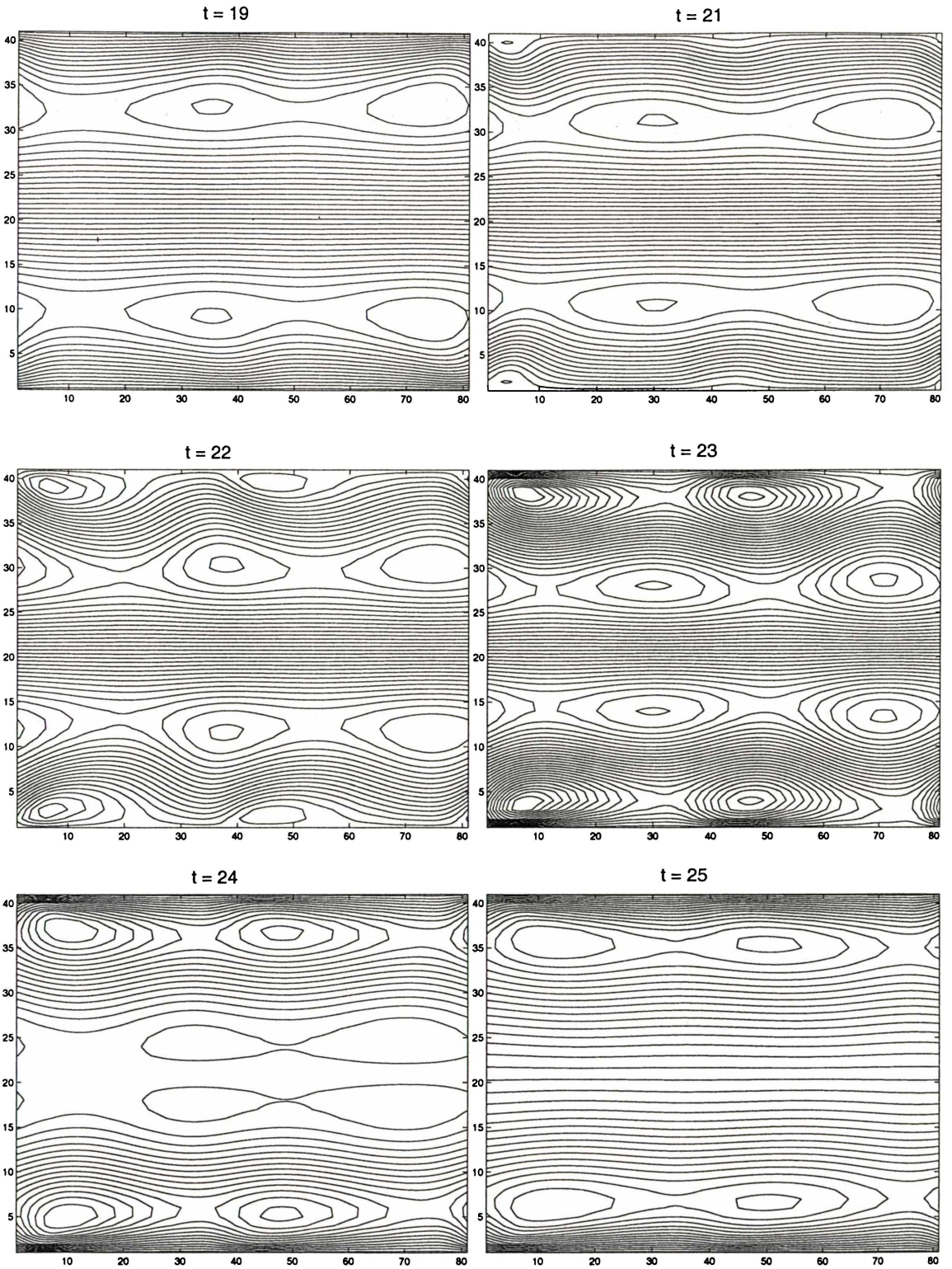

Figure 7.23: Evolution of streamlines around the time where there is a change of direction in the velocity of the applied field.

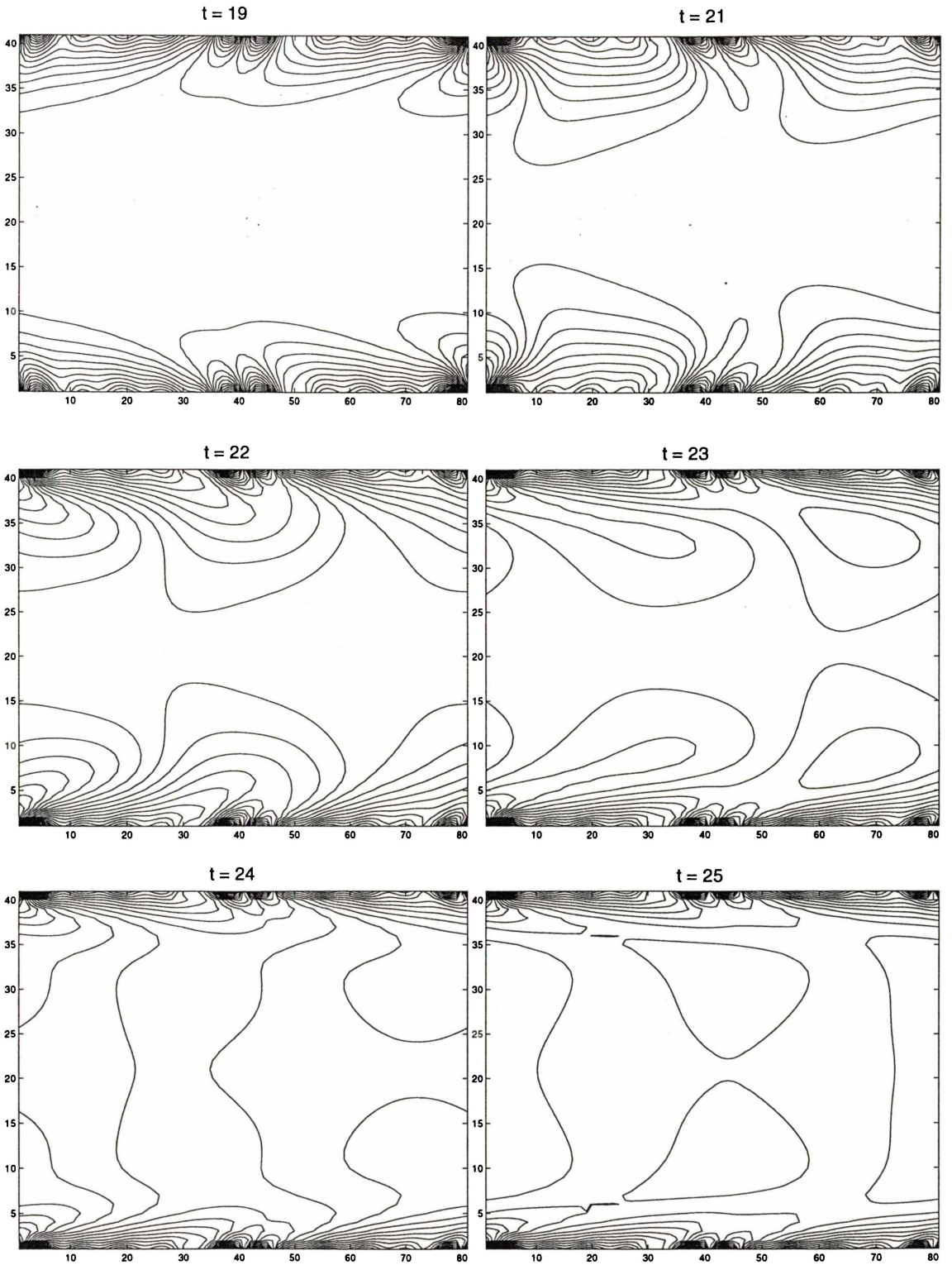

Figure 7.24: Evolution of field lines around the time where there is a change of direction in the velocity of the applied field.

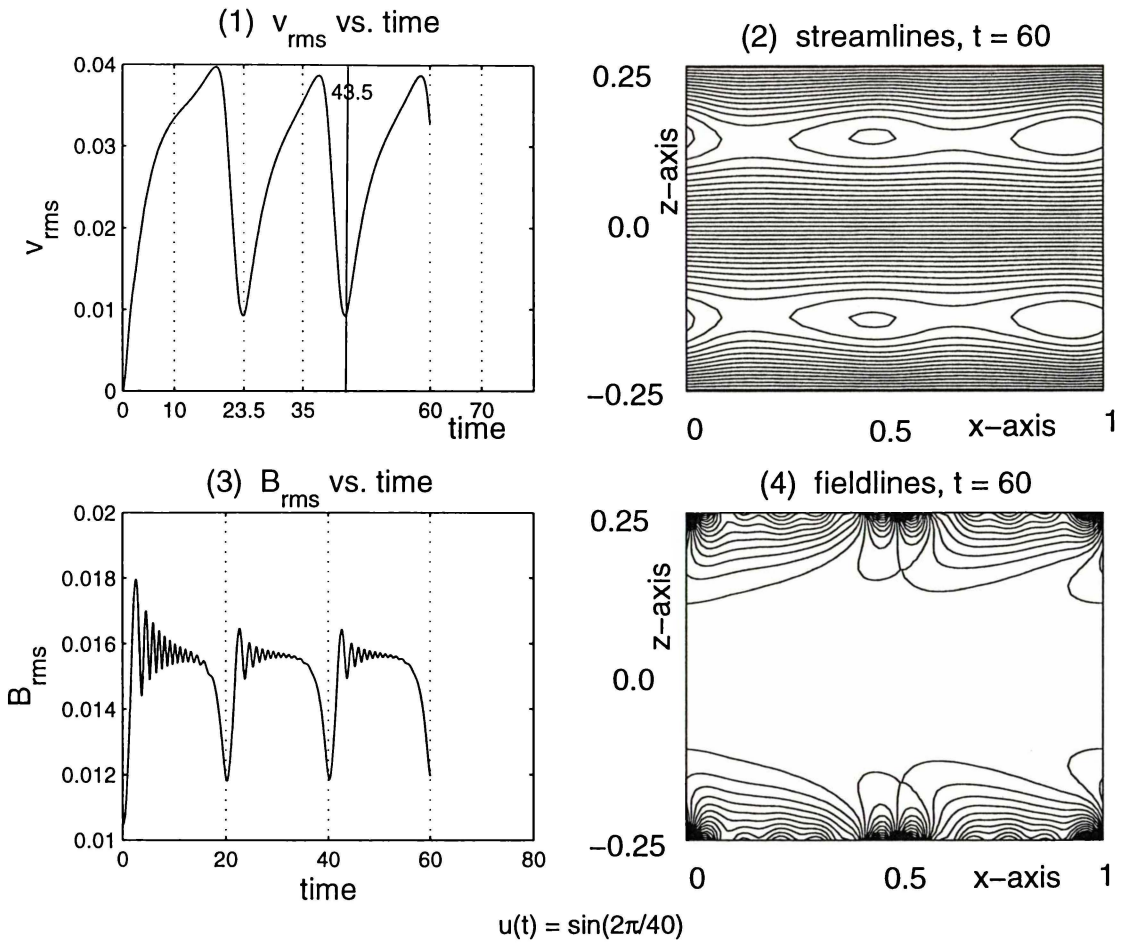

Figure 7.25: (1) v_{rms} vs. time, (2) streamlines at $t = 60$, (3) B_{rms}vs.time, (4) fieldlines at $t = 60$.

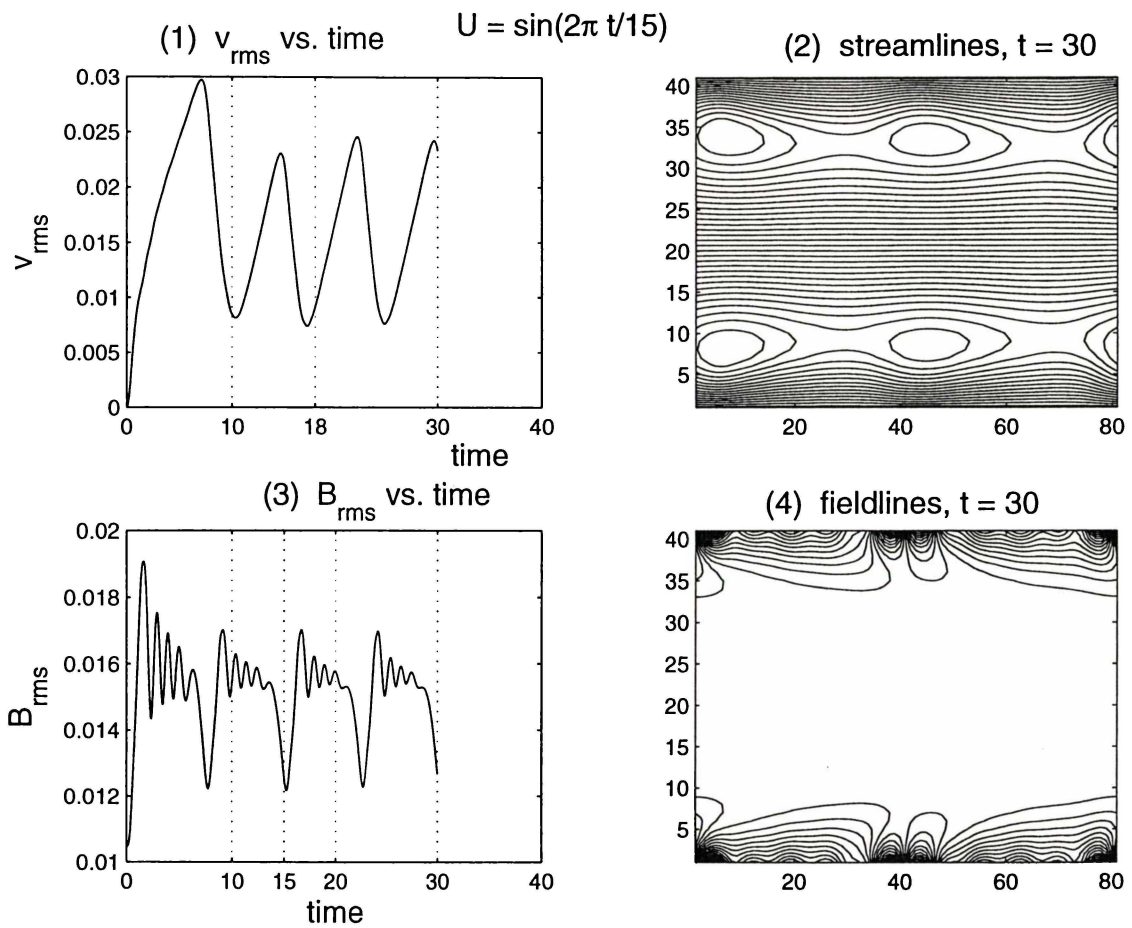

Figure 7.26: (1) v_{rms} vs. time, (2) streamlines at $t = 30$, (3) B_{rms} vs. time, (4) fieldlines at $t = 30$.

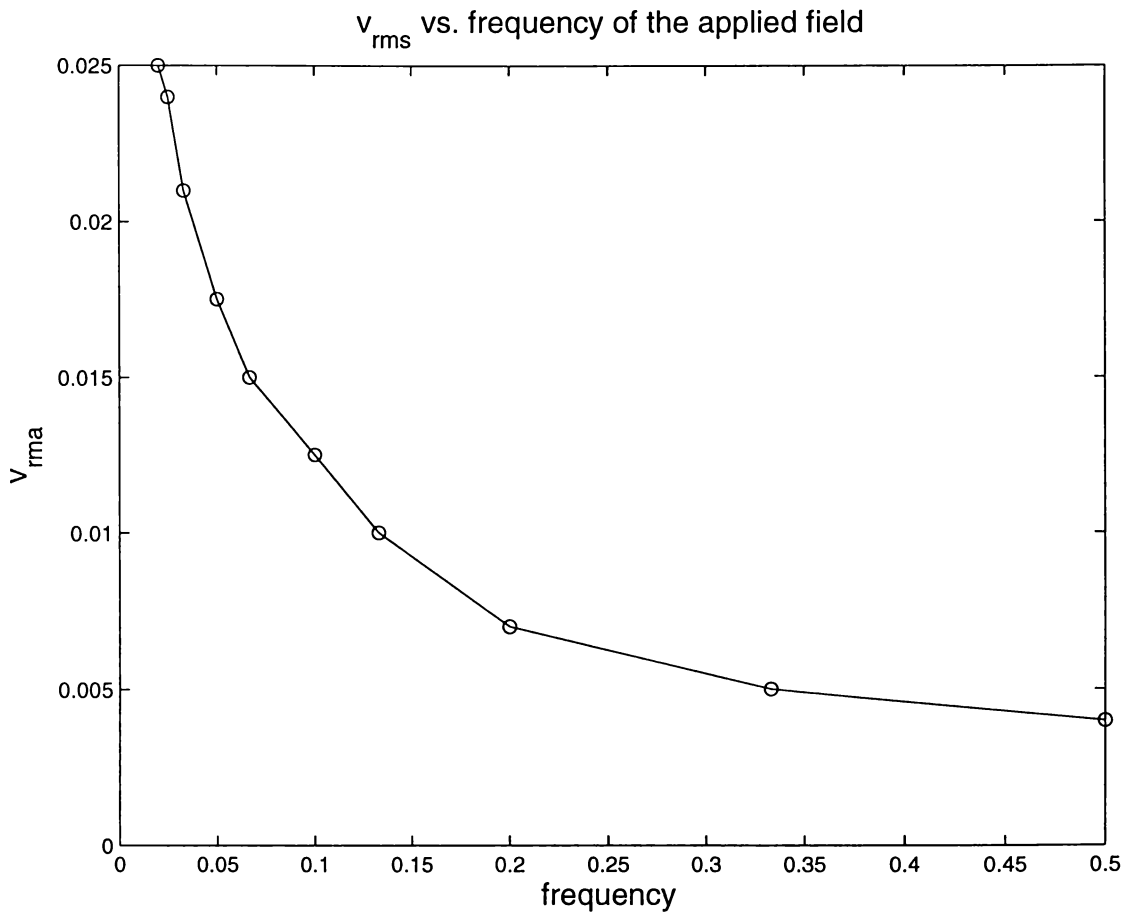

Figure 7.27: Graph of v_{rms} vs. frequency f, of the applied magnetic field, $R = R_m = 800$.

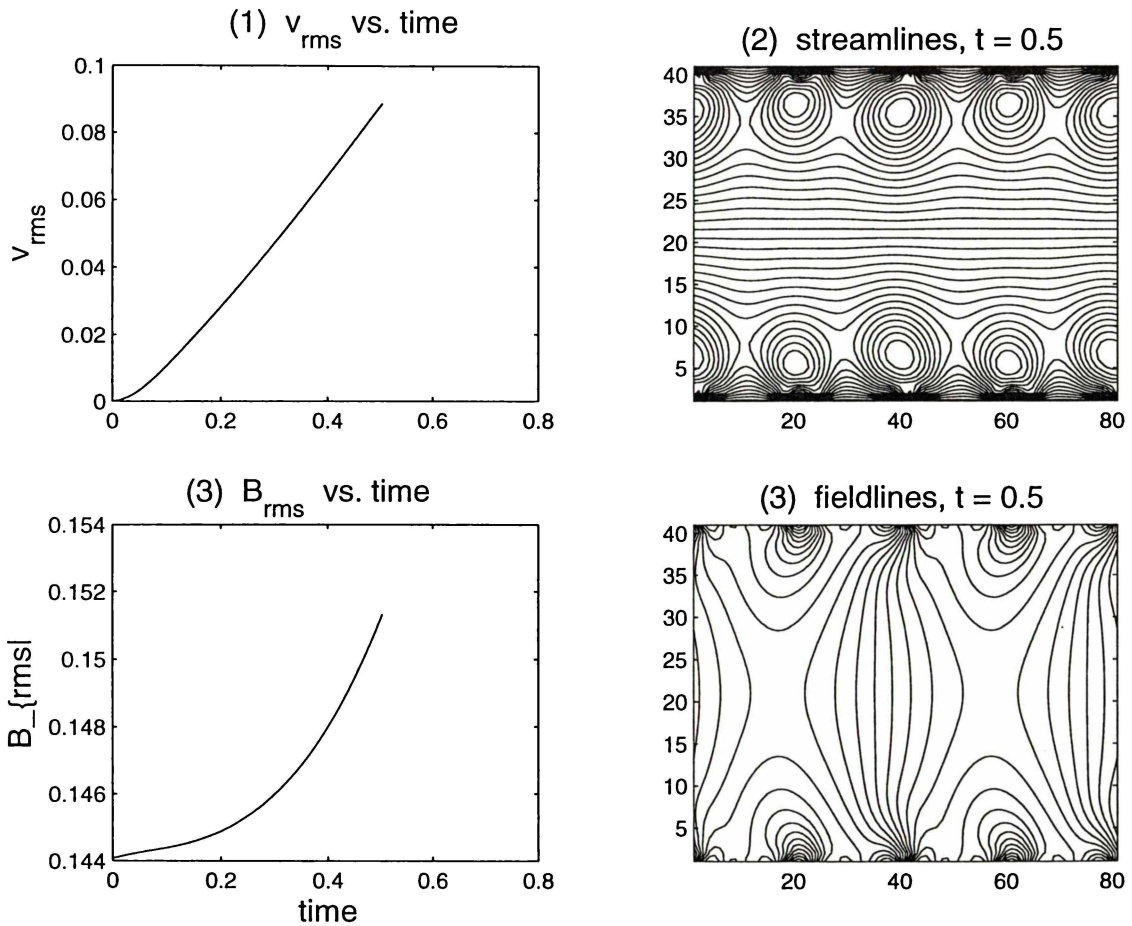

Figure 7.28: (1) v_{rms} vs. time, (2) streamlines at $t = 0.5$, (3) B_{rms}vs.time, (4) fieldlines at $t = 0.5, R = R_m = 800$.

7.5 Conclusions

An effective way of stirring using the technique of moving the magnetic field along a channel is by giving the field a simple harmonic motion. This makes use repeatedly of the vortex-pair-generation which takes place just after the time when the applied velocity changes direction. The vortex-pair-generation stirring lasts about 0.1 of a period. Increasing the frequency of the simple harmonic motion creates more vortices but at the same time also lowers the overall v_{rms} of the flow. It is also found that vortices are created from the moment the field undergoes acceleration. Magnetic field lines are swept by the flow but their inclination reverses when the central flow changes direction. During this process the fieldlines penetration also varies, being a minimum when the fieldlines are mostly parallel to the channel walls.

It can be seen that periodic motion at $R_m \gg 1$ does not tend to sweep away the field so much as uniform motion. Hence, periodic motion can be used as an effective stirring at any finite R_m.

Chapter 8

Conclusions

8.1 Summary

In this thesis we have studied the closed channel fluid flow driven by a periodic multi Fourier-component magnetic field moving at (i) a constant velocity $U\hat{\boldsymbol{x}}$, (ii) a velocity $u(t)\hat{\boldsymbol{x}}$ which is time dependent. The channel is the region $[0,\ 1] \times [-a,\ a]$. In both cases at least a two Fourier-component field is essential to produce a pair of vortices. For effective stirring the channel aspect ratio should be at most half the field wavelength and for a two Fourier-component field the two Fourier components should be approximately equal. It is possible to generate up to four vortices per field wavelength (which means better stirring) by having a ten Fourier-component field where $\boldsymbol{b} = [20.1\ \ 0.1\ \ 0.0\ \ 0.1\ \ 40.1\ \ 0.1\ \ 0.1\ \ 0.1\ \ 40.1\ \ 0.1]$

Due to the closed channel we find that the central flow is always opposite to the direction of the applied magnetic field. The boundary flow is always in the direction of the field. For every pair of eddies one has to be clockwise and the other anti-clockwise.

In chapter 4 we show that vortices become more intense as the channel narrows. It is shown that the root mean square of velocity v_{rms} and the root mean square of vorticity ω_{rms} is proportional to the magnetic interaction parameter $\mathcal{N}$. In all of this work the magnetic Reynolds number and $\mathcal{N}$ were assumed to be small.

In the later sections we focus our attention on the effects of finite R_m. A solid conductor in a moving one Fourier-component field at finite R_m is studied in chapter 5 as a test problem for our finite R_m code. The numerical and analytical results agree well for R_m in the range of 1–1200. We find that as R_m increases the solid metal behaves more and more like a perfect conductor. The flux is swept in the direction of the motion to form a thin layer of flux on the boundaries for large R_m.

In chapter 6 we consider flow at finite R_m. The graph of v_{rms} as a function of R_m has a peak at around $R_m \approx 100$ indicating when we get most effective stirring. Low R_m results in weak induced currents and hence a weak Lorentz force which produces low velocity. On the other hand at large R_m the flux is expelled to form a thin layer of magnetic field on the boundaries which also results in low velocity. Hence it is only logical that effective stirring takes place somewhere between low and high value of R_m. It is shown that the smaller the aspect ratio the better and stronger will be the penetration of the magnetic field. We also show that lowering the value of U to be between $0.5V_A$ and $0.1V_A$ for equal contribution of two Fourier-component source results in better eddies structure but lower mean speed of the flow. At high R_m the velocity of the fluid is rapidly accelerated when the applied velocity is suddenly moved to $U\hat{\boldsymbol{x}}$ at $t = 0$ due to the frozen-in effect.

In the final chapter we consider time-dependent flow. In the case of constant acceleration for the case of ten Fourier components where

$$\boldsymbol{b} = [1.1 \;\; 0.8 \;\; 0.0 \;\; 2.0 \;\; 0.1 \;\; 2.6 \;\; 0.1 \;\; 2.5 \;\; 0.1 \;\; 2.5]$$

we find that eddies are being formed from the moment the magnetic field is moved, gathering in intensity with time. Due to frozen-in effect at high R_m, vortices start to diffuse away in time. Immediately after the velocity of the applied magnetic field changes direction more intense stirring takes place due to the creation of two new pair of vortices which in the end dominate after the original two pairs diffuse away.

We show that an effective method of linear stirring with a periodic magnetic field is to move the field in simple harmonic motion in a channel where the channel width is less than the field wavelength. Increasing the frequency of the motion results in

more frequent stirring but at the expense of lowering the r.m.s. of the velocity of the flow. In the process the magnetic field layers on the boundaries are swept towards the walls or expelled waving to and fro in the direction of the central flow, like plants at the bottom of a stream being swept by the currents.

A feasible method of stirring fluid in a channel in continuous casting process is by giving the multi Fourier-component magnetic field a simple harmonic motion, using the combinations of b_n that give most number of vortex pairs. Optimising the stirring can be done by increasing the frequency of the motion which results in more frequent stirring but lowers the v_{rms} of the flow.

The problem of generating an applied magnetic field moving at a steady velocity or at a velocity dependent on time, $u(t)\hat{\boldsymbol{x}}$, involves practical considerations. One way is by the application of travelling field in the single-belt process (Spitzer and Peşteanu [22]). This method is suitable if the velocity of the belt is constant. The other way is by switching magnetic fields on and off outside the channel of conducting fluid in such a pattern that results in creating the velocity $u(t)\hat{\boldsymbol{x}}$. We think that it is possible with present advances in electronic technology to create a chip that can be programmed to turn on or off or vary the magnetic field according to a function $f(t)$ to give the affect that the magnetic field is moving along the channel at a velocity that is time-dependent, $u(t)\hat{\boldsymbol{x}}$. It should be pointed out that it is not possible for a magnetic field to be instantaneously switched on or off because of the self-inductance of the coils producing the field. Therefore for this method of switching the magnetic field to be feasible the switching on (or off) time has to be relatively short.

8.2 Suggestions for further investigations

It would be interesting to extend this study of stirring electrically conducting fluid to three dimensions, taking account of side and end-wall effects. Another way of stirring is by the travelling pulse field whose velocity is constant or time-dependent

and this can be applied to an open, rectangular or cylindrical channel.

We have considered only a few simple field motions. It should be interesting to study a great variety e.g. the generation of fluid motion in a cylinder by an unsteady applied magnetic field under small magnetic Reynolds number R_m [19], and extend it to the case of finite R_m using numerical methods. It will be advantageous to be able to check the numerical results for the cases that have analytical answers.

Notation

Latin Symbols

$\boldsymbol{B}$	magnetic field (webers m^{-2} or volt sec m^{-2})
$\boldsymbol{E}$	electric field (volts m^{-1})
$\mathbb{R}$	set of real numbers
$\mathbb{I}$	set of integers
$\boldsymbol{J}$	electric current density (amps m^{-2})
$u_a(t)$	the time-dependent speed of the applied magnetic field
$\boldsymbol{v}$	fluid velocity
$\boldsymbol{J} \times \boldsymbol{B}$	Lorentz force
$\hat{\boldsymbol{x}}$	unit vector along the x-axis
$\hat{\boldsymbol{y}}$	unit vector along the y-axis
$\hat{\boldsymbol{z}}$	unit vector along the z-axis
$\boldsymbol{\omega}$	vorticity, $\boldsymbol{\omega} = \nabla \times \boldsymbol{v}$
U	speed of the applied magnetic field
L	wavelength along along the x-axis
V_A	Alfvén speed, $V_A = \frac{B_0}{\sqrt{\mu\rho}}$
R	Reynolds number, $R = \frac{UL}{\nu}$
R_A	Reynolds number based on Alfvén speed, V_A, i.e. $R_A = \frac{V_A L}{\nu}$
R_m	magnetic Reynolds number, $R_m = \frac{UL}{\eta}$
R_{mA}	magnetic Reynolds number based on Alfvén speed, $R_{mA} = \frac{V_A L}{\eta}$
M	Hartmann number, $M = LB_0 \left(\frac{\sigma}{\nu\rho}\right)^{\frac{1}{2}}$
B_0	typical strength of the magnetic field

$\mathcal{N}$	magnetic interaction parameter, $\mathcal{N} = \frac{M^2}{R}$
p	the slightly viscous modification of the sum of the kinetic and magnetic pressures
k	wave number, $k = \frac{2\pi}{L}$
a	half of the width (the aspect ratio, dimensionless) of the channel along the z-axis i.e. $z = \pm a$
a_c	acceleration
K	dimensionless quantity where $K = ka$

Greek Alphabets

μ	magnetic permeability (newton amp^{-2})
σ	electrical conductivity (mho m^{-1}, mho = 1/ohm)
ρ	density (kg/m^3)
η	magnetic diffusivity, or 'magnetic viscosity', $\eta = \frac{1}{\sigma\mu}$
ν	kinematic (shear) viscosity
χ	fluid stream function
ψ	magnetic streamfunction
ϕ	magnetic potential function
ψ	stream function of the magnetic field

References

[1] M. Alonso and J. F. Finn. *Physics.* Addison-Wesley Publishing Company, 1970.

[2] W. Cheney and D. Kincaid. *Numerical Mathematics and Computing, Fourth Edition.* Brooks/Cole Publishing Company, 1999.

[3] I. J. D. Craig and P. G. Watson. Dynamic planar magnetic reconnection solutions for incompressible plasmas. *The Astrophysical Journal*, 516:924–933, 1999.

[4] E. Dalberg. AB Atomenergi, Studsvik, Sweden. *Rep. no. AE-447*, 1972.

[5] P. A. Davidson. Magnetohydrodynamics in materials processing. *Annual Review of Fluid Mechanics*, 31:273–300, 1999.

[6] T. Fujii. State of art electromagnetic processing in Japanese iron and steel industry. In *The 3rd International Symposium on Electromagnetic Processing of Materials EPM2000*, pages 14–19. The Iron and Steel Institute of Japan, 2000.

[7] M. Garnier. Technological and economical challenges facing EPM in the next century. In *The 3rd International Symposium on Electromagnetic Processing of Materials EPM2000*, pages 3–8. The Iron and Steel Institute of Japan, 2000.

[8] J. Heerikhuisen. *Coronal magnetic energy release by current sheet reconnection.* PhD thesis, University of Waikato, 2001.

[9] H. Kamkar and H. K. Moffatt. A dynamic runaway effect associated with flux explusion in magnetohydrodynamic channel flow. *Journal of Fluid Mechanics*, 121:107–122, 1982.

[10] P. D. Lax and B. Wendroff. Systems of conservation laws. *Comm. Pure Appl. Math.*, 13:217, 1960.

[11] H. S. Marr. Electromagnetic stirring in continuous casting of steel. In H. K. Moffatt and M. R. E. Proctor, editors, *Metallurgical Applications of Magnetohydrodynamics*, pages 143–153. London: The Metals Society, 1982.

[12] H. K. Moffatt. On fluid flow induced by a rotating magnetic field. *Journal of Fluid Mechanics*, 22:521–528, 1965.

[13] D. E. Potter. *Computational Physics.* John Wiley & Sons, 1973.

[14] R. D. Richtmyer. *A Survey of Difference Methods for Non-Steady Fluid Dynamics. (Report NCAR-TN 63-2).* Natl. Center for Atmos. Res., Boulder, Colorado, 1962.

[15] R. D. Richtmyer and K. W. Morton. *Difference Methods for Initial-Value Problems. Second edition.* New York/London:Interscience, 1967.

[16] P. J. Roache. *Computational Fluid Dynamics.* Hermosa publishers, 1972.

[17] P. H. Roberts. *An Introduction to Magnetohydrodynamics.* Longmans, 1967.

[18] M. N. Saad. Generation of fluid motion in a channel by an applied magnetic field moving at a constant velocity. Master's thesis, University of Waikato, 1990.

[19] A. D. Sneyd. Generation of fluid motion in a circular cylinder by an unsteady applied magnetic field. *Journal of Fluid Mechanics*, 49:817–827, 1971.

[20] A. D. Sneyd. Fluid flow induced by a rapidly alternating or rotating magnetic field. *Journal of Fluid Mechanics*, 92:35–51, 1979.

[21] A. D. Sneyd. Theory of electromagnetic stirring by AC fields. *IMA Journal of Mathematics Applied in Business & Industry*, 5:87–113, 1993/4.

[22] K. H. Spitzer and O. Peşteanu. Application of travelling magnetic fields in metallurgy. In *The 3rd International Symposium on Electromagnetic Processing of Materials EPM2000*, pages 409–414. The Iron and Steel Institute of Japan, 2000.

[23] E. Takeuchi, M. ZeZe, T. Toh, and S. Mizoguchi. Applied MHD in the process of continuous casting. In J. W. Szekely, J. W. Evans, K. Blazek, and N. El-Kaddah, editors, *Magnetohydrodynamics in Process Metallurgy.* TMS, 1992.

[24] M. Witkowski, P. Marty, and J. S. Walker. Liquid-metal flow in a finite-length cylinder with a high-frequency rotating magnetic field. *Journal of Fluid Mechanics*, 436:131–143, 1999.

[25] C. S. Yih. *Fluid Mechanics, A concise introduction to the theory.* McGraw-Hill Book Company, 1969.